GFZ

Helmholtz Centre
POTSDAM

HELMHOLTZ CENTRE POTSDAM
GFZ GERMAN RESEARCH CENTRE
FOR GEOSCIENCES

Sadegh Modiri

On the Improvement of Earth Orientation Parameters Estimation

Using Modern Space Geodetic Techniques

Scientific Technical Report STR - Data 21/10

www.gfz-potsdam.de

HELMHOLTZ
RESEARCH FOR GRAND CHALLENGES

Recommended citation

Modiri, S. (2021): On the improvement of earth orientation parameters estimation: using modern space geodetic techniques, PhD Thesis, (Scientific Technical Report STR; 21/10), Potsdam: GFZ German Research Centre for Geosciences. https://doi.org/10.48440/GFZ.b103-21107

Originally published as

Modiri, S. (2021): On the improvement of earth orientation parameters estimation: using modern space geodetic techniques, PhD Thesis, Berlin: Technische Universität. https://doi.org/10.14279/depositonce-11975

Imprint

Helmholtz Centre Potsdam
GFZ German Research Centre for Geosciences
Telegrafenberg
D-14473 Potsdam

Published in Potsdam, Germany
July 2021

DOI: https://doi.org/10.48440/GFZ.b103-2117
URN: urn:nbn:de:kobv:b103-2117

This work is published in the GFZ series Scientific Technical Report (STR) and electronically available at GFZ website https://www.gfz-potsdam.de

On the Improvement of Earth Orientation Parameters Estimation

Using Modern Space Geodetic Techniques

vorgelegt von
M.Sc.
Sadegh Modiri
geb. in Teheran

von der Fakultät VI - Planen Bauen Umwelt
der Technischen Universität Berlin
zur Erlangung des akademischen Grades

Doktor der Ingenieurwissenschaften
-Dr.-Ing.-

genehmigte Dissertation

Promotionsausschuss:
Prof. Dr.-Ing. Frank Neitzel:
Prof. Dr.-Ing. Dr. h.c. Harald Schuh:
Prof. José M. Ferrándiz:
Prof. Alireza A. Ardalan:
:
:
Tag der wissenschaftlichen Aussprache: 26. Januar 2021

Berlin 2021

Zusammenfassung

Die Erde dreht sich um ihre Rotationsachse auf unregelmäßige Art und Weise. Die Erdrotationsachse und ihre Orientierung im Raum variieren in Bezug auf das Referenzsystem (sowohl im terrestrischen wie auch im zälestischen System) aufgrund des breiten Spektrums von Prozessen, die zur Rotationsanregung beitragen. Daher kann die Untersuchung der Erdrotation wesentliche Informationen über das Erdsystem liefern. Weltraumgestützte geodätische Sensoren liefern Informationen über erdgebundene Orientierungsparameter (EOP), die das Verhalten der Erde im Weltraum vollständig beschreiben. EOP werden für verschiedene Bereiche und Anwendungen, wie beispielsweise für grundlegende astronomische und geodätische Referenzsysteme, benötigt. Des Weiteren sind sie auch für die präzise Bestimmung von Satellitenorbits und die weltraumgestützten Navigation, bis hin zu Anwendungen im Katastrophenschutz von Bedeutung.

In den letzten drei Jahrzehnten zeigen sich bereits die negativen Auswirkungen des Klimawandels auf Biosphäre, menschliche Aktivitäten und sozioökonomische Aspekte. Der Klimawandel unterliegt Fluktuationen und verändert die Wettermuster, wie z.B. die Niederschlagsverteilung, sowie Meeres- und Ozeanspiegel. Er bedroht aber auch die biologische Vielfalt der Ökosysteme, die Ernährungssicherheit, die menschliche Gesundheit und verschlimmert Naturkatastrophen. Die Intensität und Häufigkeit von Naturgefahren werden zunehmen, hierbei ist ihre Verteilung aufgrund von Klimaveränderungen allerdings unregelmäßig; auch der Grad von Schadensanfälligkeiten und die Einteilung von Risikozonen werden sich zukünftig ändern. Die Analyse von Naturgefahren, wie atmosphärische und hydrologische Ereignisse, kann zur Verbesserung des Krisenmanagements beitragen. Daher werden Satellitenbeobachtungen und simulierte Daten, die von verschiedenen atmosphärischen Modellen abgeleitet werden, für die Gefahr- und Risikomodellierung benötigt; dies kann Frühwarn- und Vorhersagesysteme unterstützen. Obwohl kontinuierliche Sensormessungen und Archivdaten (historische Daten/Klimadaten) für die Wettervorhersage in entwickelten Ländern zur Verfügung stehen, kamen es im Mai 2016 in der Nähe von Stuttgart in Süddeutschland bei einer katastrophalen Überschwemmung zu Verlusten von Menschenleben, die möglicherweise durch ein präzises Wetterwarnsystem vermeidbar gewesen wären.

Eine Echtzeitschätzung der geodätischen Weltraumtechnik wäre notwendig, um sie als Eingangsdaten in Wettervorhersagemodellen zu verwenden. Für die Analyse von raumgeodätischen Techniken in (nahezu) Echtzeit sind Vorhersagen der EOP unerlässlich. EOP werden durch das Rapid Service Prediction Centre des International Earth Rotation and Reference Systems Service (IERS) am USNO, Washington D.C., mit einer Verzögerung von Stunden bis Tagen zur Verfügung gestellt. Demzufolge wurden in der Vergangenheit mehrere Methoden für die EOP-Vorhersage entwickelt und angewendet. Die Genauigkeit dieser EOP-Vorhersagen ist jedoch

nach wie vor - selbst für einen Vorhersagezeitraum von nur wenigen Tagen - unbefriedigend. Um die Genauigkeit der EOP-Vorhersage zu verbessern, beschäftigt sich die vorliegende Studie mit der Untersuchung von der Vereinbarkeit von Erdrotationstheorien mit Beobachtungen. Darüber hinaus wird das Potenzial verschiedener geophysikalischer Phänomene analysiert, um die Wechselwirkungen verschiedener Prozesse, die die zeitabhängige Anregung der Erdrotation beeinflussen, besser zu verstehen.

Die meisten Theorien und Lösungen zur Erdrotation basieren auf der Lage der Hauptträgheitsachsen der Erde (PAI). Diese Position wird durch die Stokes-Koeffizienten zweiten Grades des Geopotentials, das mit Hilfe der Satellitenmission Gravity Recovery and Climate Experiment (GRACE) und der Satelliten-Laser-Entfernungsmessung (SLR) genau beobachtet wird, definiert. In dieser Studie wird zum ersten Mal die Entwicklung der Trägheitsachsen der Erde analysiert. Bemerkenswert an den vorgestellten Ergebnissen ist, daß sich die Trägheitsachsen während der Untersuchungsperiode nicht um eine mittlere Position, die in einem bestimmten terrestrischen Bezugsrahmen festgelegt ist, bewegen, sondern sich in nicht zu vernachlässigender Weise von ihrem ursprünglichen Position entfernen.

Darüber hinaus schlägt diese Studie einen neuartigen hybriden Ansatz zur EOP-Vorhersage vor. Es gibt eine gut eingeführte stochastische Methode, die “kopula-basierte Analyse”, die wir mit der “Singulär-Spektrum-Analyse” (SSA) für die EOP-Vorhersage kombiniert haben . Wir analysierten das Potenzial kopula-basierter Methoden zur Vorhersage von Erdrotationsparametern, die aus der Kombination verschiedener geodätischer Satellitensensoren und aus anderen geophysikalischen Parametern, wie z.B effektiven Drehimpulsen, abgeleitet werden. Die Kopula ist eine statistische Methode, die lineare und nicht-lineare Beziehungen zwischen zwei oder mehreren Variablen nutzt, indem eine theoretische Kopula-Funktion an eine empirische, bivariate oder multivariate Verteilungsfunktion angepasst wird. Wir haben eine hybride Vorhersagemethode entwickelt, die auch auf andere geophysikalische Parameter angewendet werden kann.

In dieser Studie wird der Zusammenhang zwischen der Bewegung des Himmelspols (CPM) und dem geomagnetischen Feld (GMF) untersucht, um die derzeitigen CPM-Vorhersagemethoden zu verbessern. Während des letzten Jahrzehnts wurden mehrere Untersuchungen durchgeführt, um eine mögliche Verbindung zwischen polaren Bewegungen und geomagnetischen Ausbrüten - hierbei handelt es sich um rasche Veränderungen der säkularen Variationen des GMF - zu erörtern. Weniger Aufmerksamkeit wurde jedoch den Auswirkungen der GMF-Änderungen auf die CPM, z.B. der Wechselbeziehung der geomagnetischen Ausbrüte, des geomagnetischen Dipolmoments, der geomagnetischen Feldelemente und der CPM-Variationen, gewidmet. In dieser Studie verwenden wir CPM-Zeitreihen, die aus Beobachtungen der Very Long Baseline Interferometry (VLBI) gewonnen wurden und aktuelle GMF-Daten, um die Korrelation zwischen CPM und GMF zu untersuchen. Unsere vorläufigen Ergebnisse zeigen einige auffallente Gemeinsamkeiten in den CPM- und GMF-Variationen, die das Potenzial besitzen, unser Verständnis des GMF-Beitrags zur Erdrotation zu verbessern. Alles in allem veranschaulichen die Ergebnisse mathematisch die Kohärenz zwischen den GMF-Parametern und der CPM und weisen damit perspektivisch den Weg für eine Verbesserung der EOP-Produkte.

Abstract

The Earth is rotating around its rotation axis in an irregular manner. The Earth rotation axis and its orientation in space vary with respect to the reference system (both the terrestrial and the celestial) due to the wide range of processes that contribute to the rotation excitation. Therefore, the study of the Earth rotation can provide essential information concerning the Earth system. Spaceborne geodetic sensors can determine Earth orientation parameters (EOP), which fully describe Earth's behaviour in space. The EOP are needed for several fields and applications such as fundamental astronomical and geodetic reference systems, precise satellite orbit determination, space navigation, and disaster prevention.

Over the past three decades, climate change has caused undesirable alterations in living organisms, human activities, and socio-economic aspects. Climate change is fluctuating and alters weather patterns such as precipitation patterns and sea and ocean levels. It also threatens the biodiversity of ecosystems, food security, and human health, and exacerbates natural disasters. The intensity and frequency of natural hazards are increasing with erratic distribution due to changes in the climate. Also, the level of vulnerability and zonation of risk are changed. Analysis of natural hazards, such as atmospheric and hydrological events, can help improve crisis management. Therefore, satellite observation data and simulated data derived from different atmospheric models are needed in order to model different types of hazards and risks, which can help early warning and prediction systems. Even though continuous sensor measurements and archive data (historical data/climate) are used for weather forecasting in developed countries, deadly flooding happened close to Stuttgart in southern Germany in May 2016, which might be avoided by a precise weather warning system. Therefore, real-time space geodetic technique data estimation is necessary to use as input data in weather prediction models. For the analysis of space geodetic techniques in (near) real-time, predictions of the EOP are required. EOP are made available by the International Earth Rotation and Reference Systems Service (IERS) Rapid Service Prediction Centre at USNO, Washington D.C., with a delay of hours to days. Accordingly, in the past, several methods were developed and applied for the EOP prediction. However, the accuracy of EOP prediction is still unsatisfactory, even for prediction of just a few days in the future.

To improve the EOP prediction accuracy, this study investigates the consistency between Earth rotation's theories and observations. Moreover, the potentials of different geophysical phenomena are examined to better understand the interaction of different processes that affect the Earth rotation excitation with the time. Most of the Earth's rotation theories and solutions are based on the location of the Earth's principal axes of inertia (PAI). That location is defined by the second-degree Stokes coefficients of the geopotential, which are accurately observed by the Gravity Recovery and Climate Experiment (GRACE) and satellite laser ranging (SLR).

In this study, the evolution of the Earth's axes of inertia is analyzed for the first time. The presented results are remarkable, as the inertia axes do not move around a mean position fixed to a given terrestrial reference frame in the study period, but drift away from their initial location in a non-negligible manner.

Moreover, this study proposes a novel hybrid approach to predict EOP. There is a well-introduced stochastic method called copula-based analysis, and I combined it with singular spectrum analysis (SSA) for EOP prediction. I analyzed the potential of copula-based methods for predicting Earth rotation parameters that are derived from the combination of different satellite geodetic sensors and from other geophysical parameters like effective angular momentums. The copula is a statistical method that exploits linear and non-linear relationships between two or more variables by fitting a theoretical copula function into an empirical bivariate or multivariate distribution function. I introduced a hybrid prediction method that can be applied to other geophysical parameters is introduced in this thesis.

In this study, the interconnection between the celestial pole motion (CPM) and geomagnetic field (GMF) is investigated to improve the current CPM prediction methods. During the last decade, several investigations have been conducted in order to discuss a possible interconnection of polar motion and geomagnetic jerks, which are rapid changes in GMF secular variations. However, less attention has been paid to the impact of the GMF changes on the CPM, e.g., the interrelation of the geomagnetic jerks, geomagnetic dipole moment, geomagnetic field elements, and CPM variations. In this study, I use the CPM time series obtained from very long baseline interferometry (VLBI) observations and the latest GMF data to explore the correlation between CPM and the GMF. Our preliminary results revealed some impressive common features in the CPM and GMF variations, which show the potential to improve our understanding of the GMF's contribution to the Earth's rotation. All in all, the results mathematically illustrate the coherency between the GMF parameters and CPM, which helps improve EOP products.

Acknowledgements

In the beginning, from the bottom of my heart, I would like to express my sincere gratitude to my supervisor Prof. Dr.-Ing. Dr. h.c. Harald Schuh for his kind support, warm encouragements, smart guidance, and valuable comments. He established a friendly research environment at Dep.1 Geodesy, Helmholtz Centre Potsdam, GFZ German Research Centre for Geosciences. Also, he gave me the freedom to create my own path and network. What I learned from him is not only scientific knowledge but also the way of thinking. For all of this, I owe him more than I can describe.

I would like to express my deep gratitude to Prof. José M. Ferrándiz for giving me the opportunity to work in his department at the University of Alicante, Spain. His precious comments have opened new doors for research possibilities, from which my thesis benefited tremendously. My gratitude extends to Prof. Alireza A. Ardalan for agreeing to evaluate this thesis.

Special thanks to Dr. Robert Heinkelmann, head of the VLBI group at GFZ, whose door was always opened for consultations, advice, and discussions. His encouragement, tolerance, and talent provided a conducive working environment.

I would like to express my genuine thanks to Santiago Belda for his immense support and consultation. He is one of the main instrumental in getting me to this point. The idea of this Ph.D. research has been laid through discussions with him. I am deeply grateful to my dear Brother Ehsan Modiri for his generous help and non-stop support since 1989. He always provides solutions to my questions.

I also much appreciate all of my colleagues at GFZ for their help, feedback, and emergency assistance. I would like to give my special thanks to my roommates, Kyriakos Balidakis, for his positive energy, James Andeson, and Chaiyaporn Kitpracha for their friendly supports. Many thanks go to my former roommates Maria Karbon, Benedikt Soja, Santiago Belda, and Minghui Xu. I would like to express my dear VLBI group members, Georg Beyerle, Susanne Glaser, Okky Syahputra Jenie, Susanne Lunz, and Nicat Mammadaliyev, and my dear friend Shrishail Raut, as well as our Honorary member, Franz Kuglitsch.

Being at GFZ helps me to develop my network, and I would like to thank Prof. Mahdi Motagh, Milad Asgharimehr, Mahmud Haghshenas, and Mostafa Hoseini for their kind help and support. I would like to thank all my friends, especially Milad Moharekpour and Meysam Rauofi, for their support during the last year.

Last but not least, I am very thankful for my two lifelines (parents) and my beloved siblings Elham and Ehsan for all the encouragement and support they gave to me, and this thesis is dedicated to them.

Table of Contents

Title Page i

Zusammenfassung iii

Abstract v

List of Figures xiii

List of Tables xvii

List of Abbreviations xix

1 Introduction 1
- 1.1 Overview . . . 1
- 1.2 Motivation and Research Objectives . . . 3
  - 1.2.1 State of the Art . . . 3
  - 1.2.2 Research Questions . . . 5
  - 1.2.3 Innovation . . . 5
- 1.3 Structure of the Dissertation . . . 5
- 1.4 Supporting Publications . . . 7

2 Methodology 9
- 2.1 Copula-based Analysis . . . 9
  - 2.1.1 Sklar's Theorem . . . 9
  - 2.1.2 Copula Properties . . . 10
  - 2.1.3 Frecht-Hoffding Bounds . . . 10
  - 2.1.4 Empirical Copula . . . 10
  - 2.1.5 Archimedean Copula . . . 11
    - 2.1.5.1 Archimedean 12 Copula . . . 11
    - 2.1.5.2 Archimedean 14 Copula . . . 12
    - 2.1.5.3 Clayton Copula . . . 13
    - 2.1.5.4 Frank Copula . . . 13
    - 2.1.5.5 Gumbel Copula . . . 14
    - 2.1.5.6 Joe Copula . . . 14
  - 2.1.6 Copula Parameter θ Estimation and Classical Dependence Parameter . . . 15
  - 2.1.7 Copula-based Simulation Random Data . . . 16

2.2 Singular Spectrum Analysis . . . 17
2.3 Combination of Copula-based Analysis and SSA . . . 18
2.4 Wavelet Analysis . . . 20
2.4.1 Wavelet Coherence Analysis . . . 21

3 Theory, Fundamental Definition, and Data sets 23
3.1 Earth Motion . . . 23
3.2 International Celestial Reference System (ICRS) . . . 24
3.3 International Terrestrial Reference System (ITRS) . . . 25
3.4 Reference Frames . . . 25
3.5 Earth Orientation Parameters (EOP) . . . 26
3.6 Geomagnetism Field Data and Model . . . 27
3.6.1 Geomagnetic Field Elements . . . 27
3.6.2 Geomagnetic Field Models . . . 28
3.6.3 CHAOS – A Satellite-based Geomagnetic Field Model . . . 29

4 Space Geodetic Techniques for EOP Determination 31
4.1 Introduction . . . 31
4.2 Doppler Orbitography and Radiopositioning Integrated by Satellite . . . 32
4.3 Global Navigation Satellite System . . . 33
4.4 Laser Ranging . . . 35
4.4.1 Lunar Laser Ranging . . . 35
4.4.2 Satellite Laser Ranging . . . 36
4.5 Very Long Baseline Interferometry . . . 37

5 Earth Rotation Theory Versus Space Geodetic Techniques Observation 41
5.1 Introduction . . . 41
5.2 Analytical Method . . . 42
5.2.1 Basic Equations . . . 42
5.2.2 Introduction of An Auxiliary Terrestrial Reference Frame (ATRF) . . . 43
5.2.3 Expression of the Earth's Principal Axes . . . 43
5.2.4 Rotation Providing the Principal Axes . . . 44
5.3 Data Analysis . . . 45
5.4 Results . . . 45
5.5 Discussion . . . 48
5.6 Conclusions and Outlook . . . 50

6 A New Hybrid Method for EOP Prediction 53
6.1 Introduction . . . 53
6.2 First Group: PM Prediction . . . 54
6.2.1 Data Description . . . 55
6.2.2 Data Analysis . . . 55
6.2.2.1 SSA Periodic Terms Estimation . . . 55
6.2.2.2 Copula Anomaly Modeling . . . 57
6.2.2.3 Estimating Empirical Copula . . . 59

6.2.2.4 Fitting A Theoretical Copula Function 60
6.2.3 365 Days Ahead Prediction 61
6.2.4 Discussions of Results 63
6.3 Second Group: LOD Prediction 64
6.3.1 Data Description 65
6.3.1.1 Length of Day (LOD) 65
6.3.1.2 Effective Angular Momentum (EAM) Functions 66
6.3.2 Data Analysis 67
6.3.3 Data Processing and Analysis 67
6.3.3.1 Copula-based Joint Distribution Function of LOD and EAM_Z 67
6.3.3.2 EAM_Z Prediction 68
6.3.3.3 LOD Prediction from Predicted EAM_Z Using the Calibrated Copula + SSA Model 70
6.3.4 Discussion of the Results 71
6.4 Summary and Conclusion 73

7 Interconnection Between Celestial Pole Motion and Earth's Magnetic field 75
7.1 Introduction 75
7.2 Data Set 77
7.2.1 FCN Data 77
7.2.2 GMF Data 77
7.2.2.1 GMJ 77
7.2.2.2 Magnetic Dipole Moment 78
7.2.2.3 Geomagnetic Field Model 80
7.3 FCN Prediction Error and GMJ 82
7.4 FCN and GMF Models 83
7.4.1 Geomagnetic Spherical Harmonic Coefficients (SHC) and FCN 83
7.4.2 FCN and Magnetic Dipole Moment 87
7.4.3 Near-Earth Magnetic Field and FCN 91
7.5 Discussion 99

8 Conclusions and Remarks 103

References 109

List of Figures

1.1 Main pillars of geodesy . . . 1
1.2 Schematic of the processes that contribute to the excitation of changes in the Earth's rotational state . . . 2
1.3 Schematic of Earth orientation parameters . . . 3
1.4 EWS send people relevant information before a disaster which is a major element of disaster risk reduction . . . 4
1.5 PhD research objectives . . . 6

2.1 Archimedean 12 Copula . . . 12
2.2 Archimedean 14 Copula . . . 12
2.3 Clayton Copula . . . 13
2.4 Frank Copula . . . 14
2.5 Gumbel Copula . . . 15
2.6 Joe Copula . . . 15
2.7 Copula + SSA algorithm for modeling and predicting the time series by using the information within the time series . . . 19
2.8 Copula + SSA algorithm for modeling and predicting the time series by using the information within the time series and other variables . . . 20

3.1 Earth at the Celestial sphere . . . 24
3.2 ITRF 2014 network sites (VLBI, SLR, DORIS, and GNSS) . . . 25
3.3 Sources coordinates of the ICRF3 . . . 26
3.4 Earth's magnetic field extends from the Earth's interior . . . 27
3.5 Earth magnetic field coordinate system: The three orthogonal components X, Y, and Z . . . 28

4.1 A simplified scheme for different space geodetic techniques . . . 32
4.2 Schematic diagram of GNSS segments . . . 34
4.3 Schematic of LLR . . . 35
4.4 Schematic diagram of SLR . . . 36
4.5 Principle of VLBI observation: The main observable is the difference in the arrival times of a plane wavefront emitted by an extragalactic radio source in direction $\hat{k}$ at two VLBI telescopes . . . 38

5.1 Results derived from the RL06 CSR Stokes coefficients with monthly resolution. Upper panel: Equivalent rotations [cm] R_x, R_y, and R_z from ATRF to PAI frame (in green, from left to right) and fit linear functions (in black). Middle panel: The residuals are also given in [cm]. The lower panel shows the results of the fast Fourier analysis. 47
5.2 Results derived from the RL06 CSR Stokes coefficients with monthly resolution. 47
5.3 Equivalent rotation (in cm) of R_x, R_y, and R_z from ATRF to PA using the data from DGFI solution 48
5.4 Joint plots of the rotations from ATRF to PAI frames derived from the RL06 CSR and SLR DGFI-TUM Stokes coefficients with their respective 95% confidence regions 51

6.1 Daily PM time series from 1990 to the present 56
6.2 Spectral analysis of the PM_x and PM_y using FFT 57
6.3 Number of singular values and vectors applied in modeling polar motion to achieve 1 mas degree of accuracy 57
6.4 PM, SSA reconstructed, and anomaly time series 58
6.5 Marginal distribution's goodness-of-fit test for PM_x and PM_y 59
6.6 Scatter plot(left) two adjacent columns in the residual matrix. The empirical Copula (right) is estimated based on the dependency structure of two columns. 61
6.7 Theoretical Copula are fitted to the empirical Copula 61
6.8 Mean value of MAE of PM_x and PM_y for 2003, 2006, and 2009 62
6.9 Absolute errors of the predicted PM_x and PM_y using SSA, SSA+Gumbel Copula, SSA+Clayton Copula, SSA+Frank Copula compared with Bulletin A product 64
6.10 Improvement of PM_x and PM_y prediction using SSA + Copula-based model . 65
6.11 Scheme of the Copula + SSA model for LOD prediction (Calibration step) . . 66
6.12 The EAM_Z being the sum of mass and motion terms of AAM, HAM, and OAM $(Z_{AAM} + Z_{HAM} + Z_{OAM})$. 66
6.13 Time series of LOD and $(Z_{AAM} + Z_{HAM} + Z_{OAM})$ between 1996 and 2008 . . 67
6.14 Scatter plot of LOD, its empirical Copula, and theoretical Copula 68
6.15 Scheme of the SSA + Copula model for PM prediction 69
6.16 Spectral analysis of the LOD and $Z_{AAM} + Z_{HAM} + Z_{OAM}$ using FFT 69
6.17 The original time series and the reconstructed time serie, and the difference between the original and reconstructed time serie 70
6.18 Scatter plot, empirical Copula, Frank Copula of two adjacent columns in the residual matrix 70
6.19 MAE of $(Z_{AAM} + Z_{HAM} + Z_{OAM})$ prediction 71
6.20 Scheme of the Copula + SSA model for LOD prediction using the calibrated Copula + SSA model 71
6.21 Absolute errors of the predicted LOD Copula + SSA 72
6.22 Absolute errors of the predicted LOD using Copula + SSA 73

7.1 CPO and FCN in X and Y direction 78

7.2 Normalized FCN products and their derivatives 79
7.3 FFT analysis of FCN products 80
7.4 DM and normalized dDM/dt, and d^2DM/dt^2 81
7.5 Geomagnetic's SHC up to degree and order 20 81
7.6 Time series of the normalized FCN amplitude and phase for the B16 model. The dashed box indicates GMJ and SA pulses at the core surface. The red color shows the confirmed GMJ. The yellow shows questionable SA of the GMJ. The green indicates a significant global SA of the GMF. 83
7.7 Time series of the normalized FCN offsets for the B16 model. The dashed box indicates GMJ and SA pulses at the core surface. The red color shows the confirmed GMJ. The yellow shows questionable SA of the GMJ. The green indicates a significant global SA of the GMF. 84
7.8 FCN prediction errors and the GMJ epochs. The black curve is the FCN amplitude. 85
7.9 PCA helps to extract all common features. 85
7.10 The Contribution of SHC to second PC. 86
7.11 FCN_{Amp}, FCN_{Phase}, and the SHC up to degree 2. 87
7.12 Correlation between FCN and SHC. 88
7.13 The relation between the FCN_X and SHC of CHAOS6. The degree up to 10 represents the Earth's core activities. 88
7.14 Contribution expected by each PC of PCA between SHC and FCN product. . . 89
7.15 Contribution expected by each PC of PCA between SHC and FCN_{Phase}. . . . 90
7.16 Contribution expected by each PC of PCA between SHC and FCN_{X_0}. 91
7.17 Contribution expected by each PC of PCA between SHC and FCN_{Y_0}. 92
7.18 The relation between the rate of FCN product and DM rate. 93
7.19 Scheme of grid-based analysis. The near-Earth geomagnetic field is divided into globally gridded conservatively interpolated onto a regular latitude-longitude grid with 5°. 93
7.20 Main behavior of GMF and its derivative [no unit]. 94
7.21 The second derivative of GMF (Normalized). 94
7.22 Wavelet coherence analysis between FCN products and d^2GMF_{Fr}/dt^2. 96
7.23 Wavelet coherence analysis between FCN products and d^2GMF_{Dec}/dt^2. 97
7.24 Wavelet coherence analysis between FCN products and d^2GMF_{North}/dt^2. . . . 98
7.25 Wavelet coherence analysis between FCN products and d^2GMF_{East}/dt^2. 99
7.26 Wavelet coherence analysis between FCN products and d^2GMF_{Up}/dt^2. 100
7.27 Wavelet coherence analysis between FCN products and d^2GMF_{Horiz}/dt^2. . . . 101

List of Tables

2.1 Archimedean Copulas, generator, parameter, and formula 16
2.2 Link between Archimedean Copula parameter and Kendall τ 16

4.1 Contribution of space geodetic techniques to EOP observation. 32

5.1 Results derived from the RL06 CSR Stokes coefficients with monthly resolution 46
5.2 Results derived from the RL06 CSR Stokes coefficients with monthly resolution 48
5.3 Results derived from the SLR DGFI-TUM Stokes coefficients with weekly resolution 48
5.4 Comparison of the linear trends of the rotations R_x, R_y, and R_z obtained from the monthly CSR and weekly DGFI-TUM solutions 50

6.1 Marginal distributions. 60
6.2 Goodness-of-fit test for marginal distribution of PM_x. 60
6.3 Goodness-of-fit test for marginal distribution of PM_y. 60
6.4 Goodness-of-fit test for Copula model. 61
6.5 Success rate of PM_x prediction [%] 65
6.6 Success rate of PM_y prediction[%] 65
6.7 Comparison of Copula + SSA prediction and EOP PCC prediction errors (unit: ms/day). 73

7.1 FFT analysis of the main behaviour of GMF. 95

List of Abbreviations

AC	Auto Covariance
AR	Auto Regressive
ARMA	Auto-Regressive Moving Average
ATRF	Auxiliary Terrestrial Reference Frame
BCRS	Barycentric Celestial Reference System
CIO	Celestial Intermediate Origin
CIP	Celestial intermediate pole
CPM	Celestial pole motion
CRF	Celestial Reference Frame
CSR/UT	Center for Space Research at the University of Texas at Austin
COM	Center of Mass
CHAMP	Challenging Minisatellite Payload
CHAOS	CHAMP, Ørsted, and SAC-C magnetic satellite data of Earth's magnetic field
CLS	Collecte Localisation Satellites
CWT	Continuous Wavelet Transform
UTC	Coordinated Universal Time
CDF	Cumulative Distribution Function
DGFI-TUM	Deutsches Geodätisches Forschungsinstitut, Technische Universität München
DM	Dipolar Moment
DWT	Discrete Wavelet Transform
DORIS	Doppler Orbitography and Radiopositioning Integrated by Satellite
EWS	Early Warning System
EOC	Earth Orientation Center
EOP	Earth Orientation Parameters
ERA	Earth Rotation Angle
ERP	Earth Rotation Parameters
EAM	Effective Angular Momentum
EOP PCC	Earth Orientation Parameters Prediction Comparison Campaign
FFT	Fast Fourier Transform
FCN	Free Core Nutation
FICN	Free Inner Core Nutation

G	Gauss
GCRS	Geocentric Celestial Reference System
GFZ	GeoForschungsZentrum Potsdam
GMF	Geomagnetic Field
GMJ	Geomagnetic Jerks
GGOS	Global Geodetic Observing System
GNSS	Global Navigation Satellite System
GPS	Global Positioning System
GRACE	Gravity Recovery and Climate Experiment
GRGS	Groupe de Recherches en Geodesie Spatiale
HAM	Hydrology Angular Momentum
iid	Independent Identical Distribution
ICRS	International Celestial Reference System
IAG	International Association of Geodesy
IAU	International Astronomical Union
ICRF	International Celestial Reference Frame
IERS	International Earth Rotation and Reference System Service
IGRF	International Geomagnetic Reference Field
ILRS	International Laser Ranging Service
ITRF	International Terrestrial Reference Frame
ITRS	International Terrestrial Reference System
IVS	International VLBI Service for Geodesy and Astronomy
LS	Least Squares
LEO	Low Earth Orbit
LLR	Lunar Laser Ranging
NOAA	National Oceanic and Atmospheric Administration
OAM	Ocean Angular Momentum
POD	Precise Orbit Determination
PAI	Principal Axes of Inertia
SAC C	Satellite for Scientific Applications
SLR	Satellite Laser Ranging
SA	Secular Acceleration
SSALTO	segment Sol Altimetrie et Orbitographie
SSA	Singular Spectrum Analysis
SVD	Singular Value Decomposition
SHC	Spherical Harmonics Coefficients

TIO	Terrestrial Intermediate Origin
TRF	Terrestrial Reference Frame
IGS	International GNSS Service
USNO	U.S. Naval Observatory
UN	United Nations
UT1	Universal Time
VLBI	Very Long Baseline Interferometry
WCA	Wavelet Coherence Analysis
WT	Wavelet Transform
WTA	Wavelet Transform Analysis

1

Introduction

1.1 Overview

Geodesy is the knowledge of Earth through observing and modeling that provides information about Earth's shape, e.g., topography, sea level, and rotation, and information on its space, e.g., polar motion, precession, and nutation. Also, geodesy measures the gravity field of the Earth to provide the gravity and geoid of the Earth. These three pillars are the basis of the realization of the reference frames required to assign time-dependent coordinates to objects (see Figure 1.1). Space geodesy provides measurements between the ground-based instruments

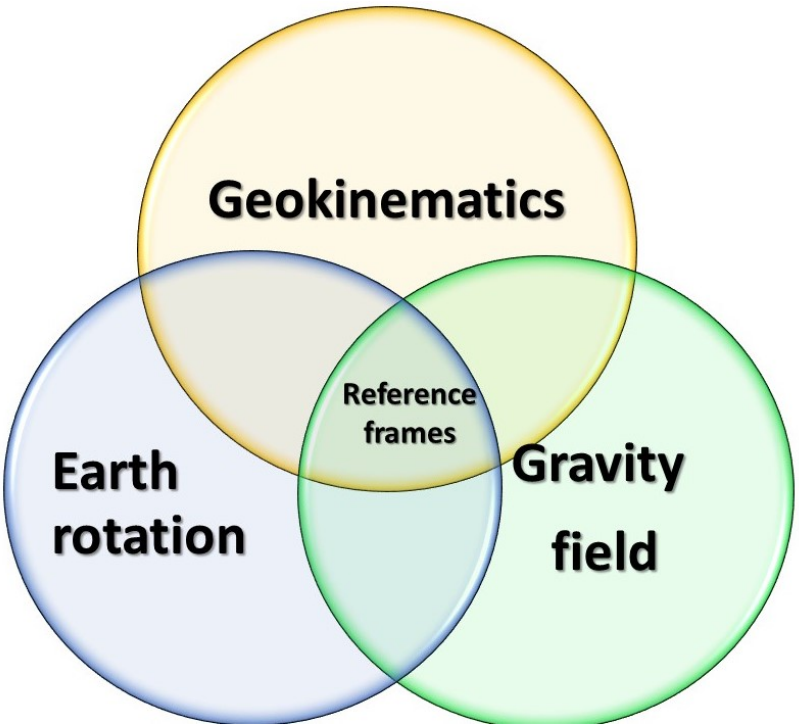

Figure 1.1: Geokinematics, Earth rotation, and gravity field are the three main pillars of geodesy (Plag and Pearlman, 2007).

and objects (satellites, radio sources, etc) in space. Space geodetic techniques provide global

and local information on Earth that is associated with a wide range of geophysical and meteorological processes. The quality and the quantity of the observations are improving through the advancement of space geodetic techniques. The Global Geodetic Observing System (GGOS) of the International Association of Geodesy (IAG) provides the geodetic infrastructure needed to monitor the Earth system (Schuh et al., 2015). The accuracy goals pursued by the GGOS are 1 mm accuracy and 0.1 mm/year stability on global scales in terms of the terrestrial reference frame defining parameters (Plag et al., 2009). Therefore, the understanding of geodesy's fundamental pillars could bring us significantly closer to meeting the goals of GGOS. Earth rotates once per day, around its rotation axis, which undergoes slow variation on the Earth's crust with respect to the celestial system. The rotation of the Earth can provide essential information concerning the Earth system. The rotation of an egg on a table is a well-known example that obtains information from inside the egg since rotation is noticeably different when the egg is in a raw, semi-boiled, or boiled condition. The same idea is considered for the Earth rotation and orientation observation relative to a reference frame. Several processes contribute to the excitation of the Earth's rotation changes from the

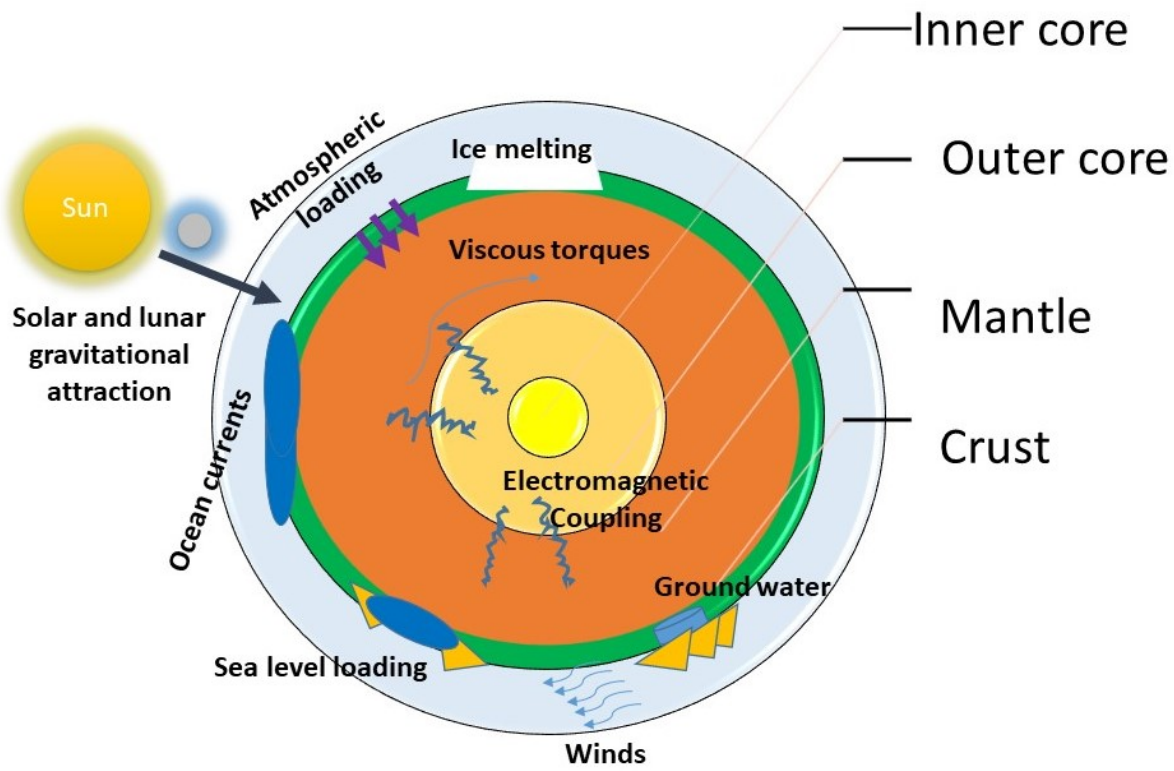

Figure 1.2: Schematic of the processes that contribute to the excitation of changes in the Earth's rotational state.

inner part of the Earth to the outer side (see Figure 1.2), e.g., viscous torque, core activities, electromagnetic coupling, sea level loading, ice melting, atmospheric loading, groundwater, ocean currents, plate tectonics, earthquakes, wind, and lunar/solar gravitational attraction (Wahr, 1988; Hide and Dickey, 1991; Dehant et al., 1997; Dehant and Mathews, 2015).
Therefore, the Earth's rotation time series became a great interest in different fields of geoscience and astronomy since their changes are related to gravitational and geodynamic processes in the Earth system. Earth orientation parameters (EOP) are the five angles that show the

orientation of the Earth in the space, and they are used to relate points in the terrestrial and celestial reference system (see Figure 1.3). The polar motion describes the variation of the celestial intermediate pole with respect to the terrestrial frame. The UT1-UTC describes the variation of the Earth's rotation angle. The variation of the Earth's orientation in the celestial frame is called the celestial pole motion (Petit and Luzum, 2010). The EOP can be observed with modern high-precision space geodetic techniques, such as a Very Long Baseline Interferometry (VLBI), Satellite Laser Ranging (SLR), Lunar Laser Ranging (LLR), Doppler Orbitography and Radiopositioning Integrated by Satellite (DORIS), and Global Navigation Satellite System (GNSS) (Schuh and Schmitz-Hübsch, 2000; Dow et al., 2009; Angermann et al., 2010; Coulot et al., 2010).

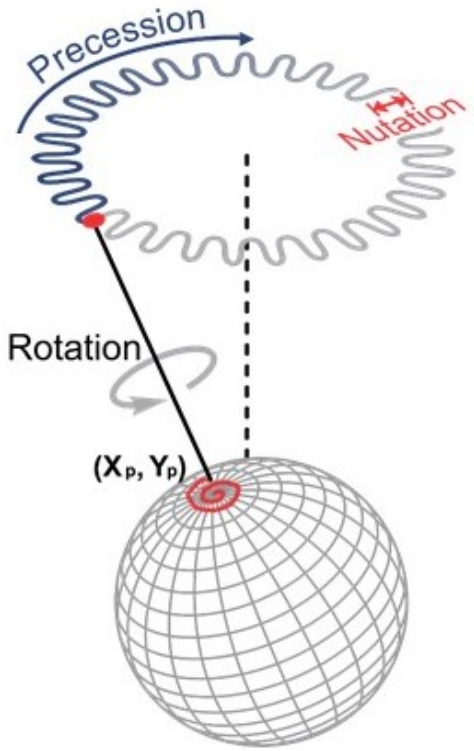

Figure 1.3: Schematic of Earth orientation parameters [not to scale]. The EOP are the five angles that show the orientation of Earth on the space, and they are used to relate points in the terrestrial and celestial reference system. The polar motion describes the variation of the celestial intermediate pole with respect to the terrestrial frame. The UT1-UTC describes the variation of the Earth rotation angle. The variation of Earth orientation in the celestial frame is called celestial pole offset.

1.2 Motivation and Research Objectives

1.2.1 State of the Art

Earth rotation monitoring is considered a fundamental topic that contributes to understanding atmospheric research to decrease natural disasters. Dangerous meteorological phenomena such as tsunamis and floods have led to the loss of several billion euros in the last decade (Baldassarre et al., 2013; Schröter et al., 2015). Besides many human casualties, the extreme

events led to more than 400 billion euros of loss between 1980 and 2017 (European Environment Agency, 2019). Also, two floods happened in Germany, which resulted in losses of more than 20 billion euros (Oldenborgh et al., 2016). The early warning system (EWS) could decrease the risk of natural hazards by sending people relevant information before a disaster. Space geodetic

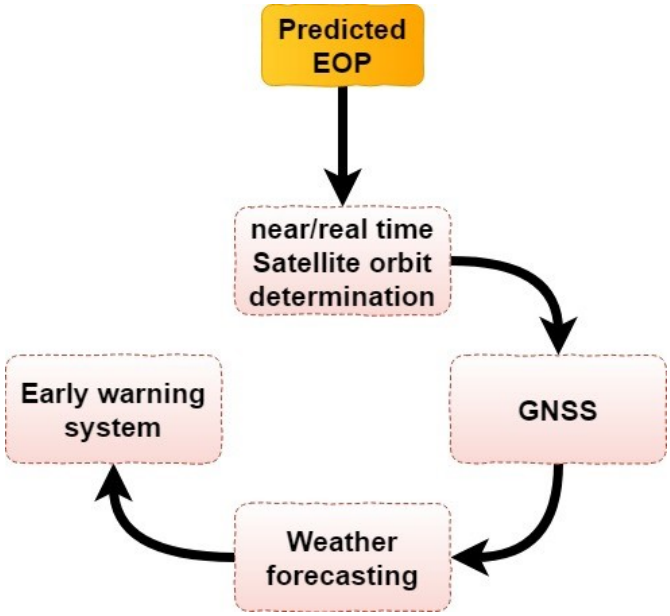

Figure 1.4: EWS send people relevant information before a disaster which is a major element of disaster risk reduction.

techniques observe the meteorological variables in high temporal and spatial resolution. Thus, the observed parameters using space geodesy play a crucial role in improving the weather prediction model, which is considered as input data for EWS (see Figure 1.4). For the analysis of space geodetic techniques in (near) real-time estimation of the EOP to days required. EOP are made available by the International Earth Rotation and Reference System Service (IERS) Rapid Service Prediction Center at U.S. Naval Observatory (USNO), Washington DC, with a delay of hours. Besides, other applications related to astronomy, geodesy, timekeeping, and geophysics could benefit from these estimations. Therefore, it is essential to predict the EOP parameters precisely (Barnes et al., 1983; Wahr, 1983; Mathews et al., 1991; F. Seitz and Schuh, 2010).

The Earth orientation center (EOC) of the IERS obtains and releases a solution with daily EOP values, named C04, which updated weekly and published in the IERS Bulletin A. Several techniques have been developed and applied for the EOP prediction (Schuh et al., 2002; Kalarus et al., 2010). However, the accuracy of EOP prediction is unsatisfactory even for prediction of just a few days in the future (Kalarus et al., 2010; Dick and Thaller, 2020). Thus, several aspects of the current techniques of modeling and prediction of EOP need to be revised and improved to meet the GGOS requirements. Therefore, it is highly demanding to develop a framework for improving the efficiency of the predicted EOP, considering the time variation of the periodicities and the excitation terms.

1.2.2 Research Questions

The main research questions which will be discussed in this thesis can be summarized as follows:

- Can the current Earth rotation theories adequately describe the motion of the Earth in space?
- How could space geodetic technique observations improve the current Earth rotation theories?
- How could EOP prediction bring us closer to the GGOS goals?
- How could we improve the accuracy of EOP prediction?
- How could the EOP prediction approach benefit from the understanding of the interconnections between EOP data and other geophysical variables?

1.2.3 Innovation

In this thesis, a new approach based on the combination of Copula-based analysis and singular spectrum analysis (SSA) is investigated to predict EOP. The Copula-based analysis method performs linear and nonlinear dependency between variables, and it is a powerful tool for dealing with multi-dimensional data and modeling the association between parameters (Favre et al., 2004; Bárdossy, 2006; Dupuis, 2007; Bárdossy and J. Li, 2008). SSA exploits data-driven base functions for deriving periodic components of the time series (Broomhead and King, 1986; Vautard et al., 1992). The combination of SSA and Copula-based methods will be applied for the first time as a novel stochastic tool for EOP determination. Despite the development of the new dynamic and hybrid method, which can capture all information underlying the time series, the relationship between the EOP and the processes contributing to the excitation of changes in the Earth's rotation should be assessed, as there are several effects that are not wholly understood. Thus, the interconnection between the Earth rotation parameters in space and geophysical phenomena such as atmosphere, ocean, hydrological loading, and geomagnetic field (GMF) variation is investigated to reveal common features between the variables independent of their theoretical implications, e.g., the dependence structure between EOP and effective angular momentum functions or EOP and geomagnetic field components.

1.3 Structure of the Dissertation

This dissertation can be divided into three levels, where level 0, aims to understand the Earth rotation theory. The level 1, pertains to investigate the interrelation of EOP and different geophysical components and the level 2 is aimed to design a robust prediction method for EOP prediction (see Figure 1.5). The dissertation is classified into eight chapters with respect to the scope of this study.

- Chapter 2 presents an overview of the Copula-based theory, SSA, and wavelet coherence analysis. Here, we deal with Archimedean Copula, which provides a useful stochastic tool for modeling the dependence structure between random variables. The mathematical

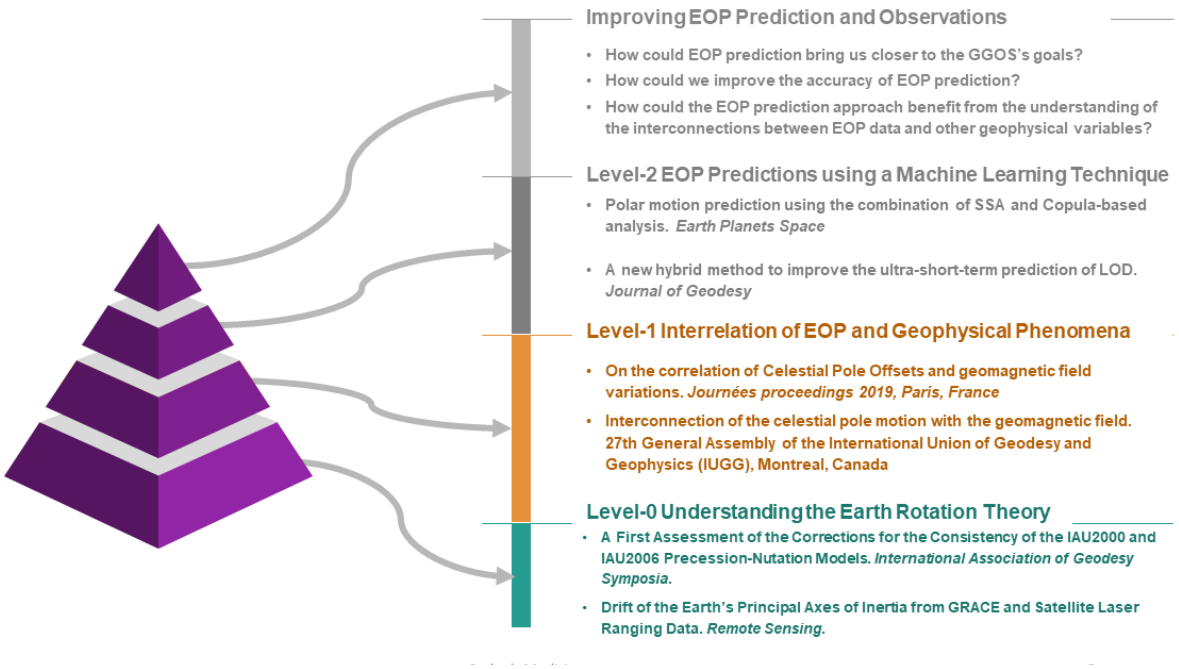

Figure 1.5: Three levels are defined to obtain the main goals of this study.

part of Copula is provided, and some of the Copula-based analysis applications are pointed out. Furthermore, the framework of the combination of Copula-based analysis and SSA is introduced as a novel prediction technique.

- Chapter 3 is dedicated to describing the theory and fundamental definition of the Earth's movements in space, the reference frames, and the data used in this study.

- Chapter 4 introduces space geodetic techniques that observe EOP. The basic concepts of DORIS, GNSS, laser ranging techniques (SLR and LLR), and VLBI are provided. The VLBI is the only approach that can provide the full EOP set.

- Chapter 5 pertains to the comparison of Earth rotation theories and observations. All the official Earth rotation theories are based on a reference system whose axes are aligned with the Earth's principal axes of inertia (PAI). The location of the Earth's PAI has a significant effect on many fields, including astronomy, geodesy, and satellite-based positioning and navigation systems. In this chapter, the PAI evolution is investigated, which might raise many questions concerning the geophysical aspects of PAI evolution.

- Chapter 6 constitutes the potential of the Copula-based + SSA methods for predicting Earth rotation parameters that are derived from the combination of different satellite geodetic sensors and from other geophysical parameters like effective angular momentums. The Copula is a statistical method that exploits linear and nonlinear relationships between two or more variables by fitting a theoretical Copula function into an empirical bivariate or multivariate distribution function. I introduced a hybrid prediction method that could be applied for EOP and other geophysical parameters.

- Chapter 7 deals with the interconnection between the Earth rotation parameters in space and geophysical phenomena. I studied the interrelation between the Earth's magnetic

field and celestial pole motion to understand the nature of Earth's interior. In this chapter, I argued the correlation between the free core nutation (FCN) changes and GMF variation. Our investigation revealed some exciting common features between these two variables, which show the potential to improve the understanding of the GMF's contribution to the Earth rotation.

- Chapter 8 summarizes the most significant achievements, conclusions, and recommendations for further research.

1.4 Supporting Publications

The publications listed below are the scientific researches which have been done in this dissertation.

- Related to Chapter 5

  - Ferrándiz, J. M., **Modiri, S.**, Belda, S., Barkin, M., Blossfeld, M., Heinkelmann, R., and Schuh, H. (2020b). Drift of the Earth's principal axes of inertia from GRACE and satellite laser ranging data. **Remote Sensing**, 12(2):314. DOI: https://doi.org/10.3390/rs12020314.

  - Ferrándiz, J. M., Al Koudsi, D., Escapa, A., Belda, S., **Modiri, S.**, Heinkelmann, R., and Schuh, H. (2020a). A first assessment of the corrections for the consistency of the IAU2000 and IAU2006 precession-nutation models. **International Association of Geodesy Symposia**. DOI:https://doi.org/10.1007/1345_2020_90.

- Related to Chapter 6

  - **Modiri, S.**, Belda, S., Hoseini, M., Heinkelmann, R., Ferrándiz, J. M., and Schuh, H. (2020). A new hybrid method to improve the ultra-short-term prediction of LOD. **Journal of Geodesy**, 94(2):23. DOI: https://doi.org/10.1007/s00190-020-01354-y.

  - **Modiri, S.**, Belda, S., Hoseini, M., Heinkelmann, R., Ferrándiz, J. M., and Schuh, H. (2019a). Eop can save human life! how?. In: Geophysical Research Abstracts (Vol. 21) **EGU 2019**, Vienna, Austria. DOI:10.13140/RG.2.2.35412.76161.

  - **Modiri, S.**, Belda, S., Heinkelmann, R., Hoseini, M., Ferrándiz, J. M., and Schuh, H. (2018). Polar motion prediction using the combination of SSA and Copula-based analysis. **Earth, Planets and Space**, 70(1):115. DOI:https://doi.org/10.1186/s40623-018-0888-3.

- Related to Chapter 7

– **Modiri, S.**, Heinkelmann, R., Belda, S., Malkin, Z., Hoseini, M., Ferrándiz, J. M., and Schuh, H. (2019b). Interconnection of the celestial pole motion with the geomagnetic field. In: 27th General Assembly of the International Union of Geodesy and Geophysics (**IUGG**), Montreal, Canada.

– **Modiri, S.**, Heinkelmann, R., Belda, S., Malkin, Z., Hoseini, M., Korte, M., Ferrándiz, J. M., and Schuh, H. (2019c). On the correlation of celestial pole offsets and geomagnetic field variations. In: **Proceedings of the Journees 2019**, Paris, France. `https://syrte.obspm.fr/astro/journees2019/journees_pdf/posters/Modiri_Heinkelmann.pdf`.

2

Methodology

2.1 Copula-based Analysis

The word "Copula" is employed for the first time in the mathematical or statistical context by Sklar, 1959 in Sklar's Theorem to illustrate the univariate joint distribution function. Traditionally, the joint distribution between variables is modeled by classical multivariate distributions such as the normal distribution. However, the main limitation of such approaches is that each variable's behavior and joint dependence between them, are characterized by the same parameter. On the contrary, the Copula-based analysis does not have such drawbacks. The Copula describes the dependence structure between random variables independent from their marginal distributions (Genest and Favre, 2007; Salvadori and De Michele, 2007). The Copula approach exploits linear and non-linear dependency between variables. The Copula-based analysis is a flexible tool offering an enormous improvement in capturing the real correlation pattern (Embrechts et al., 2002). More detailed information about Copula can be found e.g. in Joe, 1997 and Nelsen, 2007. The Copula-based analysis technique is used for different types of studies, e.g., economics (Rachev and Mittnik, 2000; Patton, 2006, 2009), biomedicine (W. Wang and Wells, 2000; Escarela and Carriere, 2003), hydrology (Bárdossy and J. Li, 2008; Bárdossy and Pegram, 2009; Verhoest et al., 2015), meteorology (Laux et al., 2011; Vogl et al., 2012), hydro-geodesy and geodesy (Modiri et al., 2015, 2018, 2020).

2.1.1 Sklar's Theorem

Sklar's theorem is the main idea of Copula-based analysis, and it indicates that a Copula function C connects a given multivariate distribution function with its univariate one. For bivariate distribution, there is a bivariate Copula C, which models the joint cumulative probability distribution function of two variables X and Y based on the marginal cumulative distribution functions $F_X(x)$ and $F_Y(y)$.

$$\begin{aligned} P(X \leq x, Y \leq y) = F_{X,Y}(x,y) &= C(F_X(x), F_Y(y)) \\ &= C(u,v) \end{aligned} \tag{2.1}$$

where C is the joint distribution function $F_{X,Y}(x, y)$. The variables u and v are transformations of X and Y to a uniform distribution, respectively.

2.1.2 Copula Properties

In the bivariate case, a Copula is indicated as a function C from $[0, 1]^2$ to $[0, 1]$. The general properties of Copula can be itemized as follows (Genest and Rivest, 1993; Nelsen, 2007):

- $C(u, 0) = C(0, v)$,
- $C(x, 1) = x$ and $C(1, y) = y$,
- The Copula is unique when the marginals are continuous function.

Besides, it should be mentioned, the variables transformed by any monotonic increasing functions will not affect its Copula.

2.1.3 Frecht-Hoffding Bounds

The probability distributions of a multivariate Copula is within the unit cube I^n. The theory by Frecht-Hoffding states that for any Copula $C : [0, 1]^n \to [0, 1]$ and $(u_1, u_2, \ldots, u_n) \in [0, 1]^n$ the following bounds hold:

$$W(u_1, u_2, \ldots, u_n) \leq C(u_1, u_2, \ldots, u_n) \leq M(u_1, u_2, \ldots, u_n), \tag{2.2}$$

where, W is called the lower Frecht-Hoffding bound and it is yielded by:

$$W(u_1, u_2, \ldots, u_n) = \max\{0, \Sigma_{i=1}^{n} u_i - (n - 1)\}, \tag{2.3}$$

Also, M is the upper Frecht-Hoffding bound and it is given by:

$$M(u_1, u_2, \ldots, u_n) = \min\{u_1, u_2, \ldots, u_n\} \tag{2.4}$$

For the bivariate case, the Frecht-Hoffding theorem states as follow

$$\max\{u + v - 1, 0\} \leq C(u, v) \leq \min\{u, v\} \tag{2.5}$$

2.1.4 Empirical Copula

The empirical Copula is an estimator for the unknown theoretical Copula distribution (Deheuvels, 1979). Also, it is the best representation of the theoretical Copula as it is purely data-based. The empirical Copula is defined on the rank space as (Genest and Rivest, 1993; Genest and Favre, 2007):

$$C_e(u, v) = \frac{1}{n} \sum_{i=1}^{n} \mathbf{1}(\frac{r_i}{n + 1} \leq u, \frac{s_i}{n + 1} \leq v) \tag{2.6}$$

where,

$(r_1), (r_2) \ldots, (r_n)$ denote the pairs of ranks of the variable $(x_1), (x_2), \ldots, (x_n)$,

$(s_1), (s_2) \ldots, (s_n)$ denote the pairs of ranks of the variable $(y_1), (y_2), \ldots, (y_n)$,

n is the length of the data vector,

1 is the indicator function. If the condition is true, the indicator function is equal to 1. Otherwise, the indicator function is equal to 0.

In the following, the most commonly used Copula, which is used in this thesis, is illustrated. For additional information regarding different Copula families, the reader is referred to Joe (1997) and Nelsen (2007).

2.1.5 Archimedean Copula

The Archimedean Copulas reveal a-/symmetrical upper/lower tail dependency, and they can be estimated directly in a simple form. An Archimedean Copula can be expressed in the following form:

$$C(u, v) = \phi^{-1}\{\phi(u) + \phi(v), \theta\} \tag{2.7}$$

where θ is the Copula parameter and the function ϕ is the Copula generator with the following characteristics (ibid.):

- $\forall\ u \in (0, 1), \phi(u) < 0$, ϕ is decreasing,
- $\forall\ u \in (0, 1), \phi(u) < 0$, ϕ is convex,
- $\phi(1) = 0$,

and ϕ^{-1} is pseudo-inverse of ϕ and it is illustrated by

$$\phi^{-1}(t) = \begin{cases} \phi^{-1}(t; \theta), & \text{if } 0 \leq t \leq \phi(0) \\ 0, & \text{if} \phi(0) \leq t \leq \infty \end{cases}$$

Further information about mathematical aspects of these families can be found in Salvadori and De Michele (2007).

2.1.5.1 Archimedean 12 Copula

The Archimedean 12 Copula is known to be symmetrical and shows both upper and lower tail dependence. The generator of the Archimedean 12 is given by (Nelsen, 2007):

$$\phi^{Arch12}(t) = (\frac{1}{t} - 1)^{\theta}. \tag{2.8}$$

The Copula parameter θ is defined over $1 \leq \theta$ and the Archimedean 12 Copula formula is given by (ibid.):

$$C_\theta(u, v) = (1 + [(u^{-1} - 1)^{\theta} + (v^{-1} - 1)^{\theta}]^{(\frac{1}{\theta})})^{-1}. \tag{2.9}$$

In the case of $\theta = 1$, the dependence structure between the variables shows independency.

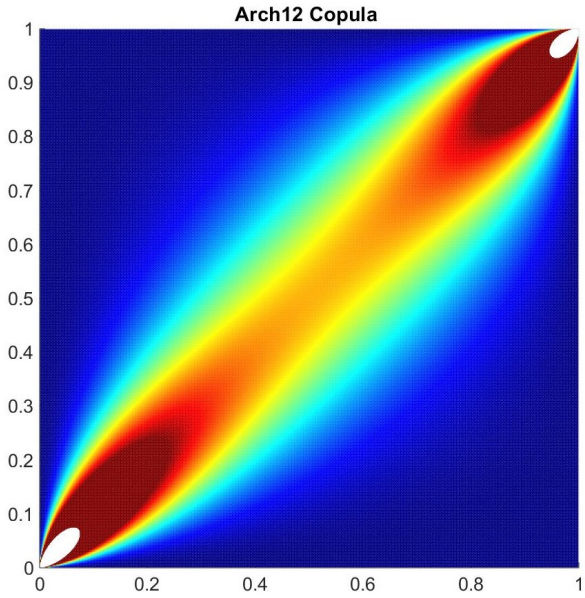

Figure 2.1: Archimedean 12 Copula with $\theta = 2$.

2.1.5.2 Archimedean 14 Copula

The generator of the Archimedean 14 which is also and a symmetric Copula is given by (Nelsen, 2007):

$$\phi^{Arch14}(t) = (t^{\frac{-1}{\theta}} - 1)^{\theta}. \tag{2.10}$$

Also, The Archimedean 14 Copula can capture the tail dependence structure. The Copula parameter of Archimedean 14 Copula is defined over $1 \leq \theta$, and the Archimedean 14 Copula formula is given by (ibid.):

$$C_{\theta}(u, v) = (1 + [(u^{\frac{-1}{\theta}} - 1)^{\theta} + (v^{\frac{-1}{\theta}} - 1)^{\theta}]^{\frac{1}{\theta}})^{-\theta} \tag{2.11}$$

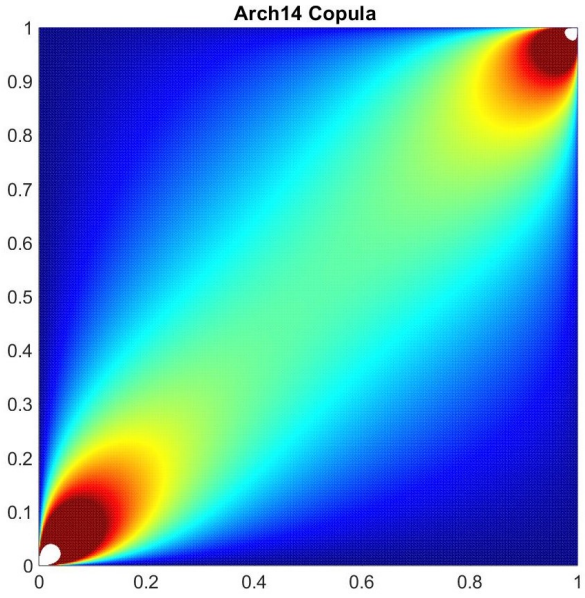

Figure 2.2: Archimedean 14 Copula with $\theta = 1.2$.

2.1.5.3 Clayton Copula

The Clayton Copula is an asymmetric Archimedean Copula, showing the lower tail dependence structure. The generator of the Clayton is given by (Clayton, 1978):

$$\phi^{Cl}(x) = \frac{1}{\theta}(t^{-\theta} - 1) \tag{2.12}$$

The Clayton Copula parameter is defined over $-1 \leq \theta$ and the Clayton Copula can be simplified to (Nelsen, 2007):

$$C_\theta(u, v) = \max[(u^{-\theta} + v^{-\theta} - 1), 0]^{-\frac{1}{\theta}} \tag{2.13}$$

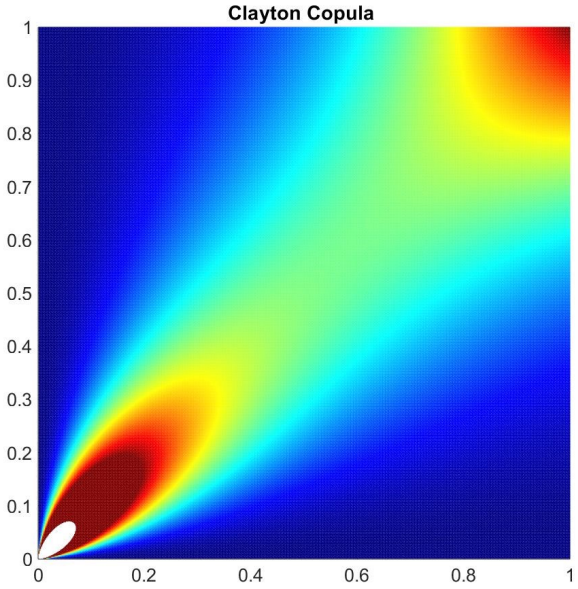

Figure 2.3: Clayton Copula with $\theta = 2$.

2.1.5.4 Frank Copula

The Frank Copula is known to be symmetrical, i.e., it shows no tail dependence structure. The generator of the Frank is given by (ibid.):

$$\phi^{Fr}(t) = -\ln\{\frac{e^{-\theta t} - 1}{e^{-\theta} - 1}\} \tag{2.14}$$

The Frank Copula parameter is defined over $-\infty < \theta < \infty$ and its formula is given by (ibid.):

$$C_\theta(u, v) = \frac{1}{\theta}\ln(1 + \frac{(e^{-\theta u} - 1)(e^{-\theta v})}{e^{-\theta} - 1}) \tag{2.15}$$

If $\theta = 0$, the Frank Copula obtains the independence Copula, and if $\theta \to \infty$ or $-\infty$, it approaches the comonitinicity Copula.

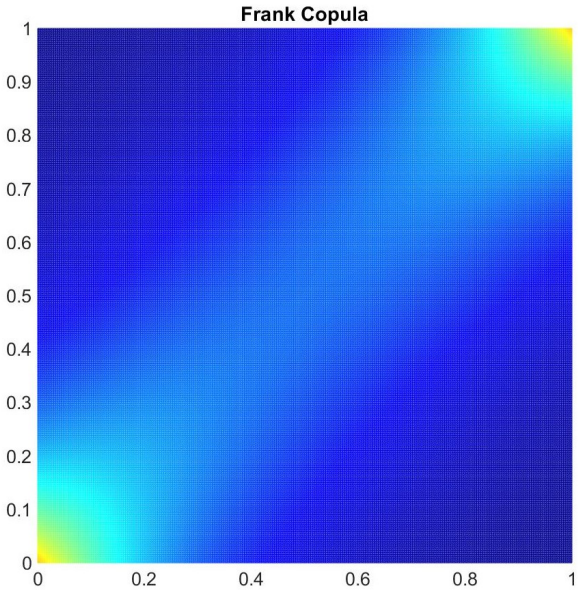

Figure 2.4: Frank Copula with $\theta = 3$.

2.1.5.5 Gumbel Copula

The Gumbel Copula is an asymmetric Archimedean Copula, presenting upper tail dependence. The generator of the Gumbel is given by:

$$\phi^{Gu}(t) = (-\ln t)^{\theta} \tag{2.16}$$

The Gumbel Copula parameter is defined over $1 \leq \theta$ and its formula is given by Nelsen, 2007:

$$C_{\theta}(u, v) = e^{-((-\ln(u)^{\theta})+(-\ln(v)^{\theta}))^{\frac{1}{\theta}}} \tag{2.17}$$

The $\theta = 1$ indicate independence structure and it is a special case, and the limit of $\theta \to \infty$ is the comonotonicity Copula. Therefore, the Gumbel Copula interprets between independence and positive dependence, and the parameter describes the strength of the relationship.

2.1.5.6 Joe Copula

The Joe Copula is an asymmetric Archimedean Copula, capturing a heavy upper tail dependence and lower dependency, which looks like a bell. The generator of the Joe is given by (Joe, 1997):

$$\phi^{Joe}(t) = -\ln[1 - (1 - t)^{\theta}] \tag{2.18}$$

The Joe Copula parameter is defined over $1 \leq \theta$ and its formula is given by (Nelsen, 2007):

$$C_{\theta}(u, v) = 1 - [(1 - u)^{\theta} + (1 - v)^{\theta} - ((1 - u)^{\theta}(1 - v)^{\theta}))]^{\frac{1}{\theta}} \tag{2.19}$$

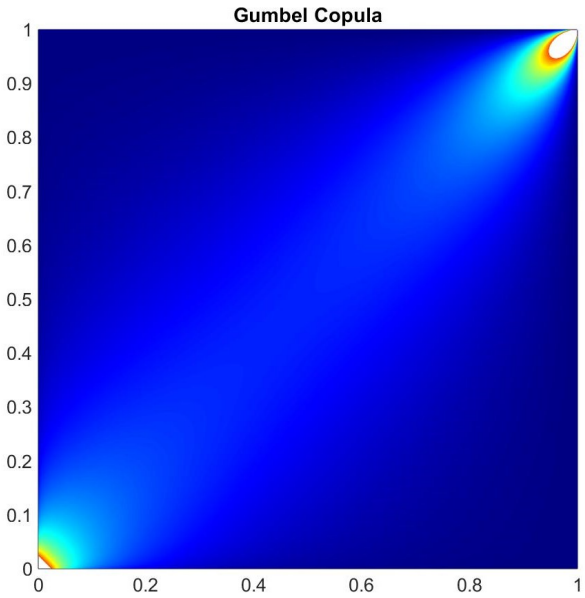

Figure 2.5: Gumbel Copula with $\theta = 2$.

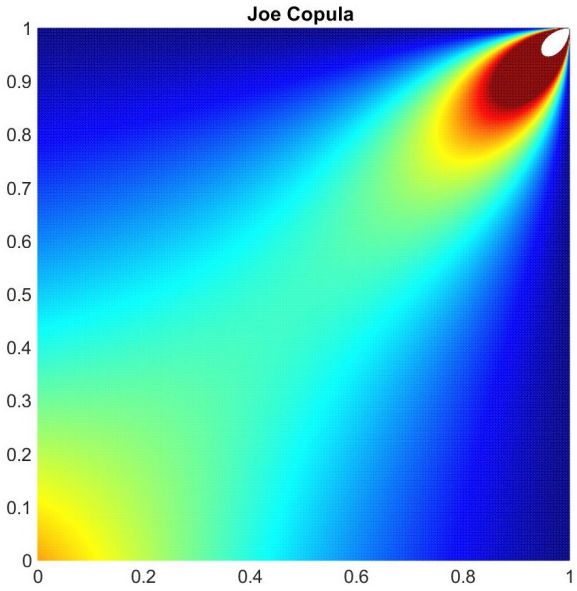

Figure 2.6: Joe Copula with $\theta = 2.15$.

2.1.6 Copula Parameter θ Estimation and Classical Dependence Parameter

There is a link between classical dependence parameters such as Kendall τ and Copula parameters. For one-parametric Copula, the functional association between the Kendall τ Copula functions is written:

$$\tau = 4 \int_0^1 \int_0^1 C_\theta(u, v) dC_\theta(u, v) - 1, \tag{2.20}$$

The relationship between the Kendall τ and Archimedean Copula generator $\Phi(t)$ is shown in Equation 2.21:

$$\tau = 1 + 4 \int_0^1 \frac{\Phi(t)}{\Phi(t)'} dt. \tag{2.21}$$

Table 2.1: Archimedean Copulas (Archimedean 12, Archimedean 14, Clayton, Frank, Gumbel, and Joe Copula) and generator, parameter space, and formula. θ is the Copula's parameter called the dependence parameter, which measures the dependence between the marginal (Nelsen, 2007).

Family	Generator	Parameter	Formula
Archimedean 12	$\phi^{Arch12}(t) = (\frac{1}{t} - 1)^{\theta}$	$1 \leq \theta$	$C_\theta(u,v) = (1 + [(u^{-1} - 1)^{\theta} + (v^{-1} - 1)^{\theta}]^{(\frac{1}{\theta})})^{-1}$
Archimedean 14	$\phi^{Arch14}(t) = (t^{\frac{-1}{\theta}} - 1)^{\theta}$	$1 \leq \theta$	$C_\theta(u,v) = (1 + [(u^{\frac{-1}{\theta}} - 1)^{\theta} + (v^{\frac{-1}{\theta}} - 1)^{\theta}]^{\frac{1}{\theta}})^{-\theta}$
Clayton	$\phi^{Cl}(x) = \frac{1}{\theta}(t^{-\theta} - 1)$	$-1 \leq \theta$	$C_\theta(u,v) = \max[(u^{-\theta} + v^{-\theta} - 1), 0]^{-\frac{1}{\theta}}$
Frank	$\phi^{Fr}(t) = -\ln\{\frac{e^{-\theta t} - 1}{e^{-\theta} - 1}\}$	$-\infty < \theta < \infty$	$C_\theta(u,v) = \frac{1}{\theta}\ln(1 + \frac{(e^{-\theta u} - 1)(e^{-\theta v})}{e^{-\theta} - 1})$
Gumbel	$\phi^{Gu}(t) = (-\ln t)^{\theta}$	$1 \leq \theta$	$C_\theta(u,v) = e^{-((-\ln(u)^{\theta}) + (-\ln(v)^{\theta}))^{\frac{1}{\theta}}}$
Joe	$\phi^{Joe}(t) = -\ln[1 - (1-t)^{\theta}]$	$1 \leq \theta$	$C_\theta(u,v) = 1 - [(1-u)^{\theta} + (1-v)^{\theta} - ((1-u)^{\theta}(1-v)^{\theta}))]^{\frac{1}{\theta}}$

Table 2.2: The link between Archimedean Copula parameter θ and Kendall τ (Cherubini et al., 2004).

Family	τ
Archimedean 12	$\frac{\theta - \frac{2}{3}}{\theta}$
Archimedean 14	$\frac{2\theta - 1}{2\theta + 1}$
Clayton	$\frac{\theta}{\theta + 2}$
Frank	$1 - \frac{4}{\theta}[1 - D_1(\theta)]^*$
Gumbel	$\frac{\theta - 1}{\theta}$
Joe	$1 - \frac{4}{\theta}D_1(\theta)$

* $D_k(x)$ is the Debye function for any positive integer k. Here D is Debye functions.

$$D_k(\theta) = \frac{k}{x^{\theta}} \int_{t=0}^{x} \frac{t^{\theta}}{e^{\theta} - 1} dt \tag{2.22}$$

Thus, the connections between the Kendall τ and the Archimedean Copula parameters are indicated in Table 2.2.

2.1.7 Copula-based Simulation Random Data

The required steps to simulate random data using Copula-based conditional random data are written in (Laux et al., 2011; Vogl et al., 2012; Modiri et al., 2018). The following steps are taken to provide the proper theoretical Copula function and simulation data

1. Independent identical distribution (iid) transformation of input time series.
2. The marginal distributions $F_X(x)$ and $F_Y(y)$ of the input data x and y are estimated.
3. Transform data to rank space using the estimated marginal distributions of data with u_i and v_i in rank space.
4. The empirical Copula is computed the dependence structure of random variables using the rank-transformed data.
5. A theoretical Copula function $C_\theta(u,v)$ is fitted to empirical Copula.
6. The conditional Copula function is computed.

7. The random data are sampled from the conditional cumulative distribution function (CDF) of Copula.

8. The sampled data are transferred back to the data space using the inverse marginal.

2.2 Singular Spectrum Analysis

The SSA method for trend extraction comprises four following steps (see e.g., Golyandina et al. (2001), Ghil et al. (2002), and Hoseini et al., 2020 for more details):
The **Embedding step** is the procedure of forming a subspace, which is spanned by a set of basis vectors derived from the time series. The Embedding step is done using a moving window with the length of to embed the time series into the subspace by constructing a set of L-dimensional lagged vectors, as follows:

$$\mathbf{X} \quad = (x_{ij})_{i,j=1}^{L,K} = \begin{bmatrix} f_1 & f_2 & f_3 & \cdots & f_K \\ f_2 & f_3 & f_4 & \cdots & f_{K+1} \\ f_3 & f_4 & f_5 & \cdots & f_{K+2} \\ \vdots & \vdots & \vdots & \ddots & \vdots \\ f_L & f_{L+1} & f_{L+2} & \cdots & f_N \end{bmatrix} , \begin{cases} 1 < L < K \\ K = N - L + 1 \end{cases} \tag{2.23}$$

The matrix $\mathbf{X}$ is called the trajectory matrix. $\mathbf{X}$ is a Hankel matrix, which means it is a symmetric matrix having equal elements on anti-diagonals. The columns (and rows) of $\mathbf{X}$ can be correlated since they might hold similar pieces of information. We need to remove redundant repeated information and group the remaining common information into uncorrelated components. Therefore, we select window length $\mathbf{L}$ to maximize the correlation between the columns of the trajectory matrix.
Moreover, the importance of each uncorrelated component compared to others should be determined. This is carried out in the decomposition step. In the **decomposition step**, a singular value decomposition (SVD) is applied to the trajectory matrix,

$$\mathbf{X} = \mathbf{U}\Sigma V^T$$

where the columns (and rows) of U and V are uncorrelated, orthonormal ($UU^T = V^T$) and are called left and right singular vectors, respectively. Σ is a diagonal matrix with non-negative entries, the singular values, which reveal the importance of the singular vectors. Singular values/vectors of $\mathbf{X}$ can be calculated using the eigenvalues and eigenvectors of the matrix $S = XX^T$.

$$XX^T = (U\Sigma V^T)(U\Sigma V^T)^T = U\Sigma^2 U^T \tag{2.24}$$

Let $\lambda_1 \geq \lambda_2 \geq \ldots \geq \lambda_L \geq 0$ denote diagonal entries of $\Lambda = \Sigma^2$ or the eigenvalues of S. The columns of U indicate their corresponding innovators of the matrix S, which are called Empirical Orthogonal Functions (EOF) of $\mathbf{X}$. The right singular vectors of $\mathbf{X}$ are eigenvectors of $X^T X$ calculable by:

$$V_i = X^T U_i / \sqrt{\lambda_i} , \begin{cases} d = max(i|\lambda_i > 0) \\ i = 1, 2, \ldots, d \end{cases} \tag{2.25}$$

where d conveys the number of uncorrelated components of $\mathbf{X}$. It should be mentioned that in practice the condition $\lambda_i > 0$ turns to $\lambda_i >$ ó, in which ó is is a selected small value. This is due to the fact that λ_i simply reveals the importance of the component, so one can choose different values for ó in order to include a desired level of details and to prevent numerical calculation problems.
Now, the trajectory matrix can be written as:

$$X = X_1 + X_2 + \ldots + X_d X_i = \sqrt{\lambda_i} U_i V_i^T \tag{2.26}$$

where $\sqrt{\lambda_i}$ is the corresponding singular value of $\mathbf{X}_i$. Each of the matrices $\mathbf{X}_i$ represent some features of the time series and summing them should produce $\mathbf{X}$.
Let A be $X_1, X_2, \ldots, X_d$, then the reconstruction of $\mathbf{X}$ begins with selecting a group from A, which is called the **grouping step**. Each member of the set A can contain different aspects of the trajectory matrix. Since the singular values are sorted in decreasing order, the most important part of $\mathbf{X}$ is retrievable using the first few singular vectors and their corresponding singular values. Analysis of the spectrum of the singular values and its variations would be a key tool for selecting the proper subset of A for different applications.
The vertical segment's singular values also hold the most important information of the time series for the trend extraction. Therefore, the corner of the L-shaped curve in which the maximum curvature of the singular values spectrum happens can be a reasonable choice for truncation.
The selected group of A using equation Eq. 2.26 form an estimation of the trajectory matrix.

$$\begin{cases} X_{trend} = X_1 + X_2 + \ldots + X_I = (\hat{x_{ij}})_{i,j=1}^{L,K} \\ X_{residual} = X_{I+1} + X_{I+2} + \ldots + X_d \end{cases} \tag{2.27}$$

where $I \leq d$, with d number of non-zero singular values.
In the **reconstruction step**, a reverse calculation (with respect to the embedding step) is needed to rebuild the time series. Having the fact that the trajectory matrix was originally a Hankel matrix with equal elements on anti-diagonals, the trend extraction is achieved by averaging the anti-diagonal entries of the matrix $\mathbf{X}_{trend}$ in Eq. 2.27. Let $L < K$, then the trend of time series $G = (g_1, g_2, \ldots, g_N)$ is:

$$g_i = \begin{cases} \frac{1}{i}\Sigma_{m=l}^{i} \hat{X}_{m,i-m+1} 1 \leq i \leq L \\ \frac{1}{L}\Sigma_{m=l}^{L} \hat{X}_{m,i-m+1} L \leq i \leq K \\ \frac{1}{N-i+1}\Sigma_{m=i-K+1}^{N-K+1} \hat{X}_{m,i-m+1} K \leq i \leq N \end{cases} \tag{2.28}$$

where $\hat{x}_{i,j}$ is an estimation of the element f_{i+j-1} of the original time series. It should be noted that the reconstructed trajectory matrix might not preserve Hankel property anymore, and thus $\hat{X}_{i,j} \neq \hat{X}_{j,i}$.

2.3 Combination of Copula-based Analysis and SSA

The combination of SSA and Copula-based analysis (Copula + SSA) is one of the machine learning (ML) techniques which can be defined as subset of artificial intelligence (AI). In ML,

machines can learn on their own without being explicitly programmed. In the last decade, ML has attained outstanding results in estimating climate variables and related biogeophysical variables (Bishop, 2006; Murphy, 2012). The Copula + SSA is developed and introduced as a novel method to predict time series. The Copula + SSA is a hybrid method that uses training data to model the data's underlying structure.

1. Deterministic part, the periodic terms, can be modeled by SSA as it is described in section 2.2.

2. The stochastic part; the subtracted time series by reconstructed time series, can be modeled using Copula-based analysis as explained in subsection 2.1.7.

The Copula + SSA approach can be employed for two cases; the first one is the algorithm that uses the information within a time series. As can be seen in Figure 2.7, the algorithm consists of two parts, the periodic and anomaly parts. The first part is dealing with the deterministic part, which can be modeled by SSA. The residual of subtracted data by the reconstructed time series can be modeled by Copula-based analysis. Then, the periodic terms are extrapolated, and the anomaly part is predicted using Copula-based analysis, separately. Finally, both predicted periodic, and anomaly terms are combined (Modiri et al., 2018). The

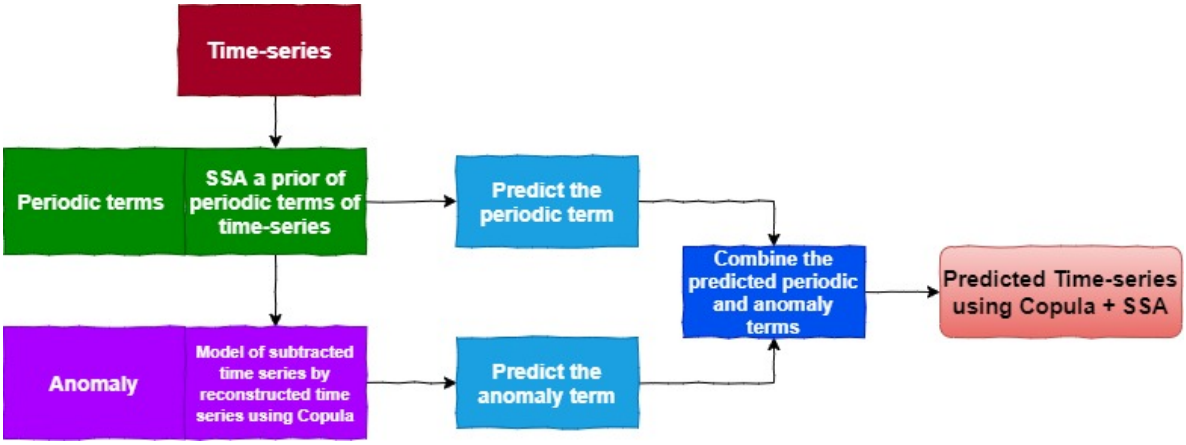

Figure 2.7: Copula + SSA algorithm for modeling and predicting the time series by using the information within the time series.

second case is the algorithm that takes into account the information within a time series and other variables (here other geophysical parameters) in addition (see Figure 2.8. The second algorithm is aimed at the possibility of utilizing some variables to forecast the EOP due to the existing relationship between them. The procedure operates as follows; first, derive the dependence structure between time series one and the time series two arising from geophysical parameters. The Copula-based analysis model the underlying relationship between the time series (T1 and T2). The T1 is predicted based on the fitted theoretical Copula by conditioning the predicted T2, as shown in Figure 2.8. Then, the remaining part is modeled using SSA and extrapolated. Finally, the Copula-based predicted data added to the SSA forecasted residual.

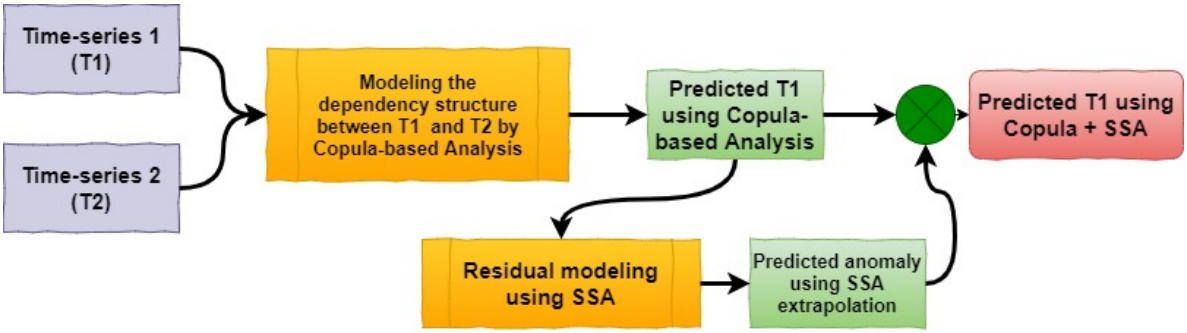

Figure 2.8: Copula + SSA algorithm for modeling and predicting the time series by using the information within the time series and other variables.

2.4 Wavelet Analysis

Wavelet transform (WT) analysis is a useful signal processing tool that is widely used to analyze the localized variation of signal power and periodicities within a time series (Bentley and McDonnell, 1994; Cohen, 1995; Akin, 2002). The WT analysis is applied in different geoscience fields, such as geophysics, meteorology, oceanography, and climatology (Meyers et al., 1993; Chakraborty and Okaya, 1995; Lau and Weng, 1995; Massel, 2001; Herrera et al., 2014). The WT can be split into two classes; the discrete wavelet transform (DWT) (Tzanetakis et al., 2001; Demirel and Anbarjafari, 2011), which mainly used for noise reduction and the continuous wavelet transform (CWT) (Rioul and Duhamel, 1992; Sinha et al., 2005), is applied for feature extraction of the signal.

The WT decomposes a signal over functions called mother wavelets which can be expressed as the function of two parameters, time position (τ) and scale of the wavelet (a) as follows (Ngui et al., 2013):

$$\Phi_{a,\tau}(t) = \frac{1}{\sqrt{a}}\Phi(\frac{t-\tau}{a}). \tag{2.29}$$

The wavelet transform of a time series $x(t)$ with respect to a chosen mother wavelet is performed as follows:

$$W_x(a,\tau) = \frac{1}{\sqrt{a}}\int_{-\infty}^{\infty} x(t)\Phi^*(\frac{t-\tau}{a})dt = \int_{-\infty}^{\infty} x(t)\Phi^*_{a,\tau}(t)dt, \tag{2.30}$$

where, $*$ denotes the complex conjugate form. The wavelet coefficients, $W_x(a,\tau)$, express the contribution of the scales (the values) to the signal at different time positions (the τ values). By moving the wavelet along the signal structures relating to a specific scale can be identified. The choice of the wavelet function (Φ) is not arbitrary. This function is normalized to have unitary variance ($\int |\Phi(t)|^2 dt = 1$) and it verifies $\int \Phi(t)dt = 0$. Thus, the wavelet decomposition is a linear illustration of the signal where the variance is preserved. This means that the original signal can be recovered using the inverse wavelet transform:

$$x(t) = \frac{1}{C_g}\int_{-\infty}^{\infty}\int_{0}^{\infty}\frac{1}{a^2}W_x(a,\tau)\Phi_{a,\tau}(t)d\tau da, \tag{2.31}$$

where, $C_g = \int_0^\infty \frac{\hat{\Phi}^2}{f}df$ and $\hat{\Phi}(f)$ indicates the Fourier transform of $\Phi(t)$.

2.4.1 Wavelet Coherence Analysis

The wavelet coherence analysis of two times series can be shown as follow (Lachaux et al., 2002; Grinsted et al., 2004):

$$R_n^2(s) = \frac{|S(s^{-1}W_n^{XY}(s))|^2}{S(s^{-1}|W_n^X(s)|^2).S(s^{-1}|W_n^Y(s)|^2)}, \tag{2.32}$$

where S is a smoothing operator. The Equation 2.32 resembles the traditional correlation coefficient, and it is useful to think of the wavelet coherence as a localized correlation coefficient in time-frequency space. The smoothing operator S is written as (Grinsted et al., 2004):

$$S(W) = S_{scale}(S_{time}(W_n(s))), \tag{2.33}$$

where S_{scale} denotes smoothing along the wavelet scale axis and S_{time} smoothing in time. The statistical significance level of the wavelet coherence is computed by using Monte Carlo methods.

3

Theory, Fundamental Definition, and Data sets

3.1 Earth Motion

The Earth is the third planet from the Sun, and like all other planets in the solar system, revolves around the Sun in an elliptical orbit. Also, it rotates on its axis. These two motions are responsible for many phenomena like day and night, season, wind. The Earth rotation is spinning around its axis, an imaginary line that passes through the center of the Earth, connecting the north pole to the south pole. The spin of the Earth around its axis is called Earth rotation, which takes one day for the Earth to complete one rotation. Earth's rotation causes the apparent westward movement of the Sun, Moon, and stars over the sky each day. If the Sun's path is observed from the Earth, it appears to move around the Earth in a tilted path, with respect to the spin axis, at 23.5°. In other words, the Earth's spin axis is tilted concerning the plane of the Earth's solar orbit by 23.5° (see Figure 3.1). The Earth's orbital plane's projection onto the celestial sphere (the sky as seen from Earth) is called the ecliptic (Dehant and Mathews, 2015). The movement of the Earth in orbit around the Sun is named Earth revolution. It takes one year for the Earth to complete one revolution. The points where the ecliptic crosses the equatorial plane of the celestial sphere are called equinoxes when the daylight and dark time are equal. The summer solstice (Jun 21st) is the point of the Sun's path farthest north on the celestial sphere, and the point of the ecliptic farthest south is called the winter solstice (Dec 21st). The gravitational force of the Sun and the Moon on the Earth cause changes in the direction of Earth's axis very slowly, and it is named precession. Consequently, the North celestial pole always will not be a point in the same direction. It describes a circle on the celestial sphere with a period of approximately 26000 years, as Hipparchus estimated it. Currently, the axis points toward Polaris, making it the North star; in 14000 years, Vega will be the North star (See Figure 3.1).

The celestial poles and equators' locations are changing on the celestial sphere. Therefore, the celestial coordinates of objects, which are defined by the reference of the celestial equator

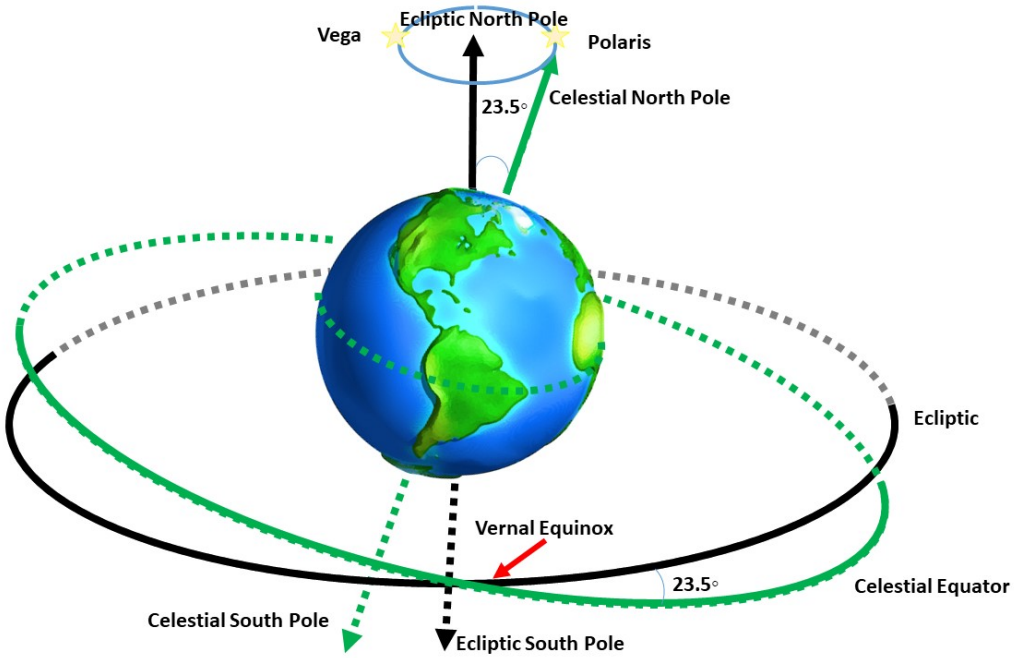

Figure 3.1: Earth at the Celestial sphere. The celestial sphere is imaginary with the equator (green), a projection of the Earth's equator onto the celestial sphere, and the ecliptic (black), the Sun's apparent path during the year. The intersection of Ecliptic and Equator are called equinoxes (Vernal equinox and Autumnal equinox) when daytime and night are of approximately equal duration. The gravitational force of the Sun and the Moon on the Earth cause changes in the direction of Earth's axis very slowly, and it is named precession. Also, The precession of Earth wobbles from pointing at Polaris (North Star) to the star Vega.

and celestial poles, are also continuously changing. Since the position of the Equinox changes with time, coordinate systems that are defined by vernal Equinox must have a reference date associated with them. The specified year is called the Equinox. The common practice is to use reference years such as 1950, 2000, and 2050 to cite the Equinox. Currently, the Equinox J2000.0 is used, the Equinox and mean equator of 2000 Jan 1st 12:00 UT (J refers to Julian year, which is 365.25 days of 86400s).

3.2 International Celestial Reference System (ICRS)

The ICRS is defined as being a space-fixed reference system (Arias et al., 1995; Ma et al., 1998). The ICRS's origin is at the solar system barycenter and with it axis $\hat{X}$ and $\hat{Y}$ in the plane of the mean equator of J2000, $\hat{X}$ being in the direction of the mean equinox of J2000. The direction of the third axis $\hat{Z}$ at this epoch explains the celestial pole of the ICRS. It is kinematically non-rotating concerning the ensemble of distant extragalactic objects. It is the idealized barycentric celestial reference system (BCRS).
If the origin of the reference system moves from barycenter (O_{XYZ}) to the geocenter ($O_{\xi\zeta\eta}$), the reference system is called the geocentric celestial reference system (GCRS). The axis of $O\hat{\zeta}$, $O\hat{\eta}$, and $O\hat{Z}$ and $O\hat{Y}$ of the two reference systems are coplanar, and $O\hat{\xi}$ and $O\hat{X}$ coincide. The GCRS is kinematically non-rotating concerning BCRS or ICRS (Dehant and Mathews, 2015).

3.3 International Terrestrial Reference System (ITRS)

The ITRS is an Earth fixed system, and it has its origin at the geocenter and has axes $\hat{x}$ and $\hat{y}$ in the plane of the true equator of date (J2000). The $\hat{x}$ is approximately on the Greenwich meridian, under the condition that there is no residual rotation about the Earth's surface. The point on the celestial sphere in the direction of the Earth's figure axis $\hat{z}$ is the pole of the ITRS (Boucher et al., 1999; Altamimi and Boucher, 2001; Altamimi et al., 2002).

3.4 Reference Frames

The realization of the ICRS and ITRS are called the international celestial reference frame (ICRF) and international terrestrial reference frame (ITRF), respectively. The IERS responsible for ITRF and ICRF. Space geodetic techniques contribute to the ITRF and ICRF like Doppler orbitography and radio positioning integrated by satellite (DORIS), Global Navigation Satellite System (GNSS), Satellite laser ranging (SLR), and very long baseline interferometry (VLBI). Currently, the latest released frames are ITRF 2014 (Altamimi et al., 2016) and ICRF 3 (Malkin et al., 2015; Charlot et al., 2020). Figure 3.2 shows the ITRF 2014 network sites and Figure 3.3 presents the source's coordinates of ICRF 3.

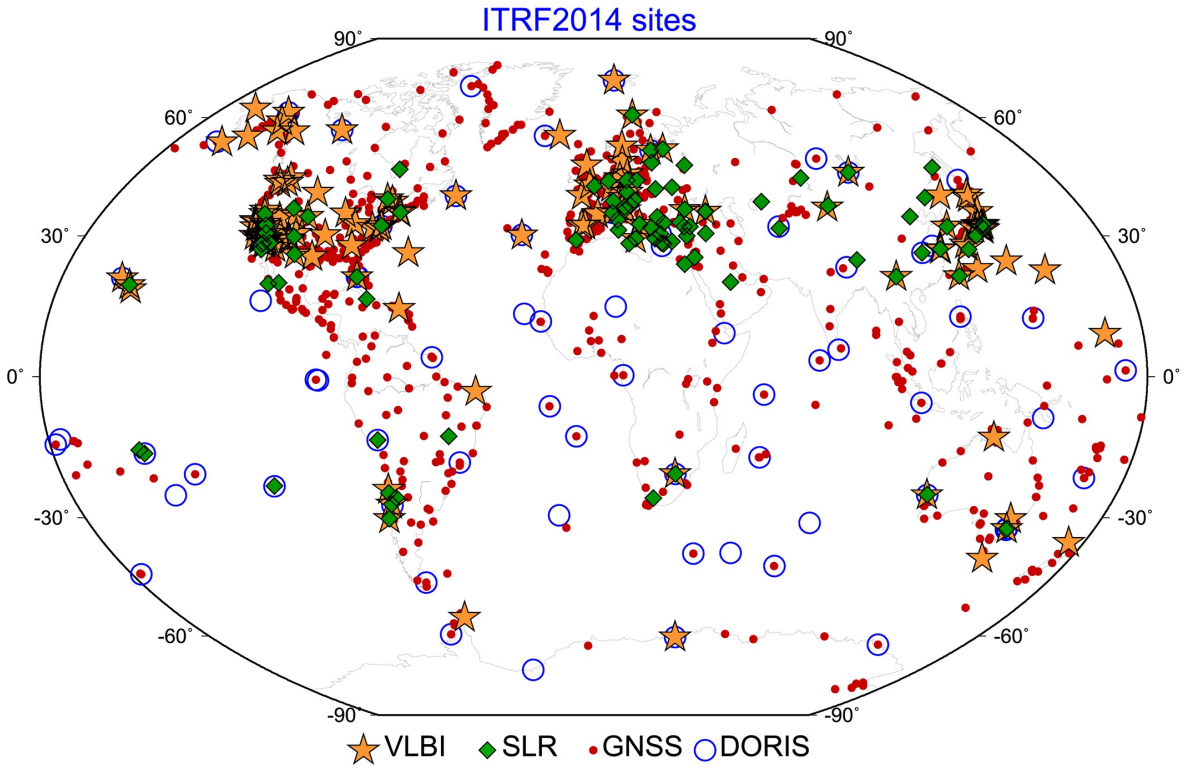

Figure 3.2: ITRF 2014 network sites (VLBI, SLR, DORIS, and GNSS). The Figure is taken from (Altamimi et al., 2016). International VLBI Service for Geodesy and Astronomy (IVS) contributes daily solution in the period 1980-2015. The International Laser Ranging Service (ILRS) submitted weekly SLR from 1993 to 2015. The International GNSS service (IGS) provides daily data from 1994 to 2015, and the International DORIS service (IDS) submitted weekly solutions from 1993 to 2015 to ITRF.

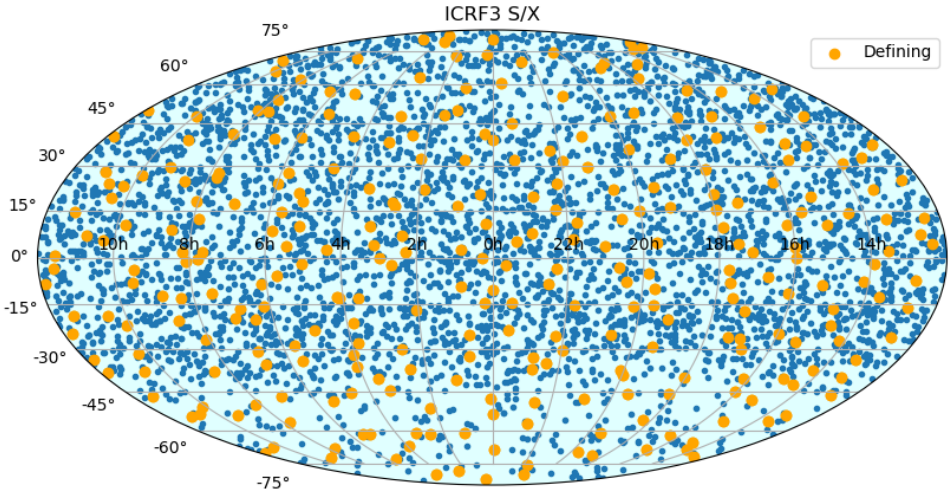

Figure 3.3: S/X -band coordinates for 4536 sources of the ICRF3. The Figure is taken from: [http://hpiers.obspm.fr/icrs-pc/newwww/icrf/icrf3sx.txt].

3.5 Earth Orientation Parameters (EOP)

The rotation of the Earth can be interpreted as a variation of the orientation of a terrestrial reference system relative to a celestial reference system. Observations and the Earth rotation theory, show that the spectral content of the motion of the Earth's figure axis in space is almost entirely in the low-frequency domain. The spectrum of the Earth's rotation pole motion relative to the Earth itself (i.e., polar motion in the classical sense) is also almost exclusively in the low-frequency domain. Therefore it made sense to break up the transformation between celestial and terrestrial frames into precession-nutation and polar motion parts (apart from an axial rotation) such that each part contains only spectral components of low frequencies between -0.5 and 0.5 cpsd (Dehant and Mathews, 2015). The International Astronomical Union (IAU) proposed in 2000 to adopt the celestial intermediate pole (CIP) (Capitaine, 2002; Capitaine et al., 2003, 2005). The CIP is introduced into the transformation between the celestial reference frame (CRF) and the terrestrial reference frame (TRF) (Seidelmann and Kovalevsky, 2002). The IERS gives the location of the CIP in the Earth-fixed reference system based on space geodetic observations and underlying models. The CIP performs motion with periods longer than two days to the space fixed reference system. In the Earth-fixed system, retrograde motions of CIP with frequencies between 0.5 and 1.5 cycles per sidereal day are allocated to nutation, whereas all other motions are interpreted as polar motion. IERS convention provides a three-dimensional rotation to describe the relationship between the GCRS orientation to ITRS orientation. The rotation between ITRS and GCRS is specified by a set of 5 Earth Orientation Parameters (EOP) as following equation (Petit and Luzum, 2010):

$$[GCRS] = Q(X, Y, s).R(-ERA).W(-s, x_p, y_p)[ITRS], \tag{3.1}$$

where, Q describe celestial pole offsets, the observed corrections to the conventional celestial pole needed to obtain the CIP. The conventional celestial pole position is given by the IAU

precession and nutation models. R is the Earth rotation, an angle measured along the intermediate equator of the CIP between the terrestrial intermediate origin (TIO) and the celestial intermediate origin (CIO) (Capitaine, 2007). Variation in the rotational speed of the Earth and consequent variation in the Earth rotation angle (ERA) are conveniently represented by UT1 time differences (dUT1). The Universal time (UT1) is defined by conventionally adopted linear proportionality to the ERA. The W represents the polar motion, the coordinates of the CIP concerning the IERS reference pole in the ITRS. The corrections angle s and s' locate the position of the CIO and TIO on the equator of the CIP, respectively (Petit and Luzum, 2010).

3.6 Geomagnetism Field Data and Model

Earth behaves like a bar magnet, and a magnetic field surrounds it (see Figure 3.4). The magnetic field is a zone with the forces active along imaginary lines from the south magnetic pole to the north magnetic pole. The imaginary bar magnet has an axis with a tilt approximately 11 degrees to Earth's rotation axis (Glassmeier et al., 2008). The Earth's magnetic field originates in the Earth's core. The core is made mainly of Iron and Nickel. In the inner core, these metal are on the solid-state, and in the outer core, they are liquid with a constant motion under the influence of the Earth rotation. According to the dynamo theory, the movement of the fluid (molten iron) outer core of the Earth generates a magnetic field (Gilbert and Wright, 1967; McElhinny and McFadden, 1998).

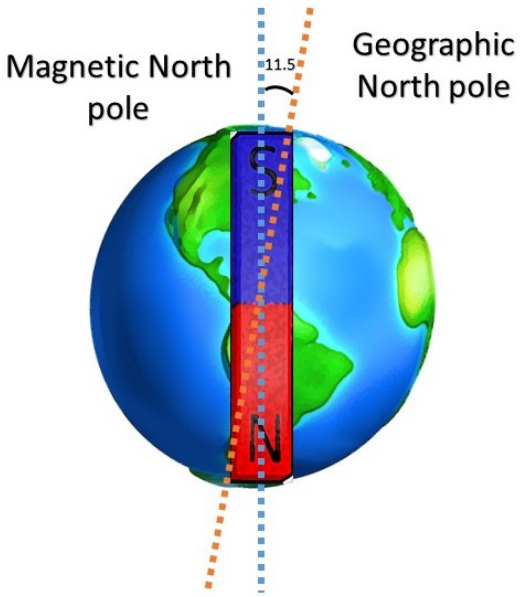

Figure 3.4: Earth's magnetic field extends from the Earth's interior. Unlike a bar magnet, geomagnetic field changes over time as it is generated by the geodynamo process from the motion of molten iron alloys on the outer core (Roberts and Glatzmaier, 2000).

3.6.1 Geomagnetic Field Elements

The geomagnetic field is a vector field, which can be described on the Earth's surface by its three orthogonal components X (pointing in the geographic North direction), Y (pointing

Eastward), Z (pointing downward) (see Figure 3.5. The horizontal component H is yielding by two horizontal components X and Y with:

$$H = \sqrt{X^2 + Y^2}, \tag{3.2}$$

which is aligned in the direction of the compass needle. The intensity of the total field F is obtained as

$$F = \sqrt{X^2 + Y^2 + Z^2}. \tag{3.3}$$

The intensity of the field is often measured in Gauss (G) and nanoteslas (nT), with $1G = 100000nT$ (Gauss, 1839). The angle between the horizontal component and geographic north is defined as declination D. The declination is positive for an Eastward deviation of the field relative to true north. The magnetic inclination is the angle between the horizontal plane and the total field vector. The inclination is given by an angle that has values between $-90°$ (up) to $90°$ (down) (Glassmeier et al., 2008).

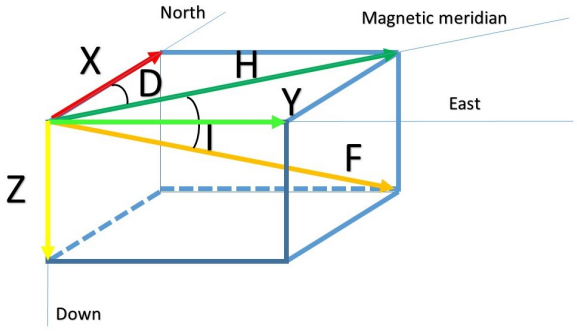

Figure 3.5: Earth magnetic field coordinate system: The three orthogonal components X, Y, and Z. The total field F, and the horizontal component H as well as the declination D and the inclination I.

3.6.2 Geomagnetic Field Models

The geomagnetic field models offer a global representation of the magnetic field based on the observational data from ground and satellites which can be used for several practical and scientific purposes such as predicting the field distribution at locations or times without direct observations or studying the field evolution and its underlying processes deep within the Earth. The most commonly used method to obtain a global magnetic field is developed by Gauss, 1839 using spherical harmonic analysis. In a source-free region, the magnetic field B can be written as the negative gradient of a scalar potential V, $B = -\nabla V$, which fulfills Laplace's equation (Langel, 1987):

$$\nabla^2 V = 0$$

For the field originating inside the Earth, the potential V_i can be developed in a series of spherical harmonic functions (Langel, 1987; Lühr et al., 2009):

$$V_i(r, \theta, \phi) = \sum_{n=1}^{\infty} \sum_{m=0}^{n} R_E (\frac{R_E}{r})^{n+1} [g_n^m \cos m\phi + h_n^m \sin m\phi] P_n^m(\theta), \tag{3.4}$$

where R_E is the Earth's radius, r, θ, ϕ are the spherical coordinates radius, co-latitude, and longitude, and P_n^m are the Schmidt quasi-normalized associated Legendre function of degree n and order m. Core and lithospheric field models are parameterized by a set of Gauss coefficients, g, and h, which can be determined from the data using least-squares inversion. Field arising outside the sphere of observation can furthermore be expressed by a potential V_e (Langel, 1987; Lühr et al., 2009):

$$V_e(r, \beta,) = \sum_{n=1}^{\infty} \sum_{m=0}^{n} R_E(\frac{r}{R_E})^n [q_n^m \cos m + s_n^m \sin m] P_n^m(\beta). \tag{3.5}$$

The International Geomagnetic Reference Field (IGRF) provides the most widely known geomagnetic field model, which is used for different applications like navigation. The IGRF model is based on the spherical harmonic analysis, and the main field and linear secular variation data are used since 1900 (Peddie, 1982; Thébault et al., 2015). Also, concerning the scientific approaches, some models are better tailored for specific aims (Olsen et al., 2000; Maus et al., 2006).

3.6.3 CHAOS – A Satellite-based Geomagnetic Field Model

The CHAOS model series, which stands for CHAMP, Ørsted, and SAC-C magnetic satellite data of Earth's magnetic field, describes the latest geomagnetic field by using high-precision satellite observations at low-Earth-orbit (LEO) (Olsen et al., 2006). In particular, the CHAOS models represent the core field variation with high spatial and temporal resolution. The first version in the series, called CHAOS (ibid.), was based on 6.5 years (March 1999 to December 2005) of Ørsted, CHAMP and SAC-C satellite data; CHAOS-2 (Olsen et al., 2009) is derived from 10 years of satellite data (until March 2009) expanded by monthly observatory averages for 1997 to 2006. The CHAOS-3 (Olsen et al., 2010), is based on more than ten years of satellite data (up to December 2009) and 13 years of ground observatory data. CHAOS-4 used more than 14 years of satellites, augmented with the magnetic monthly mean value (Olsen et al., 2014). CHAOS-5 updated the low-degree internal field model (up to degree 14) compared to CHAOS-4 (Finlay et al., 2015). The CHAOS-6 employed more than two years of magnetic data from the SWARM mission, and monthly mean from 160 ground observatories since 2016, to update the CHAOS geomagnetic field model (Finlay et al., 2016). The CHAOS-7 is the latest version of the CHAOS model, which provides high spatial and temporal resolution between 1999 and 2020. In this study, the CHAOS-6 has been investigated as it was the latest released version.

4

Space Geodetic Techniques for EOP Determination

4.1 Introduction

Space geodetic technique is the use of precise measurements between space objects such as orbiting satellites and quasars to determine positions of points on the Earth, positions of the Earth's pole, and Earth's gravity field and geoid (Seeber, 2008). The derived data from space geodetic technique observation are utilized for direct science observations and geodetic studies like EOP, gravity field earthquake displacements, and effective angular momentum. Also, the data contribute to the determination of the TRF, precise orbit determination (POD), weather forecasting models, and deep space navigation (Gambis, 2004; Rothacher et al., 2009; Schuh et al., 2015). Among the space geodetic techniques, laser ranging, GNSS, DORIS, and VLBI, contribute to Earth's orientation parameters and observations. (Dickey et al., 1985; Schuh and Schmitz-Hübsch, 2000; Dow et al., 2009; Angermann et al., 2010; Coulot et al., 2010; Nilsson et al., 2010, 2011, 2014).

A simplified scheme of the satellite geodetic techniques is shown in Figure 4.1 for EOP observation. As can be seen, the two VLBI telescopes equipped with x/s wide-band receivers register the signal from the radio source to measure differences in signal arrival time. The GNSS are equipped with precise clicks, transmitting messages such as ephemeris and clock offset to ground receivers to measure station to satellite pseudo-range. The laser ranging ground-based transmits a short-pulse laser to a satellite or moon that is equipped with corner cubes to measure the round trip pulse time of the flight to the satellite. The DORIS satellite equipped with DORIS receiver and up-link hardware transmits signals to ground beacons to measure Doppler shift on radio-frequency signals.

Table 4.1 shows the VLBI is the only technique that can observe the full set of EOP and other space geodetic techniques, as mentioned earlier, that contribute to the Earth rotation parameters (ERP) and length of day (LOD). In this chapter, the basic principle of each

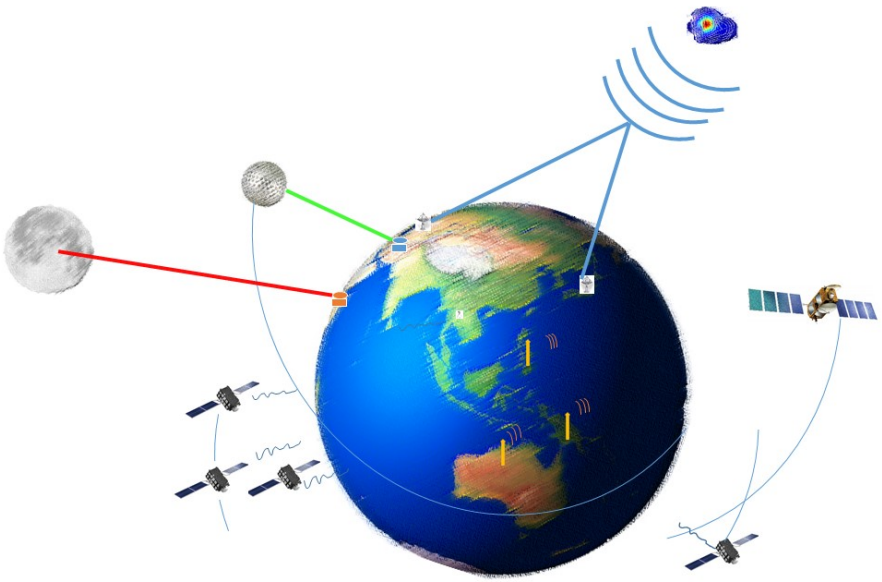

Figure 4.1: A simplified scheme for different space geodetic techniques, e.g., VLBI, GNSS, DORIS, and laser ranging.

Table 4.1: Contribution of space geodetic techniques to EOP observation.

EOP	VLBI	GNSS	DORIS	Laser ranging
Polar motion				
LOD				
UT1-UTC				
CPO				

technique is illustrated as follows:

4.2 Doppler Orbitography and Radiopositioning Integrated by Satellite

DORIS is a French microwave tracking system and an uplink radio system based on the Doppler law, needing a host satellite and a global network of ground-based tracking stations, called DORIS beacons. DORIS's system was designed by the French space agency (CNES), Institut Geographique National (IGN), and Groupe de Recherches en Geodesie Spatiale (GRGS) to offer high precision orbit determination and beacon positioning (Willis et al., 2010a). DORIS has been performed since 1990 when the first technology demonstration system was started on-board the SPOT-2 satellite (Auriol and Tourain, 2010). The DORIS system principally consists of a space segment where beings satellites, and the ground segment with three types of centers, and DORIS instrument. The DORIS system was designed for the precise orbit computation required for observing the oceans by altimetry (Tavernier et al., 2005; Willis et al., 2010b). The DORIS receivers operate on LEO satellites for precise orbit determination as well as for geodetic purposes. The ground segment is responsible for the maintenance and

operation of the DORIS constellation. The ground segment is comprised of the following elements: A beacon installation and management center at IGN coordinates the global network of orbit determination beacons. The segment Sol Altimetrie et Orbitographie (SSALTO) multi-mission control center is operated by Collecte Localisation Satellites (CLS) on behalf of CNES. Three master beacon sites can upload commands to the instrument: Toulouse, Kourou, and Hartebeetshoek. The master beacon sites are tied to an atomic clock, enabling synchronization of the DORIS system with an international reference time. The DORIS instrument is on-board the DORIS receiver developed by Thales airborne systems (TAS), receives two RF chains at the frequencies 2036.25 and 401.25 MHz (Lourme and Leloup, 2010). The DORIS system includes all the instruments on-board the carrying satellite (antenna, receiver, oscillator), an international network of autonomous stations spread around the globe, and a control and processing center that calculates the orbit of the satellites. The ground beacons broadcast signals. The DORIS receives on-board satellites that make the Doppler shift measurements and stores them in its internal memory. The data are transmitted to the ground on each pass of the satellite over a station. Then they are sent to SSALTO at regular periods, the DORIS mission control center in Toulouse, France.

4.3 Global Navigation Satellite System

GNSS are satellite constellations orbiting the Earth to provide continuous position and timing information over the globe (Hofmann et al., 2007; X. Li et al., 2015). GNSS are used in a growing number of applications (Dow et al., 2009; Awange, 2012). The most common application is navigation tools for regular users. Several countries developed and operated their systems due to the importance of GNSS. The American Global Positioning System (GPS) is the only fully operational GNSS (El-Rabbany, 2002). However, the Russian GLONASS system is now almost wholly deployed, and the European Galileo was designed to be independent but fully inter-operable with both GPS and GLONASS (Cai, Gao, et al., 2007). Other countries, such as China and India, are developing their local or global navigation satellite systems(Ganeshan et al., 2005; Cai, Gao, et al., 2007; Sharma and Poonia, 2018; Yang et al., 2019). The common characteristics of the GNSS constellation are satellites transmitting signals to the users, one-way communication between satellite and user, and use of atomic timekeeping devices. The potential compatibility and interoperability of the different systems could provide unparalleled coverage and positioning accuracy, even for ordinary users (Hofmann et al., 2007). All satellite systems contain the following segments:

1. Space segment: satellites,
2. Control segment: monitoring, controlling and uploading stations,
3. User segment: user community or GNSS receivers.

The space segment is formed by the satellites. The functions of the satellite are as follows:

- It receives and stores data from the ground control segment.

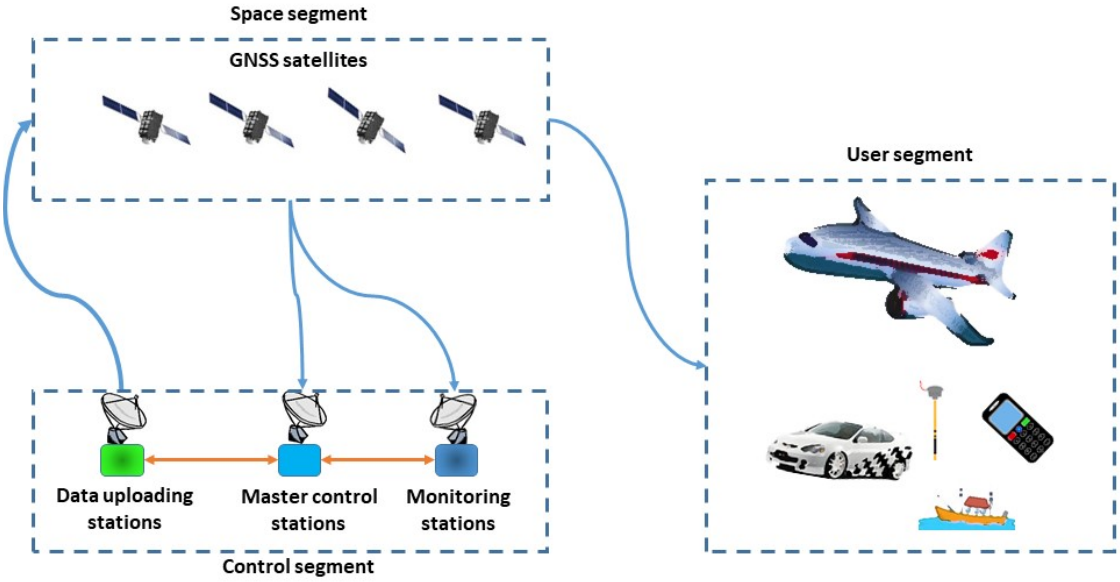

Figure 4.2: Schematic diagram of GNSS segments.

- It maintains a very precise time in order to achieve such a goal, and each satellite usually carries several atomic clocks of two different technologies (e.g., cesium and rubidium) depending on the generation of the satellite.

The main functions of the ground segment are as follows:

- Monitor the satellites, activate spare satellites to maintain system availability, and check the satellite health
- Estimate the on-board clock state and define the corresponding parameters to be broadcast
- Define the orbits of each satellite in order to predict the ephemeris data with the almanac.

The main functions of the user segments are as follows:

- Receive the data from the satellites belonging to one or several constellations on one or several frequencies,
- Receive the signal from each satellite on Sky,
- Track the signal received from the satellite on Sky.

The GNSS receiver compares the time a signal was transmitted by a satellite with the time it was received. The time difference tells the GNSS receiver the satellite's distance from the receiver location.

4.4 Laser Ranging

Laser ranging has been used to determine EOP for more than four decades routinely, determining Lunar laser ranging (LLR) measurements from 1969 when Apollo 11 lunar mission was launched and Satellite laser ranging (SLR) measurements since 1976. Therefore, laser ranging-derived EOP are required for investigating long-term variations.

4.4.1 Lunar Laser Ranging

LLR precise measurements of the Earth-Moon distance have been used in a variety of fields to perform necessary tests in areas such as general relativity. The laser pulses are transmitted via a telescope, and the reflectors which were deployed during the American Apollo lunar missions 11, 14, and 15 (Bender et al., 1973) and two Soviet Union-French missions, Lunokhods 1 and 2 between 1969 and 1973, reflect the laser pulse back (Barker et al., 1975). On Earth, the reflected pulses are registered by the telescope. The observation variable is the signal transit time of the laser pulse emitted. The performance of LLR equipment on the Moon has been affected by adverse phenomena such as solar rays and lunar librations. Only a few ground stations can perform LLR measurements to the Moon due to the atmosphere, and the diffraction effects on the reflectors. Today, there are still three stations that regularly carry out laser distance measurements to the Moon: Grasse (France), APOLLO (USA), and Matera (Italy). The distance between the Moon and Earth is calculated as follows:

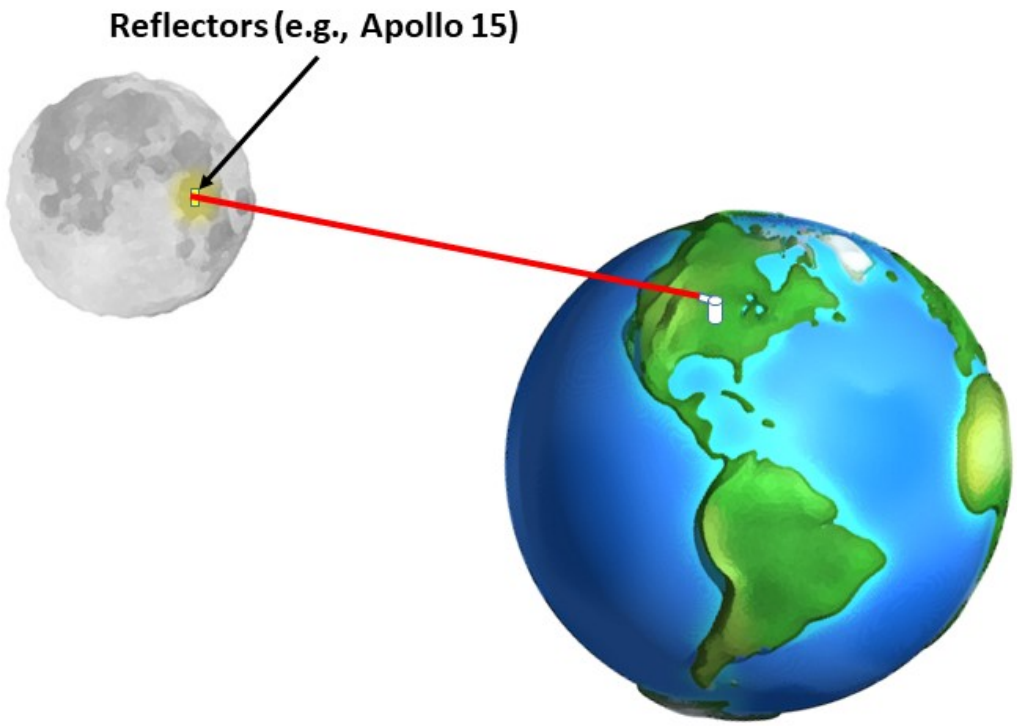

Figure 4.3: Lunar laser ranging measures the range between an observatory on Earth and a retro-reflector on the Moon. Figure not to scale.

$$D = (C * \tau)/2 \tag{4.1}$$

where d is the distance between the Earth and the Moon, C is the speed of light, and τ is the duration of delay due to reflection. Since the first LLR measurements in 1969, measurement accuracy has improved from a few decimeters to a few millimeters at the most advanced LLR observatories. LLR can be used to estimate several parameters that provide insight into the Earth-Moon system. These parameters can be categorized into different areas, e.g., reference system, dynamics of the Earth-Moon system, and physics of the Moon (Ferrari et al., 1980; Whipple, 1993; Arias et al., 1995; Bois and Vokrouhlicky, 1995; Chapront et al., 2000; Krasinsky, 2002; Williams et al., 2006).

4.4.2 Satellite Laser Ranging

SLR became an essential contributor to space geodetic techniques in particular after lunching of the first two SLR-designed geodetic satellites, Starlette in 1975 and Laser GEOdynamics Satekkite (LAGEOS) in 1976 (Degnan, 1985; Ciufolini et al., 2009). SLR measures the time

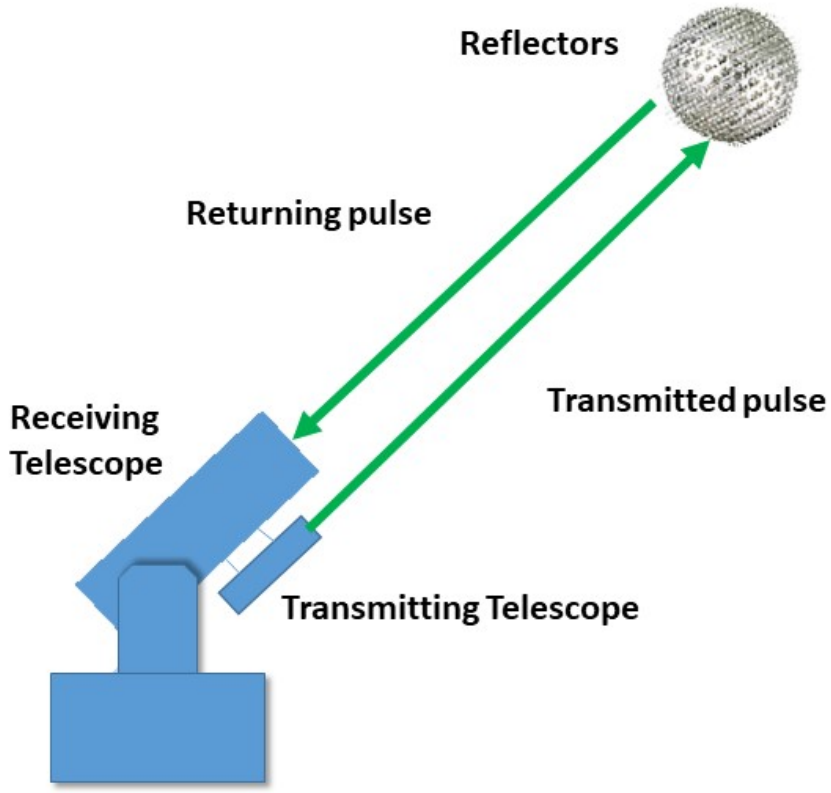

Figure 4.4: Schematic diagram of satellite laser ranging system, describing signal paths.

intervals needed for pulses emitted by a laser transmitter to travel to a satellite and return to the transmitting station. The time of firing and the pulse's time of return combine to equal the time of travel. This leads to the range measurement, using the simple model

$$R = c(t_r - t_s)/2 \tag{4.2}$$

where R is the range from the laser reference point to the average satellite retro-reflector position, and c is the speed of light. t_r is the epoch corresponding to the return of the laser pulse, and t_s is the epoch corresponding to the firing of the laser pulse. Therefore, the distance between the satellite and the observing site is approximately equivalent to half of the travel time multiplied by the speed of light. Over the last few years, a global network of precise, fixed, and mobile tracking stations have routinely tracked LAGEOS and several other satellites, producing a large quantity of exact data. SLR measurements require a correction for the dry component of the troposphere; thus, the SLR sites measure atmospheric pressure, temperature, and relative humidity to calculate this correction. Analysis of these data sets has demonstrated the potential of the laser ranging systems to make significant contributions to geodesy, geophysics, and crustal mechanics (Abshire and Gardner, 1985; Christodoulidis et al., 1985; Degnan, 1993; R. J. Eanes and S. V. Bettadpur, 1996; Bloßfeld et al., 2018a; J. M Ferrándiz et al., 2020b).

4.5 Very Long Baseline Interferometry

VLBI is a differential technique for observing the radiation of compact extragalactic radio sources at a quasi-infinite distance with several telescopes (a specific range of frequencies is recorded by VLBI antenna). The time delay in arrival can be inferred by cross-correlating the signals received by telescopes. Many primary geodetic and astrometric parameters can be determined by analyzing these delays. Karl Jansky identified the radio waves from the extragalactic in 1931 (Lovell, 1964; Richard T et al., 2017). The relevant technology was developed for long-baseline radio interferometry in the 1960s and 1970s, as seen in such innovations as the atomic clock, large scale antenna, recording technology, and signal processing. The geodetic VLBI developments and observations of 1969 laid the basis for the modern multi-band and broadband geodetic VLBI techniques that are used today (Schuh and Behrend, 2012). The geodetic VLBI consists of two components: space and ground segments (see Figure 4.5). The space segment is generally natural extragalactic radio sources. The active radio sources emit synchrotron radiation, which occurs when a charged particle is accelerated along a spiral path following the magnetic field, emitting electromagnetic radiation. The ground segments are ground stations, infrastructure, and correlators. The main task of the correlator is to process raw VLBI observations and to determine the arrival time difference at the two antennas. The main observable element of geodetic VLBI observations is the time delay (the difference in arrival times of extragalactic radio source received at VLBI stations). The time delay τ is measured by amplifying, down-converting in frequency, and digitally sampling the radiation received from the radio sources at each antenna site with electronic signal processing devices whose time, frequency, and phase information are derived coherently from an on-site atomic frequency standard, usually a hydrogen maser (Cannon, 1999; Schuh and Behrend, 2012). Figure 4.5 shows the basic idea of VLBI, a radio source emitting a planar wavefront that propagates along the unit vector to the radio source and arrives at two antennas, which are pointing simultaneously at the same radio source and are separated by the baseline vector b.

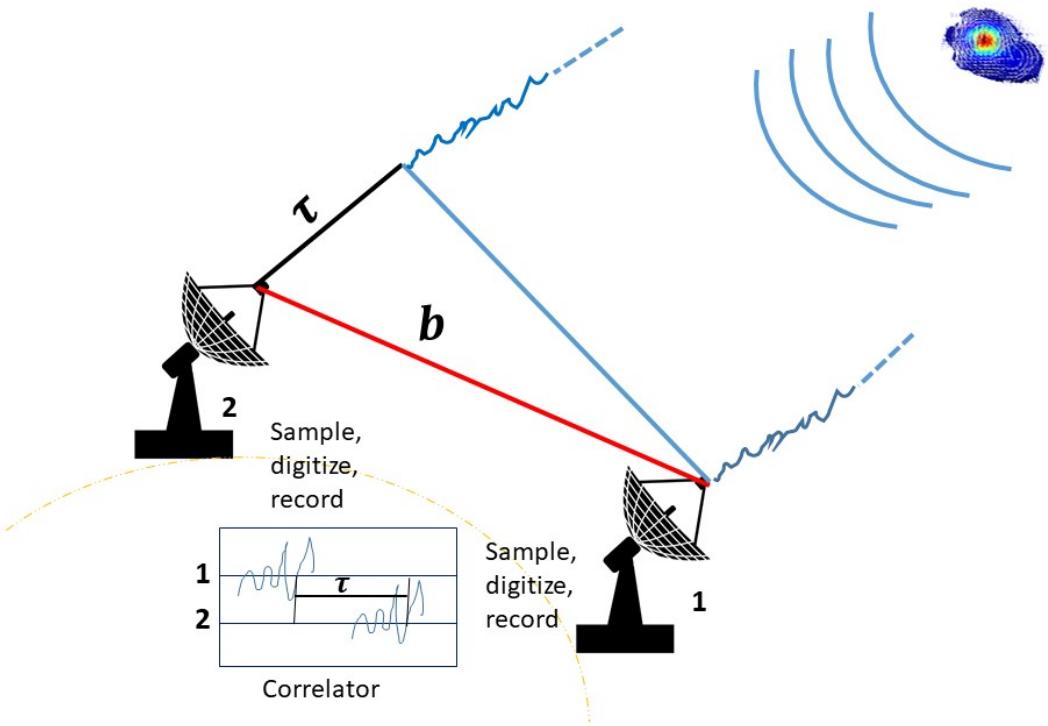

Figure 4.5: Principle of VLBI observation: The main observable is the difference in the arrival times of a plane wavefront emitted by an extragalactic radio source in direction $\hat{k}$ at two VLBI telescopes.

The geometric delay is determined as:

$$\tau_g = -\frac{b.k}{c} = t_2 - t_1 \tag{4.3}$$

where b is the baseline vector, and k is the unit vector to the radio source. The delay of the VLBI signal (τ) measured at the correlator is dominated by the geometric delay (τ_g). However, some correlations are required to be added to geometrical delays as follows (Cannon, 1999)

$$\tau = \tau_g + \tau_{ab} + \tau_{clk} + \tau_{inst} + \tau_{trop} + \tau_{iono} + \tau_{rel} \tag{4.4}$$

where τ_g is the geometric delay, τ_{ab} is a contribution due to diurnal aberration, τ_{clk} is a contribution to the signal delay arising from the mis-synchronization of the reference clocks at each observatory, and τ_{inst} is a contribution to the signal delay arising from the propagation delay through on-site cable runs and other instrumentation. The τ_{trop} is a contribution to the signal delay arising from the propagation delays through the non-ionized portions of the Earth's atmosphere, and τ_{iono} is a contribution to the signal delay arising from the propagation delays through the ionized portions of the Earth's atmosphere. The τ_{rel} are special and general relativistic corrections to the classical geometric delay (τ_g). The computation of τ_{ab} and τ_{rel} are known from physics. The calibration information is used for knowing τ_{inst}. The τ_{clk} and τ_{trop} are measured using the least square estimation, and τ_{ino} is removed based on dual-frequency observations (Finkelstein et al., 1983). More information about the concept and application of VLBI in geodesy and astronomy can be found (Ma, 1978; Clark et al., 1985; Schuh and Moehlmann, 1989; Sovers et al., 1998; Schuh, 1999, 2000; Böhm and Schuh, 2007; Heinkelmann

et al., 2009; Heinkelmann and Schuh, 2009; Böckmann et al., 2010; Heinkelmann, 2013; Schuh and Böhm, 2013).

5

Earth Rotation Theory Versus Space Geodetic Techniques Observation

Some parts of this chapter were originally taken from our published paper at the Remote sensing Journal: Ferrándiz, J. M., **Modiri, S.**, Belda, S., Barkin, M., Blossfeld, M., Heinkelmann, R., and Schuh, H. (2020b). Drift of the Earth's principal axes of inertia from GRACE and satellite laser ranging data. **Remote Sensing**, 12(2):314. DOI: `https://doi.org/10.3390/rs12020314`.

5.1 Introduction

All the official theories of Earth rotation and most of any approaches start from a reference system whose axes are aligned with the Earth's principal axes of inertia (PAI) either with the origin of the center of mass (COM) or at a point fixed relative to point fixed the body. Therefore, the Earth's PAI's location has a significant effect on many fields, including astronomy, geodesy, and satellite-based positioning and navigation systems (Chao et al., 1991; Barkin and J. Ferrándiz, 2000; Shen et al., 2008; Cheng et al., 2011).

The location of the COM was not determined with high accuracy until a few years ago. However, at present, the highly accurate mean position of the COM and its time variations is computed using modern satellite geodesy techniques. For many years, SLR was the main satellite technique to determine the gravity field of the Earth (until certain attainable degree and order of spherical harmonics coefficients (SHC))(Yoder et al., 1983; Rubincam, 1984; Chao and R. Eanes, 1995). The three first degree SHC give the COM. Also, concerning the Earth's rotation, the most relevant parameters are the second-degree SHC, linearly related to the inertia matrix (J. Chen et al., 2000; Bloßfeld et al., 2015). After launching the Gravity Recovery and Climate Experiment (GRACE) mission in 2002, the accuracy and spatial-temporal resolution of the Earth's gravity field is improved significantly (Tapley and Reigber, 2001; Tapley et al., 2004a,b). W. Chen and Shen (2010) showed the location of the PAI before and after the GRACE mission. Additionally, the geopotential models, e.g., EGM2008 and EIGEN05C with

constant Stokes coefficients that integrate GRACE data were already capable of determining the small deviations of the Earth's PAI out of the equator or the polar axis, whose magnitude is below 1 arcsecond (as) (Förste et al., 2006; Pavlis et al., 2012).
Moreover, the GRACE mission allowed detecting time variations of the Earth's gravity field with at least monthly temporal resolution (J. Chen et al., 2004; Tapley et al., 2004b, 2005; Belda et al., 2017b). Therefore, accurate mean positions of the PAI and its time variations with monthly resolution can be computed. However, the time evolution of the PAI location has never been studied since the GRACE launch, despite its relation to the Earth's rotational dynamics.
In this chapter, the evolution of the PAI is investigated, which might raise a lot of questions concerning the geophysical aspects of PAI evolution.

5.2 Analytical Method

The basic equations used in this analytical method are the same as those introduced and employed by Barkin and J. Ferrándiz (2000), where the PAI oscillations derived from the Earth's elasticity yielding to the Sun and Moon attraction and its rotation. Also, the impact of tidal and pole tide deformation on the Earth's PAI are excluded from the solution showed in this chapter as they included in the background models used to derive the SHC.

5.2.1 Basic Equations

Stokes coefficients are related to the elements of the Earth's matrix of inertia through

$$J_2 = -C_{20} = \frac{2C - A - B}{2mR^2}, \qquad C_{22} = \frac{B - A}{4mR^2}, \tag{5.1}$$
$$S_{21} = \frac{D}{mR^2}, \qquad C_{21} = \frac{E}{mR^2}, \qquad S_{22} = \frac{F}{2mR^2},$$

where A, B, and C are the inertia moments and D, E, and F are the inertia products. In case the axes are principal, the Stokes coefficients (denoted with superscript p) hold the relations

$$J_2^p = -C_{20}^p = \frac{2C_p - A_p - B_p}{2mR^2}, \qquad C_{22}^p = \frac{B_p - A_p}{4mR^2}, \tag{5.2}$$
$$S_{21}^p = \frac{D_p}{mR^2} = 0, \qquad C_{21}^p = \frac{E_p}{mR^2} = 0, \qquad S_{22}^p = \frac{F_p}{2mR^2} = 0.$$

Inertia moments and products can be computed from principal ones using the rotation matrix $M = (a_{ij})$, that relates the coordinates $X_{np} = (x, y, z)$ and $X_p = (\xi, \eta, \zeta)$ of a point in an arbitrary, non-principal reference frame and the principal one, respectively:

$$X_{np} = MX_p. \tag{5.3}$$

The relations look like as

$$A = A_p + (B_p - A_p)a_{12}^2 + (C_p - A_p)a_{13}^2, \qquad B = B_p + (A_p - B_p)a_{21}^2 + (C_p - B_p)a_{23}^2, \tag{5.4}$$
$$C = C_p + (A_p - C_p)a_{31}^2 + (B_p - C_p)a_{32}^2, \qquad D = (A_p - B_p)a_{22}a_{32} + (A_p - C_p)a_{23}a_{33},$$

$$E = (B_p - A_p)a_{31}a_{11} + (B_p - C_p)a_{33}a_{13}, \qquad F = (C_p - A_p)a_{11}a_{21} + (C_p - B_p)a_{12}a_{22}.$$

The computation of the principal moments of inertia and the rotation matrix can be performed by solving a cubic equation whose roots are the principal moments. The main steps of the procedure are presented in several references, e.g., (Barkin and J. Ferrándiz, 2000; Marchenko and Abrikosov, 2001; W. Chen and Shen, 2010).
However, when deviations are small, an analytical approximation up to the first order can be derived, which allows obtaining the rotation matrix in the form

$$M = \begin{bmatrix} a_{11} \cong 1 & a_{21} \cong \frac{F}{B_0 - A_0} & a_{31} \cong \frac{E}{C_0 - A_0} \\ a_{12} \cong \frac{F}{B_0 - A_0} & a_{22} \cong 1 & a_{32} \cong \frac{D}{C_0 - B_0} \\ a_{13} \cong \frac{E}{A_0 - C_0} & a_{23} \cong \frac{D}{B_0 - C_0} & a_{33} \cong 1 \end{bmatrix} \tag{5.5}$$

The poles of the principal axes of inertia relative to a frame deviating from them not beyond first order are given by

$$\begin{aligned} x_\xi &\cong R, & y_\xi &\cong \frac{RF}{B_0 - A_0}, & z_\xi &\cong \frac{RE}{C_0 - A_0}, \\ x_\eta &\cong \frac{RF}{B_0 - A_0}, & y_\eta &\cong R, & z_\eta &\cong \frac{RD}{C_0 - B_0}, \\ x_\zeta &\cong \frac{RE}{A_0 - C_0}, & y_\zeta &\cong \frac{RD}{B_0 - C_0}, & z_\zeta &\cong R. \end{aligned} \tag{5.6}$$

where, the superscript 0, which can be chosen in the initial moment. R is the radius of the frame.

5.2.2 Introduction of An Auxiliary Terrestrial Reference Frame (ATRF)

The ITRF (Altamimi et al., 2016) or similar frames (such as the JPL Kalman Filter and Smoother Realization of the ITRS (JTRF), DGFI-TUM realization of the ITRS (DTRF), and others (M. Seitz et al., 2012; Abbondanza et al., 2017)) are not close to the PAI frame. However, it can be transformed into a system close to it by merely performing a rotation around the third axis about 14.9° west, similar to the Groten's "best" Stokes coefficients (Groten, 2004). The result of that rotation is called ATRF. The ATRF does not have to concur with the PAI at any time, according to the above equations. The differences are matter to be small enough to obtain the rotation matrix by deriving an analytical approximation up to the first order. The three infinitesimal rotations can be used to transform the given TRF into the ATRF. In such a way, the time series of PA from any time series of second degree Stokes coefficients can be derived (Barkin and J. Ferrándiz, 2000).

5.2.3 Expression of the Earth's Principal Axes

Let us consider a body with a principal axis system O_{xyz}, subject to a mass redistribution that changes its inertia tensor and let $O_{\xi\eta\zeta}$ be the resulting principal axes system. In Barkin and J. Ferrándiz (2000), it was proved that the Cartesian coordinates of the poles of the Earth

axes of inertia after deformation, O_ξ, O_η,O_ζ could be approximated in the O_{xyz} system by:

$$x_\xi = 1, \qquad y\xi = \frac{1}{2}\frac{\Delta S_{22}}{C_{22}^0}, \qquad z_\xi = \frac{\Delta C_{21}}{2C_{22}^0 - C_{20}^0}, \tag{5.7}$$

$$x_\eta = -\frac{1}{2}\frac{\Delta S_{22}}{C_{22}^0}, \qquad y_\eta = 1, \qquad z_\eta = -\frac{\Delta S_{21}}{2C_{22}^0 + C_{20}^0},$$

$$x_\zeta = -\frac{\Delta C_{21}}{2C_{22}^0 - C_{20}^0}, \qquad y_\zeta = \frac{\Delta S_{21}}{2C_{22}^0 + C_{20}^0}, \qquad z_\zeta = 1.$$

with an error of second-order, where subscripts 0 correspond to chosen reference values of the principal moments of inertia. For the sake of studying the time evolution of them, any choice is feasible. Thus, the principal moments can be taken at the beginning of the series.
However, the equation . 5.6 and . 5.7 are valid up to first order of approximation relative to C_{2m}, S_{2m}, provided that the Stokes coefficients are referred to the ATRF or any other frame close enough to the actual PAI frame at the relevant time.
In relation to Eq. 5.6, the superscripts 0 correspond to chosen reference values of the principal moments of inertia. For the sake of studying the time evolution of them, any choice is possible, e.g., their values at the initial or other chosen time, or an average. Transforming the second-degree SHC through a rotation of angle α around the O_z axis (in the auxiliary system O_{xyz}) is straight forward since the zonal term remains unchanged and the tesseral and sectorial terms of each frame are related through

$$C_{21}^{ATRF} = cos(\alpha)C_{21}^{ITRF} + sin(\alpha)S_{21}^{ITRF}, \qquad S_{21}^{ATRF} = -sin(\alpha)C_{21}^{ITRF} + cos(\alpha)S_{21}^{ITRF}, \tag{5.8}$$

$$C_{22}^{ATRF} = cos(2\alpha)C_{22}^{ITRF} + sin(2\alpha)S_{22}^{ITRF}, \qquad S_{22}^{ATRF} = -sin(2\alpha)C_{22}^{ITRF} + cos(2\alpha)S_{22}^{ITRF}.$$

In the equations, each coefficient is identified with the superscript corresponding to its reference frame. In such a way, we can derive the time series of the PAI location from any time series giving the second-degree Stokes coefficients. It is worth mentioning that for the computation of the uncertainties of the pole locations from the Stokes coefficients, formal uncertainties Eqs. 5.8 can be applied as well, unlike when computing the PAI poles by numerical methods since the former relations are linear.

5.2.4 Rotation Providing the Principal Axes

Belda et al. (2017b) expressed the transformation of the frames through three infinitesimal rotations R_x, R_y, R_z. The differences $(\Delta x, \Delta y, \Delta z)$ between the coordinates (ξ, η, ζ) in the mean monthly principal axis frame $O_{\xi\eta\zeta}$ and the coordinates (x, y, z) in the auxiliary system O_{xyz} are related to those rotations by:

$$\begin{bmatrix} \Delta x \\ \Delta y \\ \Delta z \end{bmatrix} = \begin{bmatrix} 0 & -R_z & R_y \\ R_z & 0 & -R_x \\ -R_y & R_x & 0 \end{bmatrix} \begin{bmatrix} x \\ y \\ z \end{bmatrix}. \tag{5.9}$$

The rotations transforming the auxiliary, quasi-principal system into the principal are

$$R_x = -\frac{\Delta S_{21}}{2C_{22}^0 + C_{20}^0}, \qquad R_y = -\frac{\Delta C_{21}}{2C_{22}^0 - C_{20}^0}, \qquad R_z = \frac{1}{2}\frac{\Delta S_{22}}{C_{22}^0}, \tag{5.10}$$

where superscripts 0 stands for the initial term of the series, and the neglected terms are second-order concerning the variations of the Stokes coefficients. Let us notice that each rotation is related to one of the former pole's coordinated, for instance

$$R_x = -y_\zeta, \qquad R_y = -z_\xi, \qquad R_z = y_\xi.$$

5.3 Data Analysis

The time evolution of the Earth's PAI can be computed accurately from some of the available geopotential solutions providing a time-varying Stokes coefficients of degree 2, C_{2m}, and S_{2m} (Cheng et al., 2011, 2013a,b). In this study, I use the time series provided by the center for space research at the University of Texas at Austin (CSR/UT), which contains monthly mean estimates of those coefficients referred to the international terrestrial reference frame (ITRF) (Cheng et al., 2013a; Save et al., 2018). Also, the SLR-based analysis used with weekly time resolution from Deutsches Geodätisches Forschungsinstitut (DGFI-TUM), Munich, Germany (Bloßfeld et al., 2015). The following analysis covers the period from January 2000 to February 2018. The used data are given the degree 2 normalized Stokes coefficients $\bar{C}_{2m}$ and $\bar{S}_{2m}$ with their corresponding time tags (The basic meaning of the coefficients can be found in (Cheng et al., 2011, 2013a,b). The processing standards of this solution follow the IERS Conventions (2010) (Petit and Luzum, 2010), as indicated in Bloßfeld et al. (2015, 2018b).
The degree 2 normalized Stokes coefficients $\bar{C}_{2m}$ and $\bar{S}_{2m}$ are used with their corresponding time tags and uncertainties, with the weekly resolution, along the period from January 2000 to February 2018.
The outline of the computation flow is the following for each of the time series. First, Stokes coefficients are transformed from normalized to unnormalized using the standard approach presented, e.g., in Eqs.6.2b and 6.3 of (Petit and Luzum, 2010). Then, I obtain the SHC after performing a rotation of angle $\alpha = -14.9286648815724558$ degrees (corresponding to an initial value $S_{22} = 0$ of the CSR rotated SHC) of the reference frame. That rotation angle defines the chosen ATRF that is not principal since the $(2, 1)$ SHC not vanish but is close enough to the PAI to enable the application of the previous equations. Then, the location of the PAI at each data point is found by computing the three infinitesimal rotations given by Eqs. 5.10. Next, these three rotation time series, for each input data, are examined emphasizing on the identification of trends. All the statistics and the linear fit functions are estimated weighting the input data with their squared formal errors and using the MAPLE 17 package of Maplesoft, a division of Waterloo Maple Inc., Waterloo, Ontario (Bernardin et al., 2011).

5.4 Results

The results corresponding to the RL06 CSR and DGF-TUM SLR data are displayed in Figures 5.1, 5.2, and 5.3 in [cm]. Notice that vertical scales are different. The Figure 5.1

illustrates the three rotations R_x, R_y, and R_z (in blue) and the first-degree polynomials are fitted to them (in black); at the legend of each plot, there is a part that shows the WRMS (weighted root mean squared) of the date before and after the fit. The middle panel is made of another three plots that display the respective residuals. The lower panel shows the corresponding spectral analysis results of the residual part. All the offsets and trends are significant. The most substantial rotation corresponds to R_z, around the O_z axis of the auxiliary frame, coincident with O_z of the ITRF. Its trend reaches 321.882 ± 86.781 cm/yr on the Earth's equator (see Table 5.1).

Table 5.1 indicates the value of the WRMS after the fit and the coefficients of the linear regression line, together with their formal errors (1σ). The time origin is set to be the date JD 2000.0 (modified Julian date 51544.5). All the coefficients apart from the R_x trend are larger than 3σ, thus significant. The R_z is the largest rotation, around the O_z axis of the ATRF, coincident with the ITRF O_z. Its trend reaches 321.88 ± 86.78 cm/year on the Earth's equator, and its direction is Eastwards since it is positive (counterclockwise rotation, bringing the instantaneous O_x closer to the ATRF O_y). The trends of the other rotations are much smaller. The rotation R_x around the O_x axis is negative (clockwise), driving the ATRF O_z axis towards the positive O_y axis, with the smallest velocity of roughly -0.26 ± 0.82 cm/year. Finally, the R_y rotation is positive (counterclockwise), moving O_x and O_z Southwards (O_z towards to the ATRF O_x) by 10.40 ± 0.36 cm/year on the surface.

The R_x and $R_z$rotations also exhibit nearly annual and seasonal variations. They might be attributed to the seasonal variations visible in the GRACE gravity fields or to inaccuracy of the background models, at least to some extent. A fast Fourier analysis confirms that the main period of all the rotations is annual, although it also detects power at many other frequencies, like those associated to the semi-annual, Chandler, and semi-Chandler periods, in general with noticeably smaller amplitudes and correspondingly larger formal errors (see Figure 5.1, lower panel).

Figure 5.2 shows the motion of R_x, R_y, and R_z in blue. Also, a linear function and the annual

Table 5.1: Results derived from the RL06 CSR Stokes coefficients with monthly resolution.WRMS after fitting a linear function to each, biases, and drifts of the equivalent rotations R_x, R_y, and R_z from ATRF to PAI. Units are [cm] and [cm/year], time origin is 2000.0. The lower panel shows the results of the fast Fourier analysis.

	WRMS [cm]	Bias [cm]	Drift [cm/year]
R_x	56.66	999.12 ± 9.35	-0.26 ± 0.82
R_y	25.06	442.92 ± 4.13	10.40 ± 0.36
R_z	5955.06	-5029.83 ± 989.57	321.88 ± 86.78

oscillations of R_x, R_y, and R_z is fitted to data in black color (upper panel). Table 5.1 and 5.2 illustrate fitting the annual oscillations decreases WRMS of R_x, R_z significantly except for R_y. The trends of R_x and R_y are almost indifferent of the ones in Table 5.1, whereas the R_z trend differs by about 6% between the two fits.

The same computations have been performed for the weekly DGFI-TUM time series provided by Mathis Bloßfeld (Bloßfeld et al., 2015). Figure 5.3 is equivalent to Figure 5.1 for the former RL06 data set and thus does not require description. Let us recall that the DGFI-TUM series do not cover the same time interval than the CSR one: it starts in 2000,

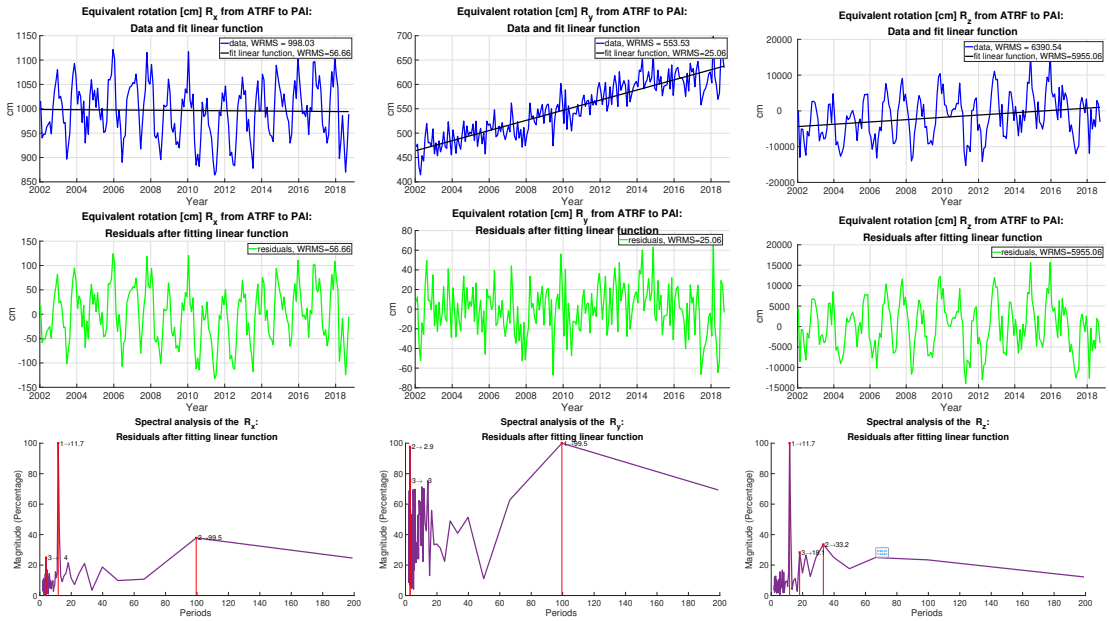

Figure 5.1: Results derived from the RL06 CSR Stokes coefficients with monthly resolution. Upper panel: Equivalent rotations [cm] R_x, R_y, and R_z from ATRF to PAI frame (in green, from left to right) and fit linear functions (in black). Middle panel: The residuals are also given in [cm]. The lower panel shows the results of the fast Fourier analysis.

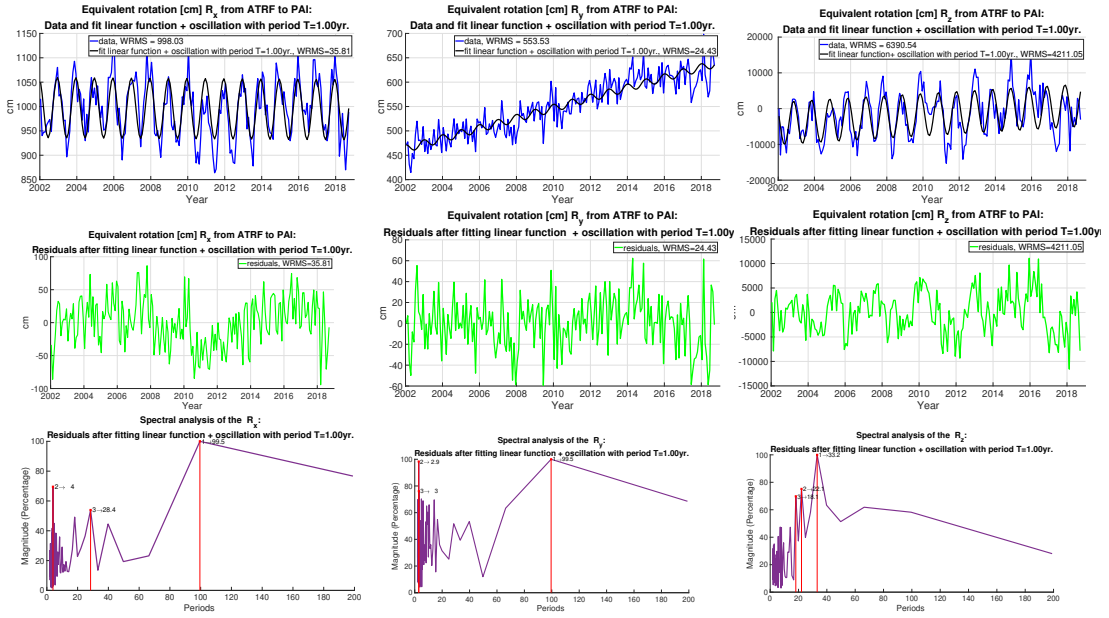

Figure 5.2: Results derived from the RL06 CSR Stokes coefficients with monthly resolution. Upper panel: Equivalent rotations [cm] R_x, R_y, and R_z from ATRF to PAI frame (in green, from left to right) and fit linear functions plus annual oscillations (in black). Middle panel: The residuals are also given in [cm]. The lower panel shows the results of the fast Fourier analysis.

two years earlier, and ends a few months earlier in 2018. The vertical scales of the plots are subject to change, like in the previous cases.

There is no complete overlapping of the confidence regions, but the trends are kept. Small differences may arise from little differences in background models or processing strategies. Table 5.3 shows the statistic results derived from the SLR DGFI-TUM Stokes coefficients with weekly resolution. To discard that the higher temporal resolution of the DGFI-TUM input

Table 5.2: Results derived from the RL06 CSR Stokes coefficients with monthly resolution.WRMS after fitting a linear function and an annual oscillation to each, biases, drifts, and annual amplitudes of the equivalent rotations R_x, R_y, and R_z from ATRF to PAI. Units [cm] and [cm/year], time origin 2000.0, null phase at the origin.

	WRMS [cm]	Bias [cm]	Drift [cm/year]	Amp. *cos* [cm]	A *sin* [cm]
R_x	35.81	998.32 ± 5.95	-0.26 ± 0.82	58.80 ± 3.58	-19.32 ± 3.64
R_y	24.43	442.67 ± 4.050	10.41 ± 0.35	7.86 ± 2.44	-0.21 ± 2.49
R_z	4211.05	-4747.51 ± 703.91	302.93 ± 61.70	3408.96 ± 420.54	-4924.77 ± 428.73

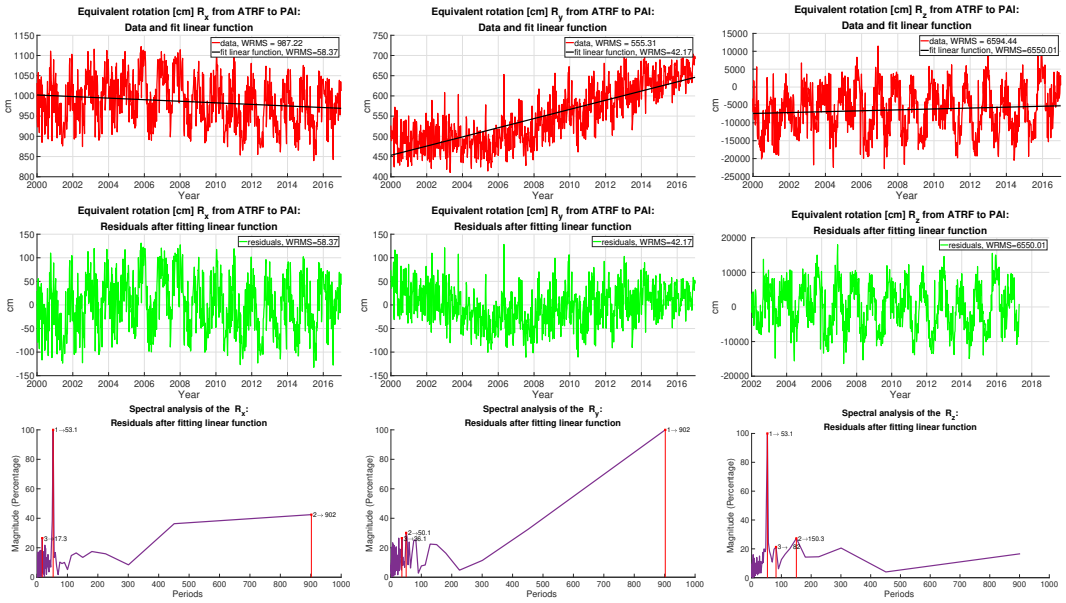

Figure 5.3: Equivalent rotation (in cm) of R_x, R_y, and R_z from ATRF to PA using the data from DGFI solution.

Table 5.3: Results derived from the SLR DGFI-TUM Stokes coefficients with weekly resolution. WRMS after fitting a linear function to each, biases, and drifts of the equivalent rotations R_x, R_y, and R_z from ATRF to PAI. Units are [cm] and [cm/year], time origin is 2000.0.

	WRMS [cm]	Bias [cm]	Drift [cm/year]
R_x	58.37	1005.23 ± 3.25	-2.15 ± 0.39
R_y	42.17	448.42 ± 2.78	11.78 ± 0.28
R_z	6550.04	-7474.45 ± 436.28	120.073 ± 43.61

data might cause some distortion of the results, I have also examined a smoothed version of them with a monthly resolution like the CSR data and found that there is no relevant difference in the results. The resulting drifts are $R'_x = -1.96 \pm 0.60$, $R'_y = 11.42 \pm 0.39$, $R'_z = 120.55 \pm 71.46$ cm/y, very close to the weekly ones.

5.5 Discussion

The results of the observed principal axes of inertia of the Earth, as computed from the Stokes coefficients provided by CSR/UT at a monthly rate and DGFI-TUM at the weekly rate, are not tight to the ITRF axes, however, exhibit a non-negligible drift.

It may be somehow striking that the trends of the R_z rotation are at least one order of magnitude larger than the ones of the other two rotations. That is because the value is obtained after a division by C_{22} according to Eqs.(5.10), while in the other two the denominators have the

order of magnitude of C_{20}. Consequently, the motion of the first two axes of inertia along the equator is expected to be much larger than the shift of the O_z axis. A similar feature appeared in the periodic tidal disturbances of the Earth's PAI computed by Barkin and J. Ferrándiz (2000), where the maximum amplitude for the third axis (corresponding to the fortnightly perturbation) was about 19 km, whereas for the other axes the oscillation at the same period is only of about 19 m, as illustrated in Table 3, row 11 of that reference.

The results derived from the two data sets, based on the UT/CSR GRACE RL06 and the DGFI-TUM SLR solutions, are compared. The corresponding trends are re-arranged on Table 5.4, where the columns refer to the individual rotations. The values of the annual trends ("drifts") fit to the data set are shown in the first row (CSR or DGFI-TUM), and the 95% confidence intervals ("CI95") are presented in the adjacent columns to the right. The values of the R_y trends are very close, but the other two look quite different. Nevertheless, the respective CI95 of the latter two do overlap, and consequently, I can conclude that the trends of R_x and R_z do not differ significantly. As for R_y, their two CI95 do not overlap, but the distance between them is only 1 mm over about 10 cm, and thus a slight increase of the level of significance would result in overlapping.

Therefore, the results are robust enough to be meaningful and can be considered a physical feature of the Earth change, not an artifact. The last column of Table 5.4 holds the mean value of the two trends, which may be considered to be a preliminary reference value of the linear trend associated with each rotation, i.e., the annual drift of the relevant axis. Though some of the values are very small, all of them are above the accuracy and stability requirements asked for by GGOS of IAG, to the reference frames and related parameters, namely 1 mm in position and 0.1 mm/year in velocity.

The small differences found between the two solutions may arise from some differences in background models or processing strategies. As can be seen in Figures 5.1 and 5.3, there is a clear trend in the R_y component in both solutions. However, the trend seems to accelerate around the years 2005-2006, the DGFI-TUM time series. The difference in the C_{21} and S_{21} derived rotation time series might be caused by the different handling of the mean pole in the CSR RL06 and the DGFI-TUM solution. Using different mean pole model could provoke a systematic long-term difference in the C_{21} and S_{21} time series (Wahr et al., 2015; Göttl et al., 2018; W. Chen et al., 2019; Dahle et al., 2019). The CSR RL06 solution is processed based on the new linear mean pole model, whereas the DGFI-TUM SLR time series is based on the conventional (cubic polynomial) mean pole model (Petit and Luzum, 2010). Our results provide a further example of the relevance of the choice of a mean pole model.

The magnitude of the R_z rotation, which drives the other two axes Eastwards along the equator at a velocity of about 2.2 m/year is surprising since that motion has not been detected till now. However, the satellite-derived time-varying gravity field solutions have been available for not too many years and have never been examined for that purpose. If we consider other ways of identifying that motion, the analysis of the evolution of the EOP is not as suitable as this approach (although the EOP may be affected by the PAI drift). In fact, most of the nutation theories are based on a symmetric Earth model; therefore, they are not sensitive at all to the rotation of the inertia axes A and B, lying almost on the equatorial plane. Similarly, most of the investigations on polar motion and length of day (or UT1) also neglect the terms

corresponding to the Earth's triaxiality and become thus insensitive to the motions of those inertia axes. An additional difficulty arises from the aliasing between the diurnal rotation (for instance UT1) and the node of the satellite orbits.
As additional evidence in support of our finding of the agreement of the two solutions, I complete this section with joint plots of the rotations computed from each data set (displayed as a line) together with their CI95 (displayed as a colored area around the line). It can be visualized easily in Figure 5.4 that the solutions for each of the three rotations R_x, R_y, and R_z are very similar across the entire time interval which reinforces the hypothesis that the two solutions do not exhibit significant differences.

Table 5.4: Comparison of the linear trends of the rotations R_x, R_y, and R_z obtained from the monthly CSR and weekly DGFI-TUM solutions. CI95 denotes the 95% confidence interval of the fit drift value. Units are cm/year.

	Drift (RL06)	CI95 (RL06)	Drift (DGFI-TUM)	CI95 (DGFI-TUM)	Mean drift
R_x	-0.26 ± 0.82	$(-1.9, 1.4)$	-2.15 ± 0.39	$(-2.9, -1.4)$	-1.21
R_y	10.40 ± 0.36	$(9.7, 11.1)$	11.78 ± 0.28	$(11.2, 12.3)$	11.09
R_z	321.88 ± 86.78	$(150.8, 493.0)$	120.07 ± 43.61	$(34.5, 205.7)$	220.97

5.6 Conclusions and Outlook

From J. M Ferrándiz et al. (2020b) (Correspondence to Sadegh Modiri):

> The computation of the motion of the Earth's principal axes of inertia using two different data sets for the time-varying second-degree Stokes coefficients, derived from GRACE and SLR solutions, shows a significant agreement, in spite of small differences in the processing standards and time interval or range of each solution, monthly and weekly, respectively. The most remarkable feature is that the determined principal axes of inertia of the Earth are clearly closely aligned to the ITRF axes nor oscillating around certain "mean" equilibrium position, but exhibit non-negligible drifts, with magnitudes clearly exceeding the accuracy threshold of GGOS, the IAG Global Geodetic Observing System. The most remarkable detected motion drives the two nearly equatorial inertia axes Eastwards, at a rate of 2.2 m/year. Besides, the axis of less inertia deviates away from the equator Southwards at 11 cm/year, and the medium axis also moves Southwards out of that plane at a smaller rate of 1 cm/year. The axis of major inertia follows the drifts of the other two.
>
> This results are intentionally limited to quantifying observational facts, but the physical causes of the drift of the Earth's principal axes is still unknown, as well as its impact on other topics, e.g. Earth rotation. Getting more insight into these topics seems to be not an easy task, but different ideas or issues may emerge from future discussions about the topic. Whether or not motion is due mainly to a sole cause, concerning external mass transport, changes in the Earth's inner layers, tectonics, or a combination of processes. In this case, the geophysical budget could be closed to some extent. Another open question is whether these variations of

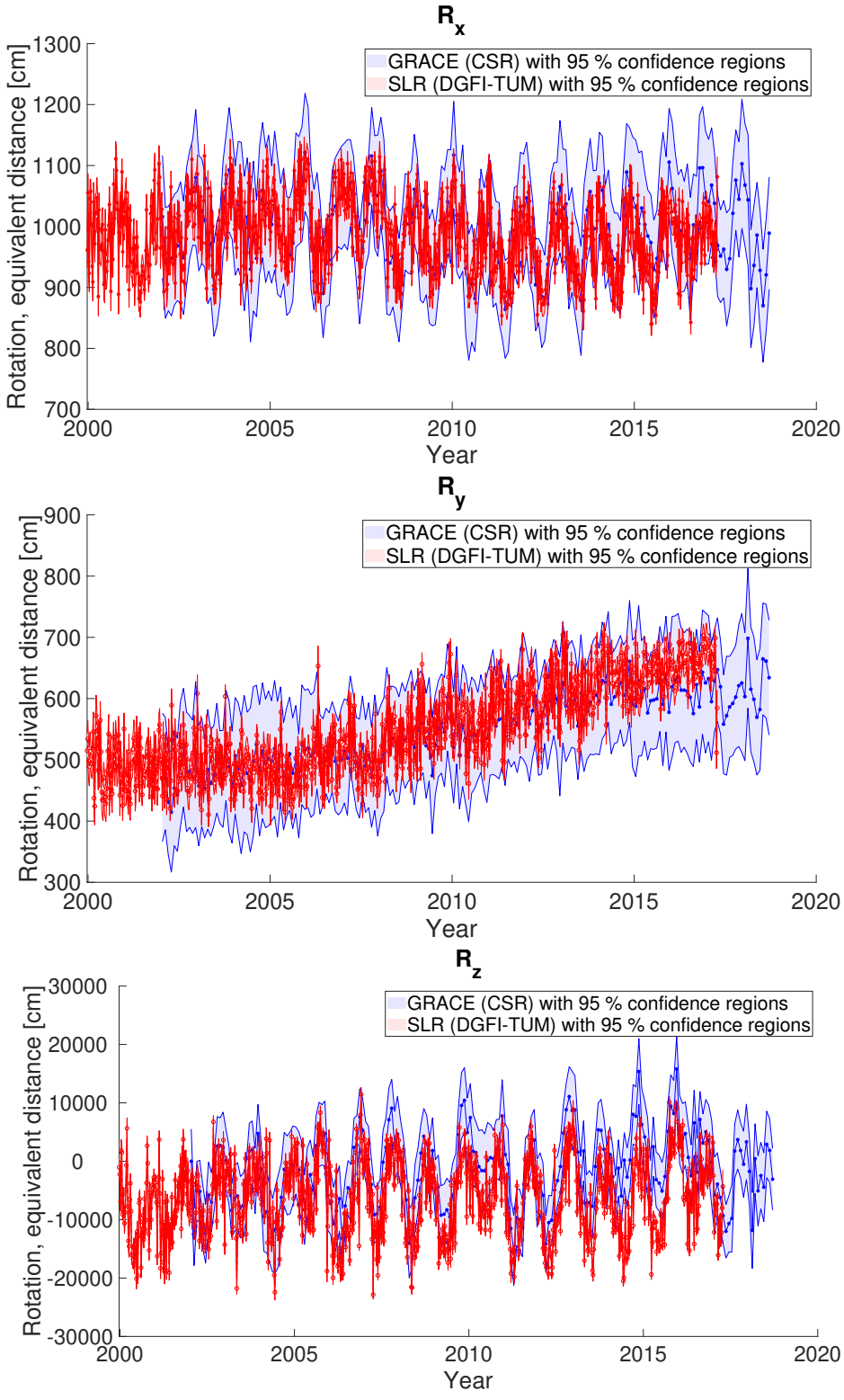

Figure 5.4: Joint plots of the rotations from ATRF to PAI frames derived from the RL06 CSR and SLR DGFI-TUM Stokes coefficients with their respective 95% confidence regions. Left R_x, middle R_y, and right R_z. Color code: CSR: curve in blue, confidence region in light blue; DGFI-TUM: curve in red, confidence region in light red. Units: cm (equivalent).

the Earth's inertia tensor might affect other processes of the Earth and could be related to, e.g., decadal or long-term EOP variations or other observed trends.

6

A New Hybrid Method for EOP Prediction

Some parts of this chapter were originally taken from our published papers at the **Journal of Geodesy** and **Earth, Planets and Space**:
Modiri, S., Belda, S., Hoseini, M., Heinkelmann, R., Ferrándiz, J. M., and Schuh, H. (2020). A new hybrid method to improve the ultra-short-term prediction of LOD. **Journal of Geodesy**, 94(2):23. DOI: `https://doi.org/10.1007/s00190-020-01354-y`.
Modiri, S., Belda, S., Heinkelmann, R., Hoseini, M., Ferrándiz, J. M., and Schuh, H. (2018). Polar motion prediction using the combination of SSA and Copula-based analysis. **Earth, Planets and Space**, 70(1):115. DOI:`https://doi.org/10.1186/s40623-018-0888-3`.

6.1 Introduction

Accurate near real-time EOP is needed for applications related to fundamental astronomical and geodetic reference frames, monitoring and modeling Earth rotation, and geophysical research (Munk and Revelle, 1952; Lambeck and Cazenave, 1973; Munk and MacDonald, 1975; Hinderer and Zurn, 1990; Brzeziński, 2000, 2005; Kalarus et al., 2010; F. Seitz and Schuh, 2010; Schuh et al., 2011; Stamatakos, 2017; Belda et al., 2018). A number of techniques have been developed and applied for the EOP prediction, which could be classified into two main groups. The first group is the methods that use the information within the EOP time series such as auto-covariance (AC) (Kosek et al., 1998; Kosek, 2002; Kosek et al., 2005), least squares (LS) collocation (Włodzimierz, 1990; Zotov et al., 2018), wavelet decomposition (Akyilmaz and Kutterer, 2004; Kosek and Popinski, 2005; Akyilmaz et al., 2011), or neural network (Schuh et al., 2002; Liao et al., 2012; Q. Wang et al., 2014; Lei et al., 2015). Also, the hybrid methods are categorized in the **first group**, for example, the combination of least squares (LS) and auto-regressive (AR), auto-regressive moving average (ARMA), or auto-covariance and neural network (Kosek et al., 1998; Akulenko et al., 2002; Kosek and Popinski, 2005; Kosek et al., 2007; Xu et al., 2012; Xu and Zhou, 2015; Wu et al., 2019).

The **second group** is the methods that take into account the geophysical parameters such as axial component of effective angular momentum (EAM_Z). Freedman et al. (1994) showed that the use of atmospheric angular momentum (AAM) wind terms in the Kalman filter technique to predict LOD variations improved near-term predictions (Freedman et al., 1994; Gross et al., 1998; Johnson et al., 2005; Niedzielski and Kosek, 2008; Kosek et al., 2011; Nastula et al., 2012; Dill et al., 2019; Sun et al., 2019). Johnson et al. (2005) used UT1 observations as determined by AAM in the UT1-UTC combination solution to predict UT1, which showed a significant reduction in the prediction errors when compared with the previous prediction method (McCarthy and Luzum, 1991). Also, Dill et al. (2019) used six days of long-predicted EAM values for the PM and UT1-UTC prediction using LS extrapolation and AR model.
The EOP prediction comparison campaign (EOP PCC) took place within (2005–2009) due to the initiative of Prof. Harald Schuh (Kalarus et al., 2008). The results of EOP PCC indicate that there is no particular approach preferred over others for all prediction intervals (ultra/short-term, and long-term) (Kalarus et al., 2010). Also, as the EOP prediction accuracy profits from atmospheric angular momentum (AAM) forecast data, EOP PCC recommended paying more attention to the analysis and prediction of AAM, the continental hydrology angular momentum (HAM), and the ocean angular momentum (OAM). Among these techniques, the combination of LS and AR process is considered to be one of the most effective for EOP prediction. The mentioned combination method achieved reasonable results for short-term forecasting. However, due to the complexity of the EOP excitation model, it is not able to reproduce the time variation of the periodic terms that affect the long-term predictive accuracy of EOP.
Accordingly, a new prediction approach is required that could bring us significantly closer to reaching the accuracy goals pursued by the GGOS of the IAG, i.e., 1 mm accuracy and 0.1 mm/year stability on global scales in terms of the ITRF defining parameters (Plag et al., 2009).
Thus, new methods, or a combination of the existing approaches, must be investigated to develop the efficiency of the predicted EOP considering the time variation of the periodic terms and the trend.
I explored the combination of Copula-based analysis and SSA to predict EOP (Modiri et al., 2019). In Modiri et al. (2018), I applied the combination of SSA and Copula for the first time as a novel deterministic-stochastic tool for PM prediction using only PM past data (first group). Also, in Modiri et al. (2020), I applied our hybrid technique for LOD prediction by taking the advantages of the EAM (second group). Please see the methodology part for more details about the model. The two above-mentioned groups will be examined in this chapter as follows:

6.2 First Group: PM Prediction

PM consists of two parts: trend and undulation. Our hybrid model consists of a deterministic annual and the Chandler component as well as long-term lower frequency parts, which are estimated by SSA. The difference between the deterministic solution and the PM data is then

used in a Copula-based model to predict stochastic processes. Then, the final PM prediction is a combination of the deterministic prediction (derived from the SSA solution) and the stochastic prediction (obtained from the Copula solution).

6.2.1 Data Description

The PM_x and PM_y time series is taken from the International Earth Rotation and Reference System Service (IERS) combined (EOP) solutions 08 C04 (available at `http://hpiers.obspm.fr/eop-pc/analysis/excitactive.html`). The EOP 08 C04 series is derived from different geodetic techniques, and it is consistent with ITRF 2008. The EOP 08 C04 time series covers the period from 1962 to present, with daily resolution (Figure 6.1). I used 6 years of observed PM time series, from January 1997 to December 2002, for the 365-days-ahead prediction. To verify the reliability of this method, the results were compared with the IERS Bulletin A predictions (`https://datacenter.iers.org/web/guest/bulletins/-/somos/5Rgv/version/6`). The IERS Bulletin A contains the PM parameters and the predicted PM for one year into the future, and they are released weekly by IERS RS/PC, hosted by USNO (Petit and Luzum, 2010; Gambis and Luzum, 2011).

6.2.2 Data Analysis

The SSA is used to model the deterministic part of PM time series, which is dealing with the periodic terms, e.g., Chandler wobble, annual variation, and geophysical tides. Then, the Copula-based analysis model is employed to model the difference between the observed PM and SSA-estimated data. After that, the periodic terms of PM are extrapolated using the SSA a priori model. Moreover, the anomaly part is predicted using the Copula-based model. Eventually, the anomaly solution is added to the SSA-forecasted time series. Consequently, the final PM predicted data is the sum of the results of predicted periodical terms and the anomaly using SSA and the Copula-based model, respectively.

6.2.2.1 SSA Periodic Terms Estimation

Choosing the window length is the most challenging part of the SSA model as it has a significant impact on the decomposition of the time series. As can be seen in Figure 6.2, it depicts the Chandler period as the main period of both time series, which would be a reasonable choice. Also, the least common multiple of the Chandler and annual periods are recommended by Golyandina and Zhigljavsky (2013). After the selection of the window length, the number of singular vectors or empirical functions for the reconstruction of the time series should be determined. The goal of this procedure is to find and apply a proper set of constructive components. Most significant periodicities, as well as excitation mechanisms, are rather low-frequency components and reveal their impact in the first few singular vectors while high-frequency components fall in later singular vectors. The singular value spectrum reflects the importance of each singular vector. As can be seen in Figure 6.3, in order to achieve an accuracy of about 1 mas for PM modeling, at least the first 70 singular vectors are needed to be employed, which correspond to using all components with periods more than or equal to 14

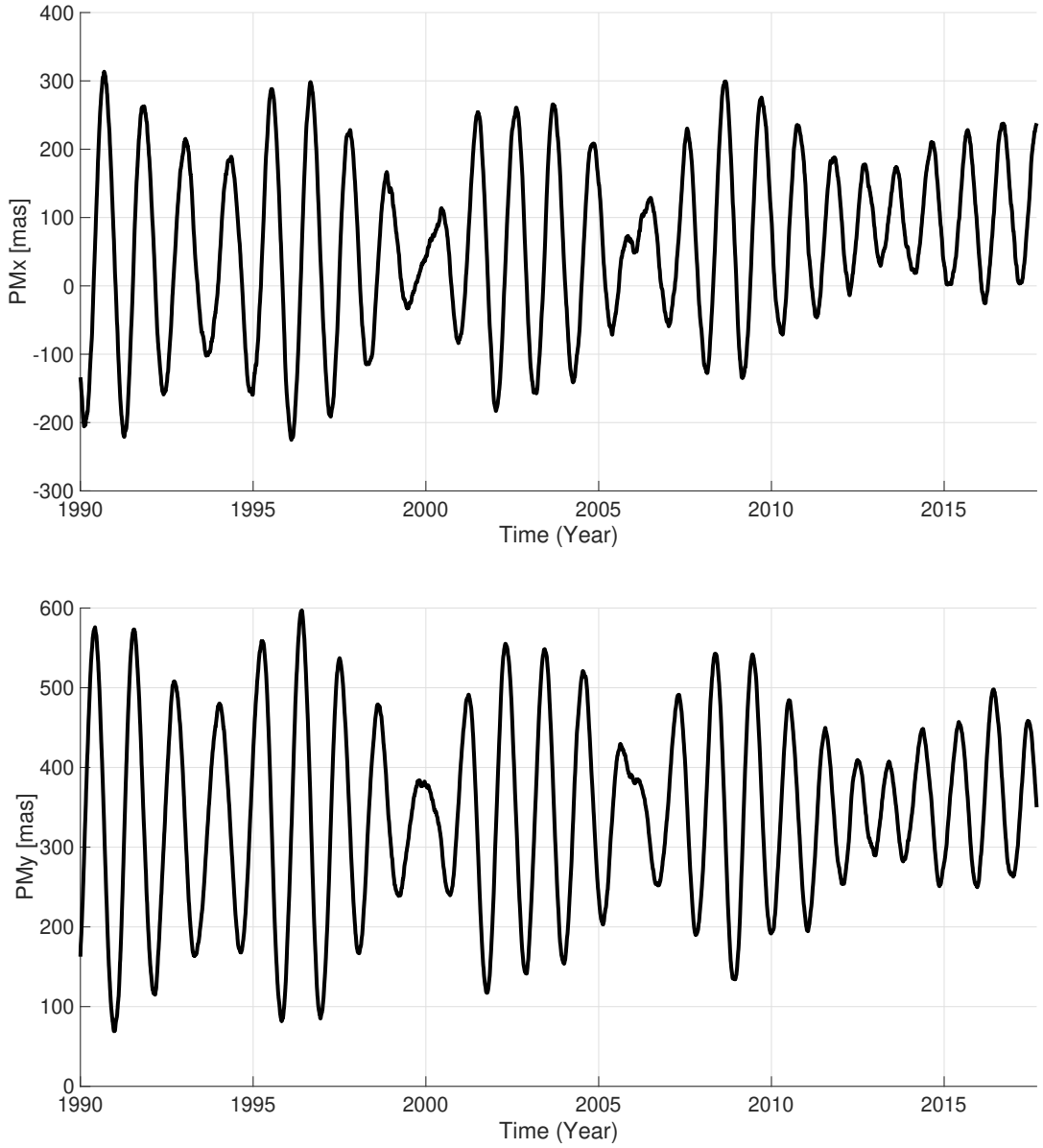

Figure 6.1: Daily PM time series from 1990 to the present.

days. Then, the trajectory matrix is constructed, having the window length and the number of singular values. As can be seen in Figure 6.4, the data between 1997 and 2003 is used as the training period. The cyan curve is the SSA-reconstructed Pm_x time series. Prediction of the future entries starts by adding the initial guess of future entries to the end of the time series. Then, the iteration of the SSA process is done until the result of two successive iterations has a difference less than a certain threshold. This will map the initial values onto the estimated periodic terms of the time series. The remaining part of the difference between the original PM_x time series and SSA estimated time series is named anomaly of PM_x, which has a stochastic behavior. Therefore, the anomaly part will be investigated by the Copula-based technique.

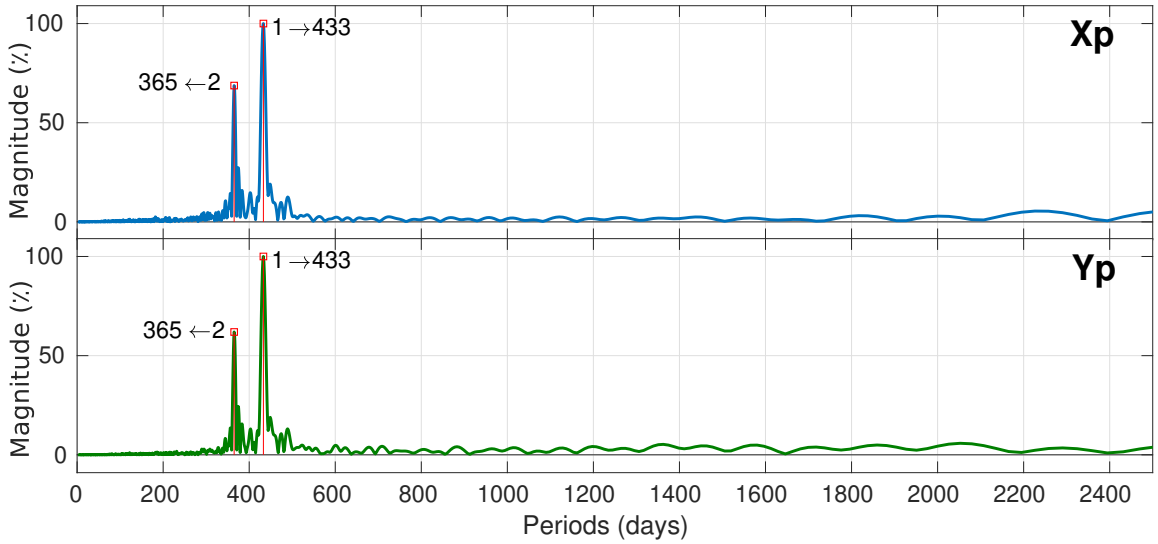

Figure 6.2: Spectral analysis of the PM_x (up), PM_y (down) using Fast Fourier Transform (FFT) (Modiri et al., 2018).

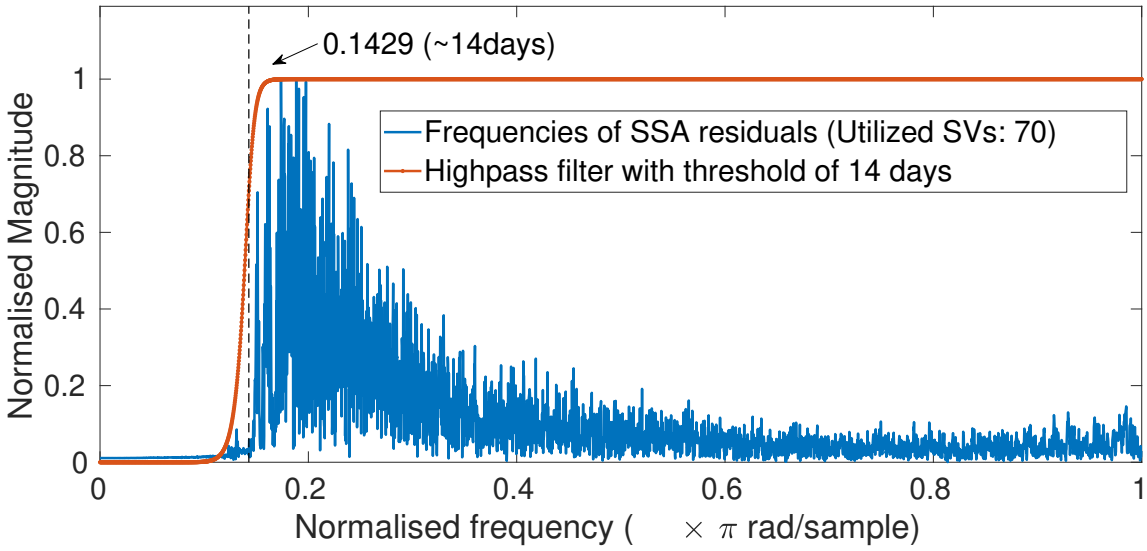

Figure 6.3: Number of singular values and vectors applied in modeling polar motion to achieve 1 mas degree of accuracy (Modiri et al., 2018).

6.2.2.2 Copula Anomaly Modeling

The anomaly part, which is shown in Figure 6.4 (lower panel) with dark violet, is formed into a matrix with the same window length L. Then, the dependency structure between the column$_i$ and column$_{i+1}$ is investigated for the whole data set.

In this study, three univariate distribution functions are investigated in order to fit the marginal distribution of data as follows: extreme value (Stephens, 1977), generalized extreme value (Bali, 2003), and generalized Pareto distribution (Hosking and Wallis, 1987) (see Table 6.1). Then, the root mean square error (RMSE) is estimated to identify which univariate distribution is the best fit for PM. Besides the goodness of fit, the marginal distribution is tested with Akaike and the Bayesian information criterion (AIC and BIC) (Bozdogan, 1987; Vrieze, 2012).

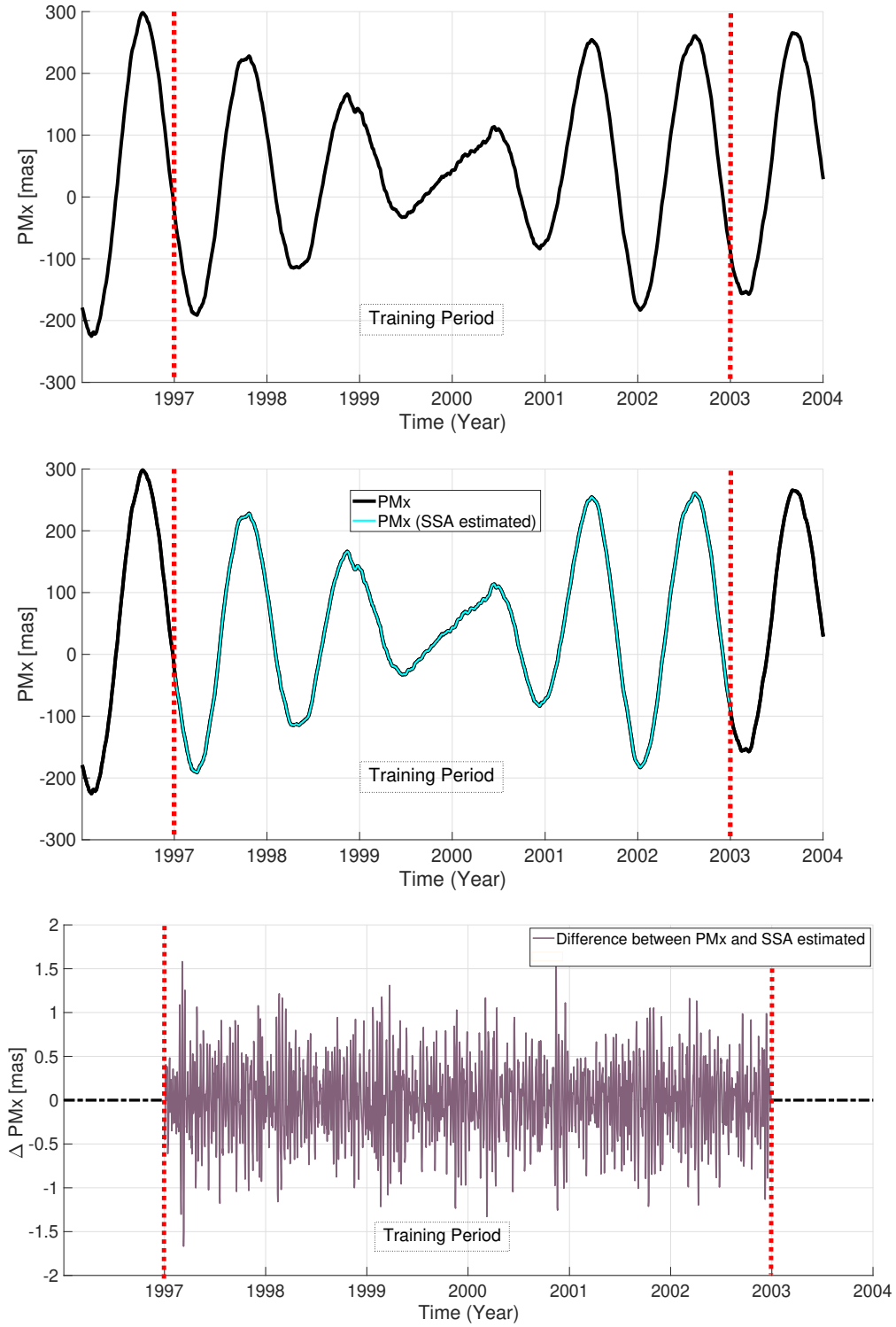

Figure 6.4: The original time series (upper panel), the reconstructed time series (middle panel) and the difference between original and reconstructed time series (lower panel) for PM_x (Modiri et al., 2018).

$$AIC = 2k - \ln(L) \tag{6.1}$$

and

$$BIC = k\ln(n) - 2\ln(L) \tag{6.2}$$

where k denotes the number of the free parameters in the model, n is the sample size, and L is the maximized value of the likelihood function of the estimated model. The smallest amount of AIC or BIC, respectively, infers the best fitting model or distribution.
After the estimation of the parameters by maximum likelihood approach, the AIC, BIC, and RMSE values are calculated for both PM_x and PM_y distribution. As it can be seen in Figure 6.5, the generalized extreme value (black) provides the best fit in comparison with the generalized Pareto distribution function (blue) and extreme value distribution function (green). Furthermore, Tables **??** and 6.3 illustrate the result of the AIC, BIC, and RMSE,

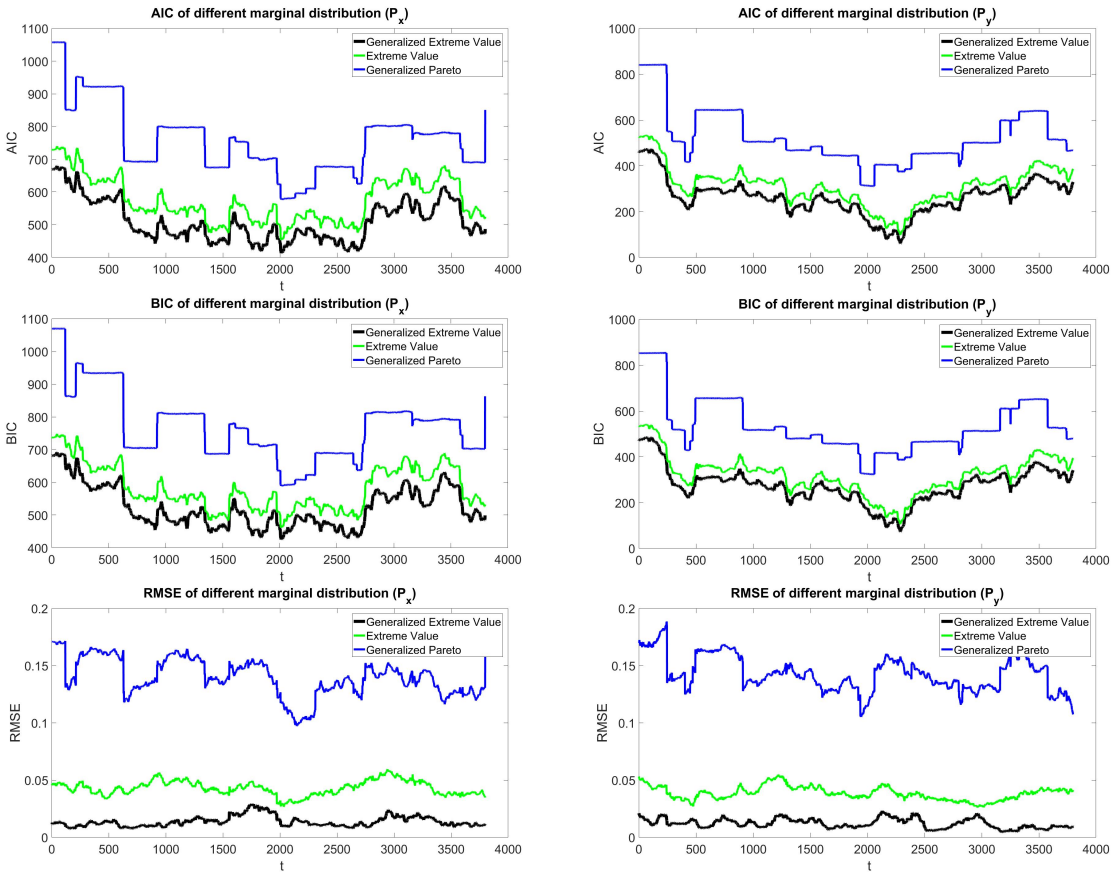

Figure 6.5: Marginal distribution's goodness-of-fit test for PM_x (left) and PM_y (right). Generalized extreme value distribution is the black curve, green shows the extreme value distribution, and the blue curve is generalized Pareto distribution (Modiri et al., 2018).

which confirmed that the generalized extreme value provides the best fit in both PM_x and PM_y distribution. Therefore, generalized extreme value distribution was selected in this study.

6.2.2.3 Estimating Empirical Copula

Once the univariate marginal distribution is fitted, the dependence structure between the time series has to be investigated. The first step is to calculate the empirical Copula using the Equ. 2.6. As can be seen in Figure 6.6, there is a scatter plot of two adjacent columns, and it

Table 6.1: Marginal distributions.

Distribution	Formula	Parameters
Extreme value	$f(x;\mu,\sigma) = \sigma^{-1}\exp(\frac{x-\mu}{\sigma})\exp(-\exp(\frac{x-\mu}{\sigma}))$	location μ scale σ
Generalized extreme value	$f(x;\mu,\sigma,\xi) = \begin{cases} \left(1+\xi(\frac{x-\mu}{\sigma})\right)^{-1/\xi} & \text{if } \xi \neq 0 \\ e^{-(x-\mu)/\sigma} & \text{if } \xi = 0 \end{cases}$	location μ scale σ shape ξ
Generalized Pareto	$f(x;\sigma,\xi) = f_{(\xi,\mu,\sigma)}(x) = \frac{1}{\sigma}\left(1+\frac{\xi(x-\mu)}{\sigma}\right)^{\left(-\frac{1}{\xi}-1\right)}$	location μ scale σ shape ξ

Table 6.2: Goodness-of-fit test for marginal distribution of PM_x.

Distributions	AIC	BIC	RMSE
Extreme value	574.60	582.66	0.04
Generalized extreme value	511.14	523.23	0.01
Generalized Pareto	758.22	770.31	0.13

Table 6.3: Goodness-of-fit test for marginal distribution of PM_y.

Distributions	AIC	BIC	RMSE
Extreme value	310.99	319.05	0.03
Generalized extreme value	261.25	273.34	0.01
Generalized Pareto	523.99	536.09	0.14

shows a scatter linear dependency structure with the heavy tail, which can be fully modeled using the Archimedean Copula.

6.2.2.4 Fitting A Theoretical Copula Function

The next step is fitting a theoretical bivariate Archimedean Copula function with its parameters estimated by the maximum likelihood approach. Here, three different theoretical Copula functions are tested (Figure 6.7): Clayton, Frank, and Gumbel Copula.

For the three different Copula functions, the goodness-of-fit test, which is based on the Cramer-von-Mises statistics, is utilized. Then, one thousand values of the test statistics are sampled to evaluate the performance of the Copulas. The proportion of values larger than S_n is estimated by calculating the corresponding p-values. The results based on S_n show that the performance of them is approximately similar with slightly less error for Frank Copula (Table 6.4).

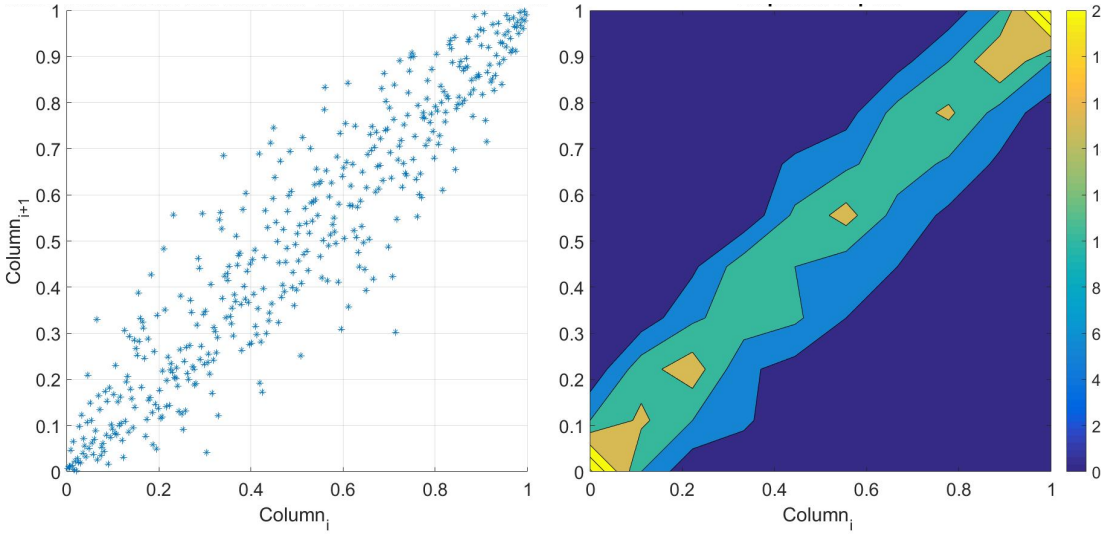

Figure 6.6: Scatter plot(left) two adjacent columns in the residual matrix. The empirical Copula (right) is estimated based on the dependency structure of two columns.

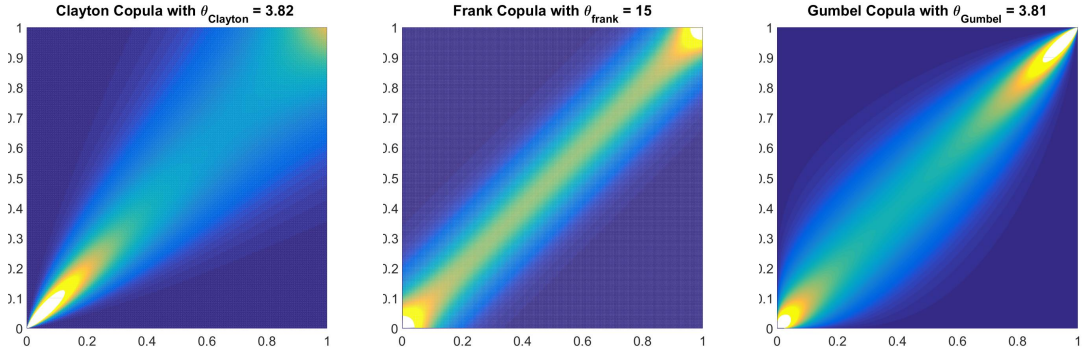

Figure 6.7: Theoretical Copula are fitted to the empirical Copula. The Copula parameter is 3.82, 15, and 3.61 for the Clayton, Frank, and Gumbel Copula, respectively (Modiri et al., 2018).

6.2.3 365 Days Ahead Prediction

Six years of observed PM time series, from January 1997 to December 2002, is used for the 365 ahead prediction. The predicted data are compared with the IERS Bulletin A prediction (`https://www.iers.org/IERS/EN/DataProducts/EarthOrientationData/eop.html`) to verify the reliability of our prediction hybrid method. The IERS Bulletin A contains the PM parameters and the predicted PM for one year into the future, which are released weekly by IERS Rapid Service/Prediction Center (RS/PC), hosted by the USNO. The predictions of PM from the IERS Bulletin A are produced by LS + AR method. In the current prediction method, the PM prediction was the sum of the LS extrapolation model (including the Chandler period, annual, semiannual, terannual, and quarter annual terms), and the AR predictions of the LS extrapolation residuals.

Table 6.4: Goodness-of-fit test for Copula model.

Copula name	Clayton	Frank	Gumbel
mean(S_n)	43.57	12.13	17.58

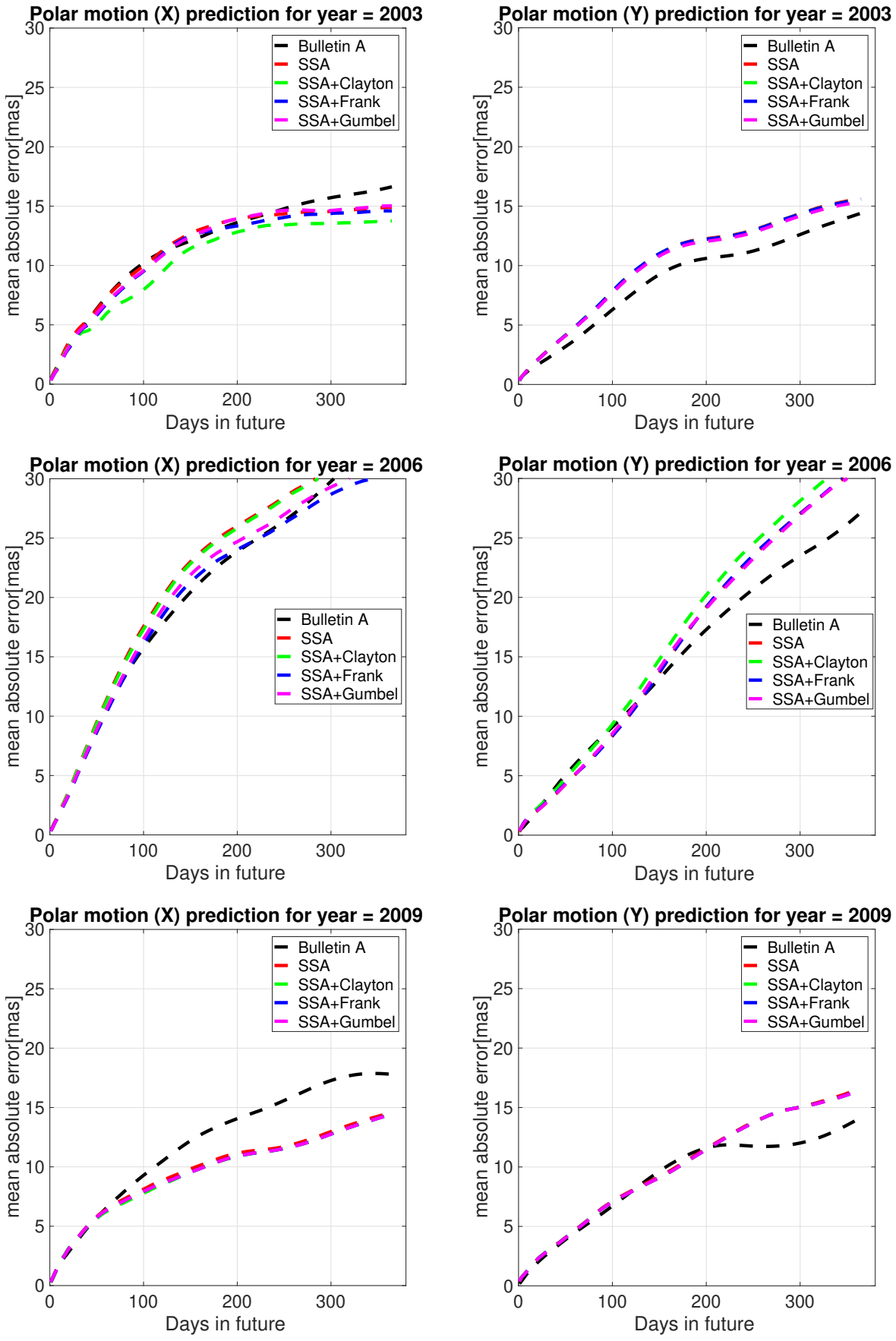

Figure 6.8: Mean value of MAE of PM_x and PM_y for 2003, 2006, and 2009 with the unit [mas].

6.2.4 Discussions of Results

In this example, the combination of the SSA and the Copula-based analysis method is demonstrated for PM prediction from 2003 to 2009 (seven years). Our method is tested based on hindcast experiments using data from the past.
Hence, the Bulletin A prediction data are available weekly; approximately 52 time series of PM predictions are available for each year. So, Figure 6.8 shows the mean value of mean absolute error (MAE) for each year. In Figure 6.8, the Bulletin A solution is shown in black, and the SSA predicted data in red. Also, the results of SSA + Copula are displayed by green, blue, and pink for Clayton, Frank, and Gumbel Copula, respectively. Compared to the results from the IERS Bulletin A, the MAE of the predictions produced by the proposed method were smaller in different short-, mid-, and long-term intervals for different cases (e.g., between 1 and 5 mas progression of PM_x prediction for different time intervals in 2003). The better prediction performance of the SSA + Copula prediction may have been due to the modeling of the linear change of the Chandler and the annual oscillation amplitudes.
Additionally, the combination of SSA + Copula improves the SSA solution because of its ability to model the stochastic behavior of the anomaly part of the PM time series. However, the proposed method did not always perform better, especially in cases of long-term predictions where the quality of the results was not as good as we expected (see Figure 6.8). This may have been caused by changes in the amplitudes of the periodic terms in these six years, where because the SSA was not able to capture all features in order to predict more precisely, we would have to increase the interval of training time. Figure 6.9 presents the absolute error of 365 days ahead of the prediction between 2003 and 2009. Different patterns and features can be seen in our solution and Bulletin A's solution. For instance, Bulletin A predicted that PM_x from January to March 2003 displays errors of more than 30 mas, which cannot be found in our results, and there is a clear feature in PM_x Bulletin A that means an absolute error plot from August to December 2008, which does not appear in our prediction. However, our predicted PM results indicate a periodic error in mid- and long-term predictions although the results of the combined SSA + Copula show smoother errors in comparison to the SSA results. To understand this particular periodic error of our method better, I plot Figure 6.10, which demonstrates the improvement of the SSA + Copula-predicted solution compared to Bulletin A. The yellow color in the heat map shows improvements in predictions with fewer errors. The red color indicates where our method shows more errors in the prediction process. Also, the orange shows where both PM prediction techniques display the same number of errors. The results illustrate that SSA + Copula can improve the accuracy of PM prediction in the different time intervals of prediction (short, mid, and long). Tables 6.5 and 6.6 indicate the success rate of PM prediction when using the SSA + Copula algorithm.

$$\textit{Success rate of PM prediction} = \frac{\textit{number of improvement in the predicted PM}}{\textit{total number of PM prediction}} * 100 \qquad (6.3)$$

The improvement of the prediction is up to 64.99% for PM_x using SSA + Frank Copula. Also, as it can be seen in Table 6.6, the success rate for PM_y is up to 46.66 using SSA + Copula method.

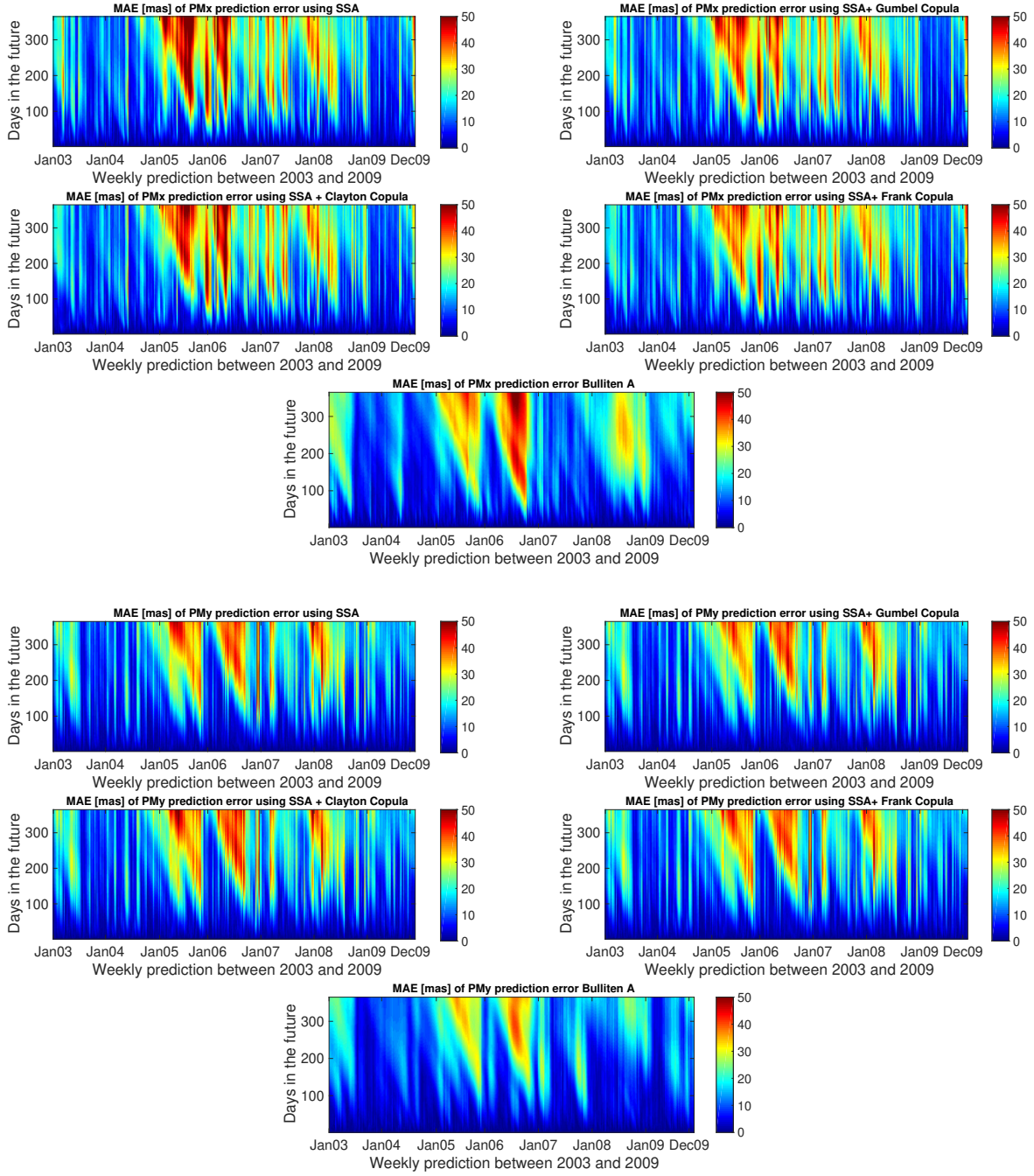

Figure 6.9: Absolute errors of the predicted PM_x (up) and PM_y (down) using SSA, SSA+Gumbel Copula, SSA+Clayton Copula, SSA+Frank Copula compared with Bulletin A product. The unit is [mas] (Modiri et al., 2018)

.

6.3 Second Group: LOD Prediction

In this example, the combination of Copula-based analysis and SSA is explored to predict LOD. First, the dependence structure between the LOD and the axial component of EAM is derived. Then, the LOD data is simulated based on the fitted theoretical Copula from EAM_Z data. Next, the difference between the LOD time series and its Copula-based estimation is modeled using SSA. After that, the LOD will be computed from the predicted EAM_Z. Finally, the difference will be predicted and will be added to LOD predicted by Copula.

Table 6.5: Success rate of PM_x prediction [%]

$Method \backslash Year$	2003	2004	2005	2006	2007	2008	2009
SSA	55.29	33.31	26.52	40.16	22.90	45.94	64.70
SSA + Clayton	61.71	33.88	31.91	40.17	22.91	45.96	64.95
SSA + Frank	58.31	34.31	33.61	42.50	22.91	45.97	64.99
SSA + Gumbel	55.90	33.81	28.31	41.00	22.90	45.94	64.97

Table 6.6: Success rate of PM_y prediction[%]

$Method \backslash Year$	2003	2004	2005	2006	2007	2008	2009
SSA	35.95	44.99	25.43	45.28	39.50	29.21	39.50
SSA + Clayton	35.99	44.84	24.93	41.27	39.57	29.14	39.65
SSA + Frank	35.94	44.82	25.54	46.66	39.45	29.30	39.70
SSA + Gumbel	38.45	44.60	26.66	44.46	39.36	29.55	39.74

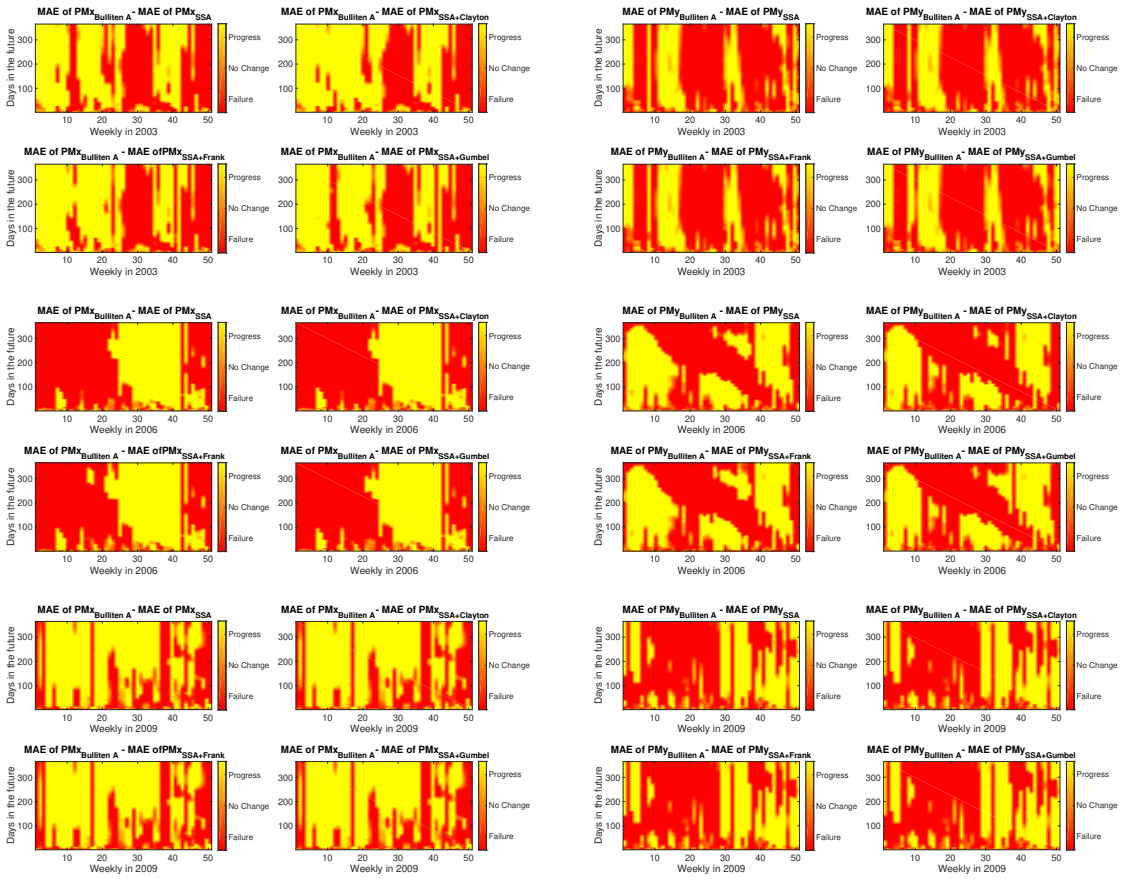

Figure 6.10: Improvement of PM_x and PM_y prediction using SSA + Copula-based model. The improvement in prediction is shown by yellow color.

6.3.1 Data Description

6.3.1.1 Length of Day (LOD)

The LOD time series are available from the IERS EOP 05 C04 series(`http://hpiers.obspm.fr/eop-pc`) and span the time interval from 1996 to 2008 (Kosek et al., 2005).

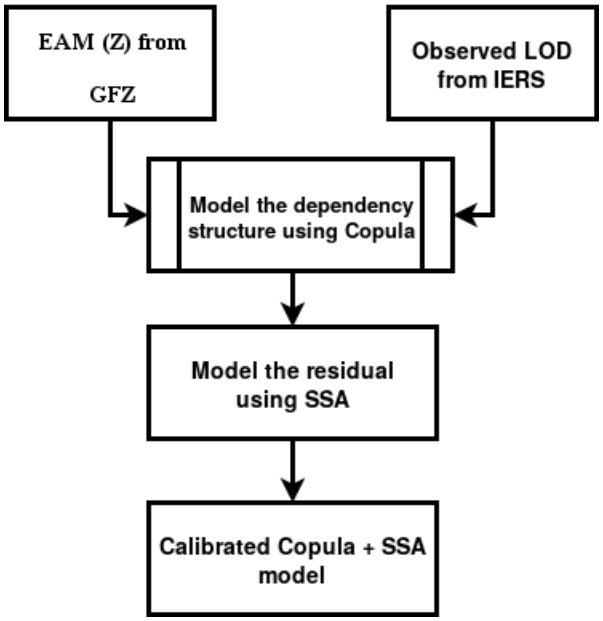

Figure 6.11: Scheme of the Copula + SSA model for LOD prediction (Calibration step).

6.3.1.2 Effective Angular Momentum (EAM) Functions

EAM functions, in both mass and motion terms, explain the non-tidal geophysical excitation of the Earth's rotation due to mass redistribution in the atmospheric and terrestrial hydrosphere, as well as the oceans. The EAM data consists of three main components: X, Y, and Z. The X and Y components are associated with the excitation of polar motion, whereas the Z component is responsible for the excitation of LOD variation. The EAM functions are dimensionless with the sampling of one day and are provided by the Earth System Modeling group at Deutsches GeoForschungsZentrum Potsdam (ESMGFZ) (Dill and Dobslaw, 2018). The EAM time series are available from: (`ftp://ig2-dmz.gfz-potsdam.de/EAM/`).

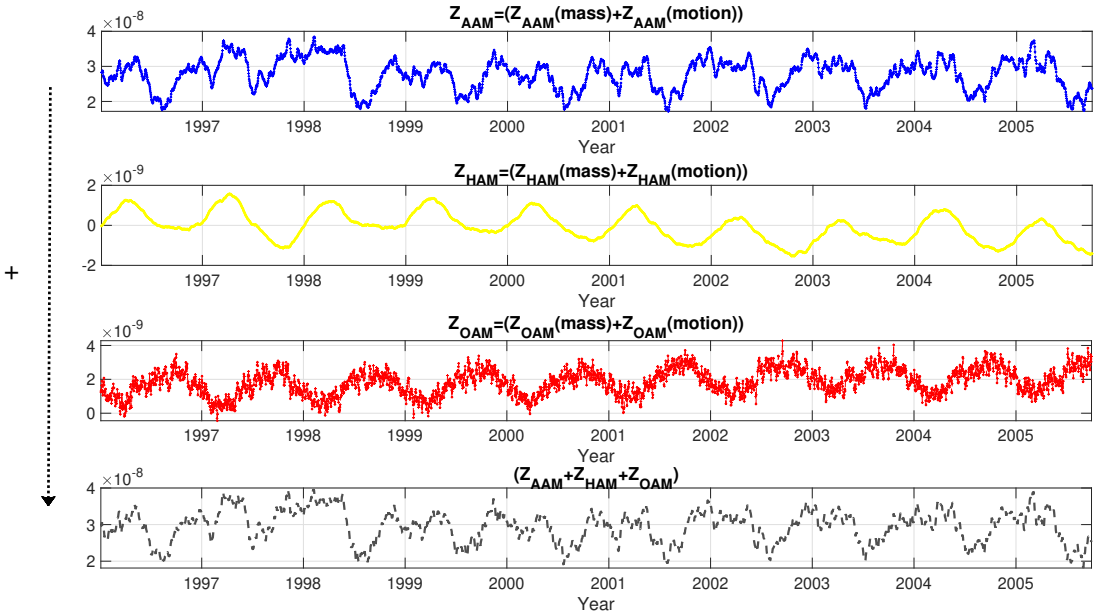

Figure 6.12: The EAM_Z being the sum of mass and motion terms of AAM, HAM, and OAM ($Z_{AAM} + Z_{HAM} + Z_{OAM}$).

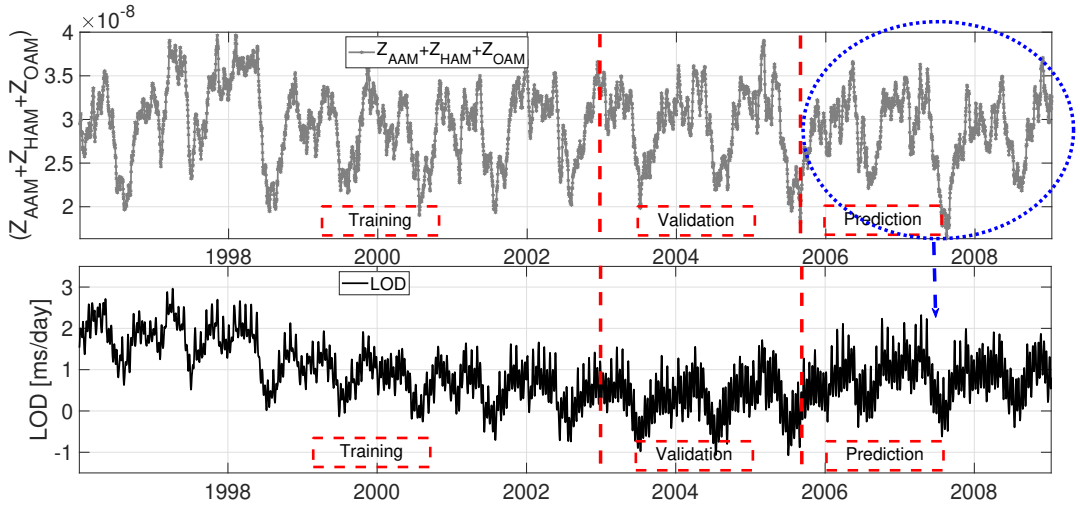

Figure 6.13: Time series of LOD and $(Z_{AAM} + Z_{HAM} + Z_{OAM})$ between 1996 and 2008. The time series is divided into three parts: training part (1996-2003), validation (2003-2005), and prediction (2005-2008). The unit of LOD is in [ms/day]. The figure is taken from (Modiri et al., 2020).

6.3.2 Data Analysis

Multiple sets of ultra-short-term (10 days) LOD predictions have been made based on the IERS 05 C04 time series to assess the capability of our hybrid model. The same conditions as EOP PCC are considered to show the performance of the presented model. Then, the prediction results are compared with those of existing techniques of EOP PCC, and the results prove that the proposed approach can efficiently predict LOD.
Here, the Copula-based analysis technique aims to estimate the models for capturing the dependence structure between observed LOD and the EAM_Z. Also, SSA is used as a deterministic technique to obtain stochastic residuals (the difference between the observed data and the Copula-generated data).

6.3.3 Data Processing and Analysis

As can be seen in Figure 6.12, the EAM_Z is the sum of mass and motion terms of AAM, HAM, and OAM. The dependence structure between LOD and the EAM_Z is captured by the Copula-based analysis method. Then, the difference between the observed LOd and Copula-based LOD estimated data is modeled by using the SSA method. Figure 6.13 shows that the time series is divided into three parts: training part (1996-2003), validation (2003-2005), and prediction (2005-2008).

6.3.3.1 Copula-based Joint Distribution Function of LOD and EAM$_Z$

In this example, the training data set, which ranges from 1996 to 2003, is used to fit a Copula-based joint distribution function; both EAM_Z and LOD are transformed to uniformly distributed values between $(0, 1)$ interval through their empirical cumulative distribution function. Thereafter, the dependence structure between the EAM_Z and LOD is investigated. First, the empirical Copula is estimated. As can be seen in Figure 6.14, there is a scatter plot

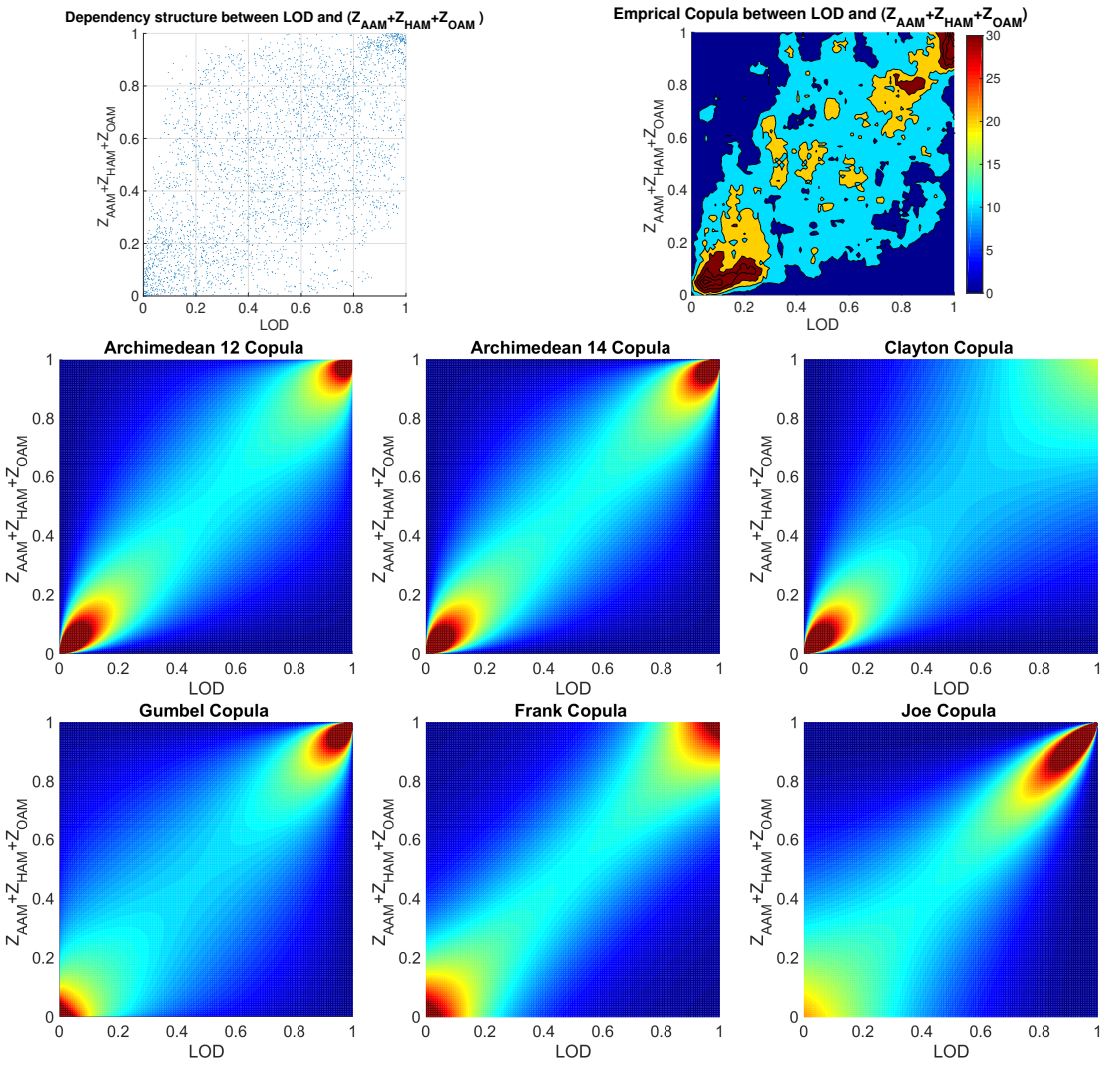

Figure 6.14: Scatter plot of LOD and (EAM_Z) and its empirical Copula (upper panel). The fitted Archimedean 12 ($\theta = 1.30$), Archimedean 14 ($\theta = 1.53$), and Clayton ($\theta = 1.31$) Copula (middle panel), Frank ($\theta = 5.10$), Gumbel ($\theta = 1.69$), and Joe ($\theta = 2.92$) Copula (lower panel) between 1996 and 2003 in the rank space [0 1].

(upper panel) of LOD and EAM_Z, and it shows approximately a linear dependence structure with both upper and lower heavy tail, which can be modeled by using the Archimedean Copula. Therefore, the theoretical bivariate Archimedean Copula functions with their estimated parameters are fitted to the estimated empirical Copula. The LOD data are sampled based on the Copula and the empirical marginal distribution of EAM_Z. Next, the residuals of the generated LOD by Copula are estimated using SSA. After that, the $(Z_{AAM} + Z_{HAM} + Z_{OAM})$ data between 2003 and 2005 are used for the validation of LOD prediction (calibration step). Here, the predicted EAM_Z are used for the LOD prediction in the time interval between 2005 and 2008 (see Figure 6.13).

6.3.3.2 EAM_Z Prediction

The prediction algorithm for EAM_Z is shown in Figure 6.15. The $(Z_{AAM} + Z_{HAM} + Z_{OAM})$ time series can be split up into two parts. The first part is dealing with periodic effects such as annual and semi-annual variations due to the spectral analysis of EAM_Z (illustrated in Figure

6.16. The SSA models the periodic terms of the $(Z_{AAM} + Z_{HAM} + Z_{OAM})$; see Figure 6.17.

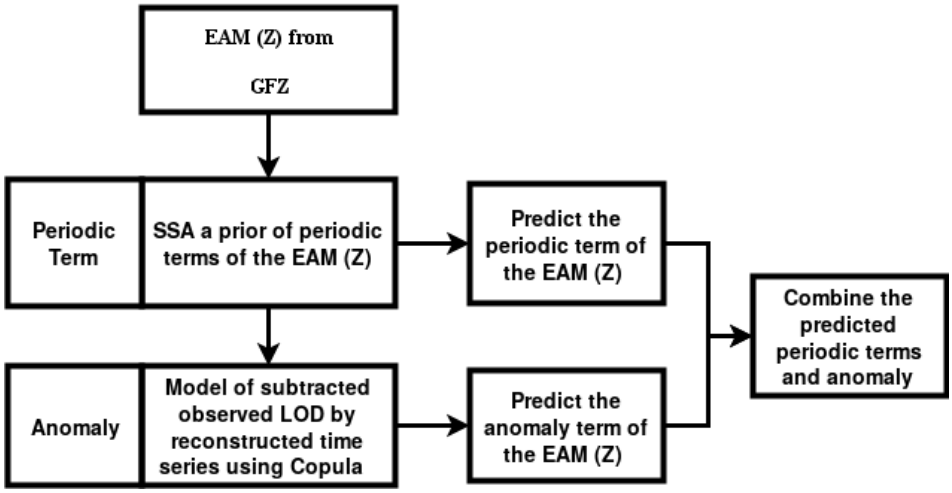

Figure 6.15: Scheme of the SSA + Copula model for PM prediction (Modiri et al., 2018)

Then, the difference between the observed EAM_Z and SSA estimated data is modeled by using the Copula-based analysis method. First, the window length (L=365 days) is selected considering the main periodicity see Figure 6.16. After that, the number of singular vectors for

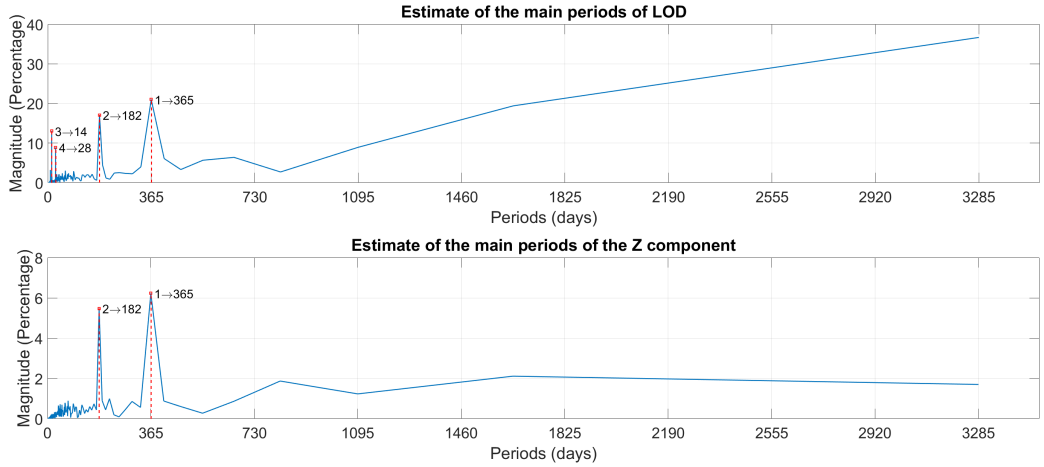

Figure 6.16: Spectral analysis of the LOD (up), $Z_{AAM} + Z_{HAM} + Z_{OAM}$ (down) using fast Fourier transform (FFT).

the reconstruction of the EAM_Z time series is determined. The trajectory matrix is constructed by having the window length and number of singular vectors. The cyan curve depicts the SSA-reconstructed EAM_Z time series. The periodic terms of EAM_Z are extrapolated using the SSA as a priori model. The difference between the values predicted by SSA and the predictions based on the EAM_Z is called EAM_Z anomaly and has a stochastic nature. This anomaly part is predicted using the Copula-based model. The anomaly part is presented in Figure 6.17 (lower panel) in violet color. This part is formed with the same window length L. The dependence structure between the column$_i$ and column$_{i+1}$ in the residual matrix is investigated. As can be seen in Figure 6.18, the scatter plot illustrates a linear dependence between the two adjacent columns, which are modeled by Archimedean Copula. Then, the empirical Copula is determined. The next step is fitting a bivariate Archimedean Copula. In this example, Frank Copula is selected for predicting the EAM_Z anomaly due to its ability to

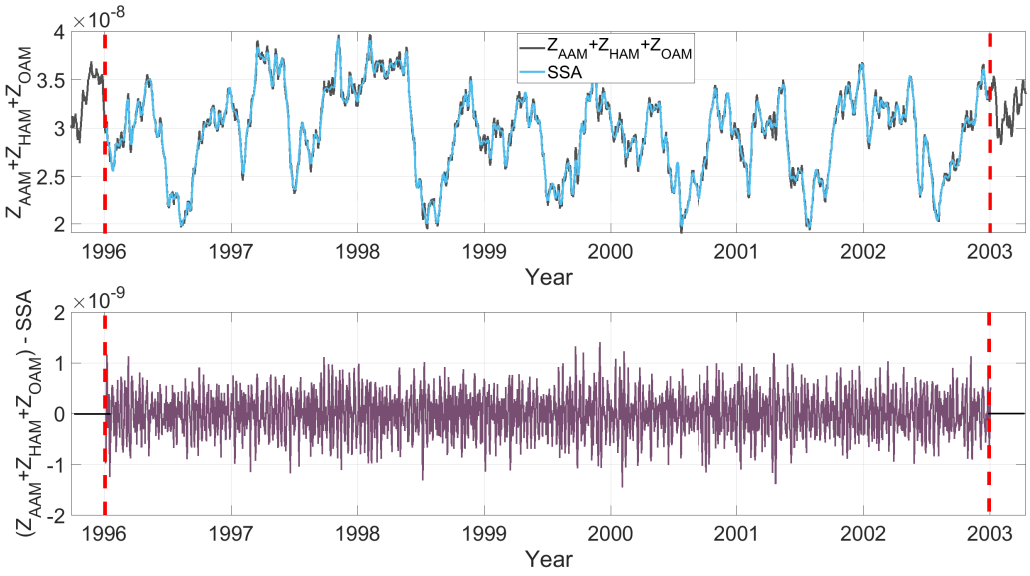

Figure 6.17: The original time series and the reconstructed time series (upper panel), and the difference between the original and reconstructed time series (lower panel) for $(Z_{AAM} + Z_{HAM} + Z_{OAM})$.

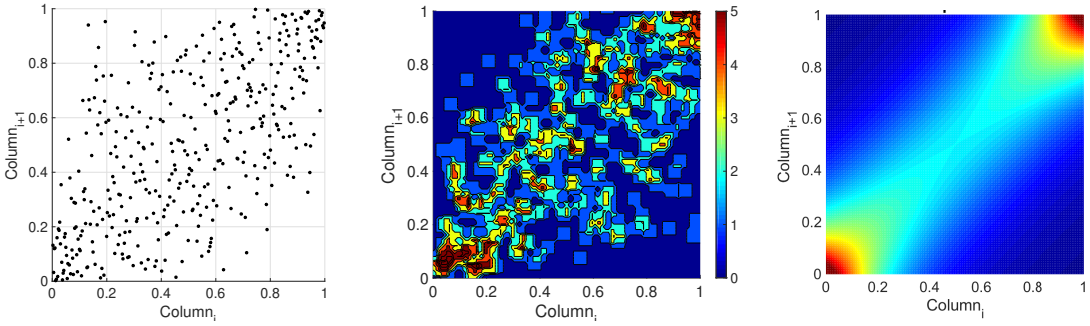

Figure 6.18: Scatter plot(left) two adjacent columns in the residual matrix. The empirical Copula (middle) is estimated based on the dependency structure of two columns. The Frank Copula with $\theta = 4.79$ is fitted to the empirical Copula (right).

capture the linear dependence structure. Finally, the Copula-based predicted anomalies are added to the previously described deterministic part. Here, I employed seven years of EAM_Z time series, from September 1998 to September 2005, for the ten-days-ahead forecasting during the interval between October 2005 and 2008, i.e., the same interval that has been used for the EOP PCC. As can be seen in Figure 6.19, the MAE of the EAM_Z prediction is up to the 0.76 for the next days which is two orders of magnitude smaller than the EAM_Z magnitude.

In Figure 6.14, the scatter plot reveals a linear relationship between $column_i$ and $column_{i+1}$. Then, the corresponding empirical Copula is estimated. Finally, the anomalies are added to the SSA-forecasted time series.

6.3.3.3 LOD Prediction from Predicted EAM_Z Using the Calibrated Copula + SSA Model

The predicted EAM_Z dataset from 2005 to 2008 is used as an input time series for the calibrated model. As seen in Figure 6.20, the periodic terms in the residual part are predicted using

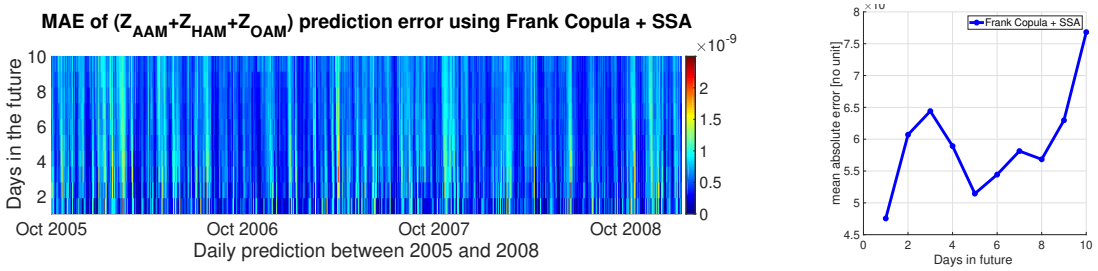

Figure 6.19: MAE of $(Z_{AAM} + Z_{HAM} + Z_{OAM})$ prediction between 2005 and 2008 (left). Mean value of MAE of $(Z_{AAM} + Z_{HAM} + Z_{OAM})$ prediction between 2005 and 2008 (right).

SSA extrapolation as well. Eventually, the Copula-based predicted data are added to the SSA forecasted residual. The results are compared with the EOP PCC solution to asses the proposed method.

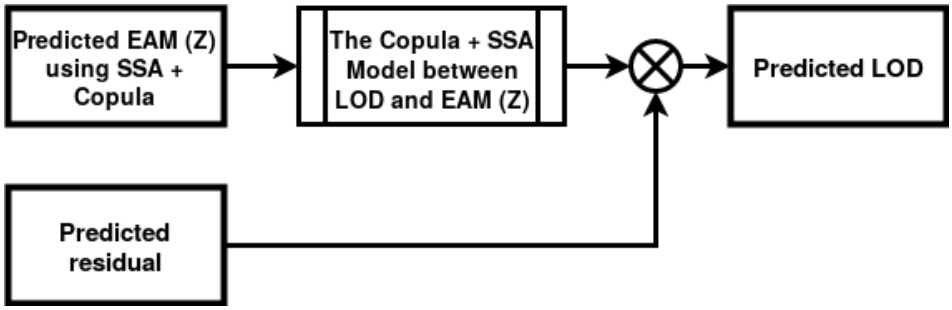

Figure 6.20: Scheme of the Copula + SSA model for LOD prediction using the calibrated Copula + SSA model.

6.3.4 Discussion of the Results

In this example, a hybrid LOD prediction method Copula + SSA has been tested by taking advantage of the EAM (second group). The proposed combination method is tested based on the hind-cast experiments using the data from the past; the LOD data are predicted using the same time span (2005–2008) as the EOP PCC (Gross et al., 1998; Akyilmaz and Kutterer, 2004; Kosek et al., 2005). Figure 6.21 shows the MAE of ultra-short-term prediction. The MAE of our hybrid Copula + SSA model, displayed in red (Archimedean 12 + SSA), yellow (Archimedean 14 + SSA), green (Clayton + SSA), blue (Frank + SSA), purple (Gumbel + SSA), and the cyan (Joe + SSA), indicates fewer errors compared to the EOP PCC solutions. Nevertheless, the Kalman filter with forecasted AAM (black curve) shows comparable performance with our proposed hybrid model with smaller MAE for the first four days in the future. Table 6.7 present the MAE of Copula + SSA and EOP PCC results in numbers. Adoptive transform, AR, LS collocation, and NN show errors of more than $0.1 ms/day$ for the first day of prediction. Also, the MAE of the wavelet, LS extrapolation, LS + AR, and HE reaches more than 0.1 ms/day after 2 or 3 days in the future. From all of the contributions to the EOP PCC solution, the Kalman filter provides the best accuracy. However, the MAE of the Kalman filter gets larger than $0.1 ms/day$ after 7 days. All Copula + SSA models show MAE smaller than 0.1 ms/day over 10 days prediction, except smaller Joe Copula + SSA. Figure 6.21 presents the MAE of

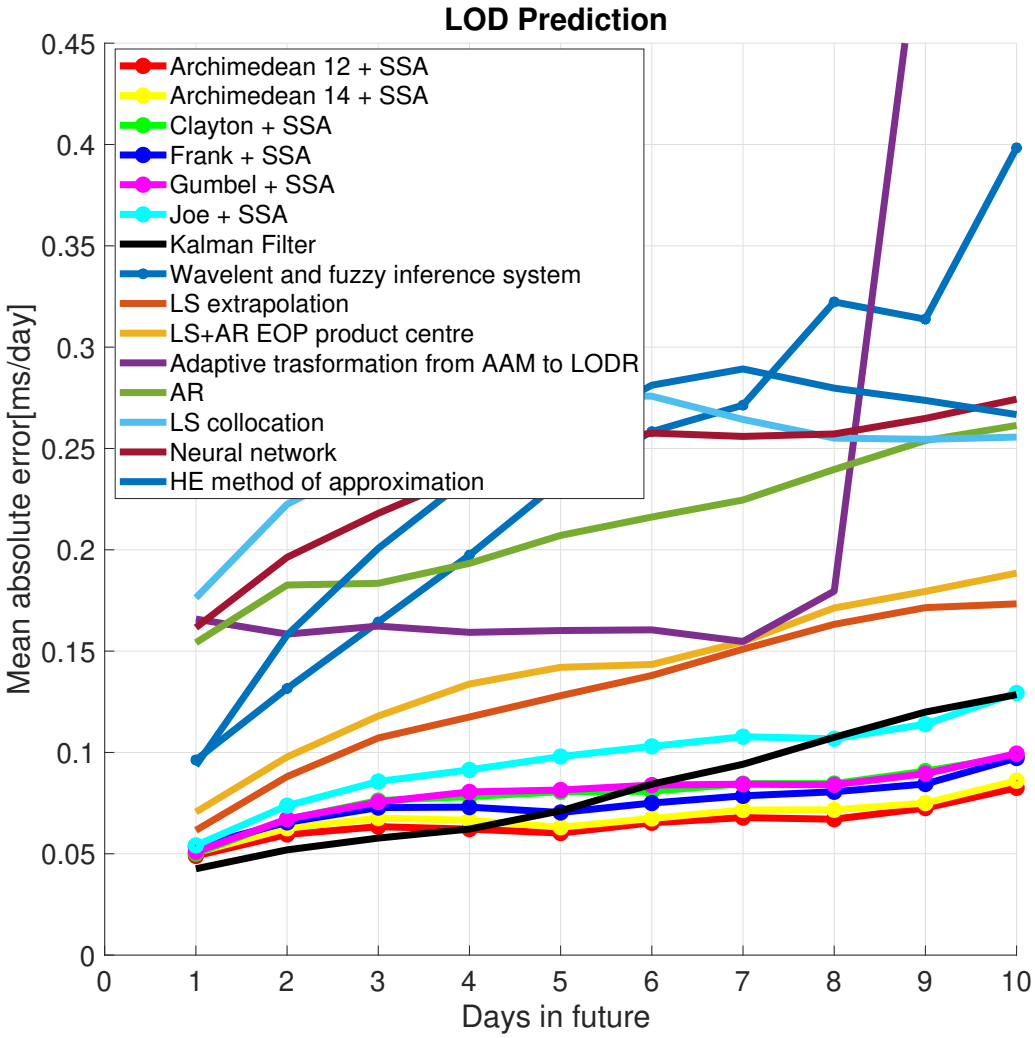

Figure 6.21: Absolute errors of the predicted LOD using Archimedean 12 + SSA, Archimedean 14 + SSA, Clayton Copula + SSA, Gumbel Copula +SSA, Frank Copula + SSA, Joe Copula + SSA, and EOP PCC results. The unit is in [ms/day].

10 days' ahead prediction between 2005 and 2008 for all 6 hybrid models to better understand the prediction performance and its causes. Different features can be seen, and there are some common patterns, such as high errors from the beginning of 2007, which might be caused by the El Niño effect or certain geomagnetic jerk events, as pointed out by Shirai et al. (2005) and Malkin (2013a). As NOAA's National Centers for Environmental Information's "State of the Climate" reported, the El Niño warm event had a peak in December 2006 and started to dissipate during January 2007. Thus, the equatorial Pacific sea-surface temperature (SST) anomalies decreased during the first 2 months of 2007, eventually declining to near average by the end of March 2007. Kalarus et al. (2010) suggested benefiting from the prediction of the AAM, OAM, and HAM. Therefore, our better prediction performance may be due to considering both mass and motion terms of EAM_Z for modeling the dependence structure between LOD and EAM_Z. It is important to note that the Copula + SSA Archimedean 12 and 14 Copula provide significantly smaller errors than the other methods. On the other hand, Joe Copula exhibits slightly larger errors than the two aforesaid models. This may have been caused by Archimedean 12 and 14 Copula's ability to capture the upper and lower heavy tail dependence structure.

Table 6.7: Comparison of Copula + SSA prediction and EOP PCC prediction errors (unit: ms/day).

Prediction day	1	2	3	4	5	6	7	8	9	10
Archi 12 + SSA	0.047	0.060	0.063	0.063	0.059	0.064	0.066	0.061	0.072	0.083
Archi 14 + SSA	0.050	0.065	0.066	0.068	0.064	0.067	0.072	0.064	0.073	0.082
Clayton + SSA	0.051	0.067	0.079	0.085	0.079	0.078	0.084	0.078	0.086	0.093
Gumbel + SSA	0.052	0.065	0.073	0.076	0.070	0.076	0.085	0.080	0.082	0.094
Frank + SSA	0.047	0.062	0.070	0.086	0.083	0.081	0.084	0.085	0.092	0.097
Joe + SSA	0.052	0.079	0.081	0.088	0.097	0.102	0.116	0.111	0.120	0.121
Kalman filter	0.042	0.051	0.057	0.062	0.071	0.084	0.094	0.107	0.119	0.128
wavelet	0.096	0.131	0.164	0.197	0.233	0.258	0.271	0.322	0.313	0.398
LSE	0.061	0.088	0.107	0.117	0.128	0.138	0.151	0.163	0.171	0.173
LS+AR EOP PC	0.070	0.097	0.118	0.133	0.142	0.143	0.154	0.171	0.179	0.188
Adaptive transform	0.165	0.158	0.162	0.159	0.160	0.160	0.154	0.179	0.528	0.593
AR	0.154	0.182	0.183	0.193	0.207	0.216	0.224	0.239	0.253	0.261
LSC	0.176	0.222	0.245	0.266	0.276	0.275	0.264	0.255	0.254	0.255
NN	0.161	0.196	0.218	0.237	0.250	0.257	0.256	0.257	0.264	0.274
HE	0.093	0.157	0.200	0.235	0.257	0.281	0.289	0.279	0.273	0.266

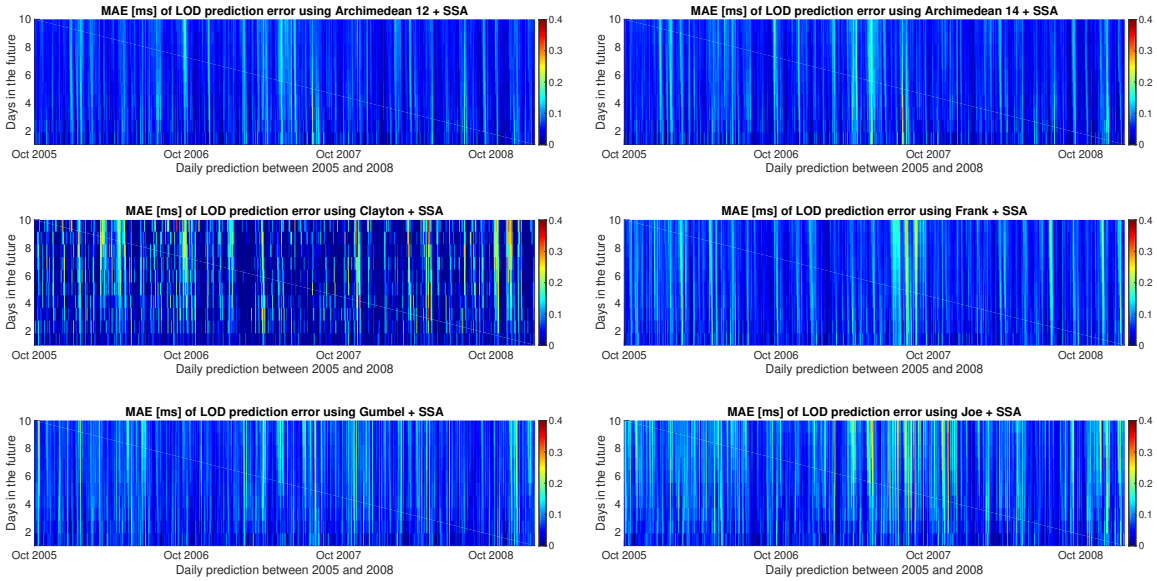

Figure 6.22: Absolute errors of the predicted LOD using Archimedean 12 + SSA, Archimedean 14 + SSA, Clayton Copula + SSA, Gumbel Copula +SSA, Frank Copula + SSA, Joe Copula + SSA. The unit is [ms/day].

6.4 Summary and Conclusion

The improvement of the Earth rotation prediction is a relevant, timely problem, as confirmed by the fact that the International Astronomical Union (IAU) Commission A2, the International Association of Geodesy (IAG) and the IERS have at present two Joint Working Groups on Prediction (JWG-P) and Theory of Earth rotation and validation (JWG-ThER). According to the United Nations (UN) resolution in 2015, the primary objective of these JWGs is to assess and ensure the level of consistency of Earth Orientation Parameter (EOP) predictions derived from theories with the corresponding EOP determined from analyses of the observational

data provided by the various geodetic techniques. Therefore, accurate EOP predictions are essential to avoid any systematic drifts and/or biases between the international celestial and terrestrial reference frames (ICRF and ITRF). The results illustrate that the proposed method could efficiently and precisely predict the PM parameters. As clearly demonstrated, the SSA + Copula algorithm shows better performance for PM_x prediction in comparison to the SSA prediction. The Copula-based analysis is entirely successful in its aim to increase the accuracy of PM prediction by modeling the stochastic part of the PM and subtracting PM by SSA reconstructed time series. I suspect the main error contributions come from the SSA extrapolation part. So, further investigations about the SSA training time will be required to clarify this issue. Also, the SSA + Copula prediction method shows periodic errors, and these errors have a significant impact on the mean absolute error. Therefore, these occasional errors should be further investigated to have a noticeable progression in the PM prediction accuracy. LOD represents the variation in Earth's rotation rate, which is most difficult to predict, because of the occurrence of extreme events in the LOD signal. In this example, I introduce several approaches based on Copulas, which were applied to bivariate frequency analysis. Using Copula is promising since it allows us to take into account a wide range of correlations, frequently observed in time series. The presented work here is aimed at the possibility of utilizing the EAM_Z data to predict LOD data due to the existing relationship between them. In order to study this relationship, two data sets were compared: the observed LOD from IERS EOP C05 and EAM_Z derived from GFZ. The comparison with the results of other methods indicates that the Copula + SSA can efficiently and precisely predict the LOD parameter at ultra-short-term. All of our methods introduced here provide comparable error with the existing methods used for their evaluation in the time interval considered of up to ten days. Besides, it is clearly demonstrated that the predicted AAM, HAM, OAM time series as additional input information can improve the LOD prediction. Among the analyzed combinations, the Archimedean 12 + SSA and Archimedean 14 + SSA show the most sophisticated performance with low errors. As the Kalman filter prediction provides better results within the first three to four days, I will investigate this topic further in future in order to find out how the EAM functions can deliver even better LOD predictions.

The EOP PCC proved once more to be very useful. As long as the data are still available for post-processing, new methods can adequately be compared in a consistent way to the methods applied in the past.

7

Interconnection Between Celestial Pole Motion and Earth's Magnetic field

7.1 Introduction

The understanding of celestial pole motion (CPM) excitation could bring us significantly closer to meeting the accuracy goals pursued by the GGOS of the IAG, i.e., 1 mm accuracy and 0.1 mm/year stability on global scales in terms of the ITRF defining parameters (Plag et al., 2009). Meteorological and geophysical phenomena cause the irregularities of the CPM. Therefore, investigation of the CPM is vital to understand the nature of the Earth's interior. The IAU adopted IAU 2006 precession and IAU2000A nutation theory to describe the CPM. However, the IAU 2006/2000A precession-nutation theory cannot explain the Earth's rotation fully for several reasons, e.g., inconsistency among products (e.g., TRF and CRF), systematic errors, and unmodeled geophysical signals (Escapa et al., 2013, 2016; Belda et al., 2017b; Escapa et al., 2017; Escapa and Capitaine, 2018; J. M Ferrándiz et al., 2020a).
Belda et al. (2017a) determined a new set of empirical corrections to the precession offsets and rates and the amplitudes of a broad set of terms included in the IAU 2006/2000A precession-nutation theory. After applying these corrections to the EOP, some signals were found in the remaining residuals. The signals could be caused by different geophysical phenomena such as strong ENSO, free inner core nutation (FICN) (Mathews et al., 2002; Koot et al., 2010; Lambert et al., 2012; Malkin, 2013b), and Geomagnetic field (GMF) (Shirai et al., 2005; Malkin, 2016). Some studies have been done to determine nutations considering the influence of the magnetic field mathematically (Buffett, 1993; Greff-Lefftz and Legros, 1999; Greff-Lefftz et al., 2000). The nutation amplitudes are computed in a displacement field approach that incorporates the influence of a prescribed magnetic field inside the Earth's core. The existence of relative nutational motions between the liquid core and its surrounding solid parts induces a shearing of the magnetic field. Then, an incremental magnetic field is created, which returns and perturbs the nutations themselves. This problem has already been addressed within a nutation model computed from an angular momentum budget approach.

The dynamic equation for the infinitesimal elastic gravitational motion for a rotating, slightly elliptical Earth is given as, in a steadily rotating reference frame constant speed Ω_0 (Smith, 1974; Dahlen and Tromp, 1998):

$$\rho D_t^2 s + 2\rho\Omega_0 \times D_t s = -\rho\Omega_0 \times (\Omega_0 \times s) + \nabla . T^e - \nabla(\gamma \nabla . s) - \rho\nabla\phi_1 - \rho s . \nabla\nabla\phi + \nabla . [\gamma(\nabla_s)^T] \quad (7.1)$$

where rigidity γ is the equilibrium pressure, and ϕ_1 is the incremental gravitational potential induced by the mass redistribution due to deformation. The stress tensor (T^e is the incremental stress, with respect to the reference stress, $T^{ref.} = -\gamma I$, where I is the identity tensor that is linked to the displacement field by two Lamé parameters (λ, μ) for an isotropic medium as

$$T^e = \lambda(\nabla . s)I + \mu[\nabla s + (\nabla s)^T], \quad (7.2)$$

where rigidity $\mu = 0$ un a liquid part of the Earth.

Huang et al. (2011) proposed a new strategy to estimate nutations, considering the magnetic field influence directly in the motion equation and in the boundary condition. Their results indicate that the Free core nutation (FCN) period decreases by 0.38 days, and the out of phase (in-phase) amplitudes of the retrograde by 18.6 years, and the retrograde annual nutations increase (decrease) by 20 and 39 μas, respectively.

Also, during the last decade, several investigations have been done to discuss a possible interconnection of GMF changes with the polar motion (Le Mouël et al., 1981; Mandea et al., 2000; Bellanger et al., 2002; Holme and De Viron, 2005; Gorshkov et al., 2012; Silva et al., 2012). However, less attention has been paid to the impact of the GMF changes, such as the geomagnetic jerks (GMJ), which are rapid changes in GMF secular variations, and other GMF variations on the FCN variations. The GMJ occurs about every one to two years. The GMJ events are registered at geomagnetic observatories (as well as satellite observations), and they can be observed worldwide (global jerks) or within specific geographic regions (regional jerks). Shirai et al. (2005) studied the association between the GMJ and FCN, which revealed a close coincidence of two FCN phase jumps with two GMJs that occurred in 1992 and 1999. Vondrák and Ron (2015) and Malkin (2016) suggested geomagnetic jerk as a potential parameter to be investigated. Malkin (2013b) showed that the extreme variations in the amplitude and phase of FCN coincide with GMJ epochs. This means that the FCN can be excited by the same processes that cause the GMJ, which could be close to reality, as the flows in the core mostly generate the GMJ, and the same flows lead to variations in the core moments of inertia and thus can cause the FCN variations (Dehant and Mathews, 2003).

However, some doubts still need to be resolved before this correlation is confirmed. Most previous studies have indicated that the FCN is excited by Earth's geophysical surface fluids (e.g., the atmosphere and oceans) because of the exchanges between their angular momentum and the solid Earth (Sasao and Wahr, 1981; Vondrák and Ron, 2015). Core–mantle couplings, which can directly affect the misalignment between the rotational axes of the mantle and outer core, are also an important excitation source (Cui et al., 2018). Various effects are mixed in the signal variation of the FCN; among these, the effects of surface fluids such as the atmosphere and ocean have significant time-varying characteristics. Therefore, it is not easy to obtain reliable results by directly connecting the amplitude and phase of FCN to the GMJ epochs

without removing other factors (Malkin, 2013b).
In this chapter, the relationship between FCN and GMJ, magnetic dipole moment and GMF models are investigated to find whether there is a dependency structure between the CPM and GMF.

7.2 Data Set

A brief analysis of the data set used in this chapter is illustrated as follows:

7.2.1 FCN Data

Belda et al. (2016) have developed a new empirical FCN model with a higher temporal resolution by fitting the amplitude parameters directly to the VLBI solution calculated.
FCN models can be characterized by a weighted least-squares fit of these equations (Lambert, 2007):

$$FCN_X = A_C cos(\sigma_{FCN} t) - A_S sin(\sigma_{FCN} t) + X_0 \tag{7.3}$$

$$FCN_Y = A_S cos(\sigma_{FCN} t) - A_C sin(\sigma_{FCN} t) + Y_0$$

where $\sigma_{FCN} = \frac{2\pi}{P}$ is the frequency of FCN in the Celestial Reference Frame (CRF), A is the amplitude, t is the time relative to $J2000.0$, P is the period, and X_0 and Y_0 are constant offsets. These offsets accumulate the low-frequency part of the signal. Therefore, the contribution of the FCN to the CIP offsets (CPO) can be computed by using Eq. 7.3 without taking into account the shift terms X_0 and Y_0. Figure 7.1 illustrated CPO observation using VLBI and the B16 FCN, which was empirically estimated between 1990 and 2015. The B16 model is empirical and fitted to VLBI data using a sliding window length of 400 days, a displacement step size of one day, and a fixed period of 431.18 sidereal days.
In this study, we are interested more in the dynamic behavior signal. Then, the FCN data and its products are transformed from data space into the normalized space between 0 and 1. Figure 7.2 shows the normalized FCN (left panel), the first derivative of FCN (right panel), and the second derivative of FCN (lower panel). The spectral analysis of the FCN's products is done using the fast Fourier transform (FFT). The results show that the dominated signals of FCN_X are 12.2 (410 days, primary signal), 18.9, and 9.9 months. Also, the dominated signals of other products are shown in Figure 7.3, in which the magnitude of the main signals is approximately less than %20. However, both FCN_{X_0} and amplitude of FCN held in common signals for 29.7 and 52 months from 1997 to 2017.

7.2.2 GMF Data

7.2.2.1 GMJ

GMJs occurred mainly in 1991, 1999, 2003/2004, 2007/2008, 2011, and 2014 (Olsen and Mandea, 2007; Chulliat et al., 2010; Mandea et al., 2010; Torta et al., 2015). Besides these confirmed jerks, Sabaka et al. (2004) derived a comprehensive model (CM4) of the geomagnetic field based on hourly magnetic observatories and satellite data and found another jerk of questionable global extent in 1997. Malkin (2013b) also considered a possible jerk in 1994

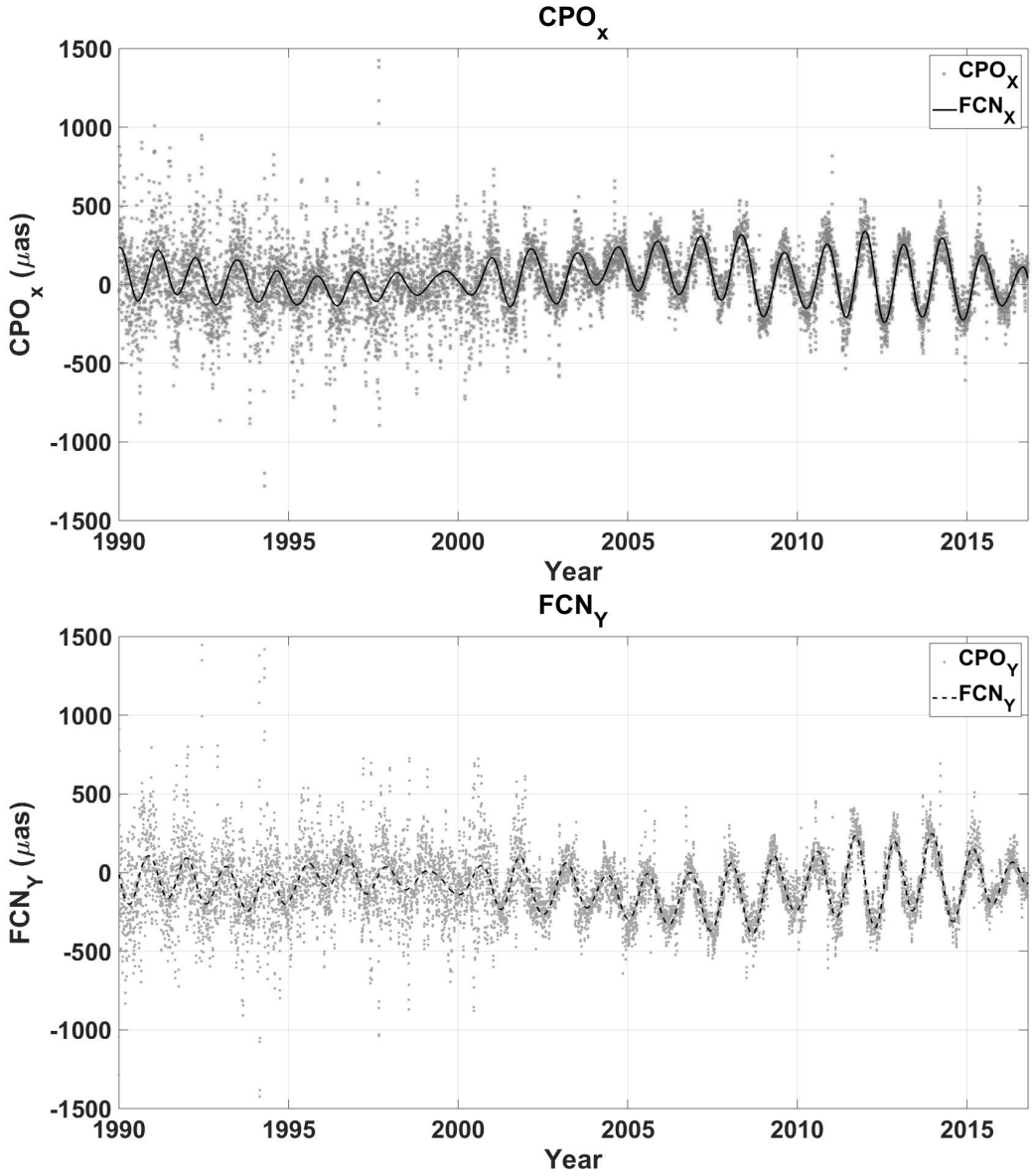

Figure 7.1: CPO and FCN in X and Y direction.

based on some observations at geomagnetic stations. Because satellite data have made it possible to calculate the global secular acceleration (SA) of the geomagnetic field, some large SA pulses at the core surface were found in 2006, 2009, and 2012.5, which may be related to GMJs observed at Earth's surface (Chulliat et al., 2015).
GMJ usually has a time scale of several months to a year. In comparison, the inflection points of the FCN period changes (i.e., 1991/1992, 1997, 1999, 2003/2004, 2006/2007, 2009, 2011, 2012.5, and 2014) all corresponded to times when GMJ or SA pulses at the core surface occurred. Only the epoch of the questionable GMJ in 1994 did not occur at an inflection point in the variation of the FCN period.

7.2.2.2 Magnetic Dipole Moment

The Earth's main dipolar magnetic (DM) field results from the convective movement of the electrically conducting fluid iron-sulfur mix that forms the liquid outer core at depths between

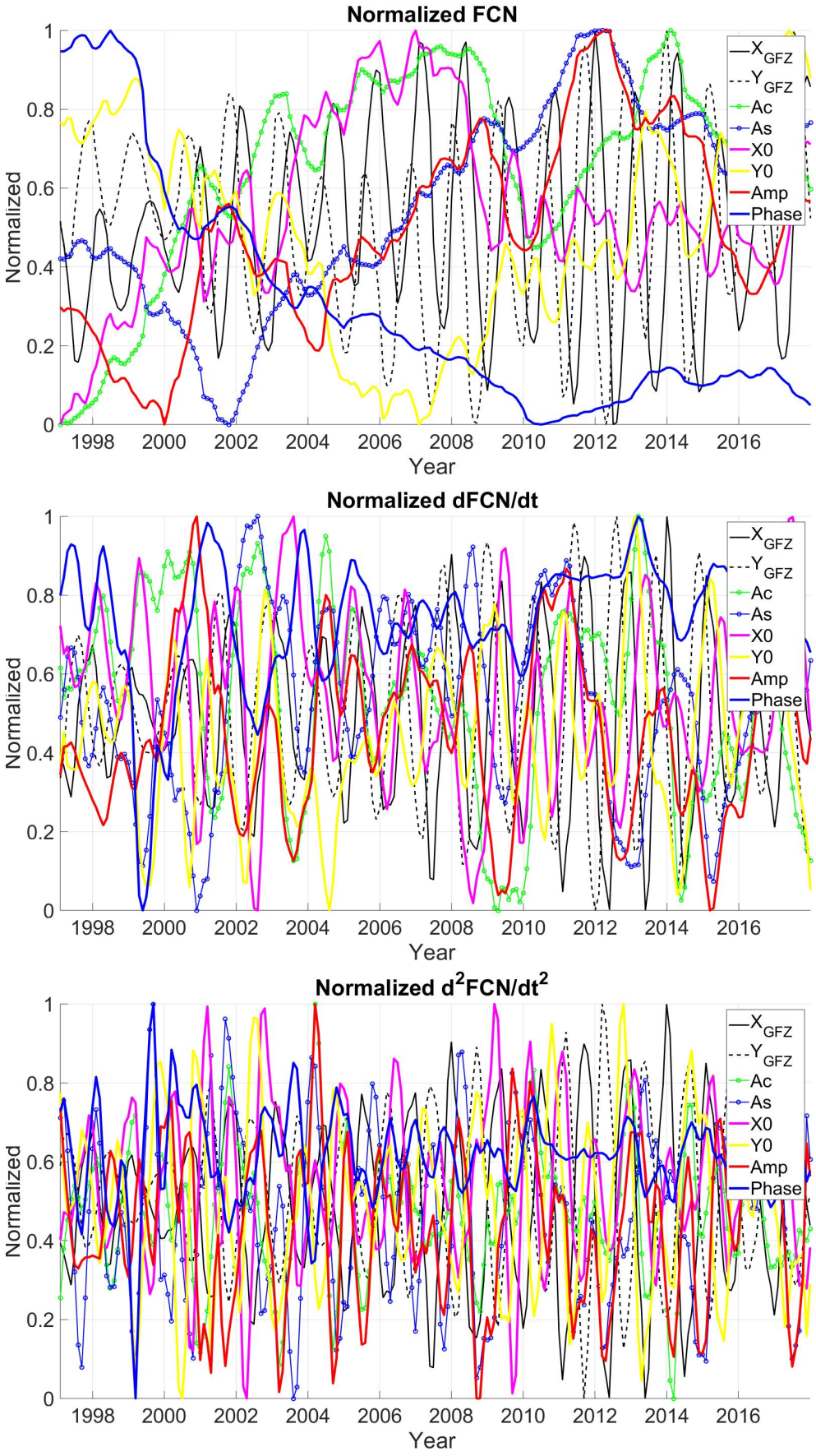

Figure 7.2: Normalized FCN products and their derivatives.

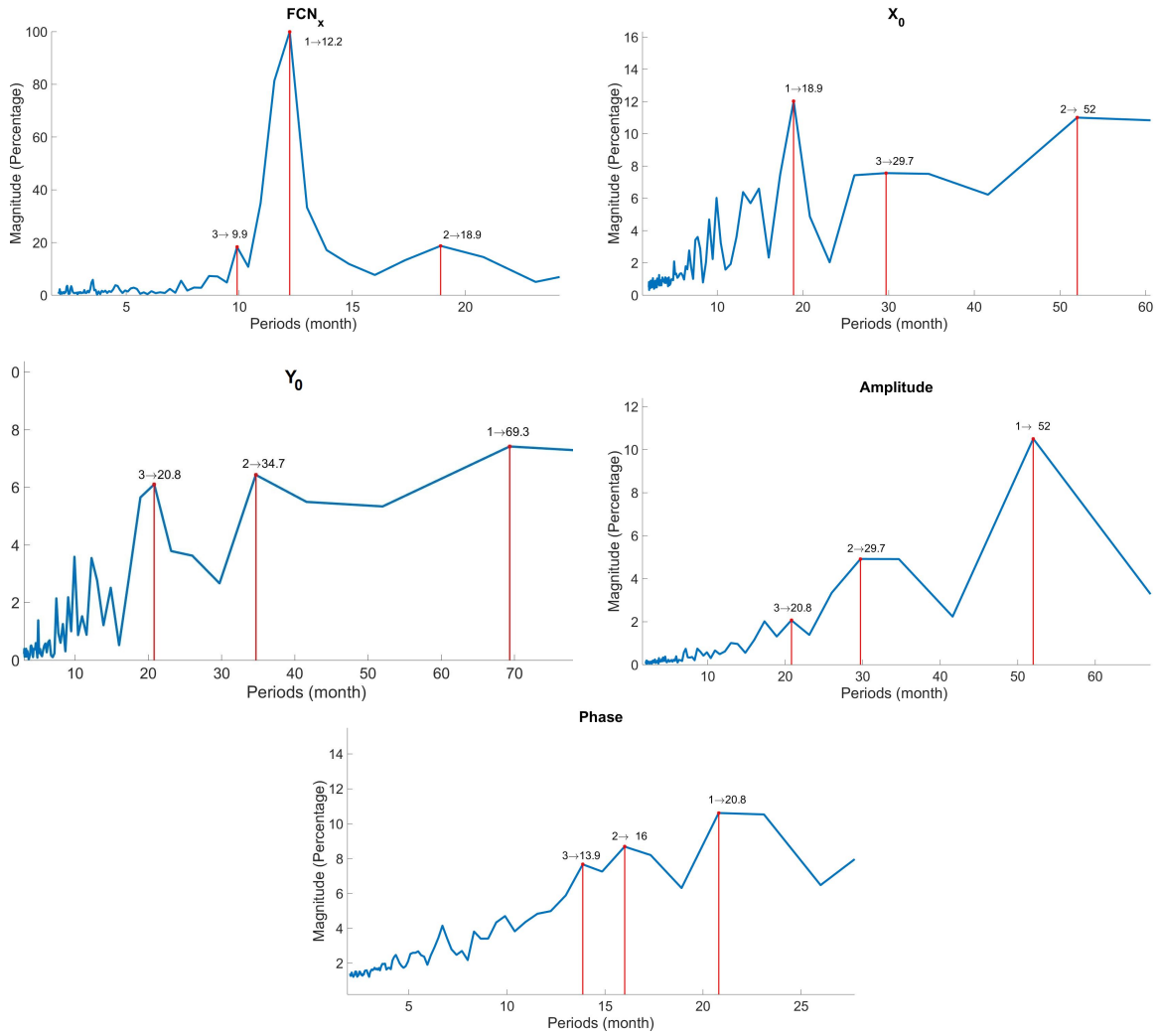

Figure 7.3: FFT analysis of FCN products.

3480 and 5150 km. This field is tilted by about 10.5° from the Earth's rotational axis and varies smoothly in space and time due to changing current interactions in the core. Figure 7.4 shows the DM and normalized DM rate and the second derivative of DM. As can be seen in Figure 7.4, the DM rate is increasing after mid-1999 to 2003. Also, the d^2DM/dt^2 is changing between 2002 and 2005: very sharp.

7.2.2.3 Geomagnetic Field Model

CHAOS-6 core field provides information on time variations of the core generated as part of the Earth's magnetic field (Finlay et al., 2016). The CHAOS model series aims to estimate the internal GMF at the Earth's surface with high resolution in space and time. The CHAOS model derived primarily from magnetic satellite data, although ground space activity indices and monthly observatory means are also used. The CHAOS model series are considering vector measurements at mid- to low-latitudes and scalar data (Olsen et al., 2006, 2009, 2010, 2014). The CHAOS's validity is restricted to post-1999 when the Orset satellite was launched. In this study, the CHAOS-6 core field model is used to investigate the dependency structure between the GMF model and the FCN time series. The CHAOS-6 provides information on time variations of the core generated part of the Earth's magnetic field. It is one of the latest

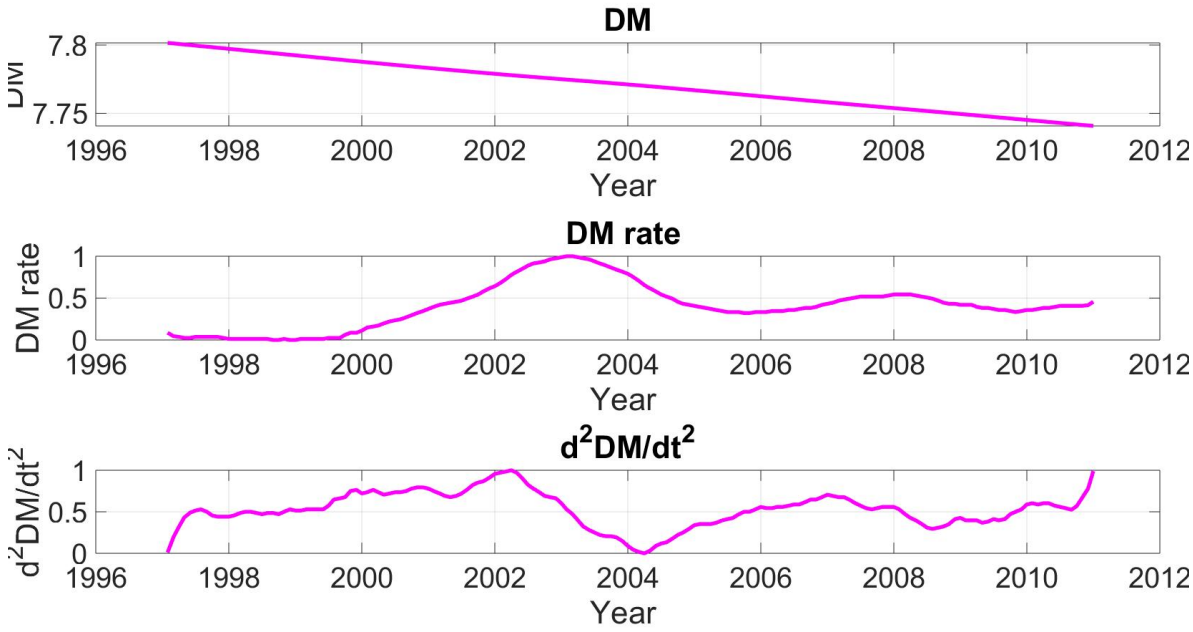

Figure 7.4: DM and normalized dDM/dt, and d^2DM/dt^2.

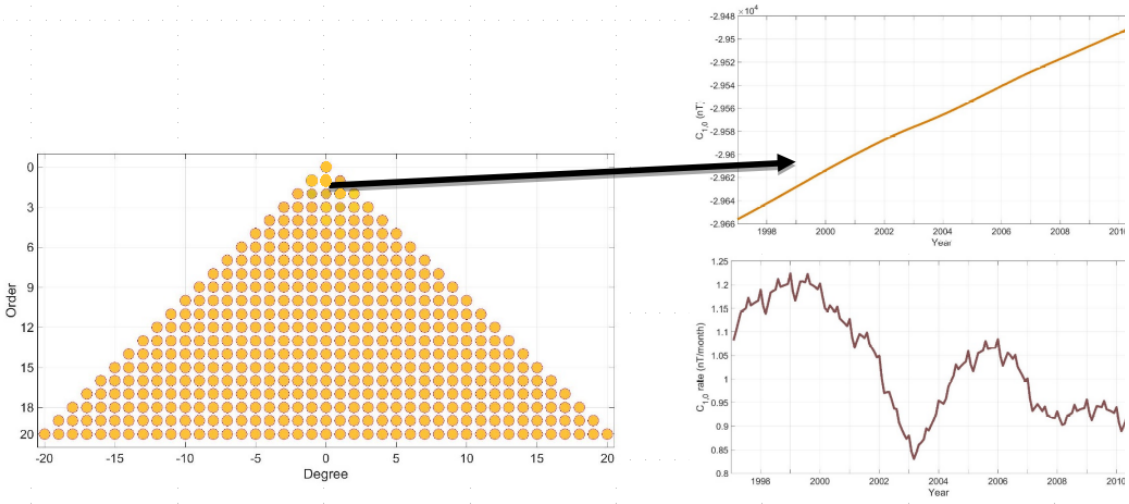

Figure 7.5: Geomagnetic's SHC up to degree and order 20 (right). The $C_{1,0}$ time series and its rate (left).

generations of the CHAOS series of global geomagnetic field models developed by (Olsen et al., 2006, 2009, 2010, 2014).

The CHAOS-6 model parameterization follows that of CHAOS-5 and CHAOS-4. See Olsen et al. (2014) for a more detailed account of the CHAOS field modeling scheme, including the external model. The time-dependent internal field $B_{int}(t) = -\nabla V_{int}$ is designed as the gradient of the scalar potential:

$$V_{int} = a \sum_{n=1}^{20} \sum_{m=0}^{n} [g_n^m(t) cosm\phi + h_n^m(t) sinm\phi](\frac{a}{r})^{n+1} P_n^m(cos\theta) \tag{7.4}$$

where $a = 6371.2km$ is a reference radius, (r, θ, ϕ) are geographical coordinates, and $P_n^m(cos\theta)$ are the Schmidt semi-normalized associated Legendre functions of degree n and order m. $g_n^m(t)$

and $h_n^m(t)$ are time-dependent Gauss coefficients (Geomagnetic's SHC up to degree and order 20 are shown in Figure 7.5).
The description in terms of spherical harmonics with constant Gauss coefficients is applicable for static snapshot fields. However, since the magnetic field changes in space and time, all field models use time-dependent Gauss coefficients. The commonly adopted approach is to model the temporal evolution with spline functions.

7.3 FCN Prediction Error and GMJ

As mentioned in the introduction, some investigations have been done to indicate the association between GMJ and changes in FCN's amplitude and phase. However, the relationship between the FCN prediction error and GMJ was not investigated. Here, the connection between the FCN prediction and GMJ is studied.
As the GMJ and significant SA pulses at the core surface could affect the FCN's amplitude or phase at those epochs or with some months' delays, some errors are expected in the FCN prediction results.
The FCN amplitude, phase, and offsets of the FCN (B16 model) are computed and transformed into normalized space. Also, the first derivative of these time series is determined and then normalized. The uncertainty of GMJ epochs is approximately one year; therefore, all the epochs are shown by a box with one-year coverage. Hence, the epochs of the FCN variations and the GMJ epochs coincide when the difference between the two epochs is not greater than two years with a possible general lag. As can be seen in Figure 7.6 and 7.7, the changes in the FCN amplitude and phase are approximately related to the GMF sudden disturbance. Observed extremes in the FCN amplitude and phase variation occurred at the epochs close to the GMJ epochs. Most of the minima of the FCN amplitude followed corresponding GMJs with a delay of 1–3 years, which is consistent with the conclusion of Gibert et al. (1998) and Bellanger et al. (2002), who found that the rapid changes in the Chandler Wobble phase follow the GMJ with a delay of 1–3 years. All the maxima of the first derivative of the FCN amplitude also occurred near the GMJ epochs. The correlation between the FCN variations and GMJ was verified for all five GMJs that occurred from 1991 to 2016, including the supposed jerks in 1994 and 1997, which are not yet widely accepted in literature. The substantial FCN amplitude and phase disturbance was around 1999 and 2000 at the epoch close to GMJ, and it was detected for the first time by Shirai et al. (2005).
As can be seen in Figure 7.8, the FCN prediction errors occur coincidentally with observed GMJ and sharp SA pulses epochs, e.g., in 1991, 1999, 2006, 2009, 2011, and 2016. Also, some errors can be seen after the GMJ epochs, which could prove the assumption as mentioned above. However, the association between the FCN prediction errors and GMJ was not approved in 1994 and 1997, which are not officially recognized in the literature and GMJ due to different features of disturbances, but a significant SA pulse at the core surface occurred at those epochs. In addition to the prediction error, the computed amplitude, phase, and prediction offset could be investigated.

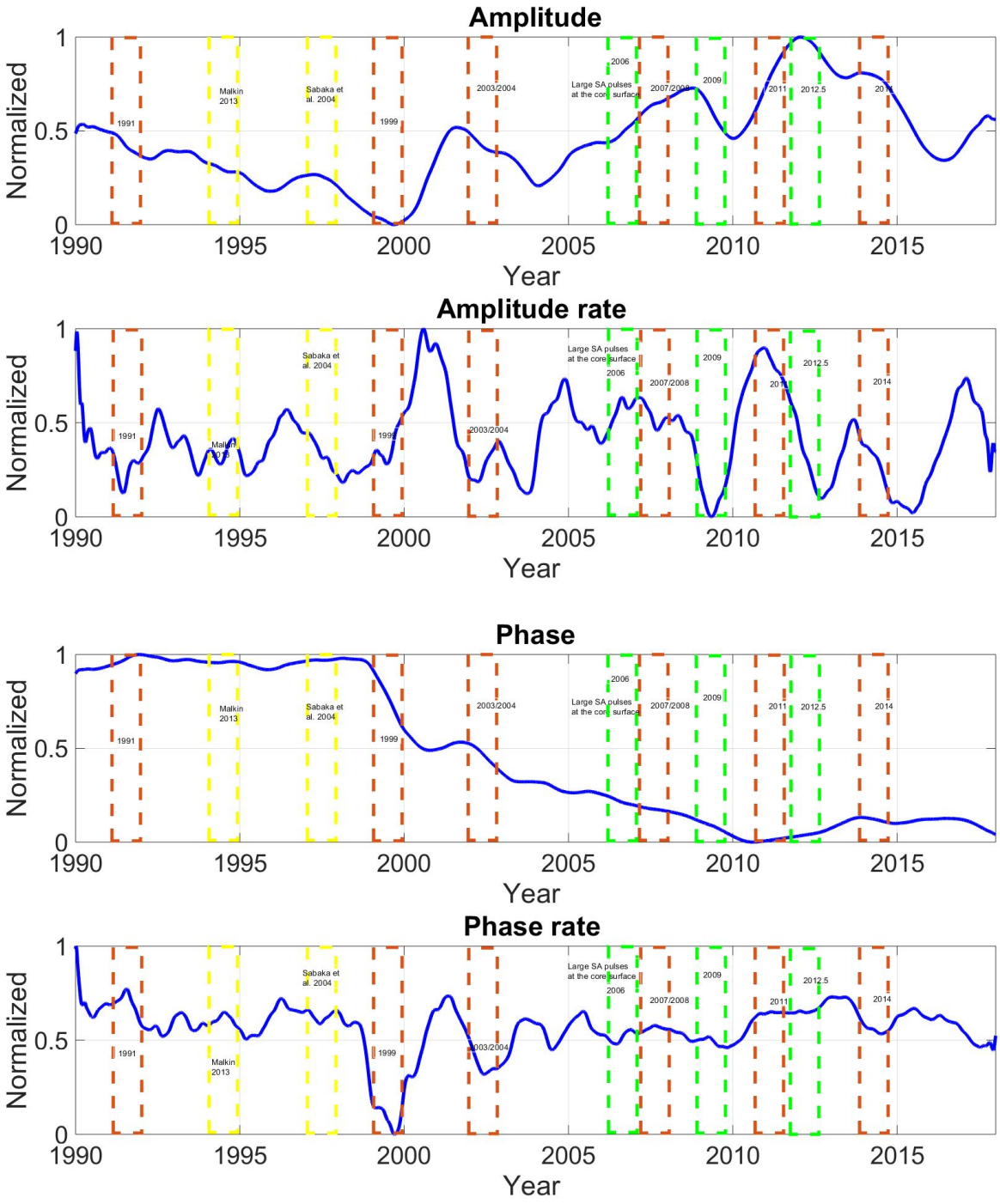

Figure 7.6: Time series of the normalized FCN amplitude and phase for the B16 model. The dashed box indicates GMJ and SA pulses at the core surface. The red color shows the confirmed GMJ. The yellow shows questionable SA of the GMJ. The green indicates a significant global SA of the GMF.

7.4 FCN and GMF Models

7.4.1 Geomagnetic Spherical Harmonic Coefficients (SHC) and FCN

The spherical harmonic coefficients are widely used to describe the magnetic field as a derivative of potential in a spherical coordinate system. This is the representation of the magnetic field

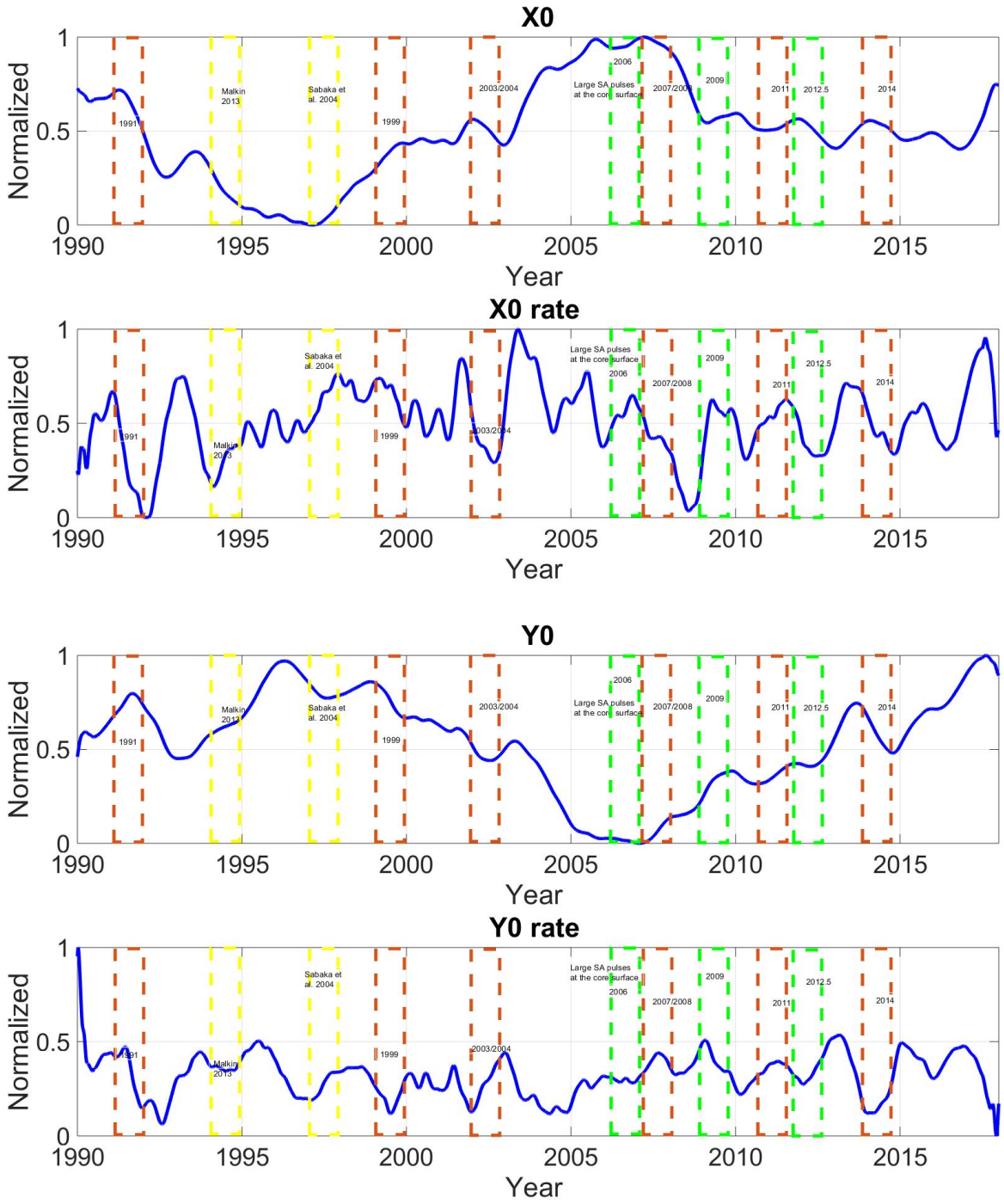

Figure 7.7: Time series of the normalized FCN offsets for the B16 model. The dashed box indicates GMJ and SA pulses at the core surface. The red color shows the confirmed GMJ. The yellow shows questionable SA of the GMJ. The green indicates a significant global SA of the GMF.

potential as a series of multi-poles, $n = 1$ represents the dipole contribution, and $n = 2$ represents the quadrupole contribution. In this study, the SHC up to degree and order 20 have been taken from the CHAOS 6 model. The CHAOS model is based on satellite and observatory data, paying special attention to variations on sub-decadal time scales.

Figure 7.5 shows the schematic of SCH degree and order up to 20 in the left panel, and the time series of SHC C_{40} in the right top panel, and its rate is shown in the right bottom panel.

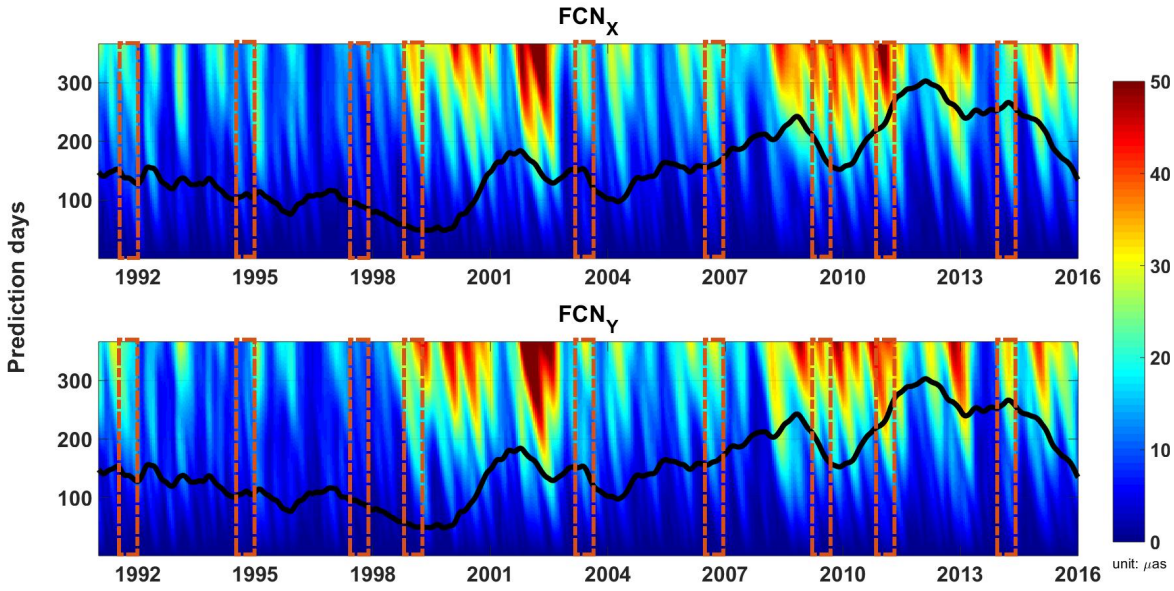

Figure 7.8: FCN prediction errors and the GMJ epochs. The black curve is the FCN amplitude.

The relation between geomagnetic SHC rate and FCN data analysis is shown in the following steps:

- Perform WCA between each coefficient and FCN to extract all co-movements.
- Perform the principal component analysis (PCA) over the results of WCA to detect common patterns of feathers.

As can be seen in Figure 7.9, around 45% of the SHC show the local coherence, which is almost near to the GMJ epochs. The contribution of the first principal component (PC) is shown in

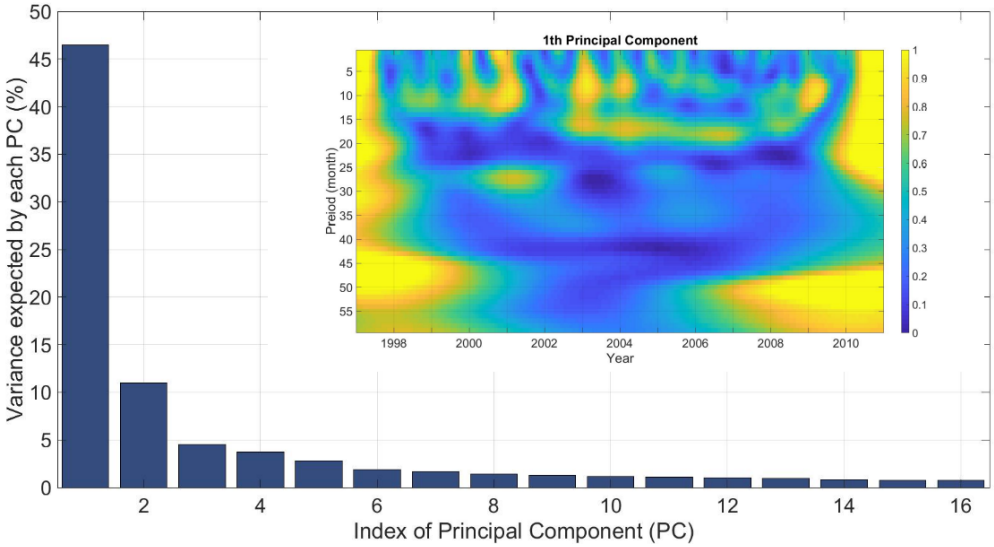

Figure 7.9: PCA helps to extract all common features.

Figure 7.9. The first PC indicates the primary behavior of detected feathers between SHC and FCN (here FCN_x is displayed as an example). Several episodic terms can be seen with a period of 10 to 30 months over the time of 1997–2010. The second PC shows extended-term coherence

with a period of 30 to 35 months and some episodic co-movement terms (see Figure 7.10). The lower degrees agree more with the first PC, and higher degrees have more contribution to the second PC. Several studies have been done to show how the lower degree of SHC relates more

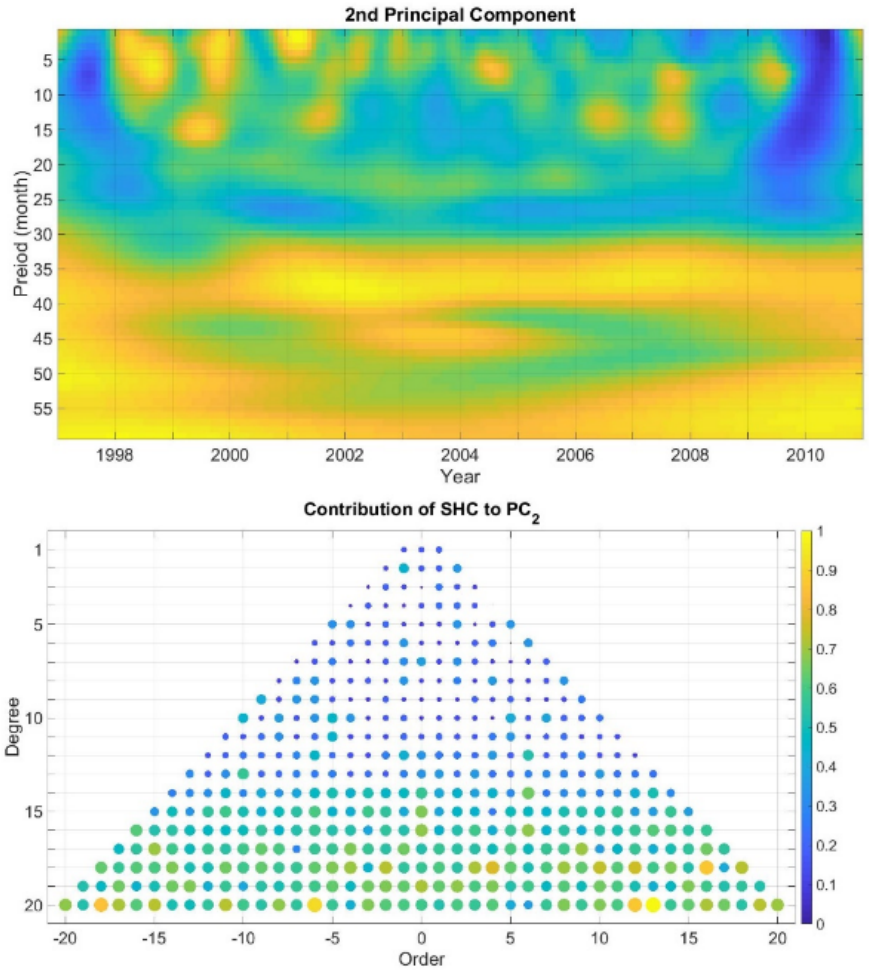

Figure 7.10: The Contribution of SHC to second PC.

to the core activity. Also, the presented results confirm the mentioned fact. Therefore, the lower SHC should be investigated more due to their direct relationship with the Earth's core activity (Lühr et al., 2003).

The time series of FCN_{Amp}, FCN_{Phase} rate, and the SHC rate up to degree 2 are shown in Figure 7.11 as an example to show the dynamic behavior of the studied time series. The red curve shows the amplitude of FCN, and the FCN phase is in blue. The rate of FCN_{Amp} shows sharp changes in the years 1999 and 2003, which coincide with the GMJ epochs. As can be seen in Figure 7.11, the shown SHC indicate different dynamic behavior. The S_{11} and C_{22} time series are increasing up to 2000, and then they decrease. The C_{21} and S_{22} decrease up to 2002 and dramatically increase after this year. Also, C_{10} indicates a sharp variation between 2002 and 2004. Accordingly, all SHC should be investigated in order to find the most relevant coefficient to FCN variation.

First, the correlation coefficient between the SHC rate and FCN products is determined to evaluate the linear dependency between them. Figure 7.12 displays the Pearson coefficient, which is defined as between -1 and 1. The positive linear correlation is shown in red, and the negative is in blue. The linear correlation is significant in the amplitude of the sin and cos

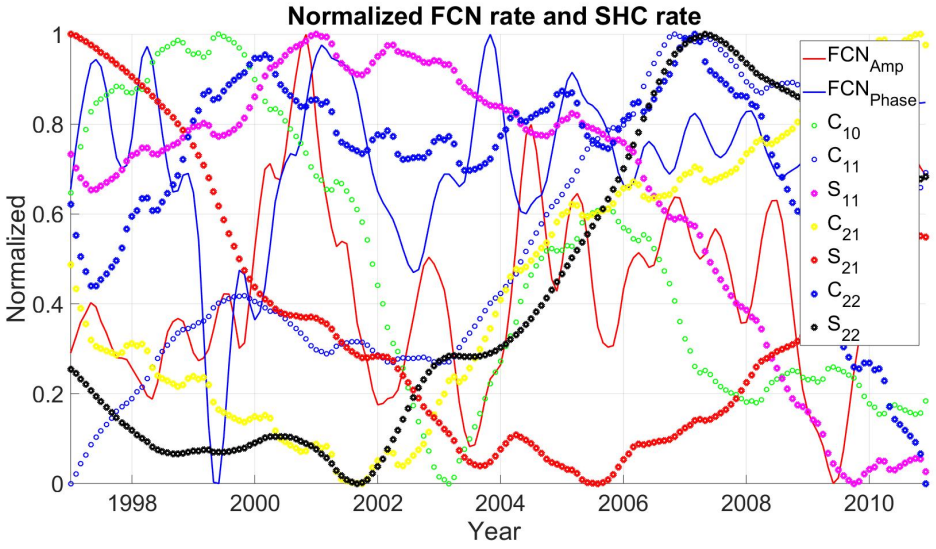

Figure 7.11: FCN_{Amp}, FCN_{Phase}, and the SHC up to degree 2.

part of FCN. Nevertheless, the Pearson coefficient is only able to show a linear correlation.

Thus, coherence between the FCN products and SHC is examined using wavelet transformation analysis. The result of PCA, which shows the contribution of SHC on the primary principal component around %70 and less than %10 of SHC, contributes to the PC_2 and PC_3. The results shown in Figure 7.13 illustrate a meaningful contribution of the SHC to the principal component by approximately 70%. Also, the sum of the first seven components is presented on the right panel. The red color box shows the corresponding GMJ epochs.

The Figure 7.14 shows the coherence analysis between the $FCNAmp$ rate and SHC rate and the contribution of each coefficient in the specific pattern. Three statistically significant long term coherency with a period of approximately 3–5, 18–24, and 36 months are detected over the whole interval of time. The contribution of each SHC for the first three PC is shown on the right side.

Figure 7.15 shows the coherence analysis between the $FCNPhase$ rate and SHC rate. A statistically significant long-term coherence with a period of approximately 30 months and some local patterns can be seen with a period of 2 to 4 months. The coherence analysis between $FCNX_0$ rate and SHC rate is shown in Figure 7.16. Some local patterns are detected with a period of 2 to 4 months. Also, two episodic patterns can be observed in 1999 with a period of 7 and 30 months, which nearly related to the second PC, and it is highly related to the degree 1 and 2. The coherence analysis between $FCNY_0$ rate and SHC rate is shown in Figure 7.17. A significant lengthy-term agreement with a period of 30 months is detected during 1997–2005, which is related more to the third PC with a degree up to 4. Several local co-movements are detected with a period of 2 to 6 months.

7.4.2 FCN and Magnetic Dipole Moment

The association between the rate of change of FCN's products and DM rate is investigated performing wavelet coherence analysis. The dipole moment time series from 1997 to 2010 with monthly temporal resolution is prepared for this research. The daily FCN data are converted to monthly series by block averaging to enable the comparison with the dipole moment. Then,

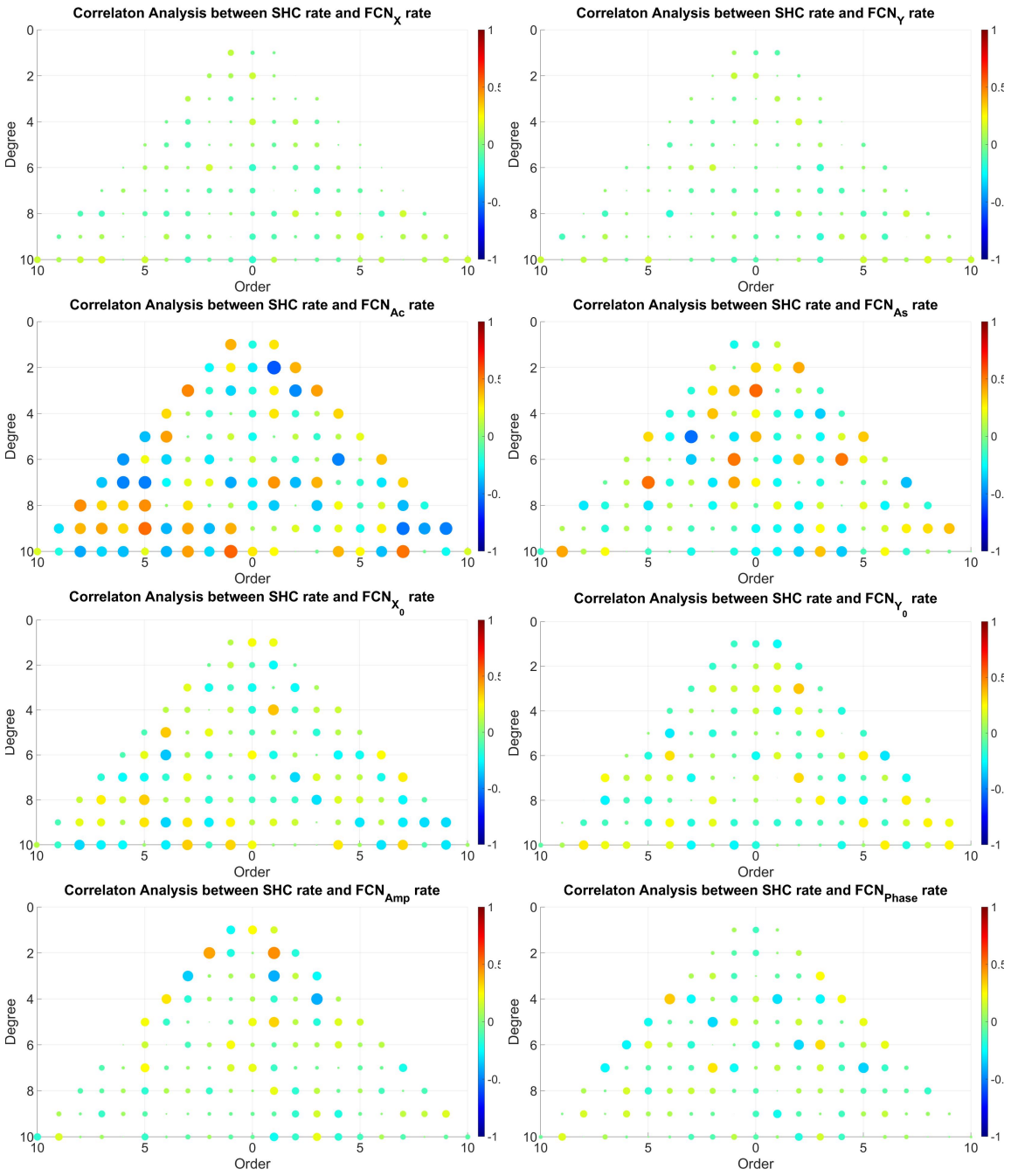

Figure 7.12: Correlation between FCN and SHC.

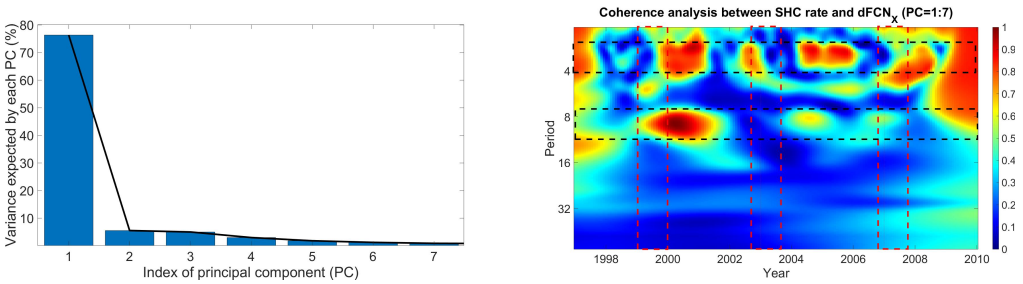

Figure 7.13: The relation between the FCN_X and SHC of CHAOS6. The degree up to 10 represents the Earth's core activities.

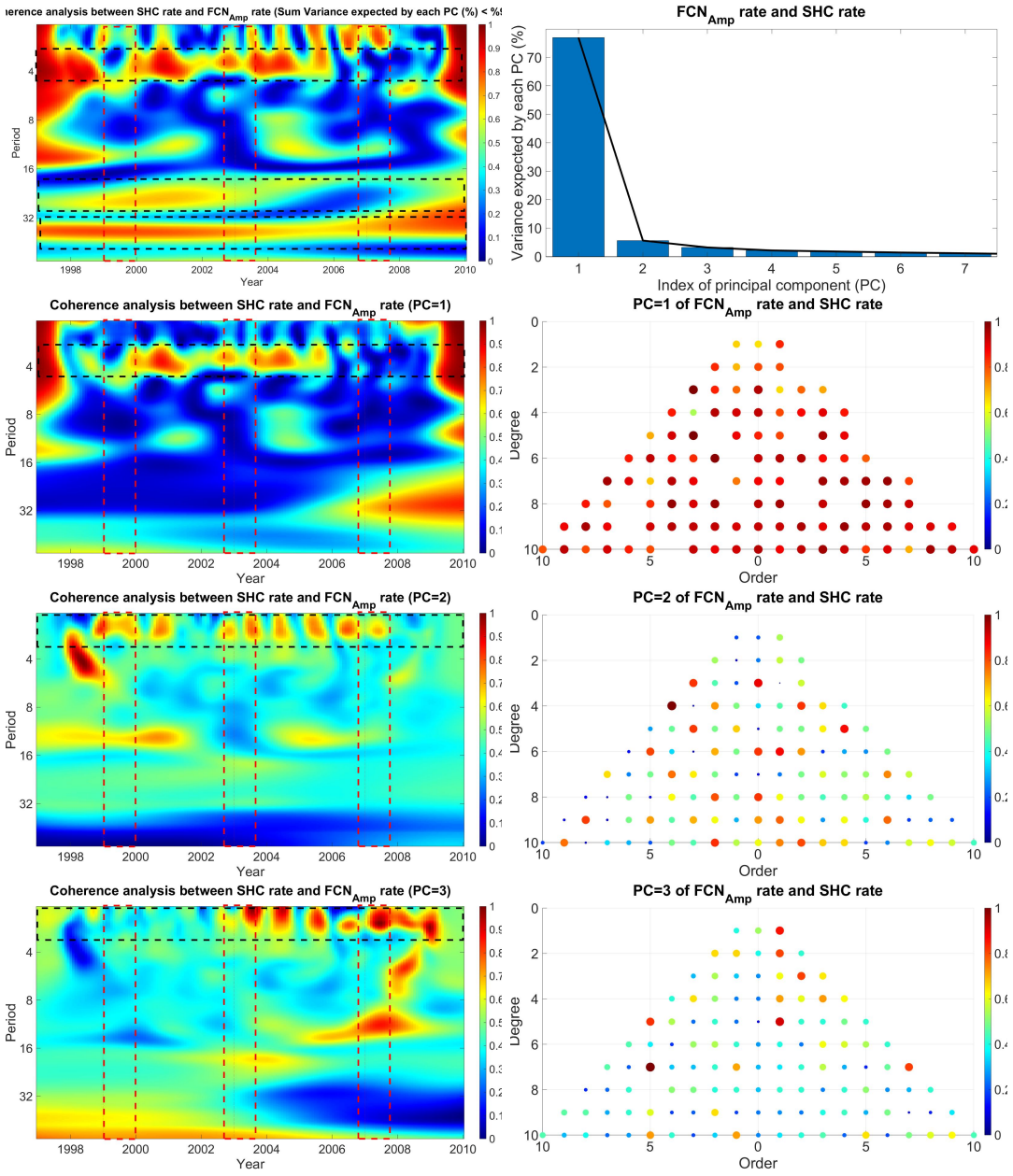

Figure 7.14: Contribution expected by each PC of PCA between SHC and FCN product.

the dynamic relationship between FCN product rate and DM rate is identified using WCA. The cone of influence separates the true (full colors) and less reliable (pale colors) regions. The phase difference, such as a lag or lead relationship, is shown by oriented arrows. The arrows show phase relationships (pointing to the right is a positive correlation; a negative correlation by one to the left; leadership of the DM rate is shown by a downward pointing arrow; the upward-pointing arrow means FCN rate is leading DM rate).

The WCA detected statistically significant coherence at a higher period year extending from 1997 and 2010. In particular, the approximate period of 30 months can be identified in all cases Figure 7.18. Moreover, some little statistically significant local coherence is found where the epochs of GMJ are reported. Figure 7.18 (top left panel) indicates the co-movements between the rate of changing FCN_Y and DM rate, and it shows a coherence at 16 months. Also, some episodic terms can be seen around 1999, 2003, and 2007 with a period of 4 months

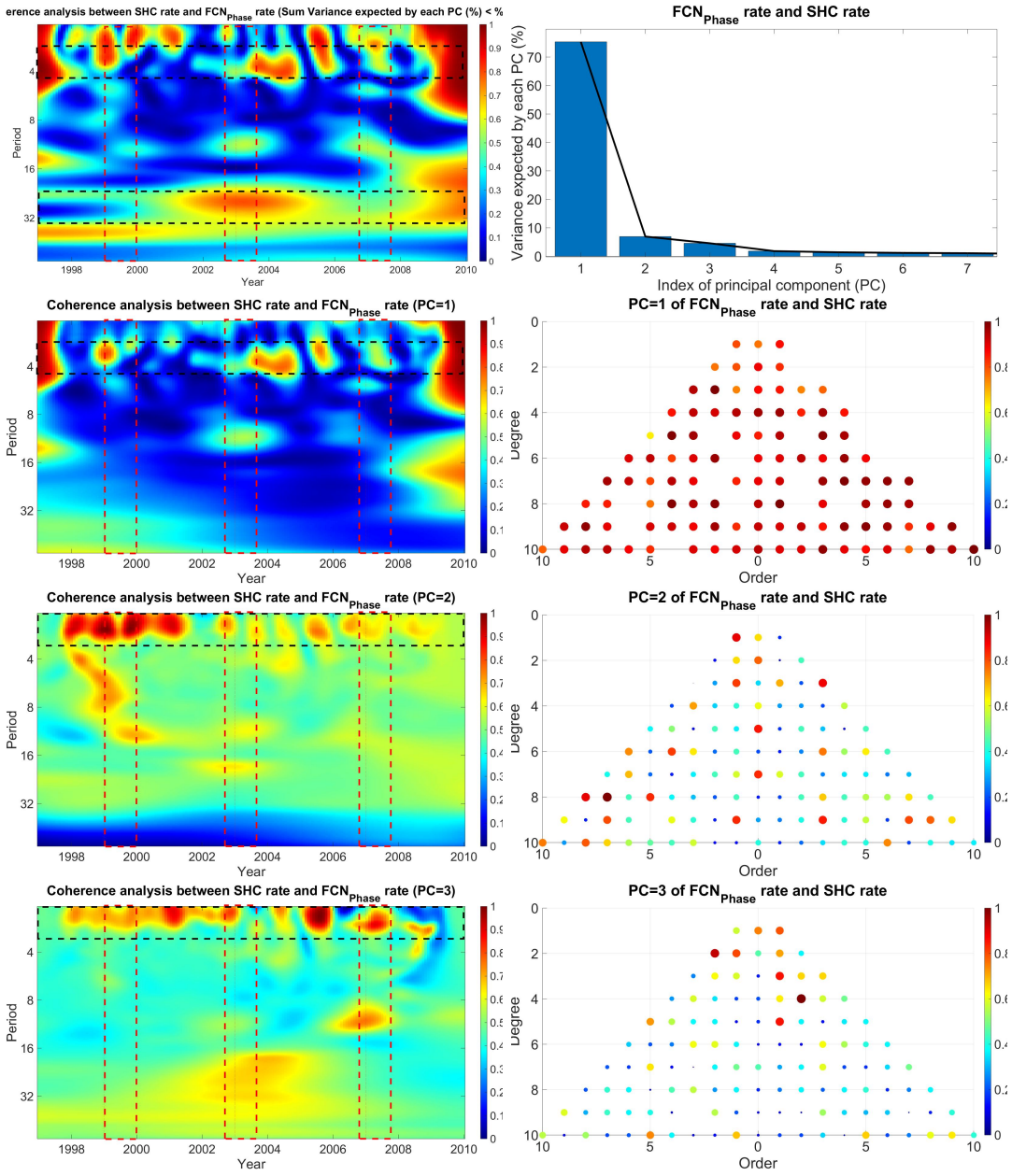

Figure 7.15: Contribution expected by each PC of PCA between SHC and FCN_{Phase}.

where GMJ is observed. The connection between the offset of FCN_Y rate and the DM rate is illustrated by a strong correlation with the same phase at 30 months (approximately 1024 days). Additionally, some local co-movement can be discovered in 1999, 2003, and 2007. However, the phase local wavelet spectra of the FCN_Y offset rate and DM rate in 2003 is quite different from other FCN products, which shows almost anti-phase. The coherence analysis between DM rate and FCN_{As} illustrates a strong coherency between theses variables with a period of 32–64 months from 1997 to 2010. The results of FCN amplitude, phase rate, and DM rate indicate statistically significant local co-movement in 2003 with different periods, 2–6 and 8–16 months, in addition to the long-term coherence with a period of 32 months over 1997–2010.

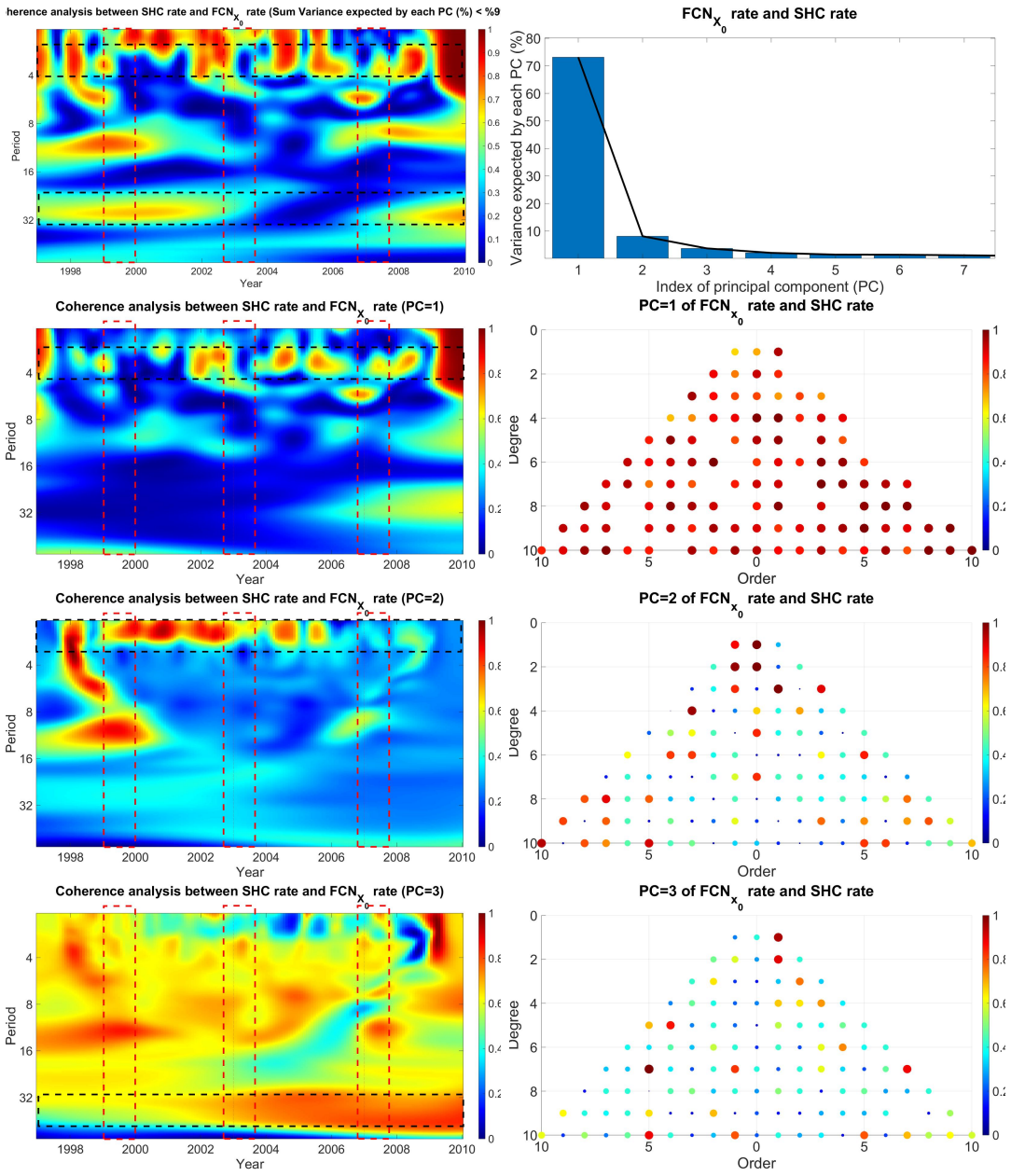

Figure 7.16: Contribution expected by each PC of PCA between SHC and FCN_{X_0}.

7.4.3 Near-Earth Magnetic Field and FCN

In this section, the near-Earth magnetic field is analyzed. The CHAOS 6 model gives a near-Earth magnetic field in the Cartesian coordinate. First, the near-Earth magnetic field data are transformed from geocentric coordinates (X, Y, Z) to local coordinates (east, north, up). As can be seen in Figure 7.19, the near-Earth geomagnetic field is divided into globally gridded conservatively interpolated onto a regular latitude-longitude grid with 5°. Thus, the coherence between the time series of Earth's magnetic field of each grid and FCN is examined using WCA.

Each grid has a time series of GMF in its local coordinate from 1997 to 2017. First, the primary behavior of GMF and its first and second derivatives are estimated using PCA (see Figure 7.20). As can be seen in Figure 7.20, the primary behavior of total GMF, declination, horizontal, northward, eastward, and upward of GMF is shown. The GMF is in black, the first derivative is

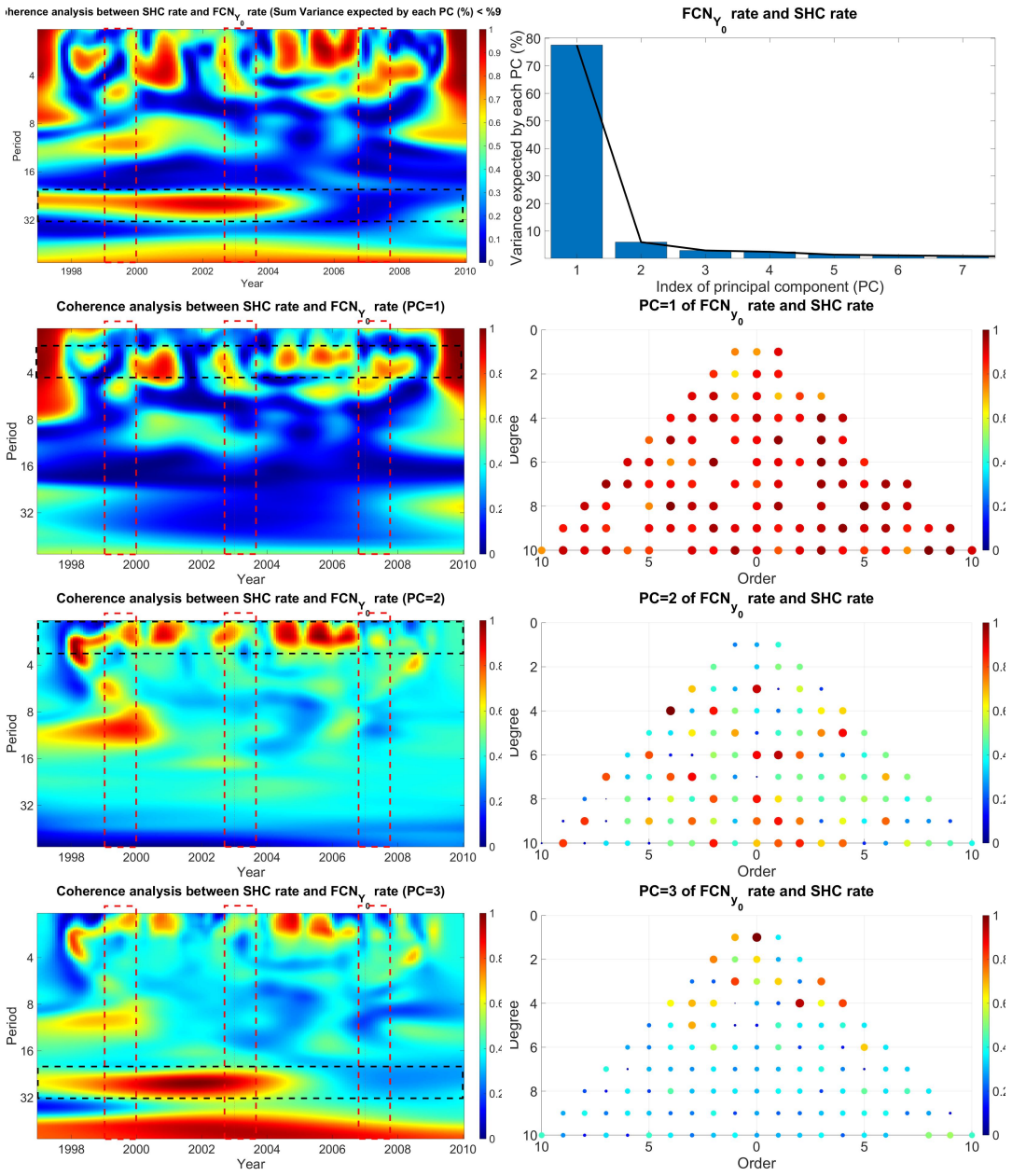

Figure 7.17: Contribution expected by each PC of PCA between SHC and FCN_{Y_0}.

displayed in a dashed back curve, and the second derivative is green. All shown time series are normalized. The main principal components of GMF values tend to decrease over time, except $GMF_{Horizontal}$ values. It clearly highlights the sudden drop in all GMF's rate values around 2004. Figure 7.21 illustrates the second derivative of GMF. There is no apparent trend in the second derivative of GMF over this period. As can be seen in Figure 7.21, the second derivative of GMF shows some strong cyclic behavior. The d^2GMF_{East}/dt^2 show a different pattern compare to GMF_{Fr} or GMF_{total}. When one is increasing, the other one decreases over this time. The dominated signals of d^2GMF/dt^2 are shown in Table 7.1. The first dominated signal of d^2GMF_{Fr}/dt^2, $d^2GMF_{Horizontal}/dt^2$, d^2GMF_{North}/dt^2, and d^2GMF_{Up}/dt^2 is 69.3 months, and it is 104 months for $d^2GMF_{Declination}/dt^2$ and d^2GMF_{East}/dt^2. Also, the FFT results indicate 52, 34, 20, and 16 months signals as dominated signal, which they have in common with the FCN product's signals. Figure 7.22 demonstrates the coherence between the d^2GMF_{Fr}

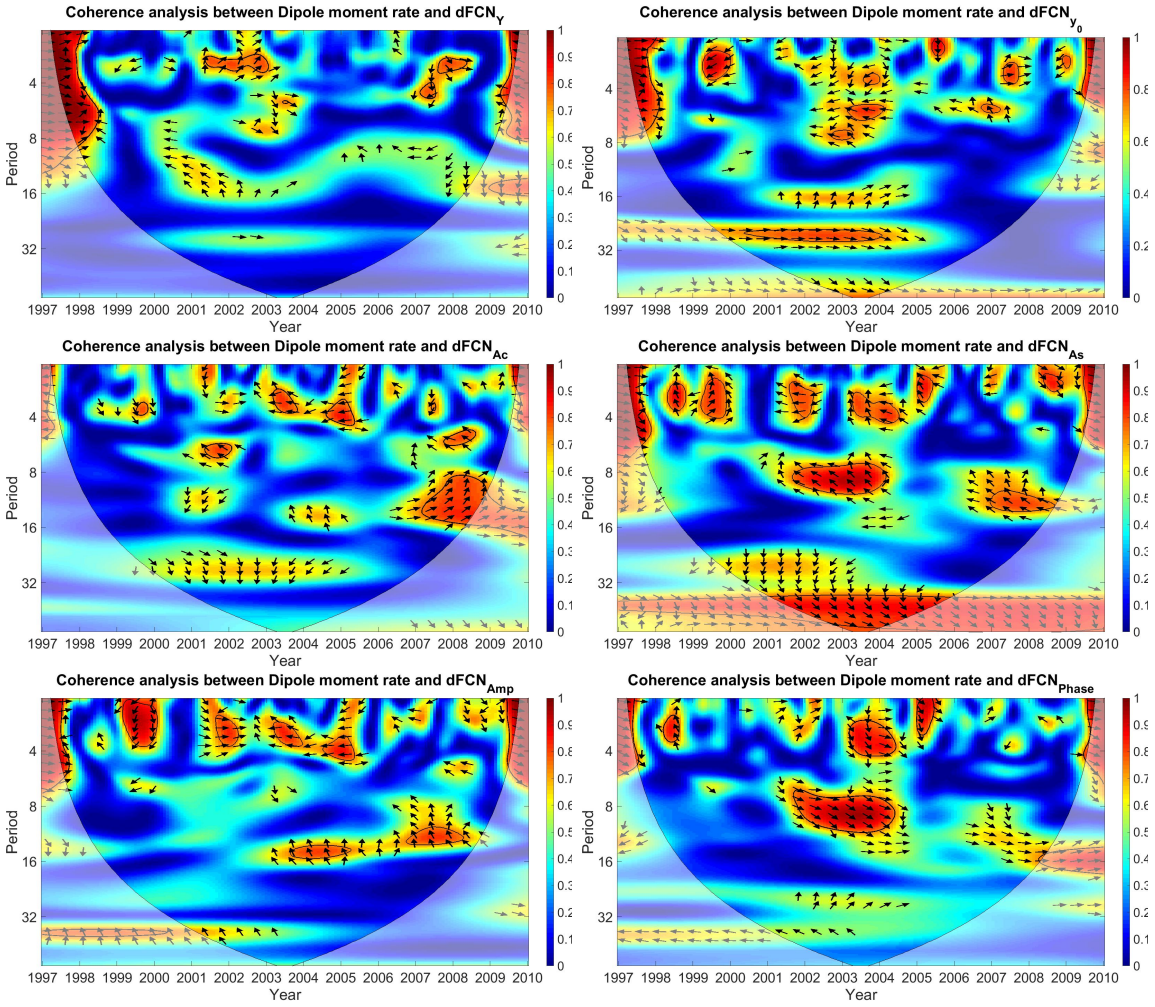

Figure 7.18: The relation between the rate of FCN product and DM rate.

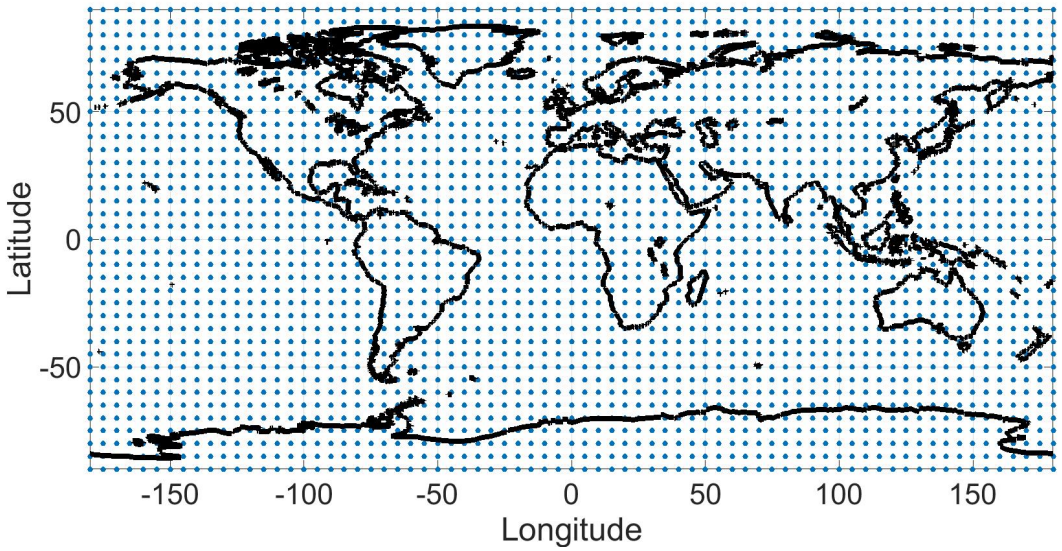

Figure 7.19: Scheme of grid-based analysis. The near-Earth geomagnetic field is divided into globally gridded conservatively interpolated onto a regular latitude-longitude grid with 5°.

and FCN rate from 1997 to 2017. The top left panel shows some local correspondence between FCN_X and d^2GMF_{Fr} with a period of 2–6 months. Furthermore, some significant local

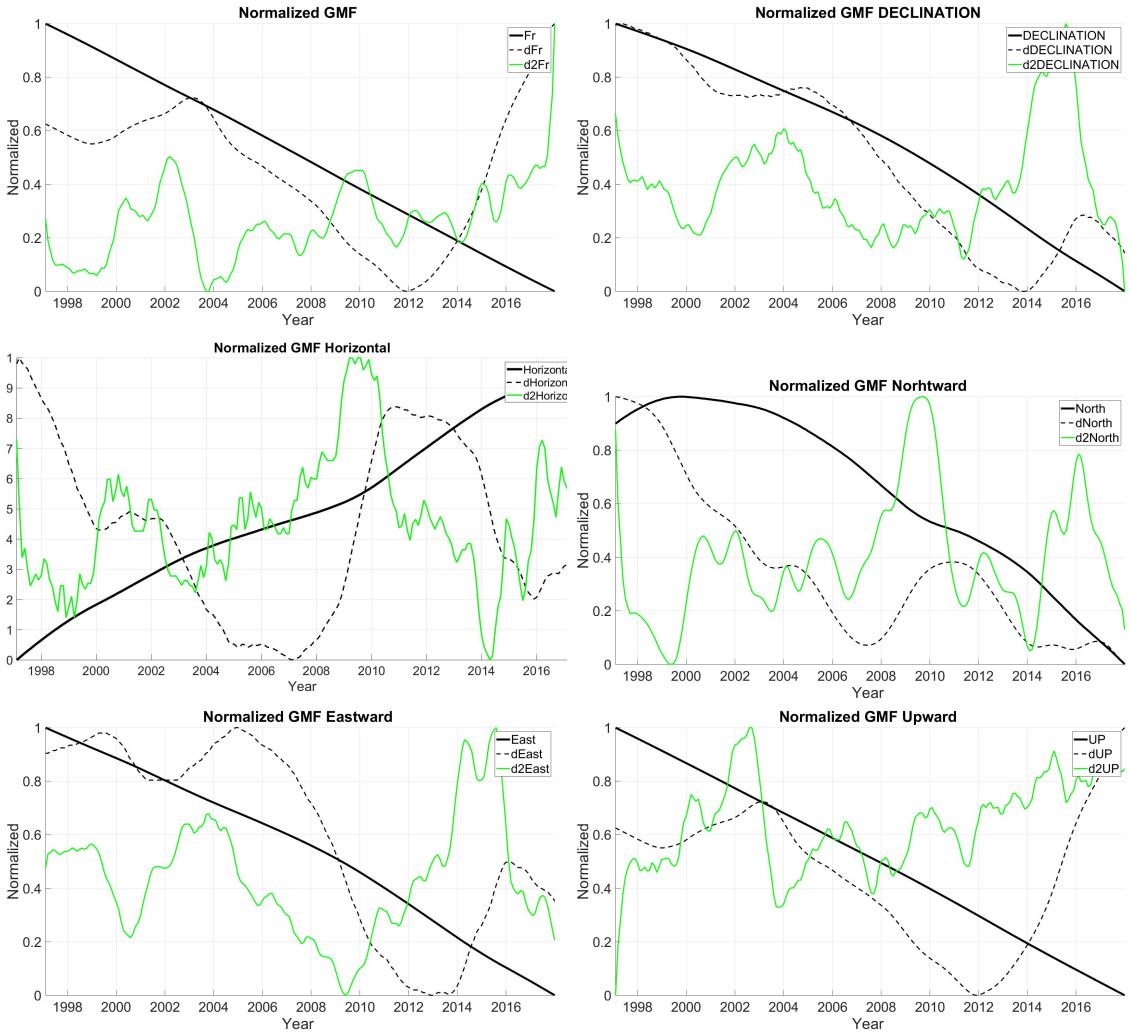

Figure 7.20: Main behavior of GMF and its derivative [no unit].

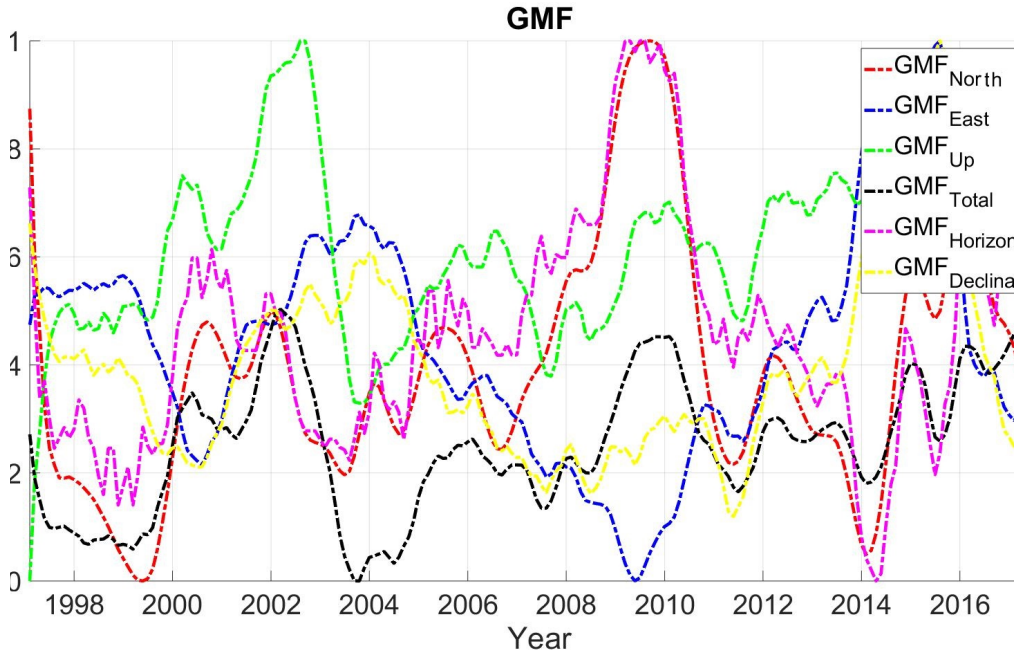

Figure 7.21: The second derivative of GMF (Normalized).

Table 7.1: FFT analysis of the main behaviour of GMF.

	d^2GMF_{Fr}	$d^2GMF_{Declination}$	$d^2GMF_{Horizontal}$	d^2GMF_{North}	d^2GMF_{East}	d^2GMF_{Up}
1	69.3	104	69.3	69.3	104	69.3
2	26	52	41.6	34.7	52	34.7
3	18.9	13	16	16	16	20.8
4	13.9	20.8	9.9	11.6	23.1	13
5	9.9	16	11.6	9.9	13.9	8.3

co-movements are detected from 1998 to 2003 and 2006–7 in several periods. Additionally, a long term coherence is detected within a period of 20–34 months between 1998 and 2017. Also, approximately the same pattern with a phase shift can be observed in the top right panel between FCN_Y rate and d^2GMF_{Fr}. The rate of cosine and sine amplitudes of FCN are investigated, and the results exhibit a significant association between the FCN_{As} rate and d^2GMF_{Fr} within the period of 32–64 months. The down, left figure indicates the coherence between the FCN_{Amp} rate and d^2GMF_{Fr}. Some episodic terms match with the GMJ epochs, which the FCN_{Amp} is leading during 1997–2003, and, after that, they are anti-phase with a period of 30 months. Also, the corresponded plot for the FCN_{Phase} rate and d^2GMF_{Fr} shows a statistically significant long-term coherency with a period of 20–32 months in which they are anti-phase until 2009, and, then, the FCN_{phase} is leading the GMF_{Fr}.

Figure 7.23 presents the coherence between the $d^2GMF_{Declination}$ and the FCN rate from 1997 to 2017. The FCN_X rate shows a clear relationship with d^2GMF_{Dec}/dt^2 in a period of 1–4 months. Also, some local co-movements are detected around 2000 and 2011. The FCN_{Ac} rate and $d^2GMF_{Declination}$ show a strong coherence over 1997–2017, where the FCN_{Ac} rate is leading $d^2GMF_{Declination}$ at a period of 30 months. In addition, there are some local co-movements between these two variables in 1999, 2003/4, 2007, and 2011. The association between the FCN_{Y_0} rate and $d^2GMF_{Declination}$ appears significant in the 16–30 periodic band during these times. However, they are anti-phase until 2009, and, then, the FCN_{Y_0} rate is leading the $d^2GMF_{Declination}$. The FCN_{Amp} rate shows a clear relationship with d^2GMF_{Dec}/dt^2 in a period of 34–64 months. Also, the FCN_{phase} rate shows a strong co-movement with d^2GMF_{Dec}/dt^2 in a period of 16–32 months, where d^2GMF_{Dec}/dt^2 is leading the FCN_{phase} until 2007, and, then, FCN_{phase} is leading the d^2GMF_{Dec}/dt^2.

Figure 7.24 displays the coherence between the d^2GMF_{North} and FCN_X rate. There is some periodic local coherence at the 4-month period that coincides with GMJ epochs. In addition, there are statistically significant correlations with the 32- and 64-month periods between d^2GMF_{North} and FCN_{As} rate. Also, a long term co-movement is detected at a period of 64 months between d^2GMF_{North} and FCN_{X_0} rate. The coherence analysis between d^2GMF_{North} and FCN_{Amp} rate illustrates at periods of 16–32 months. However, stronger coherence is more significant after 2007. Additionally, FCN_{Phase} and d^2GMF_{North} indicates very clear co-movement, and d^2GMF_{North} is leading FCN_{Phase}.

The coherence between the d^2GMF_{East} and FCN_X rate is displayed in Figure 7.25. There is a strong coherence with the period of 1–4 months. Moreover, some local co-movements can be seen around 2000, 2007, and 2010–2015 with a period of 8–16 months. Also, there is

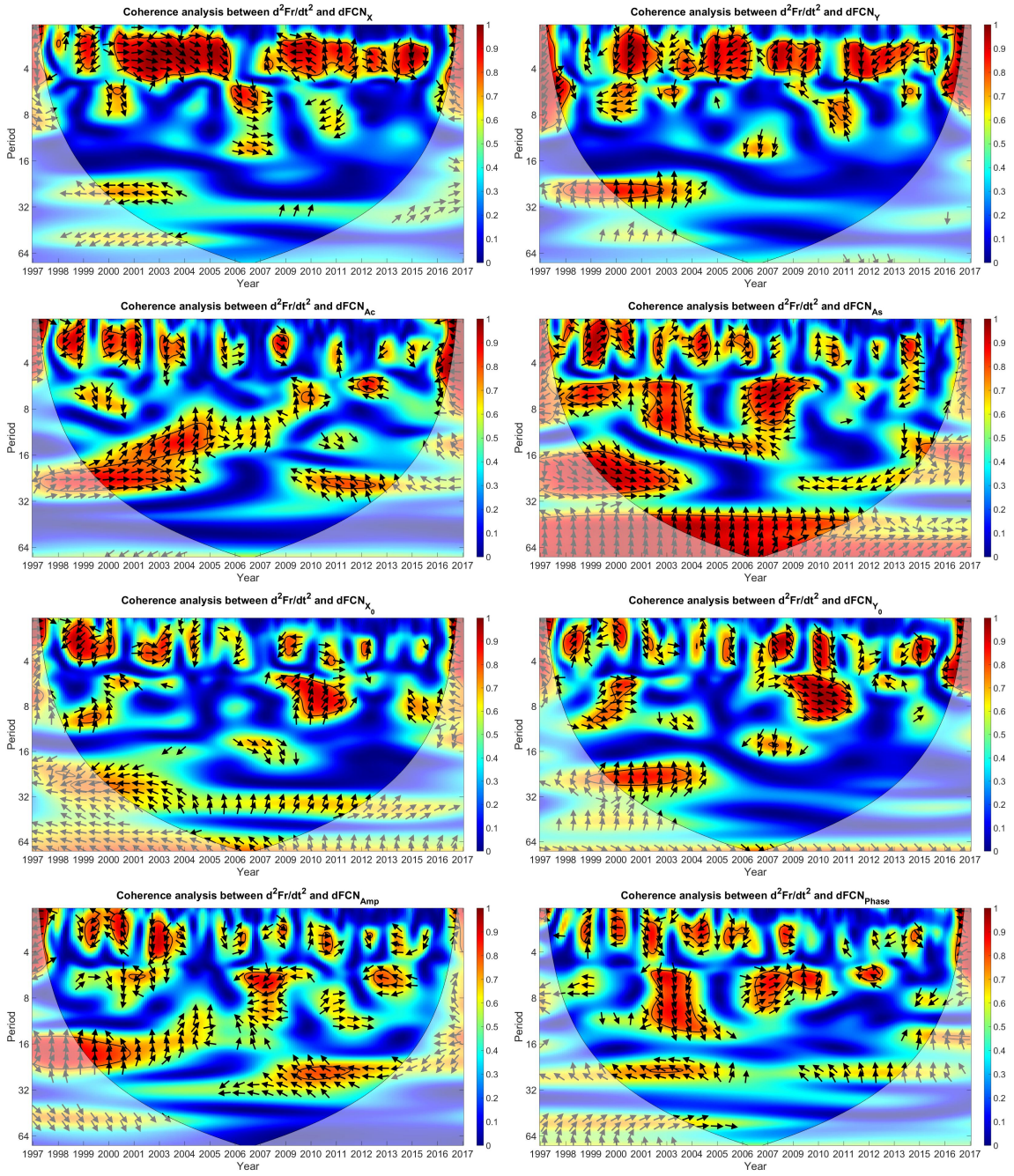

Figure 7.22: Wavelet coherence analysis between FCN products and d^2GMF_{Fr}/dt^2.

a statistically long-term significant association in period 20–34 months that the d^2GMF_{East} is leading the FCN_X rate. The coherence analysis results between d^2GMF_{East} and FCN_{Ac} rate show the local co-movements in the same epochs of GMJ with the period of 6–12 months. Besides a significant correlation with 16–32 months from 1997–2017, there is a clear coherence between d^2GMF_{East} and FCN_{Y_0} with the period of 16–32 where they are anti-phase until 2007, and then the FCN_{Y_0} rate is leading the d^2GMF_{East}. The rate of FCN_{Phase} shows a strong periodic relationship with the second derivative of GMF_{East} in 5-9 months. There is a statistically notable long-term relationship in lower frequency between d^2GMF_{East} and FCN_{Amp} rate during the period. Figure 7.26 presents the coherence between the d^2GMF_{Up} and FCN_X rate (top left), which show a periodic local relationship with d^2GMF_{Up}/dt^2 in a

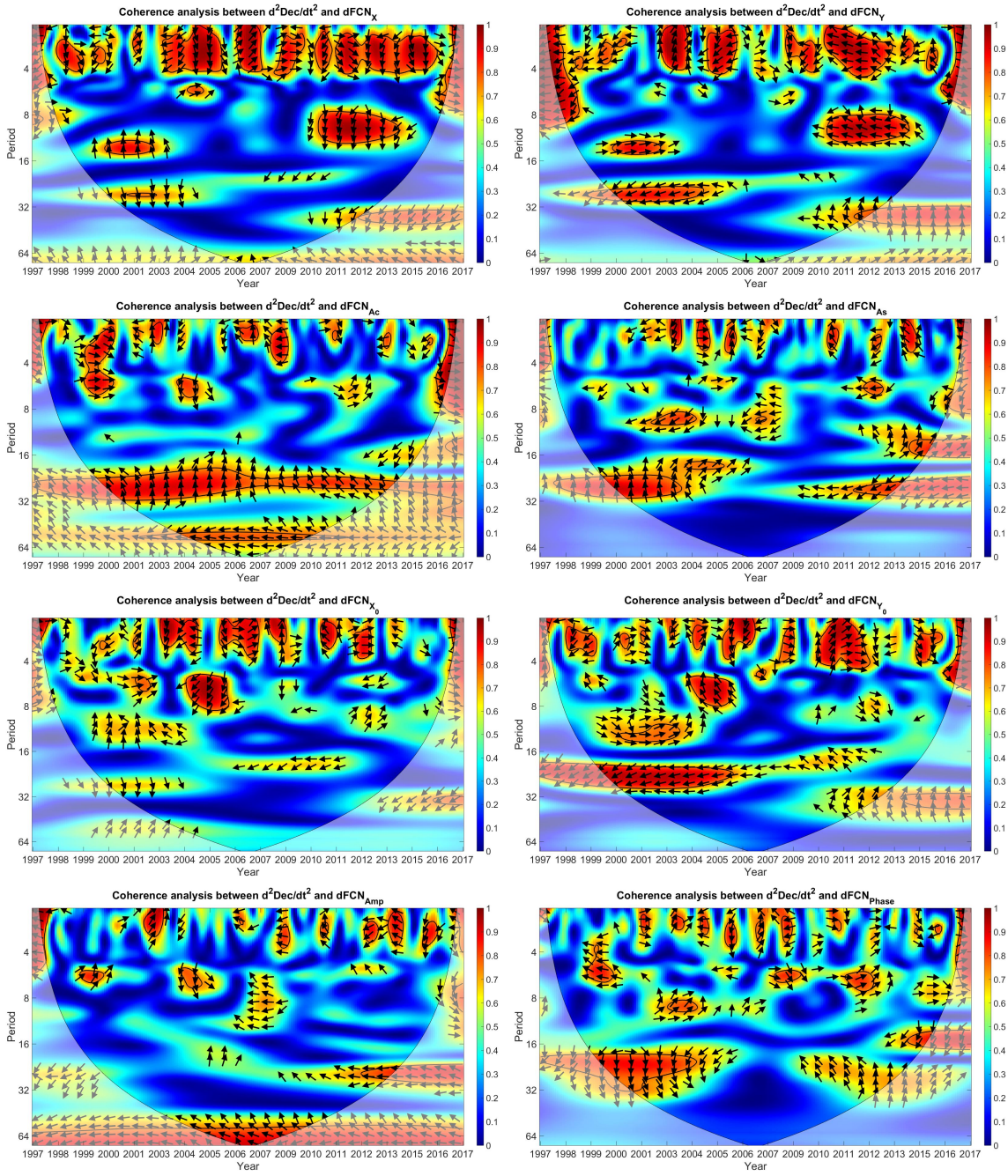

Figure 7.23: Wavelet coherence analysis between FCN products and d^2GMF_{Dec}/dt^2.

period of 1–4 months. Also, some local co-movements are detected around 2001/3, 2007, and 2011 in 8–16 months. The FCN_{As} rate and d^2GMF_{Up} show a strong correspondence from 1997 to 2017, which FCN_{As} rate is leading d^2GMF_{Up} for a period of 30–64 months. In addition, there are some local co-movement among these two variables in 1999—2003, 2007, and 2011. The association between the FCN_{X_0} rate and d^2GMF_{Up} indicates a significant agreement in the 5—14 months periodic band in 1998–2011 where FCN_{X_0} is leading d^2GMF_{Up}. In addition, a long, weak correlation is shown with a period of 32 months. The lower plots present the coherence between the rate of FCN_{Amp} and FCN_{Phase} in left and right, respectively. There is a significant long-term dynamic coherence between FCN_{Amp} and d^2GMF_{Up}, with its period decreasing from 23 months to 20 months during the time interval. Also, the local relationship

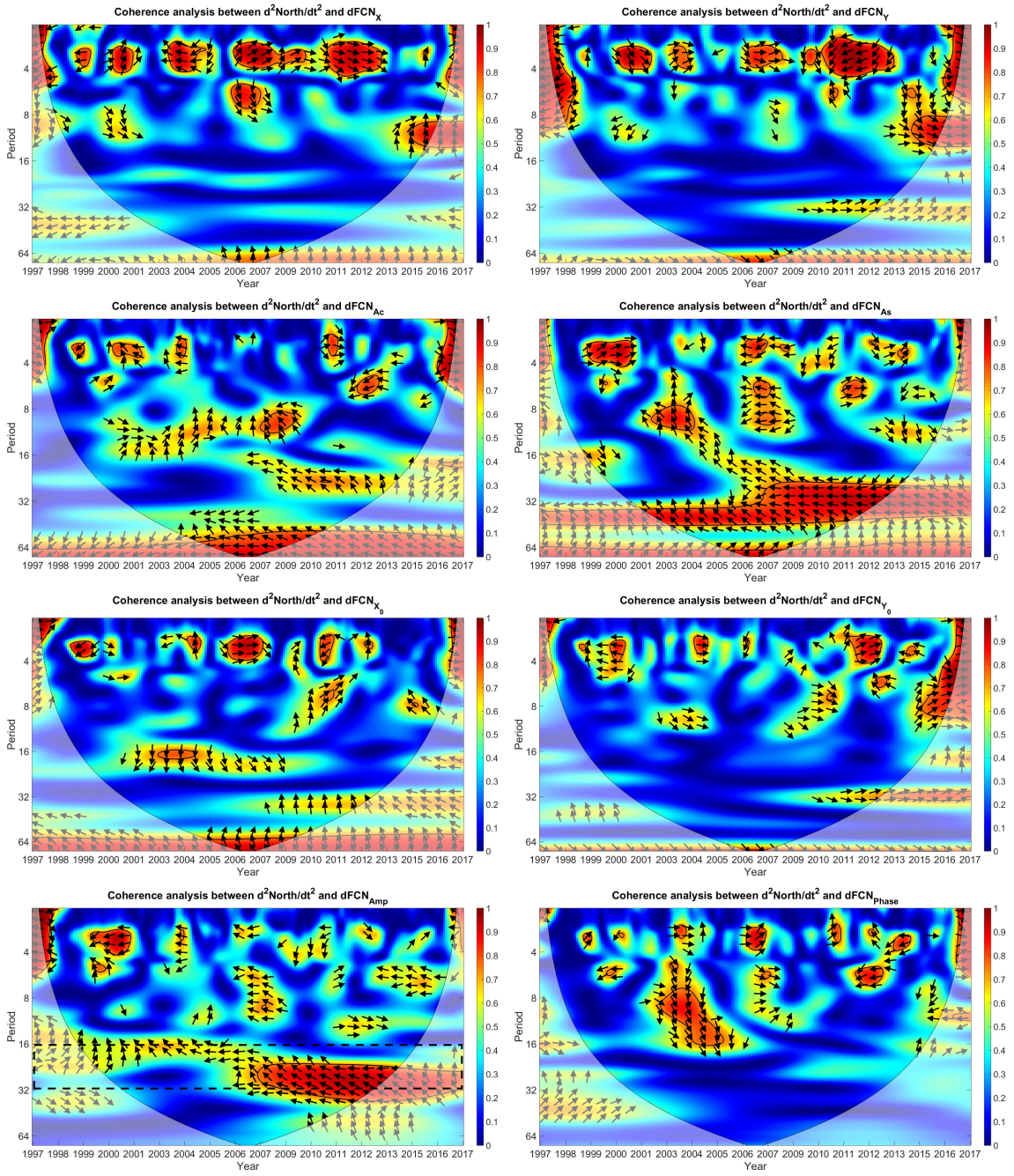

Figure 7.24: Wavelet coherence analysis between FCN products and d^2GMF_{North}/dt^2.

with a different period of 8 to 16 months could be found around 2003, 2007, and 2015. It is an obvious long-term coherence with a period of 16–32 months between FCN_{Phase} and d^2GMF_{Up}.

Figure 7.27 illustrates the coherence between the $d^2GMF_{Horizontal}$ and the FCN rate. There are some episodic terms in a period of 1–4 months and a weak coherence with a period of 32 months in the FCN_X rate. There is a clear coherence between $d^2GMF_{Horizontal}$ and the FCN_{As} rate throughout the studied time with 32–64 months. Besides, some local co-movement can be seen which co-occur with GMJ epochs. There is a clear notable extended-term coherence between $d^2GMF_{Horizontal}$ and the FCN_{As} rate with a period of 32 months, and it becomes more effective after 2007. It is also similar for the result of $d^2GMF_{Horizontal}$ and the FCN_{Amp}

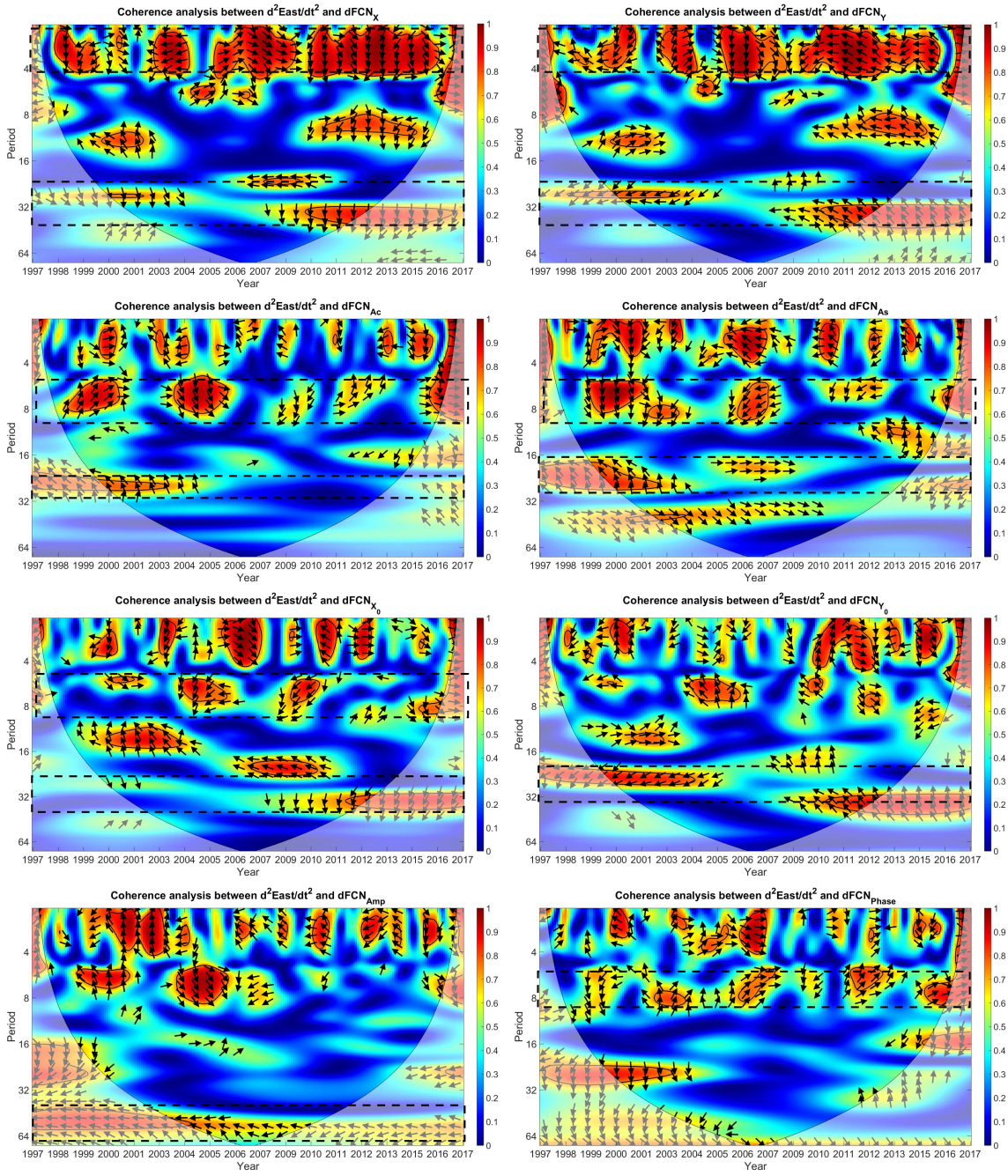

Figure 7.25: Wavelet coherence analysis between FCN products and d^2GMF_{East}/dt^2.

rate with a period of 16–32 months. Moreover, some episodic terms are distinguished, which co-occurred with GMJ.

7.5 Discussion

The CPO describes the movements of Earth's rotation axis concerning the theoretically predicted motions in the celestial reference frames. The variations of the CPO are caused by many meteorological and geophysical phenomena, which include the geomagnetic field (GMF) mutations. During the last decade, several studies have been done to discuss a potential

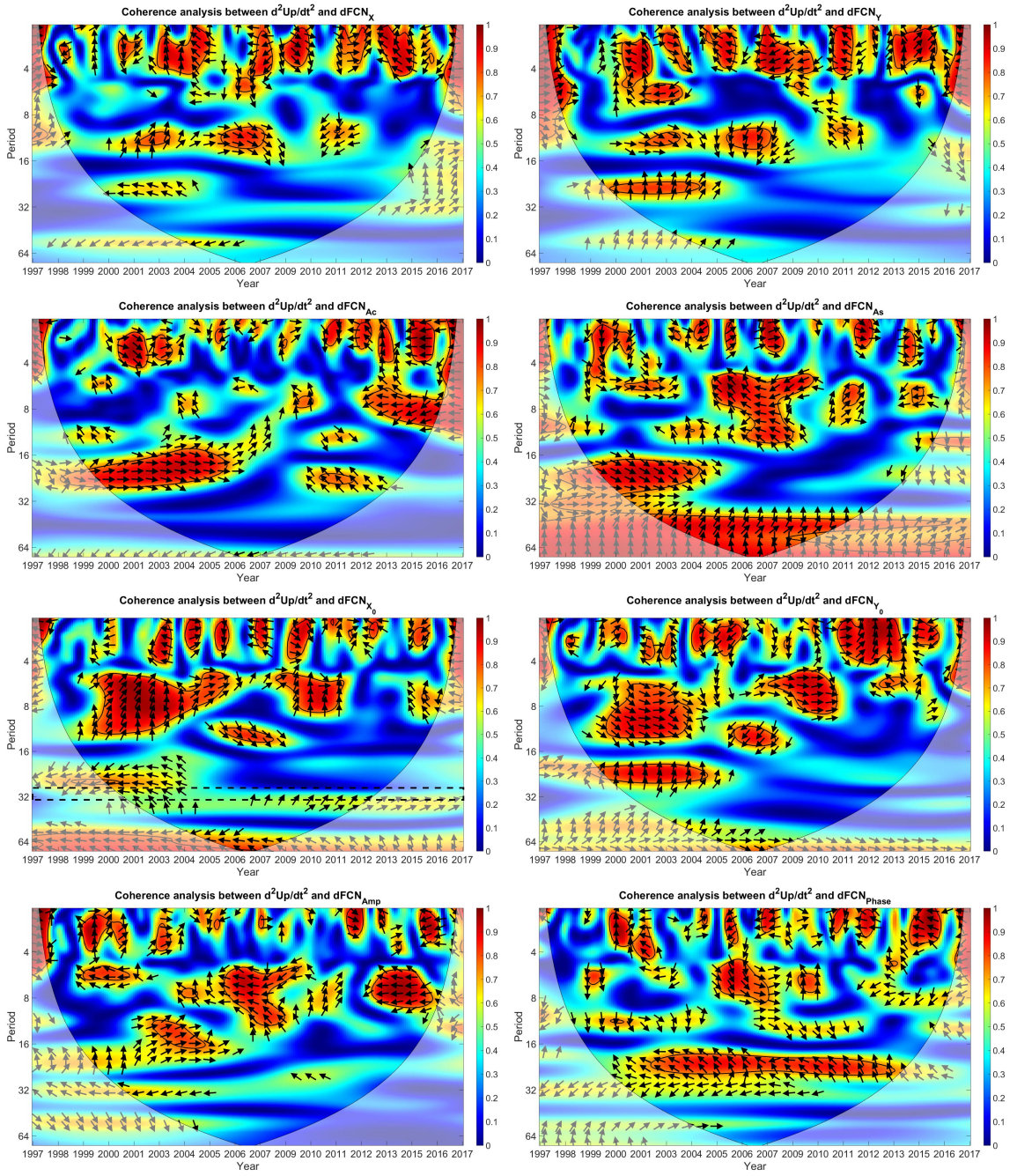

Figure 7.26: Wavelet coherence analysis between FCN products and d^2GMF_{Up}/dt^2.

interconnection of GMF changes with the polar motion. Nevertheless, less attention has been paid to the impact of the GMF changes, such as the geomagnetic jerks, which are rapid changes in GMF secular variations, and other GMF variations on the CPO variations. In this study, I use the CPO time-series obtained from VLBI observations and the latest GMF data to explore the association between CPO and the GMF. The Free Core Nutation (FCN) is a free mode of the Earth's rotation caused by the different material characteristics of the Earth's core and mantle. This causes the rotational axes of those layers to slightly diverge from each other, resulting in a wobble of the Earth's rotational axis comparable to nutations. The FCN period mainly depends on the inertia coupling and the dissipative coupling (such as viscous, electromagnetic, and topographic couplings) at the core-mantle boundary, according to the

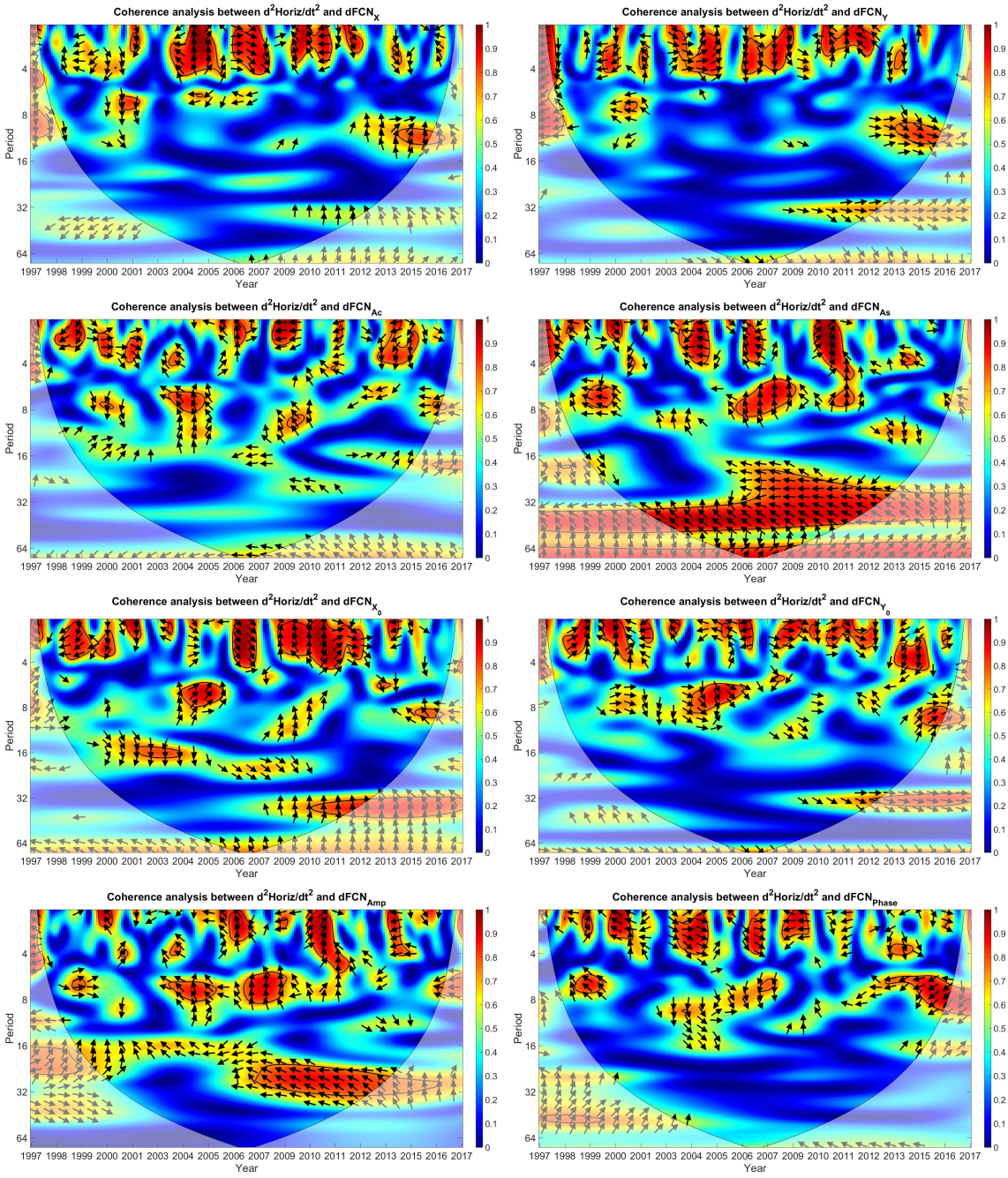

Figure 7.27: Wavelet coherence analysis between FCN products and d^2GMF_{Horiz}/dt^2.

theory of Earth rotation. Whatever the GMJ mechanism, it is most likely to affect the FCN by changing the core-mantle coupling. Also, if the GMJ mechanism is related to torsional oscillation or slow magneto-Coriolis waves, its correlation with the FCN is highly likely to originate from electromagnetic coupling, which means they have a direct relation. In this chapter, the time series of the FCN amplitude and phase and their rate are investigated to confirm the connection between the FCN variation and GMJ. The substantial FCN amplitude and phase disturbance occurred at the epochs close to the revealed GMJ events (see Figure 7.6 and 7.7). Also, as the FCN prediction method (B16) is based on past data, some errors might be visible around the GMJ epochs. Figure 7.8 argues for the direct connection between the timing of GMJ and the features of FCN prediction errors. The results show that the jerk-like

features in the FCN prediction errors can be observed with global GMJ events, not local GMJ events. The correlation analysis between the SHC rate and FCN rate provides meaningful information and shows a linear correlation, especially with the amplitude of the sin and cosine part of the FCN rate (see Figure 7.12). The amplitude and phase of FCN rate and SHC show a clear co-movement (see Figure 7.14, 7.15). Figure 7.18 confirms a clear correlation between the DM rate and the FCN rate. Figure 7.22 to 7.27 show the coherence analysis between the FCN rate and the second derivative of GMF, which, as indicated in our investigation, confirms the results of previous research. In this study, there was no physical mechanism for how GMF can influence CPO. Nevertheless, our preliminary results revealed some interesting common features in the FCN and GMF variation, which show the potential to improve the understanding of the GMF's contribution to the Earth's rotation.

8

Conclusions and Remarks

Real-time EOP is highly demanding for various geophysics and meteorology approaches, including precise tracking and navigation of satellites and spacecraft, weather modeling, and disaster prevention. Among the space geodetic sensors, DORIS, laser ranging (LLR and SLR), GNSS, and VLBI are the main active mission concepts that can observe and monitor the EOP. However, real-time estimation of EOP is not possible due to several limitations and the complexity of the measurement model and data processing.
Several attempts have been made to predict the EOP; however, the accuracy of EOP prediction is still unsatisfactory even within a few days. Therefore, advanced methods for modeling and predicting EOP should be further investigated. Also, knowledge of the interconnection between different processes that contribute to the Earth's rotation excitation is required to modify the current methods.
The main objectives of this study can be divided into three parts:

- Investigate consistency between the rotation theory of the Earth and space geodetic sensor observations.
  - Can the current rotation theories of the Earth adequately describe the motion of the Earth in space?
  - How could space geodetic technique observations improve the current rotation theories of the Earth?
- Introduce a new algorithm for EOP prediction and capturing the dependence structures between EOP and their excitation functions.
  - How could EOP prediction bring us closer to the GGOS's goals?
  - How could the Copula + SSA method improve the accuracy of EOP prediction?
  - How could the EOP prediction approach benefit from the understanding of the interconnections between EOP data and excitation functions, such as EAM?
- Investigate the interconnection between the EOP and effective processes that contribute to the Earth's rotational variation.

- How could it be possible to describe the relationship between the GMF and CPM?
- How could CPM prediction take advantage of understanding the interrelationship between the CPM and GMF?

The consistency between the current Earth rotation and the rotation axis from the space geodesy technique observation is investigated in Chapter 5. The Earth rotation theories are mostly defined based on the PAI, which considers geophysical processes that can help us better understand Earth's rotation. The origin of PAI is Earth's COM observed by using space geodetic approaches. The COM is determined by the first-degree Stokes coefficients of the geopotential that can be derived from space gravity missions (GRACE and GRACE Follow-on) and the SLR solution with a monthly and weekly temporal resolution, respectively. In Chapter 5, the evolution of the Earth's inertia axes is determined, and the investigation is conducted by taking advantage of previous analytical derivations to simplify the computations and estimations of the solutions by Ferrandiz and Barkin, 2006. The motion of the Earth's PAI using data set give time-varying, second-degree Stokes coefficients that are derived from SLR and the GRACE mission. Overall, the results from the two-time series illustrate that the Earth's PAI does not move around some mean position fixed to a given TRF in the studied period. However, Earth's PAI is exhibiting hitherto-unknown, non-negligible drifts with magnitudes that exceed the GGOS goals of delivering a TRF at an accuracy level of 1 mm and stability of 0.01 mm/yr. The results shown in Chapter 5 are limited to quantifying observational facts. The physical causes of the drift of the Earth's principal axes are still unknown, raising many questions for researchers, and the most critical questions can be summarized as:

- whether these variations of the Earth's inertia tensor might affect other Earth processes?
- Which are the causes of the observed variation of the inertia tensor?
- Can the geophysical budget be closed to some extent?
- Which are the effects on the EOP variations and the theoretical formulations?
- Can we extract more information from the time series, like a change of trends?

Two joint working groups on prediction (JWG-P) and Theory of Earth rotation and validation (JWG-ThER) of IAU commission A2, IAG, and IERS confirmed the fact of importance of the Earth rotation prediction. According to the United Nations (UN) resolution in 2015, the primary intention of these JWGs is to evaluate and ensure the level of consistency of EOP predictions derived from theories with the corresponding EOP determined from analyses of space geodetic sensor observations. Therefore, accurate EOP predictions are required to prevent any systematic drifts and biases between the ICRF and ITRF. Among the EOP parameters, ERPs (polar motion, dUT1, and its first derivative) are the most difficult to predict due to the occurrence of many geophysical processes in ERP, e.g., tides, non-tidal atmospheric and oceanic processes. Therefore, I focus mainly on the high accuracy of ERP predictions in Chapter 6.
Several methodologies have been adopted to predict EOP, but the EOP PCC evaluates the participating method, and the results indicate that there is no particular forecasting method

superior to the other techniques. Therefore, new prediction methods should be developed to provide more accurate EOP predictions. The main focus of Chapter 6 is to introduce a new algorithm that can capture all deterministic and stochastic information within the EOP time series. Chapter 6 pertains to the introduction of the new method for the first time in geodesy. Our novel technique, Copula + SSA, is a hybrid method. It can be categorized as a machine learning approach that is mainly designed for EOP prediction, but which can also be used for predicting other geophysical variables. The method consists of two parts, deterministic and stochastic, which can capture all information within the EOP time series and the dependence structure between the EOP and other geophysical parameters. Our hybrid approach can be employed for two cases: the first is the algorithm that uses the information within a time series; the second is the algorithm aimed at utilizing some variables to forecast the EOP, due to the existing relationship between them.
The results illustrate that our hybrid method could efficiently and precisely predict the EOP. In this thesis, I introduce several approaches based on different Archimedean Copulas, which were applied to the bivariate frequency analysis. The use of Copulas is promising since it allows us to take into account a wide range of correlations, which is frequently observed in time series.

- **Concerning the PM prediction**, it is demonstrated that the Copula + SSA algorithm shows better performance for PM_x prediction, compared with the SSA prediction. The Copula-based analysis is entirely successful in its intention to increase PM prediction accuracy by modeling the stochastic part of the PM and subtracting PM by the SSA-reconstructed time series. I suspect the main error contributions derive from the SSA extrapolation part. Consequently, further investigations about the SSA training time will be required to explain this issue. These infrequent errors should be investigated to have a remarkable progression in the PM prediction.

- **Concerning the LOD prediction**, the employment of the EAM data is investigated to predict LOD data due to the existing relationship between them. Compared with the results of other methods, the copula + SSA can efficiently and precisely predict the LOD parameter at ultra-short-term. All of our methods presented in this study provide comparable error with the existing techniques used for their evaluation in the time interval considered of up to 10 days. Moreover, it is demonstrated that the predicted EAM time series as additional information can improve the LOD prediction. As long as the data are still available for post-processing, new methods can adequately be compared in a consistent way to the methods applied in the past.

The third objective of this study aims to study the physical relationship between the EOP and other geophysical parameters, e.g., the correlation between the irregularities of the celestial pole motion (CPM) and GMF. Several investigations have been done to examine the potential interconnection of GMF variations with the polar motion. However, less attention has been paid to the impact of the GMF changes, such as the GMJ, which are rapid changes in GMF secular variations and other GMF variations on the CPM variations. In this study, the association between FCN and GMJ, magnetic dipole moment, and GMF models is investigated to explore the dependency structure between the CPM and GMF.

- **FCN and GMJ**: The study of FCN's amplitude and phase and the rate of changes verify the association between the FCN variation and GMJ as the substantial disturbance within the FCN time series that occurred at the epochs close to the revealed GMJ events. Moreover, the GMJ events, which are on a global scale, propagate themselves in FCN prediction errors. However, the local GMJ epochs cannot be detected over FCN prediction errors. Accordingly, our investigations confirm the results of previous research, which showed agreement between the FCN and GMJ.

- **FCN and geomagnetic dipole moment**: The results indicate a significant association between the DM and FCN, which can be a potential external parameter to improve the FCN prediction model by considering DM information. WCA detects the coherence between the offset of FCN rate and DM rate at 30 months (approximately 1024 days), as well as statistically significant local coherency around 1999, 2003, and 2007 within a period of four months when GMJ happened.

- **FCN and GMF models**: The lower degree of SHC describes the core activity, and our investigation proves the mentioned fact. Therefore, the lower SHCs are investigated because of their direct relationship with the Earth's core activity. The coherence analysis between the $FCNAmp$ rate and SHC rate indicates statistically significant long term coherence with a period of 3–5, 18–24, and 36 months over the whole interval of time. The coherence analysis between $FCNY_0$ rate and SHC rate shows significant long-term association with a period of 30 months in 1997–2005. Also, several local co-movements are detected with a period of 2 to 6 months. In the near-Earth magnetic field, the d^2GMF_{East}/dt^2 show a different dynamic behavior compared to GMF_{Fr} or GMF_{total}. The first dominated signal of d^2GMF_{Fr}/dt^2, $d^2GMF_{Horizontal}/dt^2$, d^2GMF_{North}/dt^2, and d^2GMF_{Up}/dt^2 is 69.3 months, and it is 104 months for $d^2GMF_{Declination}/dt^2$ and d^2GMF_{East}/dt^2. The FFT results indicate 52, 34, 20, and 16 months as the dominant signals, which they have in common with the FCN product's signals. The results of wavelet coherence analysis mostly indicate a statistically significant long-term co-movement period of around 30 months between 1998 and 2017. Also, some significant local co-movements are detected, which co-occur with GMJ epochs in 1999, 2003, 2007, and 2011.

Although both CPM and GMF depend on the processes in the fluid core and the core-mantle boundary, there was no physical mechanism identified to explain how GMF can influence CPO. Nevertheless, our results revealed some common features in the FCN and GMF variation, which show the potential to improve knowledge regarding the GMF's contribution to the Earth's rotation. The shown results are consistent with the conclusion of Gibert et al. (1998) who found that the rapid changes in the Chandler Wobble follow the GMJ with a delay of 1 to 3 years. Also, the WCA of the GMF's elements and FCN identify the coherency of around 30 months (approximately 1034 days), which confirms the conclusion of the Belda et al. (2017b). They pointed out that the most consistent VLBI data regarding ICRF 2 revealed two clear dominated retrograde signals at about 1034 and 2069 days. They also suggested that the periodic signal near 1034 days in FCN offsets could be caused by the GMF variation and its sudden changes.

Understanding the geophysical phenomena that excite the FCN could effectively improve the CPO predictions as the current methods are not designed to consider the geophysical effects. The primary purpose of studying the connection between the CPM and GMF is to improve the CPM prediction, as the understanding of CPM excitation could bring us significantly closer to meeting the accuracy goals pursued by the GGOS of the IAG.

References

Abbondanza, C, T. M Chin, R Gross, M Heflin, J Parker, B Soja, T van Dam, and X Wu (2017). "JTRF2014, the JPL Kalman filter and smoother realization of the International Terrestrial Reference System". In: *Journal of Geophysical Research: Solid Earth* 122.10, pp. 8474–8510.

Abshire, J and C Gardner (1985). "Atmospheric refractivity corrections in satellite laser ranging". In: *IEEE Transactions on geoscience and remote sensing* 4, pp. 414–425.

Akin, M (2002). "Comparison of wavelet transform and FFT methods in the analysis of EEG signals". In: *Journal of medical systems* 26.3, pp. 241–247.

Akulenko, L, S Kumakshev, Y Markov, and L Rykhlova (2002). "Forecasting the polar motions of the deformable Earth". In: *Astronomy Reports* 46.10, pp. 858–865.

Akyilmaz, O and H Kutterer (2004). "Prediction of Earth rotation parameters by fuzzy inference systems". In: *Journal of Geodesy* 78.1-2, pp. 82–93.

Akyilmaz, O, H Kutterer, C Shum, and T Ayan (2011). "Fuzzy-wavelet based prediction of Earth rotation parameters". In: *Applied Soft Computing* 11.1, pp. 837–841.

Altamimi, Z and C Boucher (2001). "The ITRS and ETRS89 relationship: new results from ITRF2000". In: *Report on the Symposium of the IAG Subcommission for Europe (EUREF), Dubrovnik*.

Altamimi, Z, P Rebischung, L Métivier, and X Collilieux (2016). "ITRF2014: A new release of the International Terrestrial Reference Frame modeling nonlinear station motions". In: *Journal of Geophysical Research: Solid Earth* 121.8, pp. 6109–6131.

Altamimi, Z, P Sillard, and C Boucher (2002). "ITRF2000: A new release of the International Terrestrial Reference Frame for earth science applications". In: *Journal of Geophysical Research: Solid Earth* 107.B10, ETG–2.

Angermann, D, M Seitz, and H Drewes (2010). "Analysis of the DORIS contributions to ITRF2008". In: *Advances in space research* 46.12, pp. 1633–1647.

Arias, E, P Charlot, M Feissel, and J Lestrade (1995). "The extragalactic reference system of the International Earth Rotation Service, ICRS." In: *Astronomy and Astrophysics* 303, pp. 604–608.

Auriol, A and C Tourain (2010). "DORIS system: the new age". In: *Advances in space research* 46.12, pp. 1484–1496.

Awange, J (2012). *Environmental monitoring using GNSS: Global navigation satellite systems*. Springer Science & Business Media.

Baldassarre, G, A Viglione, G Carr, L Kuil, J Salinas, and G Blöschl (2013). "Socio-hydrology: conceptualising human-flood interactions". In: *Hydrology and Earth System Sciences* 17.8, pp. 3295–3303.

Bali, T (2003). "The generalized extreme value distribution". In: *Economics letters* 79.3, pp. 423–427.

Bárdossy, A (2006). "Copula-based geostatistical models for groundwater quality parameters". In: *Water Resources Research* 42.11.

Bárdossy, A and J Li (2008). "Geostatistical interpolation using copulas". In: *Water Resources Research* 44.7.

Bárdossy, A and G Pegram (2009). "Copula based multisite model for daily precipitation simulation". In: *Hydrology and Earth System Sciences* 13.12, p. 2299.

Barker, E, O Calame, J Mulholland, and P Shelus (1975). "Improved coordinates for Lunokhod 2 based on laser observations from McDonald Observatory." In: *Proc of Open Meet of Work Group on Phys Sci of the Plenary Meet of COSPAR (Comm on Space Res), 17th, Space Res 15*.

Barkin, Y and JM Ferrándiz (2000). "The motion of the Earth's principal axes of inertia, caused by tidal and rotational deformations". In: *Astronomical and Astrophysical Transactions* 18.4, pp. 605–620.

Barnes, R, R Hide, A White, and C Wilson (1983). "Atmospheric angular momentum fluctuations, length-of-day changes and polar motion". In: *Proceedings of the Royal Society of London. A. Mathematical and Physical Sciences* 387.1792, pp. 31–73.

Belda, S, J. M Ferrándiz, R Heinkelmann, T Nilsson, and H Schuh (2016). "Testing a new free core nutation empirical model". In: *Journal of Geodynamics* 94, pp. 59–67.

Belda, S, J. M Ferrándiz, R Heinkelmann, and H Schuh (2018). "A new method to improve the prediction of the celestial pole offsets". In: *Scientific reports* 8.1, pp. 1–10.

Belda, S, R Heinkelmann, J. M Ferrándiz, M Karbon, T Nilsson, and H Schuh (2017a). "An Improved Empirical Harmonic Model of the Celestial Intermediate Pole Offsets from a Global VLBI Solution". In: *The Astronomical Journal* 154.4, p. 166.

Belda, S, R Heinkelmann, J. M Ferrándiz, T Nilsson, and H Schuh (2017b). "On the consistency of the current conventional EOP series and the celestial and terrestrial reference frames". In: *Journal of Geodesy* 91.2, pp. 135–149.

Bellanger, E, D Gibert, and J Le Mouël (2002). "A geomagnetic triggering of Chandler wobble phase jumps?" In: *Geophysical research letters* 29.7, pp. 28–1.

Bender, P, D Currie, S Poultney, C Alley, R Dicke, D Wilkinson, D Eckhardt, J Faller, W Kaula, J Mulholland, et al. (1973). "The Lunar Laser Ranging Experiment: Accurate ranges have given a large improvement in the lunar orbit and new selenophysical information". In: *Science* 182.4109, pp. 229–238.

Bentley, P and J McDonnell (1994). "Wavelet transforms: an introduction". In: *Electronics & communication engineering journal* 6.4, pp. 175–186.

Bernardin, L, P Chin, P DeMarco, K Geddes, D Hare, K Heal, G Labahn, J May, J McCarron, M Monagan, et al. (2011). *Maple programming guide*. Citeseer.

Bishop, C (2006). *Pattern recognition and machine learning*. springer.

Bloßfeld, M, D Angermann, and M Seitz (2018a). "DGFI-TUM analysis and scale investigations of the latest Terrestrial Reference Frame Realizations". In: *International Symposium on Advancing Geodesy in a Changing World*. Springer, pp. 3–9.

Bloßfeld, M, H Müller, M Gerstl, V Štefka, J Bouman, F Göttl, and M Horwath (2015). "Second-degree Stokes coefficients from multi-satellite SLR". In: *Journal of Geodesy* 89.9, pp. 857–871.

Bloßfeld, M, S Rudenko, A Kehm, N Panafidina, H Müller, D Angermann, U Hugentobler, and M Seitz (2018b). "Consistent estimation of geodetic parameters from SLR satellite constellation measurements". In: *Journal of Geodesy* 92.9, pp. 1003–1021.

Böckmann, S, T Artz, and A Nothnagel (2010). "VLBI terrestrial reference frame contributions to ITRF2008". In: *Journal of Geodesy* 84.3, pp. 201–219.

Böhm, J and H Schuh (2007). "Troposphere gradients from the ECMWF in VLBI analysis". In: *Journal of Geodesy* 81.6-8, pp. 403–408.

Bois, E and D Vokrouhlicky (1995). "Relativistic spin effects in the Earth-Moon system." In: *Astronomy and Astrophysics* 300, p. 559.

Boucher, C, Z Altamimi, and P Sillard (1999). "The International Terrestrial Reference Frame (ITRF97)." In: *ITN* 27, pp. 1–191.

Bozdogan, H (1987). "Model selection and Akaike's information criterion (AIC): The general theory and its analytical extensions". In: *Psychometrika* 52.3, pp. 345–370.

Broomhead, D and G King (1986). "Extracting qualitative dynamics from experimental data". In: *Physica D: Nonlinear Phenomena* 20.2-3, pp. 217–236.

Brzeziński, A (2000). "The CEP and geophysical interpretation of modern Earth rotation observations". In: *International Astronomical Union Colloquium*. Vol. 178. Cambridge University Press, pp. 585–594.

Brzeziński, A (2005). "Chandler wobble and free core nutation: observation, modeling and geophysical interpretation". In: *Artificial Satellites* 40, pp. 21–33.

Buffett, B (1993). "Influence of a toroidal magnetic field on the nutations of Earth". In: *Journal of Geophysical Research: Solid Earth* 98.B2, pp. 2105–2117.

Cai, C, Y Gao, et al. (2007). "Precise point positioning using combined GPS and GLONASS observations". In: *Positioning* 1.11.

Cannon, W (1999). "Overview of VLBI". In: *International VLBI Service for Geodesy and Astrometry*, pp. 13–17.

Capitaine, N (2002). "Comparison of "old" and "new" concepts: the celestial intermediate pole and Earth orientation parameters". In: *Proceedings of the IERS Workshop on the Implementation of the New IAU Resolutions, IERS Technical Note*. Vol. 29, pp. 35–44.

Capitaine, N (2007). "Definition and realization of the celestial intermediate reference system". In: *Proceedings of the International Astronomical Union* 3.248, pp. 367–373.

Capitaine, N, P Wallace, and J Chapront (2003). "Expressions for IAU 2000 precession quantities". In: *Astronomy & Astrophysics* 412.2, pp. 567–586.

Capitaine, N, P Wallace, and J Chapront (2005). "Improvement of the IAU 2000 precession model". In: *Astronomy & Astrophysics* 432.1, pp. 355–367.

Chakraborty, A and D Okaya (1995). "Frequency-time decomposition of seismic data using wavelet-based methods". In: *Geophysics* 60.6, pp. 1906–1916.

Chao, B, D Dong, H Liu, and T Herring (1991). "Libration in the Earth's rotation". In: *Geophysical research letters* 18.11, pp. 2007–2010.

Chao, B and R Eanes (1995). "Global gravitational changes due to atmospheric mass redistribution as observed by the LAGEOS nodal residual". In: *Geophysical Journal International* 122.3, pp. 755–764.

Chapront, J, M Chapront-Touzé, and G Francou (2000). "Contribution of LLR to the reference systems and precession". In: *Journées Systèmes de Référence*, pp. 96–101.

Charlot, P, CS Jacobs, D Gordon, Sébastien Lambert, A de Witt, J Böhm, AL Fey, R Heinkelmann, E Skurikhina, O Titov, et al. (2020). "The third realization of the International Celestial Reference Frame by very long baseline interferometry". In: *Astronomy & Astrophysics* 644, A159.

Chen, J, C Wilson, R Eanes, and B Tapley (2000). "A new assessment of long-wavelength gravitational variations". In: *Journal of Geophysical Research: Solid Earth* 105.B7, pp. 16271–16277.

Chen, J, C Wilson, B Tapley, and J Ries (2004). "Low degree gravitational changes from GRACE: validation and interpretation". In: *Geophysical Research Letters* 31.22.

Chen, W, J Luo, J Ray, N Yu, and J Li (2019). "Multiple-data-based monthly geopotential model set LDCmgm90". In: *Scientific data* 6.1, pp. 1–9.

Chen, W and W Shen (2010). "New estimates of the inertia tensor and rotation of the triaxial nonrigid Earth". In: *Journal of Geophysical Research: Solid Earth* 115.B12.

Cheng, M, J Ries, and B Tapley (2011). "Variations of the Earth's figure axis from satellite laser ranging and GRACE". In: *Journal of Geophysical Research: Solid Earth* 116.B1.

Cheng, M, J Ries, and B Tapley (2013a). "Geocenter variations from analysis of SLR data". In: *Reference frames for applications in geosciences*. Springer, pp. 19–25.

Cheng, M, B Tapley, and J Ries (2013b). "Deceleration in the Earth's oblateness". In: *Journal of Geophysical Research: Solid Earth* 118.2, pp. 740–747.

Cherubini, U, E Luciano, and W Vecchiato (2004). *Copula methods in finance*. John Wiley & Sons.

Christodoulidis, D, D Smith, R Kolenkiewicz, S Klosko, M Torrence, and P Dunn (1985). "Observing tectonic plate motions and deformations from satellite laser ranging". In: *Journal of Geophysical Research: Solid Earth* 90.B11, pp. 9249–9263.

Chulliat, A, P Alken, and S Maus (2015). "Fast equatorial waves propagating at the top of the Earth's core". In: *Geophysical Research Letters* 42.9, pp. 3321–3329.

Chulliat, A, E Thébault, and G Hulot (2010). "Core field acceleration pulse as a common cause of the 2003 and 2007 geomagnetic jerks". In: *Geophysical Research Letters* 37.7.

Ciufolini, I, A Paolozzi, E Pavlis, J Ries, R Koenig, R Matzner, G Sindoni, and H Neumayer (2009). "Towards a one percent measurement of frame dragging by spin with satellite laser ranging to LAGEOS, LAGEOS 2 and LARES and GRACE gravity models". In: *Space Science Reviews* 148.1-4, pp. 71–104.

Clark, T, A Corey, J Davis, G Elgered, T Herring, H Hinteregger, C Knight, J Levine, G Lundqvist, M Chopo, et al. (1985). "Precision geodesy using the Mark-III very-long-baseline interferometer system". In: *IEEE transactions on geoscience and remote sensing* 4, pp. 438–449.

Clayton, D (1978). "A model for association in bivariate life tables and its application in epidemioligical studies of familial tendency in chronic disease incidence". In: *Biometrija* 65, pp. 141–151.

Cohen, L (1995). *Time-frequency analysis*. Vol. 778. Prentice hall.

Coulot, D, A Pollet, X Collilieux, and P Berio (2010). "Global optimization of core station networks for space geodesy: application to the referencing of the SLR EOP with respect to ITRF". In: *Journal of Geodesy* 84.1, p. 31.

Cui, X, H Sun, J Xu, J Zhou, and X Chen (2018). "Influence of core-mantle coupling on the excitation of free core nutation". In: *CHINESE JOURNAL OF GEOPHYSICS-CHINESE EDITION* 61.9, pp. 3584–3591.

Dahle, C, M Murböck, F Flechtner, H Dobslaw, G Michalak, K. H Neumayer, O Abrykosov, A Reinhold, R König, R Sulzbach, et al. (2019). "The GFZ GRACE RL06 monthly gravity field time series: processing details and quality assessment". In: *Remote Sensing* 11.18, p. 2116.

Dahlen, F and J Tromp (1998). *Theoretical global seismology*. Princeton university press.

Degnan, J (1985). "Satellite laser ranging: current status and future prospects". In: *IEEE Transactions on Geoscience and Remote Sensing* 4, pp. 398–413.

Degnan, J (1993). "Millimeter accuracy satellite laser ranging: a review". In: *Contributions of space geodesy to geodynamics: technology* 25, pp. 133–162.

Dehant, V and P Mathews (2003). "Information about the core from Earth nutation". In: *Earth's Core: Dynamics, Structure, Rotation, Geodyn. Ser* 31, pp. 263–277.

Dehant, V and P Mathews (2015). *Precession, nutation and wobble of the Earth*. Cambridge University Press.

Dehant, V, C Wilson, D Salstein, B Chao, R Gross, C Provost, and R Ponte (1997). "Study of Earth's rotation and geophysical fluids progresses". In: *Eos, Transactions American Geophysical Union* 78.34, pp. 357–360.

Deheuvels, P (1979). "La fonction de dependence empirique et ses proprietes, Un test non parametrique d'independance". In: *Bulletin de la classe des sciences, Academie Royale de Belgique, 5e serie*.

Demirel, H and G Anbarjafari (2011). "Discrete wavelet transform-based satellite image resolution enhancement". In: *IEEE transactions on geoscience and remote sensing* 49.6, pp. 1997–2004.

Dick, Wolfgang R and Daniela Thaller (2020). "IERS Annual Report 2018". In: *IERS Annual Report 2018. Edited by Wolfgang R. Dick and Daniela Thaller. International Earth Rotation and Reference Systems Service*.

Dickey, J, X Newhall, and J Williams (1985). "Earth orientation from lunar laser ranging and an error analysis of polar motion services". In: *Journal of Geophysical Research: Solid Earth* 90.B11, pp. 9353–9362.

Dill, R and H Dobslaw (2018). "ESMGFZ: Operational Model Products for Geodetic Applications". In: *EGU General Assembly Conference Abstracts*. Vol. 20, p. 2772.

Dill, R, H Dobslaw, and M Thomas (2019). "Improved 90-day Earth orientation predictions from angular momentum forecasts of atmosphere, ocean, and terrestrial hydrosphere". In: *Journal of Geodesy* 93.3, pp. 287–295.

Dow, J, R Neilan, and C Rizos (2009). "The international GNSS service in a changing landscape of global navigation satellite systems". In: *Journal of geodesy* 83.3-4, pp. 191–198.

Dupuis, DJ (2007). "Using copulas in hydrology: Benefits, cautions, and issues". In: *Journal of Hydrologic Engineering* 12.4, pp. 381–393.

Eanes, R. J and S. V Bettadpur (1996). "Temporal variability of Earth's gravitational field from satellite laser ranging". In: *Global gravity field and its temporal variations*. Springer, pp. 30–41.

Embrechts, P, A McNeil, and D Straumann (2002). "Correlation and dependence in risk management: properties and pitfalls". In: *Risk management: value at risk and beyond* 176223.

Escapa, A and N Capitaine (2018). "A global set of adjustments to make the IAU 2000A nutation consistent with the IAU 2006 precession". In: *Proc. Journées*.

Escapa, A, J. M Ferrándiz, T Baenas, J Getino, J Navarro, and S Belda (2016). "Consistency Problems in the Improvement of the IAU Precession–Nutation Theories: Effects of the Dynamical Ellipticity Differences". In: *Pure and Applied Geophysics* 173.3, pp. 861–870.

Escapa, A, J Getino, J. M Ferrándiz, and T Baenas (2013). "On the changes of IAU 2000 nutation theory stemming from IAU 2006 precession theory". In: *Proceedings of the Journées*, pp. 148–151.

Escapa, A, J Getino, J. M Ferrándiz, and T Baenas (2017). "Dynamical adjustments in IAU 2000A nutation series arising from IAU 2006 precession". In: *Astronomy & Astrophysics* 604, A92.

Escarela, G and J. F Carriere (2003). "Fitting competing risks with an assumed Copula". In: *Statistical Methods in Medical Research* 12.4, pp. 333–349.

European Environment Agency (2019). *Economic losses from climate-related extremes in Europe (temporal coverage 1980- 2017)*.

Favre, A, S El Adlouni, L Perreault, N Thiémonge, and B Bobée (2004). "Multivariate hydrological frequency analysis using copulas". In: *Water resources research* 40.1.

Ferrándiz, J. M, D. Al Koudsi, A. Escapa, S Belda, S Modiri, R Heinkelmann, and H Schuh (2020a). "A First Assessment of the Corrections for the Consistency of the IAU2000 and IAU2006 Precession-Nutation Models". In: *International Association of Geodesy Symposia*.

Ferrandiz, J. M and Y Barkin (2006). "Nutations and precession of elastic Earth in angle-action variables". In: *Journées 2005-systèmes de référence spatio-temporels*. Citeseer.

Ferrándiz, J. M, S Modiri, S Belda, M Barkin, M Bloßfeld, R Heinkelmann, and H Schuh (2020b). "Drift of the Earth's Principal Axes of Inertia from GRACE and Satellite Laser Ranging Data". In: *Remote Sensing* 12.2, p. 314.

Ferrari, A, W Sinclair, W Sjogren, J Williams, and C Yoder (1980). "Geophysical parameters of the Earth-Moon system". In: *Journal of Geophysical Research: Solid Earth* 85.B7, pp. 3939–3951.

Finkelstein, A, V. J Kreinovich, and S Pandey (1983). "Relativistic reductions for radiointerferometric observables". In: *Astrophysics and space science* 94.2, pp. 233–247.

Finlay, C, N Olsen, S Kotsiaros, N Gillet, and L Tøffner-Clausen (2016). "Recent geomagnetic secular variation from Swarm and ground observatories as estimated in the CHAOS-6 geomagnetic field model". In: *Earth, Planets and Space* 68.1, p. 112.

Finlay, C, N Olsen, and L Tøffner-Clausen (2015). "DTU candidate field models for IGRF-12 and the CHAOS-5 geomagnetic field model". In: *Earth, Planets and Space* 67.1, p. 114.

Förste, C, F Flechtner, R Schmidt, R König, U Meyer, R Stubenvoll, M Rothacher, F Barthelmes, H Neumayer, R Biancale, et al. (2006). "Global mean gravity field models from combination of satellite mission and altimetry/gravimetry surface data". In: *Geophysical Research Abstracts*. Vol. 8, p. 03462.

Freedman, A, J Steppe, J Dickey, T Eubanks, and L Sung (1994). "The short-term prediction of universal time and length of day using atmospheric angular momentum". In: *Journal of Geophysical Research: Solid Earth* 99.B4, pp. 6981–6996.

Gambis, D (2004). "Monitoring Earth orientation using space-geodetic techniques: state-of-the-art and prospective". In: *Journal of Geodesy* 78.4-5, pp. 295–303.

Gambis, D and B Luzum (2011). "Earth rotation monitoring, UT1 determination and prediction". In: *Metrologia* 48.4, S165.

Ganeshan, A, S Rathnakara, R Gupta, and A. K Jain (2005). "Indian Regional Navigation Satellite System(IRNSS) Concept". In: *Journal of Spacecraft Technology* 15.2, pp. 19–23.

Gauss, C (1839). "General theory of terrestrial magnetism]". In: *results from the observations of the magnetic association in year I* 838, pp. 184–251.

Genest, C and A Favre (2007). "Everything you always wanted to know about copula modeling but were afraid to ask". In: *Journal of hydrologic engineering* 12.4, pp. 347–368.

Genest, C and L Rivest (1993). "Statistical inference procedures for bivariate Archimedean copulas". In: *Journal of the American statistical Association* 88.423, pp. 1034–1043.

Ghil, M, M Allen, M Dettinger, K Ide, D Kondrashov, M Mann, A. W Robertson, A Saunders, Y Tian, F Varadi, et al. (2002). "Advanced spectral methods for climatic time series". In: *Reviews of geophysics* 40.1, pp. 3–1.

Gibert, D, M Holschneider, and J Le Mouël (1998). "Wavelet analysis of the Chandler wobble". In: *Journal of Geophysical Research: Solid Earth* 103.B11, pp. 27069–27089.

Gilbert, W and E Wright (1967). *De magnete, magneticisque corporibus, et de magno magnete tellure: physiologia noua, plurimis & argumentis, & experimentis demonstrata*. excudebat Short.

Glassmeier, K, H Soffel, and J Negendank (2008). *Geomagnetic field variations*. Springer Science & Business Media.

Golyandina, N, V Viktorovich Nekrutkin, and A Zhigljavsky (Jan. 2001). "Analysis of Time Series Structure: SSA and Related Techniques". In: *.New York: Chapman and Hall/CRC* 90.

Golyandina, N and A Zhigljavsky (2013). *Singular Spectrum Analysis for time series*. Springer Science & Business Media.

Gorshkov, V, N Miller, and M Vorotkov (2012). "Manifestation of solar and geodynamic activity in the dynamics of the Earth's rotation". In: *Geomagnetism and Aeronomy* 52.7, pp. 944–952.

Göttl, F, M Schmidt, and F Seitz (2018). "Mass-related excitation of polar motion: an assessment of the new RL06 GRACE gravity field models". In: *Earth, Planets and Space* 70.1, p. 195.

Greff-Lefftz, M and H Legros (1999). "Magnetic field and rotational eigenfrequencies". In: *Physics of the earth and planetary interiors* 112.1-2, pp. 21–41.

Greff-Lefftz, M, H Legros, and V Dehant (2000). "Influence of the inner core viscosity on the rotational eigenmodes of the Earth". In: *Physics of the Earth and Planetary Interiors* 122.3-4, pp. 187–204.

Grinsted, A, J. C Moore, and S Jevrejeva (2004). "Application of the cross wavelet transform and wavelet coherence to geophysical time series". In: *European Geosciences Union(EGU)*.

Gross, R, T Eubanks, J Steppe, A Freedman, J Dickey, and T Runge (1998). "A Kalman-filter-based approach to combining independent Earth-orientation series". In: *Journal of Geodesy* 72.4, pp. 215–235.

Groten, E (2004). "Fundamental parameters and current (2004) best estimates of the parameters of common relevance to astronomy, geodesy, and geodynamics". In: *Journal of Geodesy*.

Heinkelmann, R (2013). "VLBI geodesy: observations, analysis, and results". In: *Geodetic sciences–observations, modeling and applications. S. Jin (ed.), InTech open, doi* 10.54446, pp. 127–156.

Heinkelmann, R, J Boehm, H Schuh, and V Tesmer (2009). "The effect of meteorological input data on the VLBI reference frames". In: *Geodetic Reference Frames*. Springer, pp. 245–251.

Heinkelmann, R and H Schuh (2009). "Very long baseline interferometry: accuracy limits and relativistic tests". In: *Proceedings of the International Astronomical Union* 5.S261, pp. 286–290.

Herrera, R. H, J Han, and M van der Baan (2014). "Applications of the synchrosqueezing transform in seismic time-frequency analysis". In: *Geophysics* 79.3, pp. 55–64.

Hide, R and J Dickey (1991). "Earth's variable rotation". In: *Science* 253.5020, pp. 629–637.

Hinderer, J and W Zurn (1990). "On the complex eigenfrequency of the" nearly diurnal free wobble" and its geophysical interpretation". In: *Variations in Earth Rotation* 9, p. 11.

Hofmann, B, H Lichtenegger, and E Wasle (2007). *GNSS–global navigation satellite systems: GPS, GLONASS, Galileo, and more*. Springer Science & Business Media.

Holme, R and O De Viron (2005). "Geomagnetic jerks and a high-resolution length-of-day profile for core studies". In: *Geophysical Journal International* 160.2, pp. 435–439.

Hoseini, M, F Alshawaf, H Nahavandchi, G Dick, and J Wickert (2020). "Towards a zero-difference approach for homogenizing GNSS tropospheric products". In: *GPS Solutions* 24.1, p. 8.

Hosking, J and J Wallis (1987). "Parameter and quantile estimation for the generalized Pareto distribution". In: *Technometrics* 29.3, pp. 339–349.

Huang, C, V Dehant, X Liao, T Van Hoolst, and M Rochester (2011). "On the coupling between magnetic field and nutation in a numerical integration approach". In: *Journal of Geophysical Research: Solid Earth* 116.B3.

Joe, H (1997). *Multivariate models and multivariate dependence concepts*. CRC Press.

Johnson, T, B Luzum, and J Ray (2005). "Improved near-term Earth rotation predictions using atmospheric angular momentum analysis and forecasts". In: *Journal of Geodynamics* 39.3, pp. 209–221.

Kalarus, M, W Kosek, and H Schuh (2008). "Summary of the Earth orientation parameters prediction comparison campaign". In: *EGU General Assembly Conference Abstracts*. Vol. 1.

Kalarus, M, H Schuh, W Kosek, O Akyilmaz, C Bizouard, D Gambis, R Gross, B Jovanović, S Kumakshev, H Kutterer, et al. (2010). "Achievements of the Earth orientation parameters prediction comparison campaign". In: *Journal of Geodesy* 84.10, pp. 587–596.

Koot, L, M Dumberry, A Rivoldini, O De Viron, and V Dehant (2010). "Constraints on the coupling at the core–mantle and inner core boundaries inferred from nutation observations". In: *Geophysical Journal International* 182.3, pp. 1279–1294.

Kosek, W (2002). "Autocovariance prediction of complex-valued polar motion time series". In: *Advances in Space Research* 30.2, pp. 375–380.

Kosek, W, M Kalarus, T Johnson, W Wooden, D McCarthy, and W Popinski (2005). "A comparison of LOD and UT1-UTC forecasts by different combined prediction techniques". In: *Artificial Satellites* 40.2, pp. 119–125.

Kosek, W, M Kalarus, T Niedzielski, and N Capitaine (2007). *Forecasting of the Earth orientation parameters: comparison of different algorithms*. Observatoire de Paris.

Kosek, W, B Luzum, M Kalarus, A Wnęk, and M Zbylut (2011). "Analysis of pole coordinate data predictions in the earth orientation parameters combination of prediction pilot project". In: *Artificial Satellites* 46.4, pp. 139–150.

Kosek, W, D McCarthy, and B Luzum (1998). "Possible improvement of Earth orientation forecast using autocovariance prediction procedures". In: *Journal of Geodesy* 72.4, pp. 189–199.

Kosek, W and W Popinski (2005). "Forecasting of pole coordinates data by combination of the wavelet decomposition and autocovariance prediction". In: *Proc. Journees*, pp. 139–140.

Krasinsky, G (2002). "Dynamical history of the Earth–Moon system". In: *Celestial Mechanics and Dynamical Astronomy* 84.1, pp. 27–55.

Lachaux, J, A Lutz, D Rudrauf, D Cosmelli, M Le Van Quyen, J Martinerie, and F Varela (2002). "Estimating the time-course of coherence between single-trial brain signals: an introduction to wavelet coherence". In: *Neurophysiologie Clinique/Clinical Neurophysiology* 32.3, pp. 157–174.

Lambeck, K and A Cazenave (1973). "The Earth's rotation and atmospheric circulation—I Seasonal variations". In: *Geophysical Journal International* 32.1, pp. 79–93.

Lambert, S (2007). "Empirical modeling of the retrograde Free Core Nutation". In: *Technical Note ftp://hpiers. obspm. fr/iers/models/fcn/notice. pdf*.

Lambert, S, S Rosat, X Cui, Y Rogister, and C Bizouard (2012). "A search for the free inner core nutation in VLBI data". In: *International VLBI Service for Geodesy and Astrometry 2012 General Meeting Proceedings, "Launching the Next-Generation IVS Network"*.

Langel, R. A (1987). "Main field". In: *Geomagnetism*.

Lau, K. M and H Weng (1995). "Climate signal detection using wavelet transform: How to make a time series sing". In: *Bulletin of the American meteorological society* 76.12, pp. 2391–2402.

Laux, P, S Vogl, W Qiu, H Knoche, and H Kunstmann (2011). "Copula-based statistical refinement of precipitation in RCM simulations over complex terrain". In: *Hydrology and Earth System Sciences* 15.7, pp. 2401–2419.

Le Mouël, J, T Madden, J Ducruix, and V Courtillot (1981). "Decade fluctuations in geomagnetic westward drift and Earth rotation". In: *Nature* 290.5809, pp. 763–765.

Lei, Y, D Zhao, and H Cai (2015). "Prediction of length-of-day using extreme learning machine". In: *Geodesy and geodynamics* 6.2, pp. 151–159.

Li, X, M Ge, X Dai, X Ren, M Fritsche, J Wickert, and H Schuh (2015). "Accuracy and reliability of multi-GNSS real-time precise positioning: GPS, GLONASS, BeiDou, and Galileo". In: *Journal of Geodesy* 89.6, pp. 607–635.

Liao, D, Q Wang, Y Zhou, X Liao, and C Huang (2012). "Long-term prediction of the earth orientation parameters by the artificial neural network technique". In: *Journal of Geodynamics* 62, pp. 87–92.

Lourme, E and P Leloup (2010). "RINEX DORIS 3.0". In: *CNES/IDS technical documentation*.

Lovell, A (1964). "Radio stars in the galaxy". In: *The Observatory* 84, pp. 191–210.

Lühr, H, M Korte, and M Mandea (2009). "The recent geomagnetic field and its variations". In: *Geomagnetic field variations*. Springer, pp. 25–63.

Lühr, H, M Rother, S Maus, W Mai, and D Cooke (2003). "The diamagnetic effect of the equatorial Appleton anomaly: Its characteristics and impact on geomagnetic field modeling". In: *Geophysical Research Letters* 30.17.

Ma, C (1978). "Very Long Baseline Interferometry Applied to Polar Motion, Relativity, and Geodesy." In: *UNIVERSITY OF MARYLAND COLLEGE PARK*.

Ma, C, E Arias, T Eubanks, A Fey, A Gontier, C Jacobs, O Sovers, B Archinal, and P Charlot (1998). "The international celestial reference frame as realized by very long baseline interferometry". In: *The Astronomical Journal* 116.1, p. 516.

Malkin, Z (2013a). "Free core nutation and geomagnetic jerks". In: *Journal of Geodynamics* 72, pp. 53–58.

Malkin, Z (2013b). "On detection of the free inner core nutation from VLBI data". In: *Journées 2013*.

Malkin, Z (2016). "Free core nutation: new large disturbance and connection evidence with geomagnetic jerks". In: *Acta Geodynamica et Geomaterialia* 1.181, pp. 41–45.

Malkin, Z, C Jacobs, E Arias, D Boboltz, J Böhm, S Bolotin, G Bourda, P Charlot, A De Witt, A Fey, et al. (2015). "The ICRF-3: Status, plans, and progress on the next generation International Celestial Reference Frame". In: *Proceedings of the Journees 2014 Systemes de Reference Spatio-temporels, St. Petersburg, Russia*.

Mandea, M, E Bellanger, and J Le Mouël (2000). "A geomagnetic jerk for the end of the 20th century?" In: *Earth and Planetary Science Letters* 183.3-4, pp. 369–373.

Mandea, M, R Holme, A Pais, K Pinheiro, A Jackson, and G Verbanac (2010). "Geomagnetic jerks: rapid core field variations and core dynamics". In: *Space science reviews* 155.1-4, pp. 147–175.

Marchenko, A and O Abrikosov (2001). "Evolution of the Earth's principal axes and moments of inertia: The canonical form of solution". In: *Journal of Geodesy* 74.9, pp. 655–669.

Massel, S (2001). "Wavelet analysis for processing of ocean surface wave records". In: *Ocean Engineering* 28.8, pp. 957–987.

Mathews, P, B Buffett, T Herring, and I Shapiro (1991). "Forced nutations of the Earth: Influence of inner core dynamics: 1. Theory". In: *Journal of Geophysical Research: Solid Earth* 96.B5, pp. 8219–8242.

Mathews, P, T Herring, and B Buffett (2002). "Modeling of nutation and precession: New nutation series for nonrigid Earth and insights into the Earth's interior". In: *Journal of Geophysical Research: Solid Earth* 107.B4, ETG–3.

Maus, S, M Rother, C Stolle, W Mai, S Choi, H Lühr, D Cooke, and C Roth (2006). "Third generation of the Potsdam Magnetic Model of the Earth (POMME)". In: *Geochemistry, Geophysics, Geosystems* 7.7.

McCarthy, D and B Luzum (1991). "Prediction of Earth orientation". In: *Bulletin géodésique* 65.1, pp. 18–21.

McElhinny, M and P McFadden (1998). *The magnetic field of the earth: paleomagnetism, the core, and the deep mantle*. Vol. 63. Academic Press.

Meyers, S. D, B. G Kelly, and J. J O'Brien (1993). "An introduction to wavelet analysis in oceanography and meteorology: With application to the dispersion of Yanai waves". In: *Monthly weather review* 121.10, pp. 2858–2866.

Modiri, S, S Belda, R Heinkelmann, M Hoseini, J. M Ferrándiz, and H Schuh (2018). "Polar motion prediction using the combination of SSA and Copula-based analysis". In: *Earth, Planets and Space* 70.1, p. 115.

Modiri, S, S Belda, M Hoseini, R Heinkelmann, J. M Ferrándiz, and H Schuh (2019). "A new hybrid method to improve EOP prediction". In: *Geophysical Research Abstracts*. Vol. 21.

Modiri, S, S Belda, M Hoseini, R Heinkelmann, J. M Ferrándiz, and H Schuh (2020). "A new hybrid method to improve the ultra-short-term prediction of LOD". In: *Journal of Geodesy* 94.2, p. 23.

Modiri, S, C Lorenz, N Sneeuw, and H Kunstmann (2015). "Copula-based estimation of large-scale water storage changes: exploiting the dependence structure between hydrological and GRACE data". In: *EGU General Assembly Conference Abstracts*. Vol. 17.

Munk, W and G MacDonald (1975). "The rotation of the earth: a geophysical discussion." In: *Cambridge (UK): Cambridge University Press, 19+ 323 p.*

Munk, W and R Revelle (1952). "On the geophysical interpretation of irregularities in the rotation of the Earth". In: *Geophysical Journal International* 6, pp. 331–347.

Murphy, K (2012). *Machine learning: a probabilistic perspective*. Cambridge, MA.

Nastula, J, R Gross, and D Salstein (2012). "Oceanic excitation of polar motion: Identification of specific oceanic areas important for polar motion excitation". In: *Journal of Geodynamics* 62, pp. 16–23.

Nelsen, R (2007). *An introduction to copulas*. Springer Science & Business Media.

Ngui, W, M Leong, L Hee, and A Abdelrhman (2013). "Wavelet analysis: mother wavelet selection methods". In: *Applied mechanics and materials*. Vol. 393. Trans Tech Publ, pp. 953–958.

Niedzielski, T and W Kosek (2008). "Prediction of UT1–UTC, LOD and AAM χ 3 by combination of least-squares and multivariate stochastic methods". In: *Journal of Geodesy* 82.2, pp. 83–92.

Nilsson, T, J Böhm, and H Schuh (2010). "Sub-diurnal Earth rotation variations observed by VLBI". In: *Artificial Satellites* 45.2, pp. 49–55.

Nilsson, T, J Böhm, and H Schuh (2011). "Universal time from VLBI single-baseline observations during CONT08". In: *Journal of Geodesy* 85.7, pp. 415–423.

Nilsson, T, R Heinkelmann, M Karbon, V Raposo-Pulido, B Soja, and H Schuh (2014). "Earth orientation parameters estimated from VLBI during the CONT11 campaign". In: *Journal of Geodesy* 88.5, pp. 491–502.

Oldenborgh, G van, S Philip, E Aalbers, R Vautard, F Otto, K Haustein, F Habets, R Singh, and H Cullen (2016). "Rapid attribution of the May/June 2016 flood-inducing precipitation in France and Germany to climate change". In: *Hydrol Earth Syst Sci Discuss* 10.

Olsen, N, R Holme, G Hulot, T Sabaka, T Neubert, L Tøffner-Clausen, F Primdahl, J Jørgensen, J Léger, D Barraclough, et al. (2000). "Ørsted initial field model". In: *Geophysical Research Letters* 27.22, pp. 3607–3610.

Olsen, N, H Lühr, C Finlay, T Sabaka, I Michaelis, J Rauberg, and L Tøffner-Clausen (2014). "The CHAOS-4 geomagnetic field model". In: *Geophysical Journal International* 197.2, pp. 815–827.

Olsen, N, H Lühr, T Sabaka, M Mandea, M Rother, L Tøffner-Clausen, and S Choi (2006). "CHAOS—a model of the Earth's magnetic field derived from CHAMP, Ørsted, and SAC-C magnetic satellite data". In: *Geophysical Journal International* 166.1, pp. 67–75.

Olsen, N and M Mandea (2007). "Investigation of a secular variation impulse using satellite data: The 2003 geomagnetic jerk". In: *Earth and Planetary Science Letters* 255.1-2, pp. 94–105.

Olsen, N, M Mandea, T Sabaka, and L Tøffner-Clausen (2009). "CHAOS-2—a geomagnetic field model derived from one decade of continuous satellite data". In: *Geophysical Journal International* 179.3, pp. 1477–1487.

Olsen, N, M Mandea, T Sabaka, and L Tøffner-Clausen (2010). "The CHAOS-3 geomagnetic field model and candidates for the 11th generation IGRF". In: *Earth, planets and space* 62.10, p. 1.

Patton, A (2006). "Modelling asymmetric exchange rate dependence". In: *International economic review* 47.2, pp. 527–556.

Patton, A (2009). "Copula–based models for financial time series". In: *Handbook of financial time series*. Springer, pp. 767–785.

Pavlis, N K, S. A Holmes, S. C Kenyon, and J. K Factor (2012). "The development and evaluation of the Earth Gravitational Model 2008 (EGM2008)". In: *Journal of geophysical research: solid earth* 117.B4.

Peddie, N. W (1982). "International geomagnetic reference field". In: *Journal of geomagnetism and geoelectricity* 34.6, pp. 309–326.

Petit, G and B Luzum (2010). *IERS conventions (2010), IERS Tech. Note, 36*. Tech. rep. Verlagdes Bundesamts für Kartographie und Geodäsie, Frankfurt am Main, Germany.

Plag, H and M Pearlman (2007). "The Global Geodetic Observing System: Meeting the Requirements of a Global Society on a Changing Planet in 2020 The Reference Document". In: *International Association of Geodesy*.

Plag, H, M Rothacher, M Pearlman, R Neilan, and C Ma (2009). "The global geodetic observing system". In: *Advances in Geosciences: Volume 13: Solid Earth (SE)*. World Scientific, pp. 105–127.

El-Rabbany, A (2002). *Introduction to GPS: the global positioning system*. Artech house.

Rachev, S and S Mittnik (2000). *Stable Paretian models in finance*. John Willey\& Sons, New York.

Richard T, A, J. M Moran, and George W Swenson J (2017). *Interferometry and synthesis in radio astronomy*. Springer Nature.

Rioul, O and P Duhamel (1992). "Fast algorithms for discrete and continuous wavelet transforms". In: *IEEE transactions on information theory* 38.2, pp. 569–586.

Roberts, P. H and G. A Glatzmaier (2000). "Geodynamo theory and simulations". In: *Reviews of modern physics* 72.4, p. 1081.

Rothacher, M, G Beutler, D Behrend, A Donnellan, J Hinderer, C Ma, C Noll, J Oberst, M Pearlman, H Plag, et al. (2009). "The future global geodetic observing system". In: *Global Geodetic Observing System*. Springer, pp. 237–272.

Rubincam, D (1984). "Postglacial rebound observed by LAGEOS and the effective viscosity of the lower mantle". In: *Journal of Geophysical Research: Solid Earth* 89.B2, pp. 1077–1087.

Sabaka, T, N Olsen, and M Purucker (2004). "Extending comprehensive models of the Earth's magnetic field with Ørsted and CHAMP data". In: *Geophysical Journal International* 159.2, pp. 521–547.

Salvadori, G and C De Michele (2007). "On the use of copulas in hydrology: theory and practice". In: *Journal of Hydrologic Engineering* 12.4, pp. 369–380.

Sasao, T and J Wahr (1981). "An excitation mechanism for the free 'core nutation'". In: *Geophysical Journal International* 64.3, pp. 729–746.

Save, H, B Tapley, and S Bettadpur (2018). "GRACE RL06 reprocessing and results from CSR". In: *EGU General Assembly Conference Abstracts*. Vol. 20, p. 10697.

Schröter, K, M Kunz, F Elmer, B Mühr, and B Merz (2015). "What made the June 2013 flood in Germany an exceptional event? A hydro-meteorological evaluation". In: *Hydrology and Earth System Sciences* 19.1, pp. 309–327.

Schuh, H (1999). "The rotation of the Earth observed by VLBI". In: *Acta Geodaetica et Geophysica Hungarica* 34.4, pp. 421–432.

Schuh, H (2000). "Contributions of VLBI to Space Geodesy". In: *Towards an Integrated Global Geodetic Observing System (IGGOS)*. Springer, pp. 33–40.

Schuh, H and D Behrend (2012). "VLBI: a fascinating technique for geodesy and astrometry". In: *Journal of Geodynamics* 61, pp. 68–80.

Schuh, H and J Böhm (2013). "Very long baseline interferometry for geodesy and astrometry". In: *Sciences of Geodesy-II*. Springer, pp. 339–376.

Schuh, H, C Huang, F Seitz, A Brzeziński, C Bizouard, B Chao, R Gross, W Kosek, D Salstein, O Titov, et al. (2011). "Commission 19: rotation of the Earth". In: *Proceedings of the International Astronomical Union* 7.T28A, pp. 33–46.

Schuh, H, R König, D Ampatzidis, S Glaser, F Flechtner, R Heinkelmann, and T. J Nilsson (2015). "GGOS-SIM: simulation of the reference frame for the global geodetic observing system". In: *REFAG 2014*. Springer, pp. 95–100.

Schuh, H and L Moehlmann (1989). "Ocean loading station displacements observed by VLBI". In: *Geophysical Research Letters* 16.10, pp. 1105–1108.

Schuh, H and H Schmitz-Hübsch (2000). "Short period variations in Earth rotation as seen by VLBI". In: *Surveys in Geophysics* 21.5-6, pp. 499–520.

Schuh, H, M Ulrich, D Egger, J Müller, and W Schwegmann (2002). "Prediction of Earth orientation parameters by artificial neural networks". In: *Journal of Geodesy* 76.5, pp. 247–258.

Seeber, G (2008). *Satellite geodesy: foundations, methods, and applications*. Walter de gruyter.

Seidelmann, P and J Kovalevsky (2002). "Application of the new concepts and definitions (ICRS, CIP and CEO) in fundamental astronomy". In: *Astronomy & Astrophysics* 392.1, pp. 341–351.

Seitz, F and H Schuh (2010). "Earth rotation". In: *Sciences of Geodesy-I*. Springer, pp. 185–227.

Seitz, M, D Angermann, M Bloßfeld, H Drewes, and M Gerstl (2012). "The 2008 DGFI realization of the ITRS: DTRF2008". In: *Journal of Geodesy* 86.12, pp. 1097–1123.

Sharma, K and R Poonia (2018). "Review study of navigation systems for indian regional navigation satellite system (IRNSS)". In: *Soft Computing: Theories and Applications*. Springer, pp. 735–742.

Shen, W, W Chen, and R Sun (2008). "Earth's temporal principal moments of inertia and variable rotation". In: *Geo-spatial Information Science* 11.2, pp. 127–132.

Shirai, T, T Fukushima, and Z Malkin (2005). "Detection of phase disturbances of free core nutation of the Earth and their concurrence with geomagnetic jerks". In: *Earth, planets and space* 57.2, pp. 151–155.

Silva, L, L Jackson, and J Mound (2012). "Assessing the importance and expression of the 6 year geomagnetic oscillation". In: *Journal of Geophysical Research: Solid Earth* 117.B10.

Sinha, S, P. S Routh, P. D Anno, and J. P Castagna (2005). "Spectral decomposition of seismic data with continuous-wavelet transform". In: *Geophysics* 70.6, P19–P25.

Sklar, M (1959). "Fonctions de repartition an dimensions et leurs marges". In: *Publ. Inst. Statist. Univ. Paris* 8, pp. 229–231.

Smith, M (1974). "The scalar equations of infinitesimal elastic-gravitational motion for a rotating, slightly elliptical Earth". In: *Geophysical Journal International* 37.3, pp. 491–526.

Sovers, O, J Fanselow, and C Jacobs (1998). "Astrometry and geodesy with radio interferometry: experiments, models, results". In: *Reviews of Modern Physics* 70.4, p. 1393.

Stamatakos, N (2017). "IERS Rapid Service Prediction Center Products and Services: Improvement, Chages, and Challenges, 2012 to 2017." In: *Proceedings of the Journées Systèmes de référence spatio-temporels*.

Stephens, M (1977). "Goodness of fit for the extreme value distribution". In: *Biometrika* 64.3, pp. 583–588.

Sun, Z, T Xu, C Jiang, Y Yang, and N Jiang (2019). "An improved prediction algorithm for Earth's polar motion with considering the retrograde annual and semi-annual wobbles based on least squares and autoregressive model". In: *Acta Geodaetica et Geophysica* 54.4, pp. 499–511.

Tapley, B, S Bettadpur, J Ries, P Thompson, and M Watkins (2004a). "GRACE measurements of mass variability in the Earth system". In: *Science* 305.5683, pp. 503–505.

Tapley, B, S Bettadpur, M Watkins, and C Reigber (2004b). "The gravity recovery and climate experiment: Mission overview and early results". In: *Geophysical Research Letters* 31.9.

Tapley, B and C Reigber (2001). "The GRACE mission: status and future plans". In: *AGU Fall Meeting Abstracts*.

Tapley, B, J Ries, S Bettadpur, D Chambers, M Cheng, F Condi, B Gunter, Z Kang, P Nagel, R Pastor, et al. (2005). "GGM02–An improved Earth gravity field model from GRACE". In: *Journal of Geodesy* 79.8, pp. 467–478.

Tavernier, G, H Fagard, M Feissel-Vernier, F Lemoine, C Noll, J Ries, L Soudarin, and P Willis (2005). "The international DORIS service". In: *Advances in Space Research* 36.3, pp. 333–341.

Thébault, E, C Finlay, C Beggan, P Alken, J Aubert, O Barrois, F Bertrand, T Bondar, A Boness, L Brocco, et al. (2015). "International geomagnetic reference field: the 12th generation". In: *Earth, Planets and Space* 67.1, p. 79.

Torta, J, F Pavón-Carrasco, S Marsal, and C Finlay (2015). "Evidence for a new geomagnetic jerk in 2014". In: *Geophysical Research Letters* 42.19, pp. 7933–7940.

Tzanetakis, G, G Essl, and P Cook (2001). "Audio analysis using the discrete wavelet transform". In: *Proc. Conf. in Acoustics and Music Theory Applications*. Vol. 66.

Vautard, R, P Yiou, and M Ghil (1992). "Singular-spectrum analysis: A toolkit for short, noisy chaotic signals". In: *Physica D: Nonlinear Phenomena* 58.1-4, pp. 95–126.

Verhoest, N, M van den Berg, B Martens, H Lievens, E. F Wood, M Pan, Y. H Kerr, A Al Bitar, S. K Tomer, M Drusch, et al. (2015). "Copula-based downscaling of coarse-scale soil moisture observations with implicit bias correction". In: *IEEE Transactions on Geoscience and Remote Sensing* 53.6, pp. 3507–3521.

Vogl, S, P Laux, W Qiu, G Mao, and H Kunstmann (2012). "Copula-based assimilation of radar and gauge information to derive bias-corrected precipitation fields". In: *Hydrology and Earth System Sciences* 16.7, pp. 2311–2328.

Vondrák, J and C Ron (2015). "Earth orientation and its excitations by atmosphere, oceans, and geomagnetic jerks". In: *Serbian Astronomical Journal* 191, pp. 59–66.

Vrieze, S (2012). "Model selection and psychological theory: a discussion of the differences between the Akaike information criterion (AIC) and the Bayesian information criterion (BIC)." In: *Psychological methods* 17.2, p. 228.

Wahr, J (1983). "The effects of the atmosphere and oceans on the Earth's wobble and on the seasonal variations in the length of day—II. Results". In: *Geophysical Journal International* 74.2, pp. 451–487.

Wahr, J (1988). "The Earth's rotation". In: *Annual Review of Earth and Planetary Sciences* 16.1, pp. 231–249.

Wahr, J, R Nerem, and S Bettadpur (2015). "The pole tide and its effect on GRACE time-variable gravity measurements: Implications for estimates of surface mass variations". In: *Journal of Geophysical Research: Solid Earth* 120.6, pp. 4597–4615.

Wang, Q, Y Du, and J Liu (2014). "Introducing atmospheric angular momentum into prediction of length of day change by generalized regression neural network model". In: *Journal of Central South University* 21.4, pp. 1396–1401.

Wang, W and M Wells (2000). "Model selection and semiparametric inference for bivariate failure-time data". In: *Journal of the American Statistical Association* 95.449, pp. 62–72.

Whipple, A (1993). "Dynamics of the Earth-Moon system". In: *Advances in Space Research* 13.11, pp. 213–219.

Williams, J, S Turyshev, D Boggs, and J Ratcliff (2006). "Lunar laser ranging science: gravitational physics and lunar interior and geodesy". In: *Advances in Space Research* 37.1, pp. 67–71.

Willis, P, C Boucher, H Fagard, B Garayt, and M Gobinddass (2010a). "Contributions of the French Institut Géographique National (IGN) to the international DORIS service". In: *Advances in space research* 45.12, pp. 1470–1480.

Willis, P, H Fagard, P Ferrage, F. G Lemoine, C. E Noll, R Noomen, M Otten, J. C Ries, M Rothacher, L Soudarin, et al. (2010b). "The international DORIS service (IDS): toward maturity". In: *Advances in space research* 45.12, pp. 1408–1420.

Włodzimierz, H (1990). "Polar motion prediction by the least-squares collocation method". In: *Earth Rotation and Coordinate Reference Frames*. Springer, pp. 50–57.

Wu, F, G Chang, and K Deng (2019). "One-step method for predicting LOD parameters based on LS+ AR model". In: *Journal of Spatial Science*, pp. 1–12.

Xu, X and Y Zhou (2015). "EOP prediction using least square fitting and autoregressive filter over optimized data intervals". In: *Advances in Space Research* 56.10, pp. 2248–2253.

Xu, X, Y Zhou, and X Liao (2012). "Short-term earth orientation parameters predictions by combination of the least-squares, AR model and Kalman filter". In: *Journal of Geodynamics* 62, pp. 83–86.

Yang, Y, W Gao, S Guo, Y Mao, and Y Yang (2019). "Introduction to BeiDou-3 navigation satellite system". In: *Navigation* 66.1, pp. 7–18.

Yoder, C, J Williams, J Dickey, B Schutz, R Eanes, and B Tapley (1983). "Secular variation of Earth's gravitational harmonic J2 coefficient from LAGEOS and nontidal acceleration of Earth rotation". In: *Nature* 303.5920, p. 757.

Zotov, L, X Xu, Y Zhou, and A Skorobogatov (2018). "Combined SAI-SHAO prediction of earth orientation parameters since 2012 till 2017". In: *Geodesy and Geodynamics* 9.6, pp. 485–490.

ISSN 2190-7110